

**A NOVEL MODEL FOR ELECTROCOAGULATION
REACTORS: PROCESS BASED APPROACH TO
ADDRESS THE DESIGN AND SCALE-UP ISSUES**

CHARUNI WIJERATHNE DISSANAYAKA MUDIYANSELAGE

A thesis submitted in partial fulfilment of the requirements of Liverpool John
Moore's University for the degree of Doctor of Philosophy

October 2021

ABSTRACT

The wider application of electrocoagulation (EC) as a water and industrial wastewater treatment technology has been hindered due to knowledge gaps in the design and operational optimization process. The conventional EC reactor design follows a black-box design approach, while white-box modelling is widely applied in other water treatment systems. This is due to the complex nature of the electrochemical effect on the pollutant abatement process. Hence, this study aimed to address this knowledge gap by developing a novel numeric computing platform model for defluoridation established on pollutant abatement mechanisms to address the design and modelling issues such as scale-up and process optimisation of EC reactors. Dissolved fluoride was selected as the pollutant, considering the vast body of knowledge available on defluoridation using electrocoagulation. A critical evaluation of the scientific and mechanistic approaches developed over the years for EC was carried out to develop a process-based conceptual model (PBCM) for batch and continuous EC reactors for defluoridation. Here, the EC process was conceptualized as a conventional water treatment process. This engineering approach of identification of the pollutant abatement and floc aggregation mechanisms resulted in the discretisation of the defluoridation process in EC reactors. Next, the model equations were numerically transformed into a scheme of integrated continuous-time models by applying the principle of conservation of mass to the system. Finally, the PBCM was implemented in two computer platforms namely, Microsoft® Excel® ver. 2016 and MATLAB® ver. R2021a which were then validated using primary and secondary data. Ten physical and chemical calibration parameters were identified from the process-based models from which the integrated effects were evaluated at the model calibration stage. Primary data for the model calibration and validation were collected through experiments that were conducted at the laboratory level for both batch and continuous reactors at two geometric scales. The extrapolation of the PBCM for batch and continuous EC for varied operating conditions, pollutant types and scales were

evaluated. Also, the optimization of retention time and the relationship of hydrodynamic parameters (pressure, flow velocity) and reactor geometry were analysed using the novel model. Evaluation of model prediction accuracy was conducted using Mean Squared Error (MSE), Root Mean Square Error (RMSE).

It could be noted that there is a good agreement between the experimental fluoride concentrations and model simulations of fluoride concentrations where R^2 is 0.994, thus proving the higher precision of the model predictions. The optimization process consisted of a local sensitivity test which was carried out in MATLAB® ver. R2021a using a programme written to analyse each calibration parameter range within the selected domain. The d_j ; colloid size which participates in the adsorption and flocculation process was found to be the most sensitive parameter for the PBCM. The extended use of the model could be well evaluated using both calibration and experimental parameters in terms of application to scale-up/down, longer operation time, different pollutants, etc. A novel numeric computing platform model for EC to simultaneously address the prediction of pollution removal, settling/flotation, scale-up and techno-economic optimization was established from this study, thus aiding wider applicability of EC reactors.

ACKNOWLEDGEMENT

I would like to take this opportunity to thank each and every one who inspired and motivated me to achieve this milestone. This achievement is very special to me, as it is proof of my resilience to myself and a reward for the challenges I was able to overcome with the support of kind and generous people in my life.

First and foremost I am extremely grateful to my former supervisor, Dr Bill Atherton who was a tremendous source of strength during my first two years of research study as a part-time distance learning student from Sri Lanka. I am extremely thankful to him for entrusting and assisting to expand the potential of this budding water researcher who dreams of creating a positive impact for the generations to come.

I also owe my deep gratitude to the former dean of the faculty of engineering & technology of Liverpool John Moores University (LJMU), Prof. Ahmed Al-Shamma'a, who took a keen interest in my project and approving the dean's scholarship.

I am deeply thankful to Dr Iacopo Carnacina, the principal supervisor of my research for his invaluable advice, continuous support, and patience during my PhD study without whom this would have not been possible. I would also like to express my sincere gratitude to Dr Clare Harris for her valuable contribution during the latter stage of my study. I would also like to thank Dr Khalid Hashim for his kind guidance and support on my work. I am forever grateful to Dr Sujithra K. Weragoda, Project Director of China Sri Lanka Research Grant Project (CSLRGP) – my research advisor from Sri Lanka for this study who was a constant guiding light for my professional and academic career since 2009. I would also like to appreciate the laboratory staff members of the department of civil engineering and the department of science especially Mal Feegan and Geoffery Henshaw for all the considerate assistance extended for my laboratory work.

I would also like to express my sincere gratitude for the financial assistance received from the British Council Small-Scale Research Project Scheme - South Asia Science

Programme, Faculty of Engineering and Technology, LJMU and National Research Council of Sri Lanka (NRC SL), project ref. no: TO-NRC-16-015 for the experimental work of this study.

I would not forget to remember Prof. Rafid Al-Khaddar, former Head of Department of Civil Engineering, LJMU for his encouragement and for his timely support whenever needed. I would also like to thank Prof. Rohan Weerasooriya from the National Institute of Fundamental Sciences Sri Lanka, Miss Apsara from CSLRGP, and especially Dr Geoffery Parker from LJMU for their kind support extended during the first two years of the study period.

This journey has been both extremely lonely and extremely convivial. I owe a deep thank you to my remarkable friend Dr Shalika Walker for her constant support and guidance whenever I was in need. I would also like to thank my dear friends Larry Wilkison and Bhagya Manjaree for their continuous motivation and support. Their moral support has made all the difference.

I take this opportunity to extend my sincere gratitude and love to my beloved mother, father and siblings for their unwavering support and belief in me. Last, but not least, I would like to express my appreciation to my husband Rasika, elder daughter Sanya, second daughter Harinya, and my little baby Amelia. It is for their unconditional love and support I was able to finish my PhD within the right time frame. As for my husband Rasika, his support was immense. He is my most enthusiastic cheerleader; he is my best friend; and he is an amazing husband and father. He is my rock. He has shared this entire amazing journey with me, so it only seems right that I dedicate this thesis to him.

CONTENTS

ABSTRACT	i
ACKNOWLEDGEMENT.....	iii
LIST OF FIGURES	ix
LIST OF TABLES	xiv
ACRONYMS.....	xvi
SYMBOLS	xvii
Chapter 1. Introduction	1
1.1. The global perspective of water	1
1.2. Electrocoagulation overview	2
1.3. Modelling of electrocoagulation	9
1.4. Aim/objectives	12
1.5. Thesis structure	12
Chapter 2. Theoretical background of EC reactor design	15
2.1. Chapter overview.....	15
2.2. Pollutant abatement mechanism.....	15
2.3. EC cell potential.....	18
2.4. EC operating parameters	20
2.5. Mathematical and statistical modelling of EC	21
2.6. EC reactor types	22
2.7. Mass balance analysis in EC reactors	24
2.8. EC reactor scale-up	27
2.9. Chapter 2 conclusion	29
Chapter 3. Research design & process based conceptual Model (PBCM) development for electrocoagulation defluoridation	31
3.1. Chapter overview.....	31
3.2. Research design.....	32
3.3. Conceptual model development for defluoridation using electrocoagulation	36
3.3.1. Conventional theoretical and empirical modelling.....	36
3.3.2. Development of the process-based conceptual model (PBCM)	37
3.3.3. Sub-model 1: electrolysis model	38
3.3.4. Sub-model 2: hydrolysis model	38
3.3.5. Sub-model 3: coagulation model	40
3.3.6. Sub-model 4: flocculation model	41
3.3.7. Sub-model 5: flotation/settling model.....	45

3.4.	Conclusion of chapter 3.....	48
Chapter 4. Materials and methods – PBCM application to batch electrocoagulation reactors		
	49	
4.1.	Chapter overview.....	49
4.2.	Discrete-continuous model conversion scheme of the PBCM.....	50
4.3.	Experimental apparatus.....	57
4.4.	Experimental method statement.....	60
4.5.	Conclusion of chapter 4.....	62
Chapter 5. Results and discussion - PBCM calibration and validation for batch electrocoagulation reactors		
	63	
5.1.	Chapter overview.....	63
5.2.	PBCM calibration and validation using experimental data.....	64
5.3.	PBCM validation using literature data.....	66
5.4.	Comparison of total pollutant mass abatement for primary and secondary data....	70
5.5.	Conclusion of chapter 5.....	72
Chapter 6. Materials and methods for PBCM validation using a continuous electrocoagulation reactor		
	73	
6.1.	Chapter overview.....	73
6.2.	Discrete-continuous model conversion scheme of the PBCM in continuous EC reactor.....	74
6.3.	Experimental procedure.....	84
6.3.1.	Continuous-flow electrocoagulation laboratory reactor experiments.....	84
6.3.2.	Experimental method statement.....	93
6.4.	Calibration and validation process of the conceptual model.....	96
6.4.1.	Overview of the calibration and validation process.....	96
6.4.2.	Calibration parameters.....	100
6.4.3.	Model accuracy measurement.....	103
6.5.	Conclusion of chapter 6.....	105
Chapter 7. Results and discussion – PBCM calibration and validation for continuous electrocoagulation reactor		
	106	
7. 1.	Chapter overview.....	106
7. 2.	Simulation of the electrolysis process.....	108
7. 3.	Simulation of the hydrolysis process.....	111
7. 4.	Simulation of the coagulation process.....	113
7. 5.	Simulation of the flocculation process.....	119

7. 6.	Simulation of the flotation process	123
7. 7.	Simulation of floc adsorption on electrodes.....	129
7. 8.	Energy calculation and economic optimisation.....	129
7. 9.	The goodness of fit and the precision of the Model.....	132
7. 10.	Scale-up/down operation.....	135
7. 11.	Sensitivity analysis for optimization of the model.....	140
7. 12.	Process-based conceptual model validation – secondary data.....	146
7. 13.	Chapter 7 conclusion	149
Chapter 8.	Conclusions and further recommendations.....	150
8. 1.	Overview of the study.....	150
8. 2.	Outcome – Proposed systematic approach for EC reactors design and scale-up...	152
8. 3.	Significance of the outcome	155
8. 4.	Contribution to knowledge	157
8. 5.	Research limitations of this study.....	157
8. 6.	Impact from the research	158
8. 7.	Recommendations for further studies.....	159
REFERENCES	161
APPENDICES	169
(A)	MATLAB® EC batch reactor process-based conceptual model.....	169
(B)	MATLAB® EC continuous reactor process-based conceptual model.....	177
(C)	Dissolved fluoride concentration (mg l – 1) results of laboratory-scale continuous EC operations	186
(D)	Residual plots and regression analysis results summaries of calibration parameters.	187
i.	Residual plots of calibration parameters	187
ii.	Regression analysis of K_L local sensitivity test.....	189
iii.	Regression Analysis of n Local Sensitivity Test.....	190
iv.	Regression Analysis of q_m Local Sensitivity Test	191
v.	Regression Analysis of d_j Local Sensitivity Test	192
vi.	Regression Analysis of K_E Local Sensitivity Test	193
vii.	Regression Analysis of K Local Sensitivity Test.....	194
viii.	Regression Analysis of ϕ Local Sensitivity Test.....	195
ix.	Regression Analysis of α_{db} & η_T Local Sensitivity Test	196
x.	Regression Analysis of α Local Sensitivity Test	197

LIST OF FIGURES

Figure 1-1: Proportion of population using safely managed to drink water services in 2020 (%) (UN-Water 2021)	1
Figure 1-2: Electricity conversion efficiency and retail price in the USA 1900-1998 (Ayres 2003)	3
Figure 1-3: Essential criteria for reactor operation optimisation	4
Figure 1-4: Industrial wastewater treatment unit in the United States of America	5
Figure 1-5: Arsenic contaminated groundwater treatment unit in South Africa (Proxa-water 2021)	5
Figure 1-6: Effect of current density and EC time on turbidity removal (%) (Tir and Moulai-Mostefa 2008)	6
Figure 1-7: Response surface for the Total floated solids (TFS) / Total Suspended Solids (TSS) relationship for three different values of initial kaolin concentration: a [kaolin] 500 mg l ⁻¹ , b [kaolin] 1000 mg l ⁻¹ and c [kaolin] 1500 mg l ⁻¹ (Rodrigo 2016)	8
Figure 1-8: Parameters involved in EC reactor optimization	8
Figure 1-9: Interactions occurring within an EC reactor	11
Figure 1-10: Thesis structure with chapter details	14
Figure 2-1: Solubility diagram of aluminum hydroxide (Al(OH) ₃ (s)) considering only mononuclear aluminum species (Holt, Barton et al. 2005)	17
Figure 2-2: Electrodes arrangement classification in electrocoagulation reactors: (a) monopolar electrodes in parallel connection, (b) monopolar electrodes in serial connection and (c) bipolar electrodes in serial connection.	21
Figure 2-3: Response surface plot (a) and contour plot (b) of predicted dye removal factor as a function of the operating temperature and initial pH at C = 1.15 g l ⁻¹	22
Figure 2-4: Most widely used EC reactors types (a) batch, (b) plug-flow, (c) continuous reactors	22
Figure 2-5: Schematic diagram of a Plug-flow Reactor. 1) 3D perforated cylindrical impeller (anode). 2) Rod (cathode). 3) Conical Hopper Bottom for Sludge collection. 4) Mechanical stirrer. 5) DC Power Supply Unit 6) Inlet for wastewater. 7) Outlet for treated water (Choudhary and Mathur 2017)	23

Figure 2-6: Schematic diagram of a continuous EC reactor (Ntambwe Kambuyi, Bejjany et al. 2021)	23
Figure 2-7: Schematic diagram of a batch EC reactor set-up (1) multiple-input DC power supply (2) single-input DC power supply (3) cathode plate (4) anode plate (5) EC cell (Muhammad Niza, Abdul Razak et al. 2021)	24
Figure 2-8: Continuous, steady-flow complete-mix reactor considered for mass balance analysis (Notations used in the figure are explained alongside Eq.16)	25
Figure 3-1: The chapter layout of the thesis	31
Figure 3-2: The step-by-step process of the overall study (Process-based conceptual model (PBCM), electrocoagulation (EC))	35
Figure 3-3: The component processes used for the fluoride removal model	37
Figure 3-4: Flocculation mechanisms – the modes of transport of colloids leading to the collision	41
Figure 3-5: Modernised flocculation models	42
Figure 3-6: Model representation of porous aggregate (Chellam and Wiesner 1993)	43
Figure 4-1: The chapter layout of the thesis	49
Figure 4-2: (a) Schematic representation of ring structure formed by six aluminium hydroxide octahedral, (b) and Electron photomicrograph of microcrystalline gibbsite (Hem and Roberson 1967).	52
Figure 4-3: Step-by-step calculation process of the model parameters of PBCM	56
Figure 4-4: Bench-scale EC batch reactor set-up at NIFS Laboratory, Sri Lanka	58
Figure 5-1: The chapter layout of the thesis	63
Figure 5-2: The model simulations for laboratory level batch experiment data	65
Figure 5-3: Process Based Conceptual Model (PBCM) simulation of intermediate parameters for lab experimental parameter inputs	66
Figure 5-4: The model simulations for laboratory level batch experiment data by Emamjomeh (2006)	67
Figure 5-5: Process Based Conceptual Model (PBCM) simulation of intermediate parameters for Emamjomeh (2006) experimental parameter inputs	68
Figure 6-1: The chapter layout of the thesis	73

Figure 6-2: (a) Schematic representation of ring structure formed by six aluminium hydroxide octahedra, (b) and Electron photomicrograph of microcrystalline gibbsite (Hem and Roberson 1967).	77
Figure 6-3: Step-by-step calculation process of the model parameters of PBCM	83
Figure 6-4: Continuous flow electrocoagulation reactor set-up	85
Figure 6-5: DC power supply unit (200W, 60 V/ 8 A, 4-Channel Linear DC Power Supply GW Instec GPS 4303)	88
Figure 6-6: Spectrophotometer (HACH DR2800) and the relevant chemicals used to analyse dissolved fluoride and aluminium.	89
Figure 6-7: (a) Variable area flow meter, (b) Multifunction pH meter	90
Figure 6-8: (a) Reactor outlets at three levels and the sampling port, (b) Fluoride ion-selective electrode & conductivity probe	91
Figure 6-9: Polarity alteration of electrodes by interchanging connections in each experiment	93
Figure 6-10: Collected samples during an experiment run	94
Figure 6-11: Microsoft® Excel® ver. 2016 template utilised for data entry	95
Figure 6-12: Data processing model layout of the PBCM in programming and numeric computing platforms	96
Figure 7-1: The chapter layout of the thesis	106
Figure 7-2: Aluminium variation with time for different current densities at initial fluoride concentration 2 mg l ⁻¹	109
Figure 7-3: Aluminium variation with time for different current densities at initial fluoride concentration 6 mg l ⁻¹	109
Figure 7-4: Model simulation of aluminium hydroxide variation with time for different current densities at initial fluoride concentration 2 mg l ⁻¹	111
Figure 7-5: Model simulation of aluminium hydroxide variation with time for different current densities at initial fluoride concentration 6 mg l ⁻¹	112
Figure 7-6: Model simulation of aluminium hydroxide variation during the initial 300 s for different current densities at initial fluoride concentration 2 mg l ⁻¹	113
Figure 7-7: Model simulation of adsorbent concentration variation with time for different current densities at initial fluoride concentration 2 mg l ⁻¹	114

Figure 7-8: Model simulation of q_e variation with time for different current densities at initial fluoride concentration 2 mg l^{-1}	114
Figure 7-9: Model simulation of dissipation of fluoride variation with time for different current densities at initial fluoride concentration 2 mg l^{-1}	114
Figure 7-10: Model simulation of fluoride variation with time for different current densities at initial fluoride concentration 2 mg l^{-1}	115
Figure 7-11: Model simulation of fluoride variation with time for different current densities at initial fluoride concentration 4 mg l^{-1}	115
Figure 7-12: Model simulation of fluoride variation with time for different current densities at initial fluoride concentration 6 mg l^{-1}	115
Figure 7-13: Experimental fluoride removal efficiency for continuous EC defluoridation experiments	117
Figure 7-14: Model simulation of pre-flocculation flocs variation with time for different current densities at initial fluoride concentration 2 mg l^{-1}	120
Figure 7-15: Model simulation of pre-flocculation flocs variation with time for different current densities at initial fluoride concentration (a) 4 mg l^{-1} , (b) 6 mg l^{-1}	121
Figure 7-16: Floc evolution during experiment O1	122
Figure 7-17: Model simulation of accumulation of floated flocs variation with time for different current densities at initial fluoride concentration 2 mg l^{-1}	124
Figure 7-18: Model simulation of accumulation of floated flocs variation with time for different current densities at initial fluoride concentration (a) 4 mg l^{-1} , (b) 6 mg l^{-1}	124
Figure 7-19: Comparison of model simulation and experimental data for accumulation of floated flocs (g) in 1 hour operation time of continuous EC reactor	125
Figure 7-20: Floated flocs accumulation after 3600 s of EC experiment O1	126
Figure 7-21: Floated flocs accumulation after 3600 s of EC experiment O4. Current density: 9.58 Am^{-2}	127
Figure 7-23: Model simulation of adsorption of flocs on electrodes variation with time for different current densities at initial fluoride concentration (a) 2 mg l^{-1} , (b) 6 mg l^{-1}	129
Figure 7-24: Energy consumption related parameters and calculation of continuous EC experiments (Calibration parameters are given in Table 7-2)	131

Figure 7-25: Percentages of error of fluoride concentration measurements in experiments O1 to O9 (Calibration parameters are given in Table 7-2)	133
Figure 7-26: Relationship between experimental fluoride concentrations and model simulations of fluoride concentrations of continuous EC defluoridation process conducted (Experiments O1 to O9)	135
Figure 7-27: Comparison of fluoride concentrations of experiments O7, O11, O12, and O13	
Figure 7-28: Model simulation of (a) aluminium hydroxide concentration (mg l^{-1}), and (b) pre-flocculation floc concentration (Nos l^{-1}) variation with time for different current densities	136
Figure 7-29: Continuous EC defluoridation reactor longer operational results (a) dissolved fluoride concentration (mg l^{-1}), (b) fluoride removal efficiency (%), (c) dissolved aluminium concentration (mg l^{-1}), and (d) pre-flocculation floc concentration (Nos l^{-1})	139
Figure 7-30: Local sensitivity results comparison of the calibration parameters and resulted RMSE value of the MATLAB® based PBCM	141
Figure 7-31: Residual plots of calibration parameters (a) d_i , (b) K_E , (c) K , (d) ϕ , (e) q_m , (f) K_L , (g) n	142
Figure 7-32: Residual plots of calibration parameters (h) α_{ab} , (i) η_T , (j) α	143
Figure 7-33: Collision frequency functions for macroscale (orthokinetic) flocculation, microscale (perikinetic) flocculation, and differential settling (MWH Americas, Crittenden Communications et al. 2012)	145
Figure 7-34: PBCM for continuous EC defluoridation efficiency simulation and experimental defluoridation efficiency comparison for Emamjomeh, Sivakumar et al. (2011) data	147
Figure 7-35: Comparison of current efficiency factor (\emptyset) against current density for both primary and secondary data considered in this study	149

LIST OF TABLES

Table 1-1: Past studies that used Response Surface Methodology (RSM) as the optimization method.....	7
Table 2-1: Dimensionless scale-up parameters used (Zolotukhin, 1989)	28
Table 4-1: Bench-scale EC reactor designed for this study.....	59
Table 4-2: The operation variables and the calculated design parameters of batch EC reactor experiments.....	60
Table 5-1: Comparison of the goodness of fit measures of the model calibration and validation results.....	65
Table 5-2: Calibration parameter values for the process-based model simulation results.....	69
Table 5-3: Comparison of total pollutant mass abatement of the simulated and observed experimental data for batch reactor experiments using equation (50b).....	71
Table 6-1: Reactor specific parameters of continuous flow electrocoagulation system – part 1	86
Table 6-2: Reactor specific parameters of continuous flow electrocoagulation system – part 2	87
Table 6-3: The operation variables and the calculated design parameters for each continuous flow EC reactor experiment.....	92
Table 6-4: Input parameters of process-based conceptual model	98
Table 6-5: Output parameters of process-based conceptual model.....	99
Table 6-6: Output parameters of process-based conceptual model.....	100
Table 6-7: Calibration parameter values for the process-based model simulation results – part 1	101
Table 6-8: Calibration parameter values for the process-based model simulation results – part 2	102
Table 7-1: Calibration parameter values for the process-based model simulation results....	107
Table 7-2: Calibration parameters used for continuous EC PBCM calibration.....	108
Table 7-3: The results of dissolved fluoride concentrations for continuous EC defluoridation experiments (Calibration parameters are given in Table (7-2)	118
Table 7-4: Comparison of total pollutant mass abatement of the simulated and observed experimental data for continuous reactor experiments using equation (65a).....	119

Table 7-5: Floated flocs accumulation after 3600 s of continuous EC experiments O1, O4 and O9	126
Table 7-6: Energy consumption related parameters and calculation of continuous EC experiments.....	130
Table 7-7: Model prediction accuracy measures of continuous EC PBCM.....	133
Table 7-8: Statistical parameters of two data sets of fluoride concentrations.....	134
Table 7-9: Hydrodynamic parameters comparison of O7 and O12 experiments	137
Table 7-10: EC energy consumption and fluoride removal efficiency data comparison	138
Table 7-11: Summary of sensitivity analysis on the calibration parameters.....	144
Table 7-12: Calibration parameters employed for PBCM for continuous EC defluoridation efficiency simulation and experimental defluoridation efficiency comparison for Emamjomeh, Sivakumar et al. (2011) data	147
Table 8-1: Calibration parameter sensitivity to experimental parameters (I/A: Current density, Co: Initial pollutant concentration, Q: Flow rate).....	154
Table 8-2: Operational advantages of the proposed model	156
Table 8-3: Operational limitations of the proposed model	156

ACRONYMS

COD	Chemical oxygen demand
CSTR	Continuous stirred tank reactors
DOE	Design of experiments
DSR	Differential side-stream reactors
EC	Electrocoagulation
Fr	Froude Number
MAPE	Mean absolute percent error
MSE	Mean square error
O&G	Oil and grease
PBCM	Process-based conceptual model
PFR	Plug flow reactors
Re	Reynolds Number
RMSE	Root-mean-square error
RO	Reverse osmosis
RSE	Relative standard error
RSM	Response surface methodology
SDG	Sustainable development goal
SGr	Gas Saturation Similarity
SS	Suspended solids
TFS	Total floated solids
TSS	Total suspended solids
UN	United Nations
We	Weber Number

SYMBOLS

A	cross sectional area of the reactor (m ²)	C _{out}	concentration of reactant leaving the reactor (mg l ⁻¹)
Al _{acc}	accumulation of aluminium ions (mg l ⁻¹)	C _{fn}	equilibrium concentration of the pollutant (mol l ⁻¹) at the n th time step.
Al _{dis}	dissipation of aluminium ions (mg l ⁻¹)	C _{Base}	pollutant concentration at the base (mg l ⁻¹),
Al _{gen}	generation of aluminium ions (mg l ⁻¹)	C _{F-in at t_n}	fluoride concentration at the inlet at time t _n (mg l ⁻¹),
Al _{out}	outflow of aluminium ions (mg l ⁻¹)	C _{F-out at t_n}	fluoride concentration at the outlet at time t _n (mg l ⁻¹),
AlOH ₃ _{acc}	accumulation of Al(OH) ₃ (mg l ⁻¹)	C _{poll}	pollutant concentration in the bulk solution (mg l ⁻¹),
AlOH ₃ _{dis}	dissipation of Al(OH) ₃ (mg l ⁻¹)	C _{Surface}	pollutant concentration at the surface (mg l ⁻¹),
AlOH ₃ _{gen}	generation of Al(OH) ₃ (mg l ⁻¹)	D	electrodes gap (m)
AlOH ₃ _{out}	outflow of Al(OH) ₃ (mg l ⁻¹)	$\frac{dm_{Al}}{dt}$	rate of aluminium dissolution (mg s ⁻¹)
AlOH ₃ _{p_acc}	accumulation of Al(OH) ₃ particles (mol l ⁻¹)	d _b	bubble diameter (m),
AlOH ₃ _{F_acc}	accumulation of Al(OH) ₃ -F (mg l ⁻¹)	D _h	hydraulic diameter
AlOH ₃ _{F_dis}	dissipation of Al(OH) ₃ -F (mg l ⁻¹)	d _i	particle size (cm),
AlOH ₃ _{F_gen}	generation of Al(OH) ₃ -F (mg l ⁻¹)	D _p	diameter of one AlOH ₃ particle in the reactor (m)
AlOH ₃ _{F_out}	outflow of Al(OH) ₃ -F (mg l ⁻¹)	E _{an}	anodic potential (V)
A/V	electrode surface area to reactor volume (m ² m ⁻³)	E _c	electrical conductivity (S m ⁻¹)
C	concentration of the pollutant (mg l ⁻¹)	E _{ca}	cathodic potential (V)
C ₀	initial pollutant concentration (mg l ⁻¹)	E _{cell}	the overall potential of the reactor (V)
C _e	equilibrium concentration of the pollutant (mol l ⁻¹)	E _{lo}	loss potential (V)
C _{in}	concentration of reactant entering the reactor (mg l ⁻¹)	E _{so}	solution potential (V)
		E	equilibrium potential (V)
		E _H	electrode height (m)

E_N	number of electrodes (Nos)	J_M	rate of attachment due to macroscale collisions (s^{-1})
E_T	electrode thickness (m)	J_μ	rate of attachment due to microscale collisions (s^{-1})
E_W	electrode width (m)	K	a percentage denoted hydrolysis efficiency
E_A	active anode area (m^2)	k_1	rate constant of the electro-flotation process (s^{-1})
EC	initial electrical conductivity ($S\ m^{-1}$)	k_2	rate constant of the sedimentation process (s^{-1})
F	Faraday number ($96487C\ mol^{-1}$)	K_f	flotation constant (s^{-1})
F_{acc}	fluoride accumulation ($mg\ l^{-1}$)	k_{ij}	rate order constant for aggregation (l^2s^{-1})
F_{dis}	fluoride dissipation ($mg\ l^{-1}$)	$K_{M+\mu}$	rate constant for particle aggregation ($l\ s^{-1}$)
F_{gen}	fluoride generation ($mg\ l^{-1}$)	k_w	water permeability ($H\ m^{-1}$)
F_i	initial fluoride concentration ($mg\ l^{-1}$)	k	Boltzmann's constant ($J\ K^{-1}$)
F_{in}	fluoride inflow ($mg\ l^{-1}$)	$K(a)$	rate of aluminium (III) dissolving process ($mg\ s^{-1}$)
F_{out}	fluoride outflow ($mg\ l^{-1}$)	K_E	electrode adsorption coefficient
f_b	friction factor	K_L	Langmuir constant ($l\ mol^{-1}$)
G	velocity Gradient (s^{-1})	$K_{M+\mu}$	rate constant for particle aggregation ($l\ s^{-1}$)
g	gravitational acceleration ($m\ s^{-2}$)	L	reactor length (duct) (m)
G_e	external mixing velocity gradient (s^{-1})	M	molar mass of the electrode material ($mg\ mol^{-1}$)
H	reactor wetted height (m)	m_{Al}	mass of metal dissolved from electrolysis (mg)
H	number of hydrogen molecules generated per electron involved in the redox reactions (=0.5).	$M_{Al(OH)_3-F}$	molar mass of aluminium-hydroxo-fluoride particle, post adsorption process ($mg\ mol^{-1}$)
hL	head loss across the duct (m)	$m_{Al(OH)_3-acc\ at\ t_n}$	aluminium hydroxide accumulation at n^{th} time step in ($mg\ l^{-1}$)
i	current density ($A\ m^{-2}$)		
I	electric current (A)		
I/V	current concentration $A\ m^{-3}$		
J_{Ds}	rate of attachment due to differential setting (s^{-1})		
J_{ij}	rate of attachment between i and j particles (s^{-1})		

$m_{\text{Al(OH)}_3\text{-gen at } t_n}$	aluminium hydroxide generation from hydrolysis process at n^{th} time step in (mg l^{-1})	N_f	number of fluoride adsorbed on to one Al(OH)_3 particle (Nos)
$m_{\text{Al(OH)}_3\text{-dis as Al(OH)}_3\text{F at } t_n}$	dissipation of Al(OH)_3 due to formation of aluminium-hydroxo-fluoride (mg l^{-1})	N_{fd}	floc density (flocs m^{-3})
$m_{\text{Al(OH)}_3\text{-dis on electrodes at } t_n}$	dissipation of aluminium hydroxide and aluminium-hydroxo-fluoride due to adsorption on electrodes (mg l^{-1})	$n_{\text{Floc at } t_n}$	post flotation particle concentration (Nos l^{-1})
$m_{\text{Al(OH)}_3}$	mass of Al(OH)_3 (s) generation (mg),	$n_i n_j$	number of i and j particles per unit volume respectively (Nos l^{-1})
$m_{\text{Al-acc at } t_n}$	aluminium accumulation at the n^{th} time step (t_n) in (mg l^{-1})	N_{fl_f}	post-flocculation flocs concentration (Nos l^{-1})
$m_{\text{Al-dis at } t_n}$	dissipation of aluminium at n^{th} time step (t_n) in (mg l^{-1})	N_{fl_i}	pre-flocculation particle concentration (Nos l^{-1})
$m_{\text{Al-gen at } t_n}$	generation of aluminium at n^{th} time step (t_n) in (mg l^{-1})	N_{float_acc}	floated sludge accumulation (mg)
$m_{F \text{ at } t_n}$	equilibrium fluoride concentration in the reactor at n^{th} time step $m_{F \text{ at } t_n}$ (mg l^{-1})	N_{post_float}	post flotation flocs concentration (Nos l^{-1})
$m_{F \text{ dis at } t_n}$	fluoride adsorption at n^{th} time step $m_{F \text{ dis at } t_n}$ in (mg l^{-1})	pH	pH level
\dot{m}_{H_2}	rate of H_2 gas generation (mg s^{-1})	Q	flow rate of the continuous flow reactor (l s^{-1})
n	particle number concentration (l^{-1})	q	flow rate of the continuous flow reactor ($\text{m}^3 \text{ s}^{-1}$)
N_A	Avogadro's number (6.0221409E+23)	q_{e_n}	amount of pollutant adsorbed per unit mass of adsorbent at equilibrium (mg g^{-1}) at the n^{th} time step
$N_{(fd)t_n}$	floc density after the flotation process at the n^{th} time (mol l^{-1})	q_{e_n}	amount of pollutant adsorbed per unit mass of adsorbent at equilibrium (mg g^{-1}) at the n^{th} time step.
N_{t_n}	pre-flocculation particle concentration (Nos l^{-1})	Q_r	reaction quotient of the cell reaction
$n_{Ad \text{ accum at } t_n}$	total adsorbent concentration at n^{th} time step (mol l^{-1})	q_e	the amount of pollutant adsorbed per unit mass of adsorbent at equilibrium (mg g^{-1})
$n_{\text{Al(OH)}_3 \text{ colloids acc at } t_n}$	aluminium hydroxide colloids accumulation at n^{th} time step in (mol l^{-1})	q_m	the maximum adsorption capacity (mg g^{-1})
		r_{poll}	rate of electro-flotation and sedimentation ($\text{mg l}^{-1}\text{s}^{-1}$)
		R	gas constant ($8.314 \text{ J mol}^{-1}\text{K}^{-1}$)

r_d	the reaction rate of dissipation of reactant (mg l^{-1})	ρ	density of liquid (kg m^{-3})
Re	Reynolds number	σ	surface tension (J m^{-2}) at 20°C
r_g	the reaction rate of generation of reactant (mg l^{-1})	ϕ_b	air dosage ($\text{m}^3 \text{ air m}^{-3} \text{ water}$)
t	electrolysis time (s)	ρ_g	density of the gas (kg m^{-3})
T	absolute temperature (K)	ϕ	correction factor, denoted current efficiency or faradic yield
t_h	hydrolysis time (s)	ΔG°	standard Gibbs free energy change in a chemical process (J)
T_{res}	residence time (min)		
TC	total cost (Rs l^{-1})		
TE	energy variation (J)		
Total_Ad	total adsorbents (mol l^{-1})		
U	cell potential (V)		
V_s	supply voltage (V)		
V	working volume of the reactor (l)		
V_b	rising velocity of air bubbles (m s^{-1})		
V_E	electrode volume (m^3)		
V_f	flow velocity (m s^{-1})		
V_{H_2}	generation of H_2 gas volume (l s^{-1})		
W	reactor width (duct) (m)		
Z	number of electrons, transferred ($Z=3$ for aluminium),		
α	collision efficiency		
α_{db}	collision coefficient between an air bubble and floc		
η_T	collision frequency between the air bubble and floc		
μ	dynamic viscosity of suspending fluid (N s m^{-2})		
ν	kinematic viscosity of suspending fluid ($\text{m}^2 \text{ s}^{-1}$)		

Chapter 1. Introduction

1.1. *The global perspective of water*

Water is a scarce resource that is considered crucial for the socio-economic development of society as a whole. Along with an increasing global population, the need for efficient water and wastewater treatment is also on the rise. 2.3 billion people live in water-stressed countries and 721 million people live in high and critically water-stressed countries (UN-Water 2021). The global figures of safe access to water exposed significant inequalities between and within regions, countries, communities, and even neighbourhoods. To address this, the United Nations has set the sixth sustainable development goal (SDG) to “ensure availability and sustainable management of water and sanitation for all”(United Nations 2019). Access to safe drinking water and sanitation are human rights. Access to these services, is fundamental to human health and well-being, thus making SDG 6 a crucial element in achieving sustainable development. As illustrated in Figure 1.1, billions of people worldwide still live without safely managed drinking water. As per the latest report by UN-Water (2021), the world is not on track to achieve the SDG 6 targets by 2030.

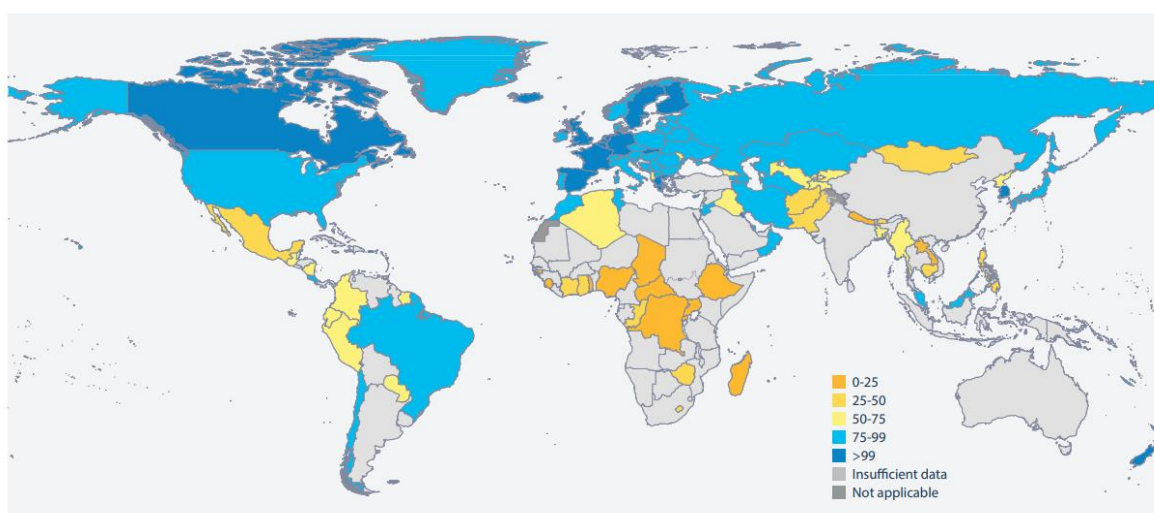


Figure 1-1: Proportion of population using safely managed to drink water services in 2020 (%) (UN-Water 2021)

To reach the global targets of SDG 6 by 2030, it is estimated that current rates of progress need to be quadrupled. Achieving these targets is essential to help protect society from many threats which could be expected in the years to come. Hence, the immediate mission consists of establishing safe water systems, investing in water use efficiency, wastewater treatment and reuse, and financing the protection of water-related ecosystems.

Worldwide, there are different water and wastewater treatment systems currently in use. The treatment methods are often chemically, operationally, and economically intensive hence, the applicability of these in developing nations is limited (Mauter, Zucker et al. 2018). Considerable infusion of capital, engineering expertise and infrastructure precludes their use in most parts of the world. Sustainable, affordable, safe, and robust methods to increase supplies and purify water should be developed and implemented to serve people throughout the world. Amongst the numerous technologies in use at present, electrocoagulation (EC) in water and wastewater treatment has emerged as being popular during the last two decades (Zhu, Zhao et al. 2007, Hakizimana, Gourich et al. 2017). Efficient pollutant removal, low energy consumption, and the possibility of automation are among the prominent reasons that an increase in EC related research has emerged during recent times. EC is also popular for its ability to remove a variety of pollutants from wastewater.

1.2. Electrocoagulation overview

The use of electricity in water and wastewater treatment was initially tested in the UK, more specifically in 1889 (Strokach 1975). Although EC with aluminium and iron electrodes was patented in the US in 1909, the EC of potable water was only first applied on a large scale in the US in 1946 (Bonilla 1947). This is due to the relatively large capital investment and the high cost of electricity supply at the time. Owing to new energy generation technologies, and new construction and transportation methods introduced during the twentieth century energy prices have substantially declined (Figure 1.2). With the reduction in costs of electricity generation during the

past few decades, electrochemical technologies have regained their importance worldwide.

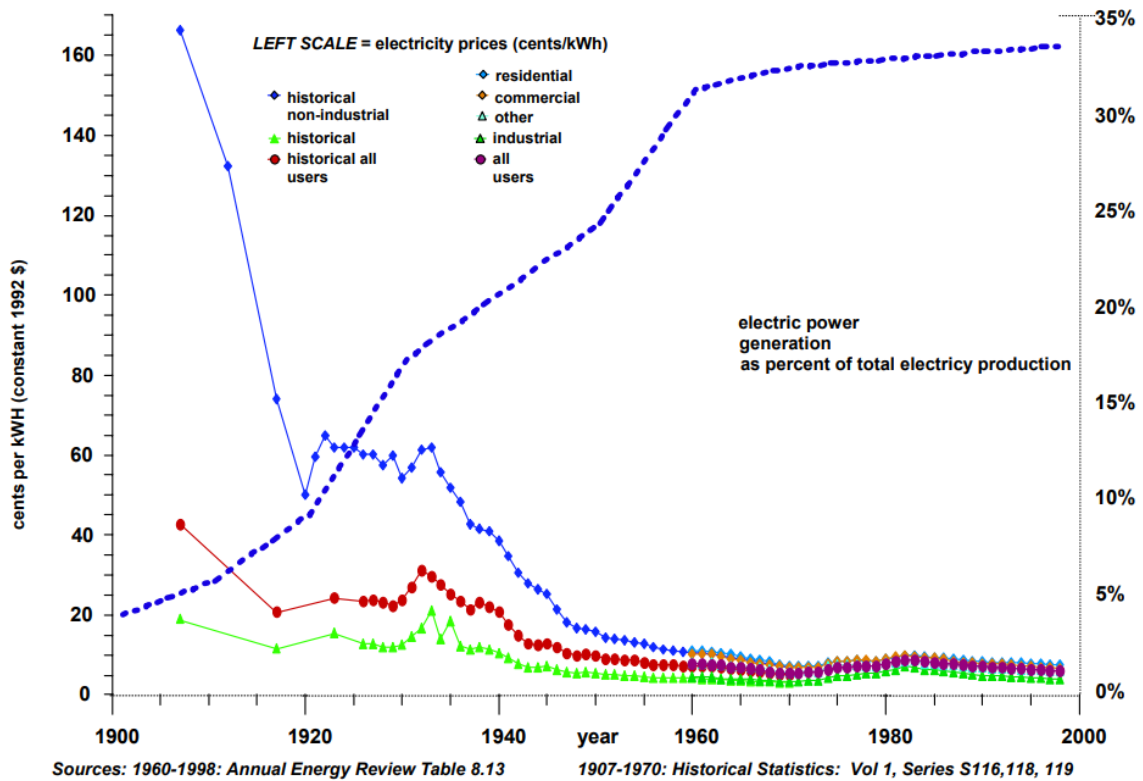


Figure 1-2: Electricity conversion efficiency and retail price in the USA 1900-1998 (Ayres 2003)

However, the rising concern for climate change makes sustainability in energy use vital in reactor operations (Duan and Shi 2014). In addition, due to competitiveness in business, the reduction of operating costs is also essential while achieving maximum efficiency in the process. A proper balance between the resources, methods and operating conditions would be required to achieve the above-mentioned requirements associated with energy, operating cost, and efficiency (Figure 1.3).

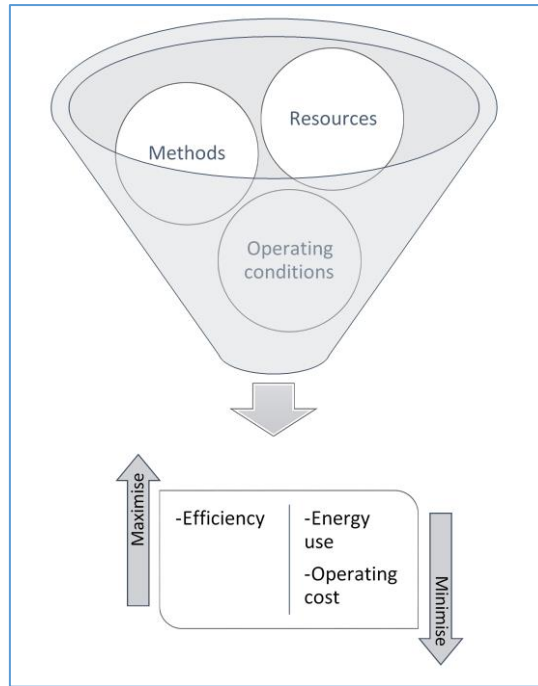


Figure 1-3: Essential criteria for reactor operation optimisation

A significant improvement in EC applications could be noted during the past three decades. EC is being tested and applied for metal recovery, treating groundwater, treating potable water or process water, treating various wastewaters resulting from the tannery, oil, oil-in-water emulsion, electroplating, dairy, textile processing, etc. (Hashim, Shaw et al. 2017). In some incidents, EC is an essential step in treating wastewaters containing refractory contaminants (Chen 2004). Figures 1.4 and 1.5 illustrate two electrocoagulation plants operating in the United States of America and South Africa respectively. However, contrary to the worldwide use of EC for water and wastewater treatment, the evolution of reactor design and process optimisation has been insignificant (Thakur and Mondal 2016). This is mainly due to the complexity of the EC treatment process.



Figure 1-4: Industrial wastewater treatment unit in the United States of America (Composition: 8.74 mg l^{-1} of Ni, 28.8 mg l^{-1} of Zn, 657 mg l^{-1} of Total suspended solids, 27 mg l^{-1} of Oil and Grease, 159 mg l^{-1} of P) (Powell-water 2016)



Figure 1-5: Arsenic contaminated groundwater treatment unit in South Africa (Proxa-water 2021)

The conventional EC reactor design is based on laboratory level reactor optimisation and scale-up. For EC reactors, the optimisation of process parameters is paramount in achieving the desired balance between efficiency, energy use, and operating cost (An, Huang et al. 2017). The conventional optimisation method involves running many experiments by varying a single factor while keeping the rest of the parameters fixed. This process neglects the interrelations between the parameters. Experimental design tools are used to minimize this issue, allowing the recognition of the interdependency between the variables to a certain extent (Güçlü 2015). The design of experiments (DOE) and response surface methodology (RSM) are the most widely used design tools in EC reactor optimization (Chavalparit and Ongwande 2009, Zhao, Huang et al. 2014, Rodrigo 2016). The details of some of the studies that used RSM as the optimisation method are listed in Table (1.1) and the response surface plots resulted from such studies are illustrated in figures 1.6 and 1.7. These studies are based on mathematical and statistical methods and are used to determine the significance of individual factors and their interactive influences with a reduced number of runs (Makwana and Ahammed 2016).

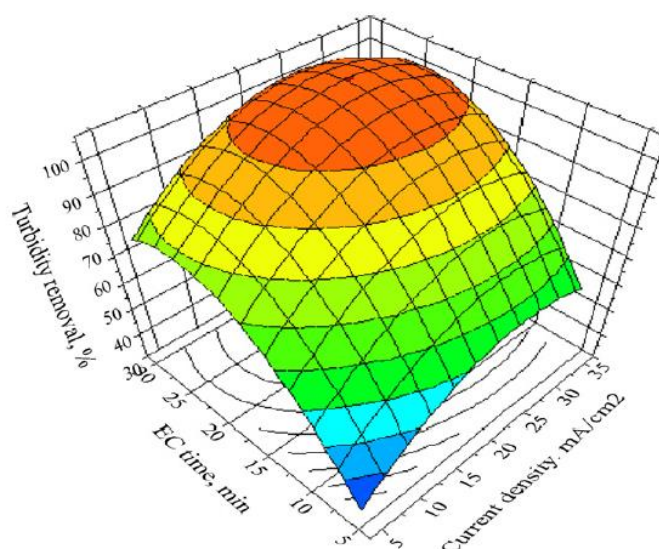


Figure 1-6: Effect of current density and EC time on turbidity removal (%) (Tir and Moulai-Mostefa 2008)

Table 1-1: Past studies that used Response Surface Methodology (RSM) as the optimization method (COD: Chemical oxygen demand, RSM: Response surface methodology, EC: Electrocoagulation, RO: Reverse Osmosis, Id: Current density, Qin: Inflow, T: Time, C: Concentration of the removal pollutant, O&G: Oil and Grease SS: Suspended Solids)

Title	Citation	Details of the testing	Variables Studied
Hardness, COD and turbidity removals from produced water by electrocoagulation pretreatment prior to Reverse Osmosis membranes	(Zhao, Huang et al. 2014)	Experimental Pilot Scale Iron anode and Carbon cathode Six monopolar electrodes Continuous EC-RO system	pH (X1), Id (X2), EC time (X3) COD (Y1), turbidity (Y2), hardness (Y3)
Optimizing electrocoagulation process for the treatment of biodiesel wastewater using response surface methodology	(Chavalparit and Ongwandee 2009)	Experimental Lab-scale Aluminium anode and a graphite cathode Monopolar Batch Reactor.	pH (X1), V (X2), EC time (X3) COD (Y1), O&G (Y2), SS (Y3)
Optimization of C.I. Acid Red 14 azo dye removal by electrocoagulation batch process with response surface methodology	(Aleboyeh, Daneshvar et al. 2008)	Experimental Lab-scale Iron (ST 37-2) anode and steel (grade 304) cathode, Monopolar batch reactor	pH (X1), Id (X2), EC time (X3)
Arsenic Removal from Natural Groundwater by Electrocoagulation Using Response Surface Methodology	(Garcia-Lara, Montero-Ocampo et al. 2014)	Experimental Lab-scale Iron electrodes	Id (X1), Qin (X2)
Optimization of oil removal from oily wastewater by electrocoagulation using response surface method	(Tir and Moulai-Mostefa 2008)	Experimental Lab-scale Aluminium anode, stainless steel cathode Monopolar Batch Reactor	Turbidity removal (Y1) and COD removal (Y2)
Optimization of a combined Electrocoagulation electro-flotation reactor	(Rodrigo 2016)	Experimental Lab-scale plants Batch mode Continuous mode Aluminium anode and stainless steel cathode	Id (X1), T (X2) and C (X3)

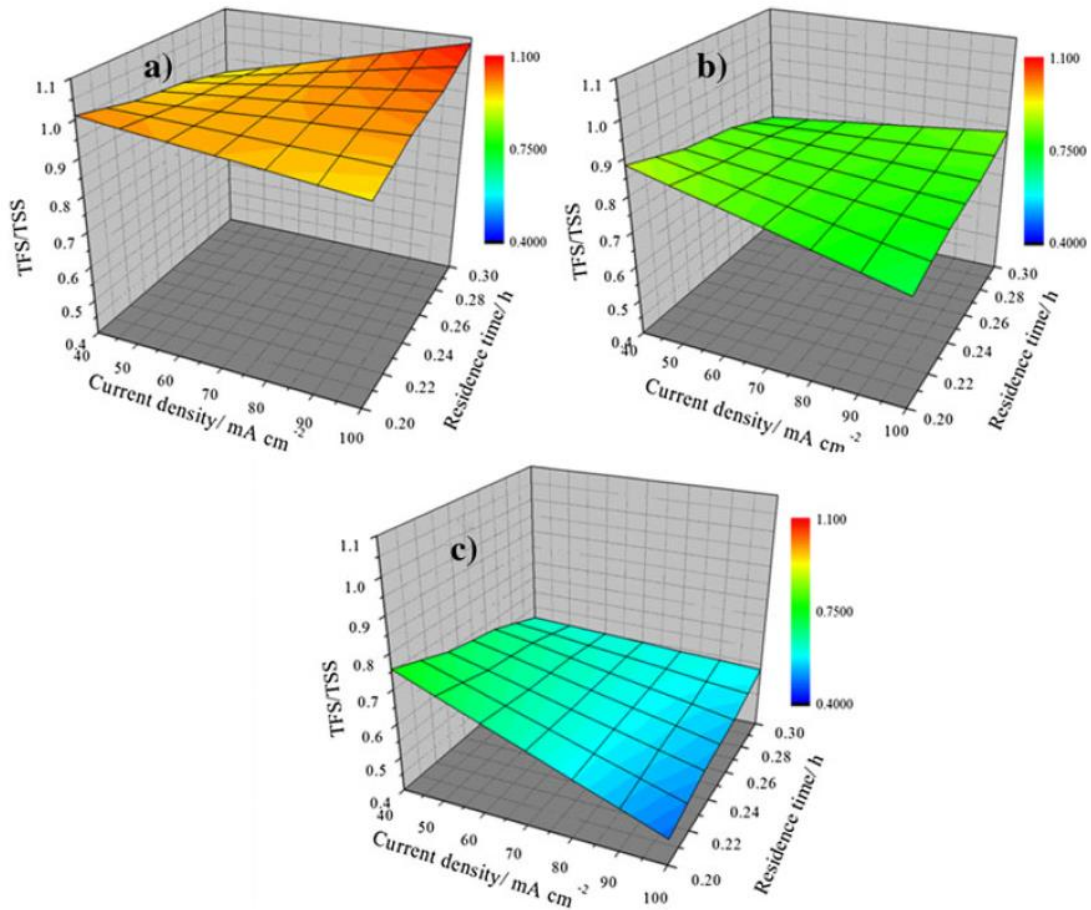


Figure 1-7: Response surface for the Total floated solids (TFS) / Total Suspended Solids (TSS) relationship for three different values of initial kaolin concentration: a [kaolin] 500 mg/ L, b [kaolin] 1000 mg l⁻¹and c [kaolin] 1500 mg l⁻¹(Rodrigo 2016)

Operating conditions	Water/ wastewater conditions	Geometry of reactor
<ul style="list-style-type: none"> • Current • Voltage • Operating time • Temperature 	<ul style="list-style-type: none"> • pH • Alkalinity • Initial pollutant concentration • Conductivity 	<ul style="list-style-type: none"> • Reactor shape/size • Electrode surface • Electrode spacing • Electrode configuration • Flow configuration

Figure 1-8: Parameters involved in EC reactor optimization

The EC reactor optimization involves many parameters related to operating conditions, water/wastewater conditions, and the geometry of the reactor as shown in Figure (1.8). During the last two decades, numerous studies in EC reactor optimisation can be found in the literature (Aleboyeh, Daneshvar et al. 2008, Tir and Moulai-Mostefa 2008, Chavalparit and Ongwandee 2009, Garcia-Lara, Montero-Ocampo et al. 2014, Zhao, Huang et al. 2014, Rodrigo 2016).

A noteworthy similarity in most of these studies is that the optimisation work has been achieved by laboratory-scale experimental investigations and statistical optimisation of operating parameters. The literature demonstrated a scarcity of systematic design and modelling approaches. The optimisation processes developed through statistical analysis for EC operations could be regarded as black-box models. Though these are produced from data sourced experimentally, the understanding gained regarding the fundamentals behind the interactions of operating parameters is poor (Akinmolayan 2017). Hence, understanding the underlying operating principles and their interactions in the EC process would help predict robust and accurate results under a wide range of operating conditions. Electrochemistry that governs the operation of EC is a complex science accompanied by charge transport, electrochemical kinetics, knowledge of electrode interfaces, and thermodynamics. In addition, there are mechanical parameters or engineering aspects that affect the operational effectiveness of EC reactors. The interaction between the mechanical parameters and the main scientific mechanisms underlying the EC process has not been fully discovered. Hence most industrial EC treatment systems are designed and scaled up using statistical approaches.

1.3. Modelling of electrocoagulation

Modelling work used in the water industry frequently tends to be empirical rather than mechanistic. Empirical modelling is limited to only specific applications and conditions; consequently, the adaptability of such models for varying scenarios is low

(Akinmolayan 2017). Hence, it is important to synthesize a conceptual understanding of the EC treatment process based on pollutant removal mechanisms in the reactor.

Four key processes inside the EC reactor are coagulant generation, weakening of the pollutants, accumulation of floc and removal of floc. The interference of electrochemistry in each of these processes is what makes EC difficult to model (Holt, Barton et al. 2005). Hence, a significant gap in the detailed technical literature on electrocoagulation modelling is evident (Hakizimana, Gourich et al. 2017). The general segregated processes of a conventional water treatment system (coagulation, flocculation, settling, or flotation) are integrated into a single cell in EC operation. The coagulant is generated in-situ by anode oxidation and the hydrogen gas bubbles are generated due to cathode reduction. The electric field is in effect throughout the treatment process with numerous interactions between the coagulant and its hydrolysis products, the pollutant, the other ionic species, and the electrolytic gas bubbles. The electric current governs the bubble density, and so the system hydrodynamics are affected by the bubble density that sequentially affects the mass transfer between pollutants, coagulant, and gas micro-bubbles (Hakizimana, Gourich et al. 2017). The bubbles aid the particle collision frequency, which is vital for the efficiency of floc formation. The qualitative and quantitative interactions between these mechanisms are vital for the optimized design of an EC reactor.

The pollutant removal pathway consists of four stages, namely, coagulant generation, weakening of the pollutants, accumulation of floc, and finally, the removal of floc (Figure 1.9). The pollutant's interactions within the system and eventual removal paths are determined by the physicochemical properties of the pollutant. The modelling of EC is governed by the second process, which is the weakening of the pollutants that could occur in numerous ways as listed below (Holt 2003, Kabdaşlı, Arslan-Alaton et al. 2012).

- i. Adsorption on precipitates

- ii. Precipitation
- iii. Co-precipitation
- iv. Adsorption on electrodes
- v. Electro-oxidation or electro reduction
- vi. Physical enmeshment
- vii. Bulk chemical reaction

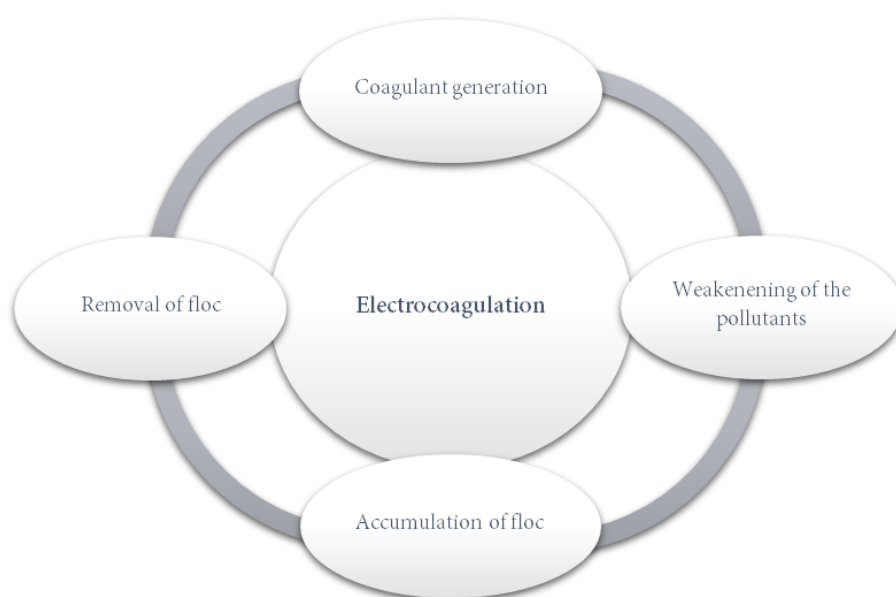


Figure 1-9: Interactions occurring within an EC reactor

Any modelling attempt that avoids quantification of the interrelationship of the four key processes in EC would be ineffective (Holt, Barton et al. 2005). The vast body of knowledge that has been developed over the years is mostly established on EC reactor modelling attempts that excluded the quantification of the aforementioned four key processes, thus encompassing a significant knowledge gap. Hence, this study aimed to develop a conceptual understanding of the EC water treatment process utilizing first principle modelling techniques. The new process-based conceptual model (PBCM) is expected to increase the controllability of the system variables and enable efficient scale-up of EC reactors.

1.4. *Aim/objectives*

This study aimed to develop a novel process-based conceptual model (PBCM) consisting of theoretical and empirical approaches to address the design and modelling issues such as scale-up, the effect of physical, chemical, and hydrodynamic parameters on the efficiency of electrocoagulation reactors in water and industrial wastewater treatment.

The objectives are listed below.

Objective 1: Critically evaluate the internal processes, industrial applications and existing knowledge on numerical and conceptual-based models to address design and performance optimization issues of EC units.

Objective 2: Design and validate an integrated PBCM for EC reactors using the process-based kinetics associated with EC operation.

Objective 3: Assess experimentally, the PBCM to address the existing design and modelling issues of EC reactors for varied operating conditions such as different inlet pollutant concentrations, varied sludge removal conditions, supply current variations and different inter-electrode distances.

Objective 4: Assess the PBCM at pilot scale to derive a systematic approach of EC reactors design and scale-up.

Objective 5: Establish a methodology/model which can simultaneously address the prediction of pollution removal, settling/flotation, scale-up and techno-economic optimisation.

1.5. *Thesis structure*

Objective one was planned to be achieved through critical evaluation of the literature by understanding the scientific and mechanistic approaches developed over the years for electrocoagulation modelling. Designing a process-based conceptual model (PBCM) for both batch and continuous electrocoagulation reactors for defluoridation

was then planned to achieve the second objective. The batch and continuous flow-based conceptual models were then implemented to achieve the next objectives, using two computer platforms namely, Microsoft® Excel® ver. 2016 and MATLAB® ver. R2021a. These were then validated using the data collected from the batch and continuous flow laboratory level EC experimental set-ups. Hence, this thesis has been presented focusing on these two themes, namely, batch and continuous flow EC. The thesis is structured into nine chapters, where the chapters 1, 2, 3, 8, and 9 detail the overall focus of the study. Chapters 4 and 5 detail the batch EC PBCM design and validation while chapters 6 and 7 detail the continuous EC PBCM design and validation process. The thesis structure with chapter details is illustrated in Figure 1.10.

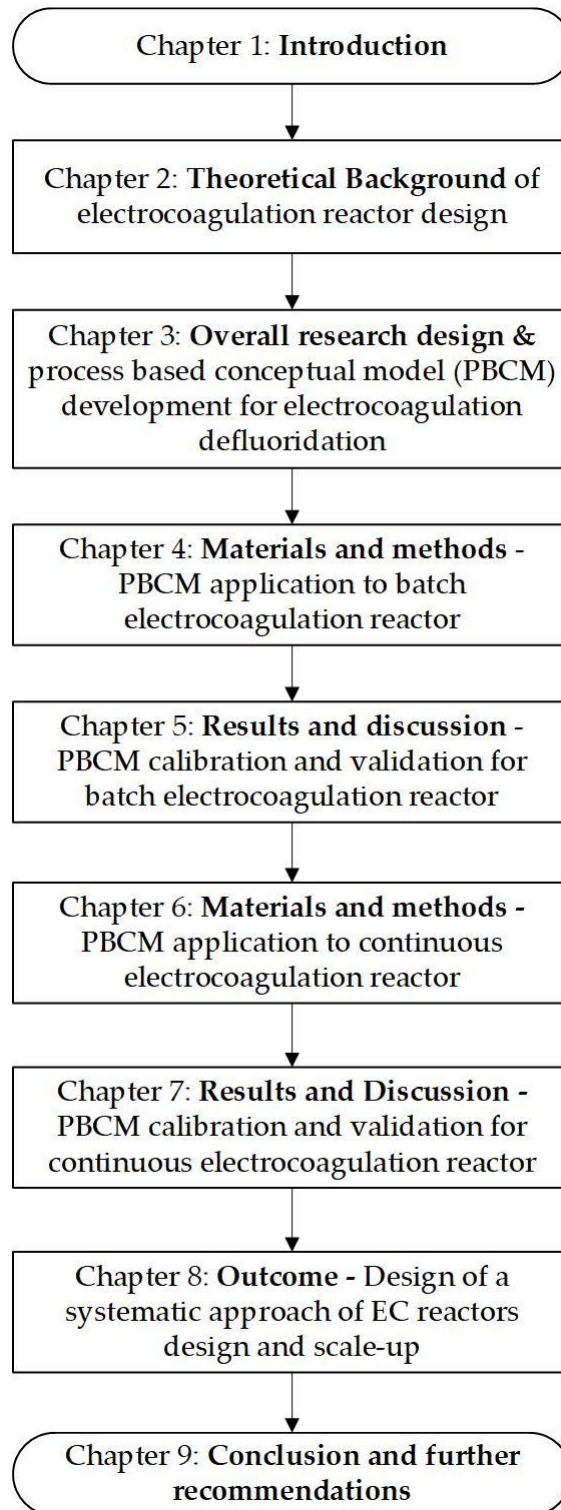


Figure 1-10: Thesis structure with chapter details

Chapter 2. Theoretical background of EC reactor design

2.1. Chapter overview

This chapter comprises the theoretical background of EC reactor design and scale-up theories that are necessary to develop a PBCM for defluoridation using EC technology. Initially, the pollutant abatement mechanism of the defluoridation process using EC technology with aluminium electrodes was studied. Additionally, the cell potential and energy calculation theories for EC reactors were researched and summarised, followed by the details of the operating parameters considered important for the determination of EC reactor efficiency. This led to the study on reactor types identification which is necessary for the mass balance application in EC reactors. Finally, the scale-up theories used for EC reactors were explored. These theories and equations studied under this chapter have been used in designing the PBCM for batch and continuous reactors that are detailed in chapters 4 and 6 respectively.

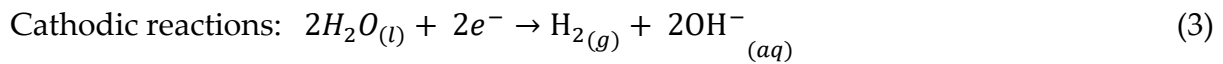
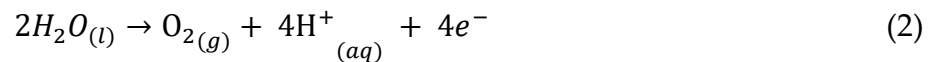
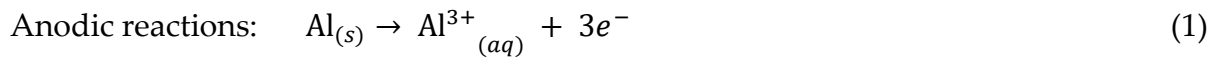
2.2. Pollutant abatement mechanism

In electrocoagulation water treatments, metal electrodes are charged with a voltage differential to generate the ions that are required to initiate the coagulation process. Coagulation is the process of destabilization of suspended, emulsified, or dissolved contaminants, allowing the formation of an agglomeration which is termed flocculation. Here, the metal cations are hydrolyzed forming the in-situ coagulants, hence no external chemicals addition is necessary. The process effectively removes suspended solids and colloids, breaking emulsions, such as oil and grease or latex, and oxidizes heavy metals from an aqueous medium without the use of filters or the addition of separation chemicals.

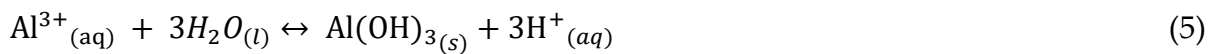
Different electrodes have been tested and used, such as carbon, mild steel, iron, graphite titanium, and aluminium. Aluminium is considered the most effective and successful in removal of most pollutants at favourable operating conditions (Ghosh, Medhi et al. 2008, Graça, Ribeiro et al. 2019). Electrocoagulation has been tested for

defluoridation in several countries during the last three decades (Mameri, Yeddou et al. 1998, Bennajah, Gourich et al. 2009). Both iron and aluminium electrodes have been tested for defluoridation and the removal efficiency is found to be higher in the latter (Tezcan Un, Koparal et al. 2013). Consequently, there is substantial knowledge on defluoridation using aluminium electrodes in EC reactors. Therefore, the model discussed in this research has been developed for defluoridation using a batch EC reactor with aluminium electrodes. The chemical reactions explained in this section are widely accepted.

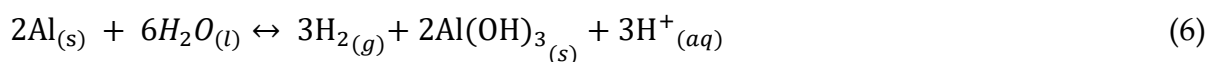
The oxidizing and reduction reactions occurring at the anode and cathode respectively result in the formation of aluminium ions at the anode, hydrogen gas bubbles at the cathode as explained in reactions (1), (2) & (3).



Depending on the pH, the electro generated Al^{3+} is converted into aluminium hydroxide (Reactions (4) & (5)), as the coagulant used in EC:



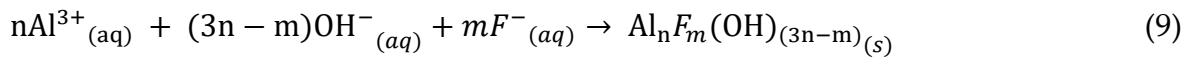
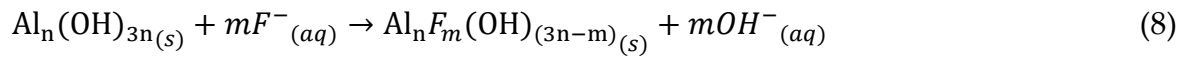
The combination of reactions (1), (2) & (3), leads to the overall electrochemical reactions (6) and (7).



The large specific surface area of the formed $\text{Al}_n(\text{OH})_{3n(s)}$ "sweep floc" is beneficial for the rapid adsorption of soluble organic compounds and trapping of colloidal particles.

The floc polymerizes and the complexes formed are easily removed from water by sedimentation and/or flotation by hydrogen gas.

Adsorption (8) and co-precipitation (9) result in:



Aluminum hydroxide solubility is pH-dependent as illustrated in Figure 2.1. According to Emamjomeh, Sivakumar and Varyani (2011), at pH 5-6, fluoroaluminium complexes are predominant (AlF^{2+} , AlF_2^+ , AlF_3 , AlF_4^-), at pH 6-8, aluminiumhydroxofluoride formation is maximum ($\text{Al}_n\text{F}_m(\text{OH})_{(3n-m)}$) and at pH values over 8, the defluoridation efficiency decreases.

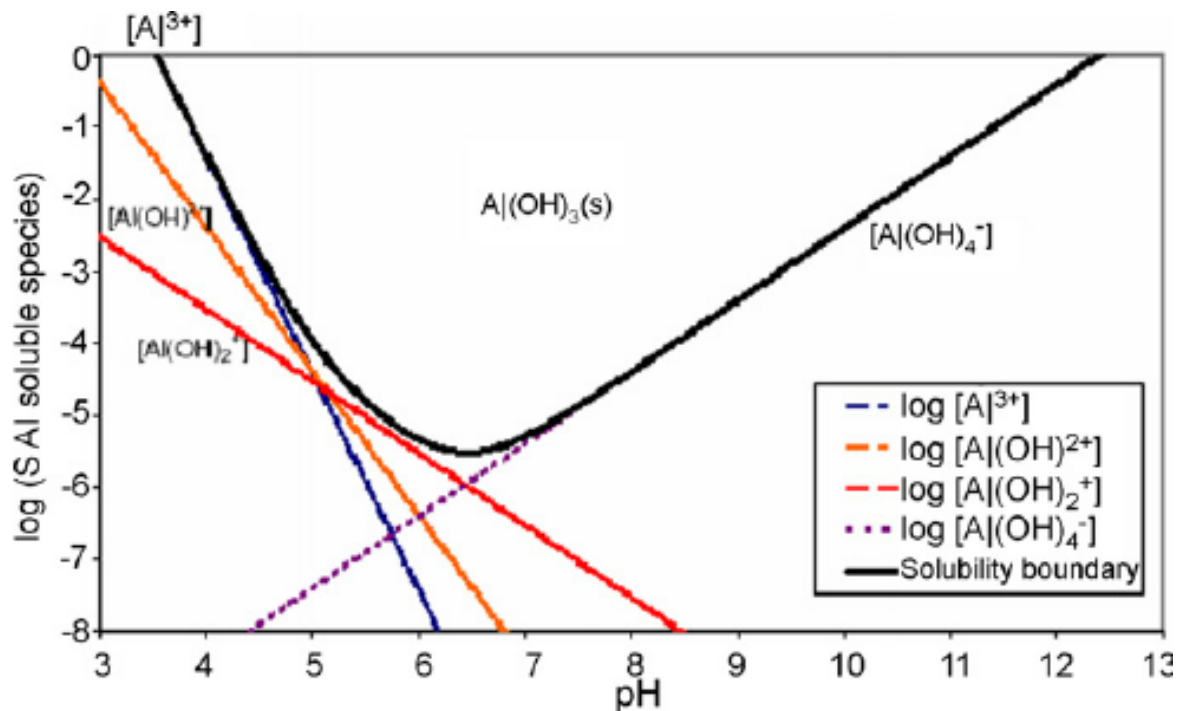


Figure 2-1: Solubility diagram of aluminum hydroxide ($\text{Al}(\text{OH})_{3(s)}$) considering only mononuclear aluminum species (Holt, Barton et al. 2005)

2.3. EC cell potential

A potential difference is required for the current to flow from one electrode to the other and complete the electrical circuit. The potential difference in an electrochemical cell could be calculated using the Nernst equation (Eq. 10) applied to half-cell reactions occurring at each electrode (Eqs. 1 & 3).

$$E = -\frac{\Delta G^\circ}{nF} - \frac{RT}{nF} \ln Q_r \quad (10)$$

Where,

E is equilibrium potential (V)

ΔG° is a standard Gibbs free energy change in a chemical process (J)

F is Faraday number ($C \text{ mol}^{-1}$)

n is the number of electrons consumed in the electrode reaction

T is the temperature (K)

R is gas constant ($8.314 \text{ J mol}^{-1} \text{ K}^{-1}$)

Q_r is reaction quotient of the cell reaction

The coagulant generation is fundamental to begin the electrocoagulation process. Hence, supplying the minimum cell potential is necessary for the half-cell reactions to occur. The overall potential equation for a reactor could be expressed from equation (11).

$$E_{cell} = E_{ca} - E_{an} - E_{so} - E_{lo} \quad (11)$$

Where,

E_{cell} is the overall potential of the reactor (V)

E_{ca} is cathodic potential (V)

E_{an} is anodic potential (V)

E_{so} is solution potential (V)

E_{lo} is loss potential (V)

Here, the loss potential represents the energy required to surpass the passivating layer. Hence the energy requirement increases with longer operation time and poor maintenance of electrodes. However, the development of the passivation layer could be reduced by applying the current reversal method. The solution potential could be calculated using equation (12) (Goodridge 1985). Here, the energy requirement could be reduced by decreasing the distance between the electrodes, increasing the conductivity of the solution, and also increasing the electrode surface area. These parameters shall be further elaborated under sections 2.4 and 7.8.

$$E_{so} = \frac{di}{E_c} \quad (12)$$

Where,

E_{so} is solution potential (V)

d is distance between electrodes (m)

i is current density ($A\ m^{-2}$)

E_c is electrical conductivity ($S\ m^{-1}$)

Usually, EC is carried out by controlling the supply current which is named galvanostatic mode. Electric energy calculation of the EC process could be processed using equations (13) and (14) for batch and continuous reactors respectively.

$$E = \frac{Uit}{V} \text{ (kWh } m^{-3}\text{)} \quad (13)$$

$$E = \frac{UI}{q} \text{ (kWh } m^{-3}\text{)} \quad (14)$$

Where,

U is cell potential (V)

I is supply current (A)

V is the volume of the batch reactor (m^3)

t is time (s)

q is the flow rate of the continuous flow reactor ($\text{m}^3 \text{s}^{-1}$)

2.4. EC operating parameters

EC reactor design is of great importance since it influences the operating parameters to flow regime and mixing, floc formation, bubble path, removal yield, and flotation/settling characteristics (Hansen, Nuñez et al. 2007, Hakizimana, Gourich et al. 2017). The reactors can be distinguished using three factors: a) the feed mode (batch or continuous), b) the separation method of aggregated pollutants, and c) the design of the geometry of the electrodes (Holt, Barton et al. 2005). The reactor working volume is ruled by the EC reactor geometry and the key to defining electrode area/volume ratio (A/V), which is the only key scale-up parameter in plant design (Aleboyeh, Daneshvar et al. 2008).

Electrode arrangement and the inter-electrode distance largely affect the EC process. The electrode arrangement can be classified as monopolar and bipolar in series and parallel connections (Figure 2.2). When the cost-effectiveness is considered, monopolar parallel electrodes arrangement is considered most advantageous, since this arrangement offers a high pollutant removal with low energy consumption (Hakizimana, Gourich et al. 2017). The operating conditions that affect the EC performance are considered as current or voltage and operation time, to water/wastewater features such as pH, alkalinity, and conductivity as well as the geometry of the EC reactor and the EC electrodes (electrode surface and electrode spacing) (Essadki, Gourich et al. 2010, Guzmán, Nava et al. 2016).

Although EC has been in use for many decades, there are numerous challenges to accepting EC as a successful technology, due to the inadequacy of the design process and its complexity. The body of knowledge gathered by past researchers for

electrocoagulation requires further reinforcement in areas such as process-based modelling and scale-up, to establish EC as a completely engineered process.

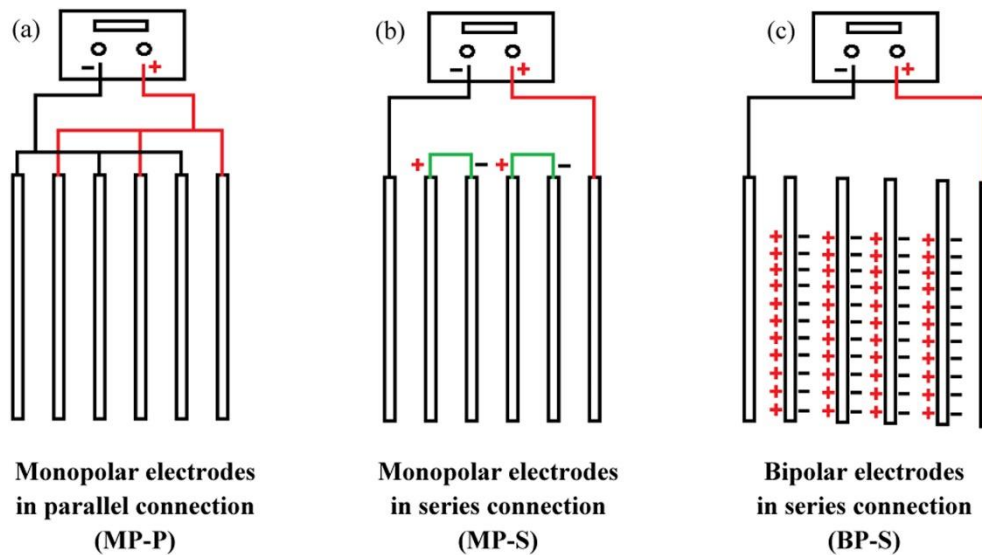


Figure 2-2: Electrodes arrangement classification in electrocoagulation reactors: (a) monopolar electrodes in parallel connection, (b) monopolar electrodes in serial connection and (c) bipolar electrodes in serial connection.

2.5. *Mathematical and statistical modelling of EC*

The use of the design of experimental methods along with the response surface methodology is quite common in EC modelling studies (Güçlü 2015; Song, Yang et al. 2016; Yoosefian, Ahmadzadeh et al. 2017; Genawi, Ibrahim et al. 2020). The collective use of mathematical and statistical methods was helpful to identify the significance of individual factors and their interactive influences as illustrated in Figure 2.3. One major limitation of using statistical modelling is the inadequacy of knowledge on internal process behaviour. The parameter evolution relating to space is another limitation, which requires a good knowledge of the mechanisms responsible for pollution abatement (physical and chemical), as well as the influence of hydrodynamics, both on the pollution abatement process and electrochemical phenomena. As a result of this, statistical modelling acts as a black-box modelling

technique thus failing to help in articulating methods for process control (Hakizimana, Gourich et al. 2017).

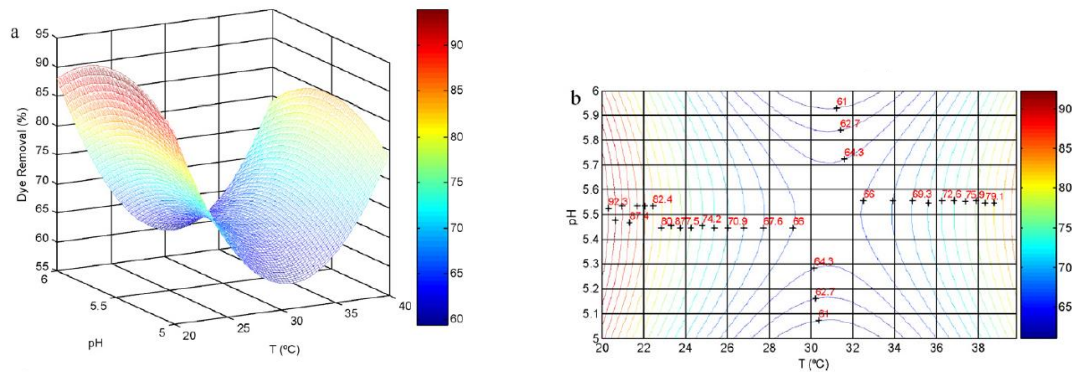


Figure 2-3: Response surface plot (a) and contour plot (b) of predicted dye removal factor as a function of the operating temperature and initial pH at $C = 1.15 \text{ g l}^{-1}$. (Khayet, Zahrim et al. 2011)

2.6. EC reactor types

In EC reactors, effective pollutant abatement is achieved by optimizing the contact pattern, particle transport and reaction kinetics. The contact pattern aids the contact between the pollutant and coagulant. The particle transport which is governed by the flow regime aids the collision between pollutants with coagulant and bubbles. The reaction time and reaction dynamics which are governed by the reaction kinetics aid generation of coagulants and bubbles. Generally, EC reactors are divided into two categories based on contact pattern, batch and continuous reactors (Figure 2.4).

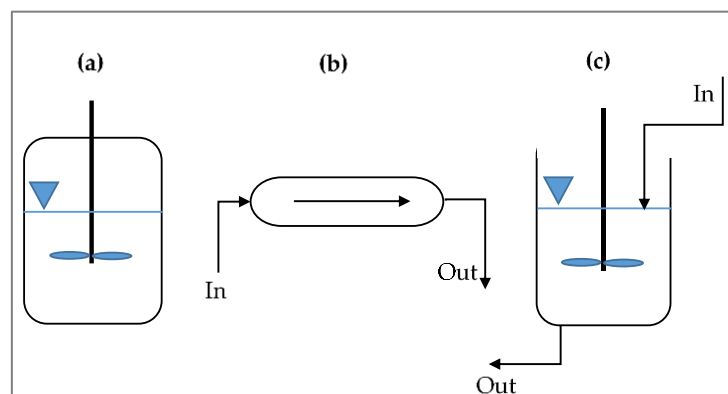


Figure 2-4: Most widely used EC reactors types (a) batch, (b) plug-flow, (c) continuous reactors

Figures 2.5 to 2.7 illustrate some of the most recent uses of different EC reactor types in water and wastewater treatment modelling studies. According to past studies comparisons between plug-flow and continuous flow reactors in electrocoagulation are limited. However, it has been highlighted that the anodic metal and energy consumption are lower in the continuous flow reactors than in batch systems (Ntambwe Kambuyi, Bejjany et al. 2021).

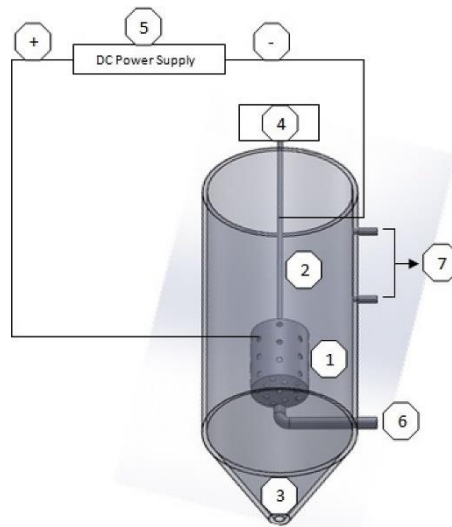


Figure 2-5: Schematic diagram of a Plug-flow Reactor. 1) 3D perforated cylindrical impeller (anode). 2) Rod (cathode). 3) Conical Hopper Bottom for Sludge collection. 4) Mechanical stirrer. 5) DC Power Supply Unit 6) Inlet for wastewater. 7) Outlet for treated water (Choudhary and Mathur 2017)

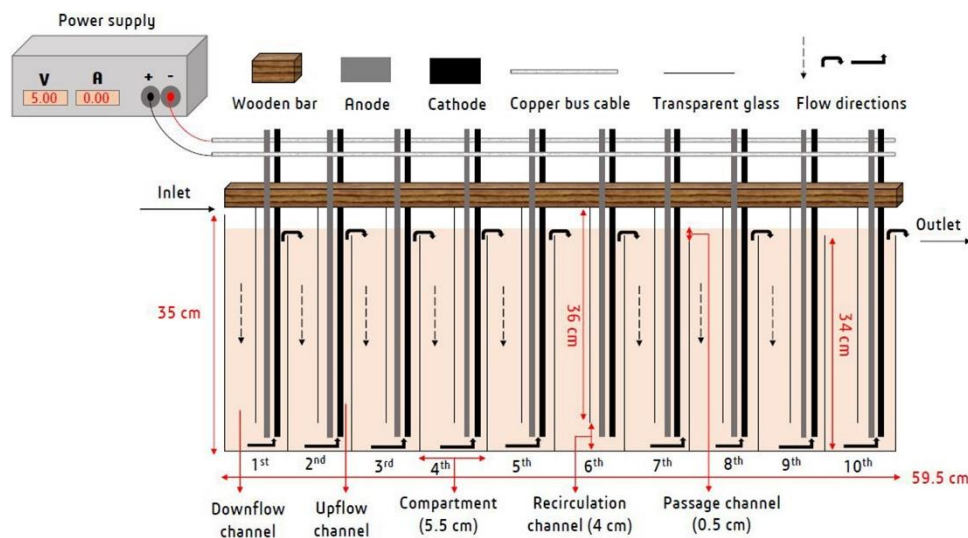


Figure 2-6: Schematic diagram of a continuous EC reactor (Ntambwe Kambuyi, Bejjany et al. 2021)

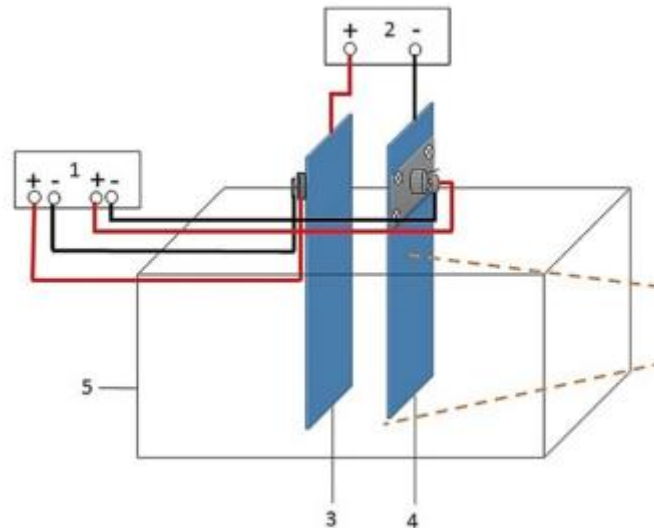


Figure 2-7: Schematic diagram of a batch EC reactor set-up (1) multiple-input DC power supply (2) single-input DC power supply (3) cathode plate (4) anode plate (5) EC cell (Muhammad Niza, Abdul Razak et al. 2021)

It is important to note that the mixing pattern strongly affects the performance and effectiveness of EC reactors. Fluid flow and agitation govern the mixing in a batch reactor, while residence time and flow path govern the mixing in a continuous reactor. Continuous reactors can be further categorised based on the mixing regime. Continuous stirred tank reactors (CSTR), plug flow reactors (PFR), and differential side-stream reactors (DSR) are a few of these classifications.

2.7. Mass balance analysis in EC reactors

The application of mass balance is of great importance in determining the economic potential of electrochemical reactors. Consideration of a complete-mix reactor, with a control volume boundary that helps to identify all the mass flows into and out of the system, is the first step to perform a mass balance analysis (Figure 2.8). In addition, there are a few assumptions made before the calculation process.

1. The volumetric flow rate of the reactor is constant.
2. The solution in the reactor does not evaporate.
3. The solution in the reactor is mixed completely.

Based on the above assumptions, the mass balance equation (Eq. 15) could be written as follows.

$$\text{Accumulation} = \text{Inflow} - \text{Outflow} + \text{Generation} - \text{Dissipation} \quad (15)$$

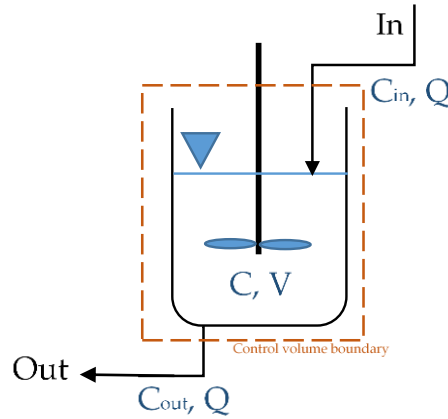


Figure 2-8: Continuous, steady-flow complete-mix reactor considered for mass balance analysis (Notations used in the figure are explained alongside Eq.16)

Symbolic representation of Eq. (15), applied to Figure 2.8 is given below.

$$\frac{dC}{dt}V = C_{in}Q - C_{out}Q + r_gV - r_dV \quad (16)$$

Where,

C is the concentration of the reactant in the reactor (mg l^{-1})

C_{in} is the concentration of reactant entering the reactor (mg l^{-1})

C_{out} is the concentration of reactant leaving the reactor (mg l^{-1})

V is the volume of the reactors (l)

t is time (s)

Q is the flow rate of the reactor (l s^{-1})

r_g is the reaction rate of generation of reactant (mg l^{-1})

r_d is the reaction rate of dissipation of reactant (mg l^{-1})

Under the complete-mix condition, the concentration of the reactant in the reactor could be considered equal to the concentration of the reactant leaving the reactor. Hence, equation (16) could be further simplified to the following expression.

$$\frac{dC}{dt}V = (C_{in} - C)Q + (r_g - r_d)V \quad (17)$$

Here, the reaction rates expressed in terms of generation and dissipation rates will depend on the nature of the rate expressions. For example, zero, first, or second-order rate equations, as explained by equations (18) to (21) where r is considered as the rate of reaction and k as the rate constant.

$$r = \pm k \quad (\text{zero-order}) \quad (18)$$

$$r = \pm kC \quad (\text{first-order}) \quad (19)$$

$$r = \pm kC^2 \quad (\text{second-order}) \quad (20)$$

$$r = \pm \frac{kC}{K+C} \quad (\text{saturation or mixed-order}) \quad (21)$$

Equations (18) to (21) are considered as the integration form of the reaction rates, and the integrated form of the same equations are expressed by equations (22) to (25). Here, C_0 and C_t represent the concentration of the pollutant at time zero and at time t , respectively.

$$C - C_0 = \mp kt \quad (\text{zero-order}) \quad (22)$$

$$\ln \frac{C}{C_0} = \pm kt \quad (\text{first-order}) \quad (23)$$

$$\frac{1}{C} - \frac{1}{C_0} = \pm kt \quad (\text{second-order}) \quad (24)$$

$$kt = K \ln \frac{C_0}{C_t} + (C_0 - C_t) \quad (\text{saturation or mixed-order}) \quad (25)$$

2.8. EC reactor scale-up

EC reactor scale-up is a mandatory process once the laboratory level operations are optimised satisfactorily. Generally, the feed flow rate is the main scale-up parameter that results in increased reactor size. It is important to maintain the same functioning efficiencies by managing the operational parameters (e.g. flow rate, supply current density, etc.) to achieve the reliability of this technology for efficient large-scale water/wastewater treatment. EC scale-up and modelling approaches are limited in the literature (Hakizimana et al., 2017). It was noted that simple projection or estimation tools are used to scale up the identified optimized parameters at the laboratory/bench scale such as the contact time (flow rate/volume), pollutant removal rate (amount of pollutant removed/coagulant amount released from the anode), etc. Although dimensional analysis is the most common engineering approach for scale-up operations, limited evidence is available in the literature on applications for EC designs (Sulaymon 2012). This could be due to the complexity of the EC process, the wide range of reactor types and pollutants. Dimensional analysis is a basic concept underlying the theory of transport processes in which various rate constants, transfer coefficients, transport properties and reactor dimensions are combined in such a way that dimensional consistency is maintained. The theory ensures that dynamic, geometric and kinetic similarities are sustained, to achieve similar flow patterns in a reactor (Andreas 2014). It was noted that little consideration has been given to dimensional modelling in EC reactor scale-up (Aleboyeh, Daneshvar et al. 2008, Garcia-Lara, Montero-Ocampo et al. 2014). Contrarily, it was noted that several studies utilized dimensional analysis theories in designing and scale-up operations of electrochemical reactors which are used in several industrial applications (Gupta and Oloman, 2006, Szpyrkowicz and Radaelli, 2006). According to Sulaymon (2012), who has performed studies on electrochemical reactors, these concepts can be easily merged with the scale-up of EC reactors which gives a systematic approach that

addresses a broader spectrum of concepts such as geometric, kinematic, thermal and current/potential similarity between the reactors.

The use of dimensional analysis for EC process scale-up parameters of EC is limited and quite conflicted, in the literature. Zolotukhin (1989) scaled up an EC-flotation system from laboratory to industrial scale by studying five dimensionless scale-up parameters given in Table (2.1), to ensure correct sizing and proportioning of the reactors (Eq. 26 to 30).

Table 2-1: Dimensionless scale-up parameters used (Zolotukhin, 1989)

Dimensionless parameter	Equation	Equation No.
Reynolds Number	$Re = \rho VD/\mu$	(26)
Froude Number	$Fr = V/\sqrt{gD}$	(27)
Weber Number	$We = \rho LV^2/\sigma$	(28)
Geometric Similarity	$L_p/L_m, A_p/A_m$	(29)
Gas Saturation Similarity	SGr $= -0.032 (\log(k_w))^2$ $+ 0.1223 \cdot \log(k_w) + 0.1489$ (Mulyadi, Amin et al. 2001)	(30)

Here,

ρ is density of liquid (kg m^{-3})

V is velocity (m s^{-1})

D is hydraulic diameter (m)

μ is dynamic viscosity (N s m^{-2}) at 20 °C

L is length (m)

σ is surface tension (J m^{-2}) at 20 °C

k_w is water permeability (H m^{-1})

However, Holt et al. (2005) dispute adapting similarity principles, the applicability of which may be inherently limited for EC, due to the complexity of the internal processes. Also, as per a study by Zlokarnik (2001) on the application of dimensional analysis in chemical reactors, it has been concluded that the theory of similarity is of limited importance in chemical processes although it has been of greater use in heat transfer reactors. Nevertheless, the correct combination of dimensionless factors could help improve the contact patterns in EC reactors for certain pollutant abatement processes. Concerning the general EC scale-up methods, there are very few EC scale-up parameters found in the literature, as listed below (Almazán-Ruiz, Caballero et al. 2012, Hakizimana, Gourich et al. 2017).

1. Electrode area to reactor volume ratio (A/V): This measured potential for generating enough coagulant and bubbles in the system
2. Current density (I/A): Current per unit active anode area, a direct measure of the potential for coagulant and bubble generation

It is surprising to note that there are no scale-up parameters that decide the feed pipe size, cross-section area of the reactor, flow direction in the reactor, ideal gap between the plates, mixing rate, etc. A scale-up methodology that takes into account these aspects would ideally help wider application possibilities and sustainable use of the EC technology.

2.9. Chapter 2 conclusion

In this chapter, the theoretical background of EC reactor design and scale-up were explored under several sub-themes. Initially, the pollutant abatement mechanism of the defluoridation process using EC technology with aluminium electrodes was studied. Adsorption and colloidal trapping in $Al_n(OH)_{3n(s)}$ "sweep floc" was found to be the main defluoridation mechanism in the EC reactor. Hence, the theoretical model which is discussed in chapter 3, will be developed using adsorption as the coagulation method. Next, the cell potential and energy calculation theories for EC

reactors were studied and summarised, followed by the details of the operating parameters important for the determination of EC reactor efficiency. This led to the study on reactor types' identification which is important for the mass balance application in EC reactors. The equations (15) to (25), explain the application of mass balance equations for different reactor types, in diverse reaction types. Finally, the scale-up theories used for EC reactors were explored. It was noted that the main two parameters used for EC reactor scale-up were (A/V) and (I/A) , while limited attention has been given to the application of dimensional analysis.

Chapter 3. Research design & process based conceptual Model (PBCM) development for electrocoagulation defluoridation

3.1. Chapter overview

The chapter layout is illustrated in Figure 3.1. The initial section of this chapter presents the overall research design, aimed at achieving the objectives listed in chapter 1. Section 3.3, details the scheme of the conceptual model that comprises five sub-models which are discussed with justifications for the selection for this study.

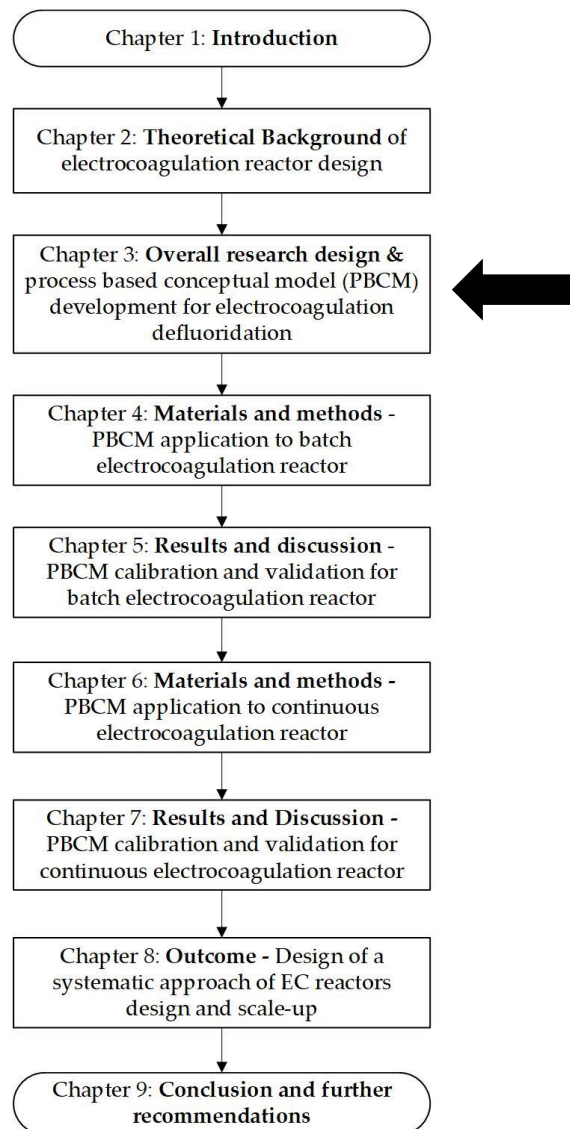


Figure 3-1: The chapter layout of the thesis

3.2. *Research design*

The understanding of scale-up properties and geometric parameters for electrocoagulation reactors is presently limited due to the complexity of the treatment processes involved (Lu, Wang et al. 2017). Application of dimensional analysis theory of similarity is of limited importance in EC process scale-up although it has been of greater use in heat transfer reactors (Zlokarnik 2001). The wider application of EC technology has been hindered due to this gap in knowledge. Addressing this gap in EC technology at this time could be a great resource to achieve the SDG 6 targets by 2030.

To address this gap of knowledge, this study aimed to develop a process-based conceptual model (PBCM) for the EC water treatment process utilizing first principle modelling techniques. The PBCM for EC water treatment is a white-box design approach that could increase the controllability of the system variables thus enabling efficient scale-up of EC reactors. The PBCM would vary according to the pollutant abatement mechanism. The pollutant considered in this study was fluoride, hence the main abatement mechanism is adsorption. Additionally, the model could be applied to different pollutants which follow the same pollutant abatement pathway. The study was designed as experimental research with four key phases that are described in the following section.

Phase 1: During phase 1, achieving objectives 1 and 2 was focused on. Understanding the scientific and mechanistic approaches developed over the years for electrocoagulation was studied initially. Then the design of a process-based conceptual model (PBCM) for a batch electrocoagulation reactor for defluoridation was carried out followed by parameterization of the process kinetics. Here, the EC process was conceptualized as a conventional water treatment process. This engineering approach helped identify the pollutant abatement and floc aggregation mechanisms, which resulted in the discretisation of the defluoridation process in the EC reactor. The next step was the numerical transformation of the model equations

into a system of integrated rate equations. These process models were interconnected based on the principle of conservation of mass. The PBCM was then implemented in two computer platforms namely, Microsoft® Excel® ver. 2016 and MATLAB® ver. R2021a which were then validated using literature data.

Phase 2: In relation to objective 2, phase 2 was implemented to retrieve primary data for the calibration and validation process of the PBCM for batch electrocoagulation defluoridation. This stage of the study consisted of the design and implementation of experiments using a laboratory-based benchtop scale batch electrocoagulation reactor. These experiments were conducted at the National Institute of Fundamental Studies (NIFS), Sri Lanka. The retrieved data from these tests were then applied in the numerical PBCM models processed in the aforementioned computer platforms for batch electrocoagulation system, to accomplish the calibration and validation of the model.

Phase 3: At phase 3, to achieve objectives 3 and 4, the design and validation of the PBCM for continuous electrocoagulation defluoridation were conducted. Following a similar approach to the phase 1 - batch model, the numerical transformation of the model equations into a system of integrated rate equation were carried out. Here, the continuous electrocoagulation reactor was considered an open system. Uniformly mixed, steady-state flow conditions were assumed for the application of the mass balance principle. Next, obtaining primary data to calibrate and validate the PBCM for continuous electrocoagulation defluoridation was aimed. A continuous electrocoagulation laboratory-scale reactor was designed and built. The experiments were conducted at two geometric scales at the Industrial Chemistry Laboratory of Liverpool John Moores University, United Kingdom. The retrieved data from these tests were then applied in the numerical PBCM models processed in the aforementioned computer platforms for the continuous electrocoagulation system, to calibrate and further validate the model along with the interim parameters.

Phase 4: At phase 4, the extrapolation of the PBCM for batch and continuous electrocoagulation for varied operating conditions and scales was evaluated. Additionally, the optimization of retention time and the relationship of hydrodynamic parameters were analysed using the novel model. As aimed in objective 5, the study established a methodology/model which was able to simultaneously address the prediction of pollution removal, settling/flotation, scale-up and techno-economic optimization.

The above-listed phases and associated flow of the sub-work packages are illustrated in the following flow-chart (Figure 3.2).

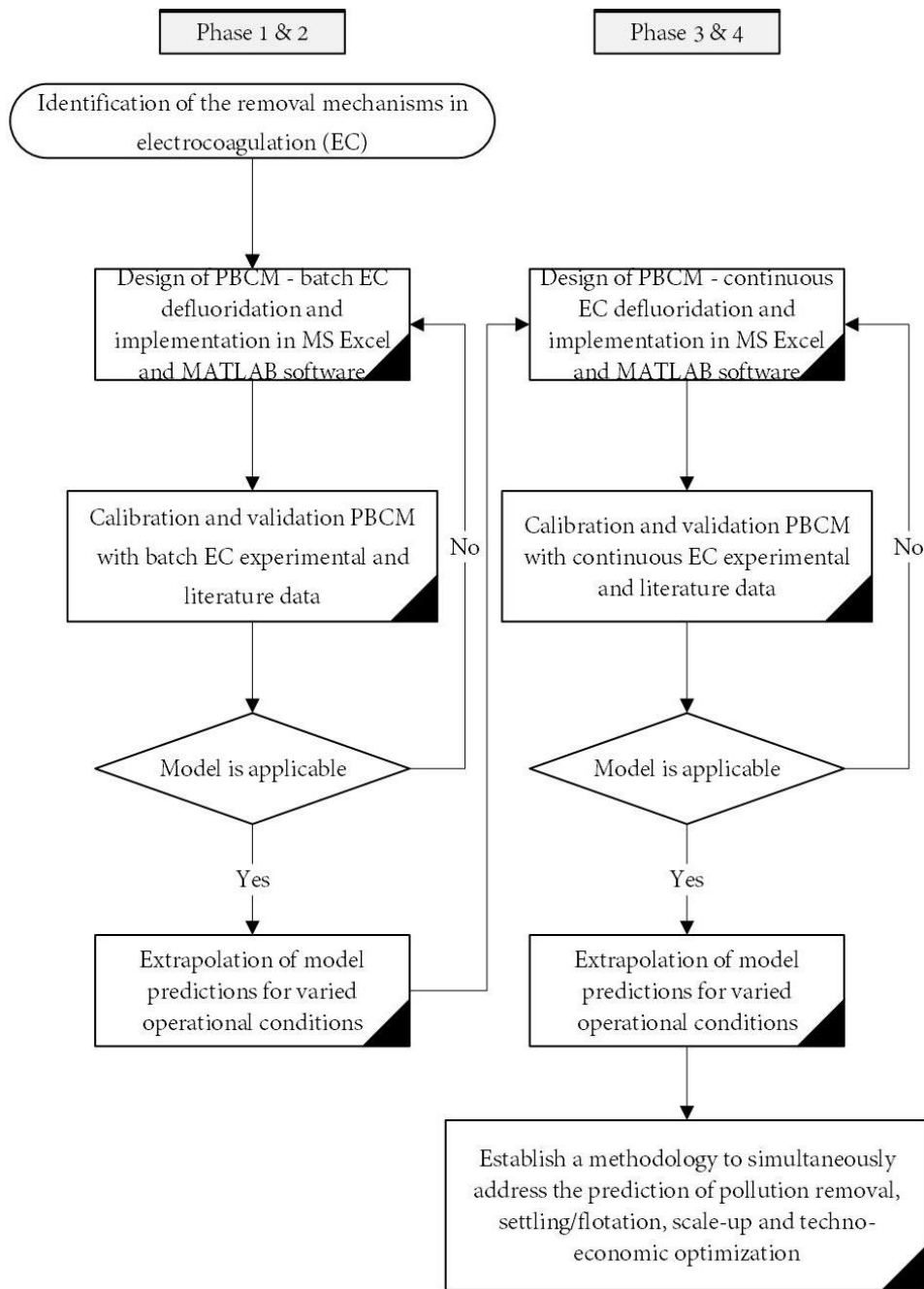


Figure 3-2: The step-by-step process of the overall study (Process-based conceptual model (PBCM), electrocoagulation (EC))

3.3. Conceptual model development for defluoridation using electrocoagulation

3.3.1. Conventional theoretical and empirical modelling

The EC process has been modelled using the classical kinetic law to simulate and design the EC system (Eq. 31) in various studies. The removal of pollutants such as fluoride, boron, nitrates, and heavy metals by EC exhibited best fits with the n-order kinetic model (Mameri, Yeddou et al. 1998, Isa, Ezechi et al. 2014, Yehya, Chafi et al. 2014).

$$\frac{dC}{dt} = KC^n \quad (31)$$

Where,

C is concentration of the pollutant (mg l^{-1})

K is reaction rate constant (unit depends on the value of n)

n is the order of reaction

t is time (s)

Also, there are some models developed based on the electrode reaction, adsorption kinetics, and mass balance. These models are generally synthesized using reaction rate equations built on the chemical reactions (Zhang, Yang et al. 2020).

The model described in eq. 10 helped recognise the capability of the technology to remove pollutants for a specific operational condition. In contrast, those models have failed to quantify the key underlying pollutant abatement mechanisms in EC. Hence, process-based modelling is imperative due to its ability to understand and control the principal processes of EC (Holt, Barton et al. 2005). The process-based models are generally developed based on electrochemical phenomena, adsorption, flocculation, and lastly, flotation and settling processes. The studies carried out by Holt (2003) and Emamjomeh and Sivakumar (2009) provide detailed insights into this modelling technique. The study by Holt (2003) uses an approach that combines coagulant generation, hydrolysis, flocculation, and settling or flotation. The latter study had explored the process-based modelling technique but concluded with an empirical

relationship of the parameters. Additionally, a recent study by Graça, Ribeiro et al. (2019) developed a mathematical model considering the electrochemical dissolution of the Al anode, water electrolysis, hydrolysis of dissolved Al, and water dissociation reaction involved in the electrocoagulation process. One of the main limitations of all these models is the insensitivity for the pH evolution with time or space, which governs the efficiency of the hydrolysis process. In addition to that, integrating hydrodynamic parameters into the model is yet to be addressed.

3.3.2. Development of the process-based conceptual model (PBCM)

The methodology introduced in this paper individuates the processes relevant for dissolved fluoride removal, using EC with aluminium electrodes these are electrolysis, hydrolysis, coagulation, flocculation, and flotation/settling (Figure 3.3). The interconnection of these key processes that occur serially within the same space in the EC batch reactor is derived using the mass balance equations for a continuous stirred tank reactor (CSTR) in a series operating at a steady-state.

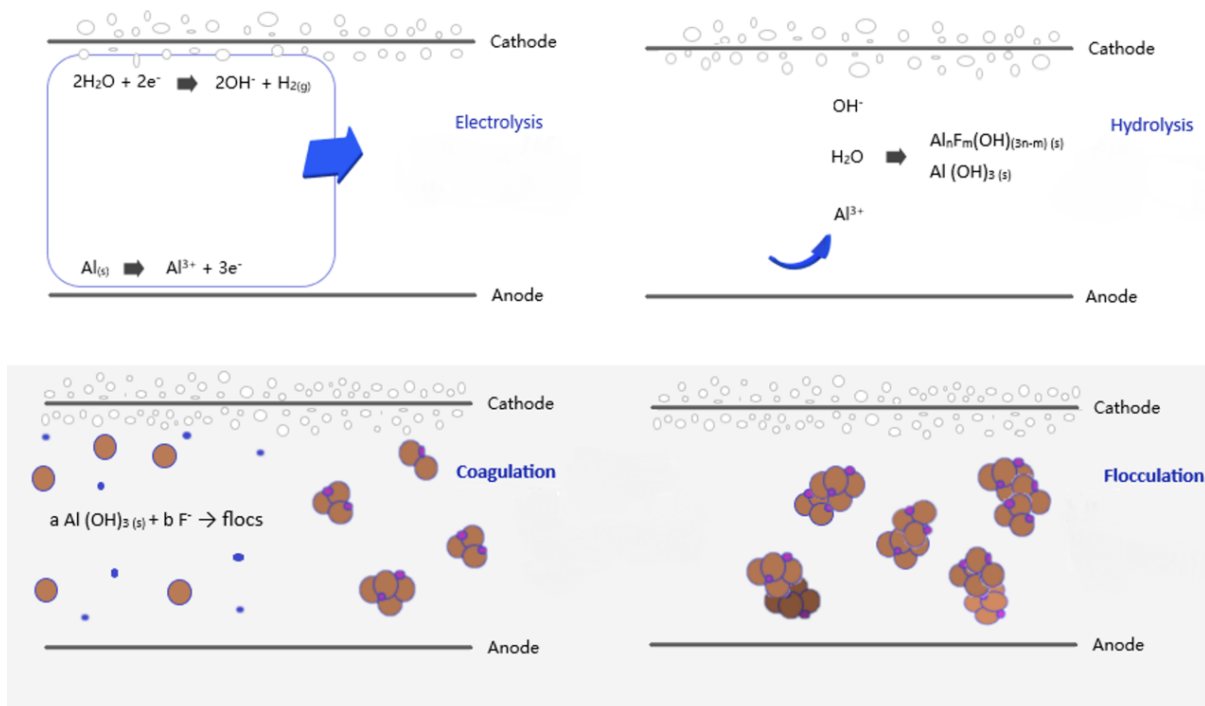


Figure 3-3: The component processes used for the fluoride removal model

3.3.3. Sub-model 1: electrolysis model

When the electrical current is supplied, the anode dissolution and oxygen evolution on the anode (Eq. (1) and (2)) and the hydrogen evolution on the cathode (Eq. (3)) are initiated. The rate of aluminium dissolution on the anode can be determined based on Faraday's law (Eq. (32)) (Mbacké, Kane et al. 2016, Hakizimana, Gourich et al. 2017)

$$\frac{dm_{Al}}{dt} = \phi \frac{IM}{ZF} \quad (32)$$

Where:

I is electric current (A)

M is the atomic weight of the electrode material (mg mol^{-1}),

F is Faraday's constant (96487 C mol^{-1}),

ϕ is a correction factor, denoted current efficiency or faradic yield,

m_{Al} is mass of metal dissolved from electrolysis (mg),

t is electrolysis time (s),

Z is number of electrons, transferred ($Z=3$ for aluminium),

$\frac{dm_{Al}}{dt}$ is the rate of aluminium dissolution (mg s^{-1})

3.3.4. Sub-model 2: hydrolysis model

Different hydrolysis reactions could occur after the dissolution of aluminium from the anode producing many aluminium hydroxide monomeric and polymeric species.

In addition to the reactions (Eqs. (4)-(9)) in chapter 2.1, the monomeric species that are formed from the hydrolysis of Al^{3+} cations according to pH level are listed below (Eqs. (33)-(36)).



According to the Pourbaix diagram for aluminium in an aqueous solution where dissolved fluoride is present, at pH 5-6, fluoroaluminium complexes are predominant (AlF^{2+} , AlF_2^+ , AlF_3 , AlF_4^-) since soluble Al^{3+} cations prevail when pH is lower. When the pH is larger than 8, the defluoridation efficiency decreases due to the prevalence of soluble aluminate anions at higher pH levels. The insoluble $\text{Al}(\text{OH})_3$ form predominates at pH6-8 since aluminiumhydroxofluoride formation is maximum $\text{Al}_n\text{F}_m(\text{OH})_{(3n-m)}$ (Emamjomeh, Sivakumar et al. 2011). Additionally, the polymeric species $\text{Al}_6(\text{OH})_{15}^{3+}$, $\text{Al}_7(\text{OH})_{17}^{4+}$, $\text{Al}_8(\text{OH})_{20}^{4+}$, $\text{Al}_{13}\text{O}_4(\text{OH})_{24}^{7+}$ have also been reported (Essadki, Gourich et al. 2009). The counterbalancing effect described by Lewis acidity of aluminium leads to a final pH between 7 and 8 as a result of the formation of OH^- anions at the cathode that induces a buffer effect. Hence, eventually the monomeric and polymeric species contribute to the formation of the amorphous $\text{Al}(\text{OH})_3$ "sweep flocs" which have large surface areas (Eq. (7)).

As stated, the pH condition governs the hydrolysis reaction and the hydroxide products (Graça, Ribeiro et al. 2019). Also, it could be identified from the hydrolysis equations that the dissolving of Al(III) is the rate-determining step during EC defluoridation (Mameri, Yeddou et al. 1998). Adopting this concept, Hu, Lo et al. (2007) developed a model where an efficiency factor (ϵ_{Al}) was used to calculate the amount converted as hydro-fluoro-aluminium. The Langmuir equation was used to describe EC defluoridation reaction. However, for the present model, the requirement was to explain the prior step to this, which is the hydrolysis of aluminium cations. Therefore, in this model, a new efficiency factor shall be considered to calculate the amount converted as aluminium hydroxide species, which are ready to adsorb the

dissolved fluoride. This efficiency factor is symbolized as K in equation (37). Hence, the hydrolysis model can be introduced as follow:

$$\frac{dm_{Al(OH)_3}}{dt} = K \cdot K(a) \quad (37)$$

Where:

$m_{Al(OH)_3}$ is the mass of $Al(OH)_3(s)$ generation (mg),

t is hydrolysis time (s),

K is a percentage denoted hydrolysis efficiency,

K(a) is the rate of aluminium (III) dissolving process ($mg\ s^{-1}$).

3.3.5. Sub-model 3: coagulation model

Typically, the contaminants in water and wastewater remain in colloidal form. These colloids form a suspension, as far as the colloids remain separated, so that gravity forces will not cause precipitation of these colloidal particles. The destabilization of such a suspension is called coagulation (Bratby, 2006). Overpowering the aiding factors of colloidal stability is the primary function of coagulation. There are different methods to destabilize colloids, namely, (a) double layer compression, (b) adsorption and charge neutralization, (c) adsorption, and inter-particle bridging, (d) enmeshment in a precipitate (sweep floc). When considering the fluoride removal using the aluminium anodes in EC, the coagulation occurs via processes (c) and (d) outlined above.

The majority of prior research has applied Langmuir isotherm or Freundlich isotherm and also the Langmuir–Freundlich model that combines both (Essadki et al., 2010; Vasudevan and Lakshmi, 2011; Yoosefian et al., 2017). Besides, Hu, Lo and Kuan (2007) introduced a variable-order-kinetic model (VOK), which was derived by combining adsorption isotherm models and Faraday's law. In his study on fluoride removal using aluminium anodes, the use of the Langmuir isotherm had proven effective. Also, the present model developed in this study employs Farraday's model

separately. Hence, the use of Langmuir Isotherm (Eq. 38) is considered as the coagulation model for the present study.

$$q_e = \frac{q_m K_L C_e}{1 + K_L C_e} \quad (38)$$

Where:

q_e is the amount of pollutant adsorbed per unit mass of adsorbent at equilibrium (mg g^{-1}),

q_m is the maximum adsorption capacity (mg g^{-1})

K_L is Langmuir constant (l mol^{-1})

C_e is the equilibrium concentration of the pollutant (mol l^{-1}).

3.3.6. Sub-model 4: flocculation model

The process of inducing the destabilized particles to come together, make contact, and thereby form larger (settlable) agglomerates is called flocculation (Bratby 2006). The flocculation mechanism has two steps, i.e., transport leading to the collision and attachment. The first step can occur by (a) Brownian motion of the particles (perikinetic flocculation), (b) fluid motion (orthokinetic flocculation), and (c) differential settling velocities due to gravity (differential sedimentation) (MWH Americas, Crittenden Communications et al. 2012) as illustrated in Figure 3.4.

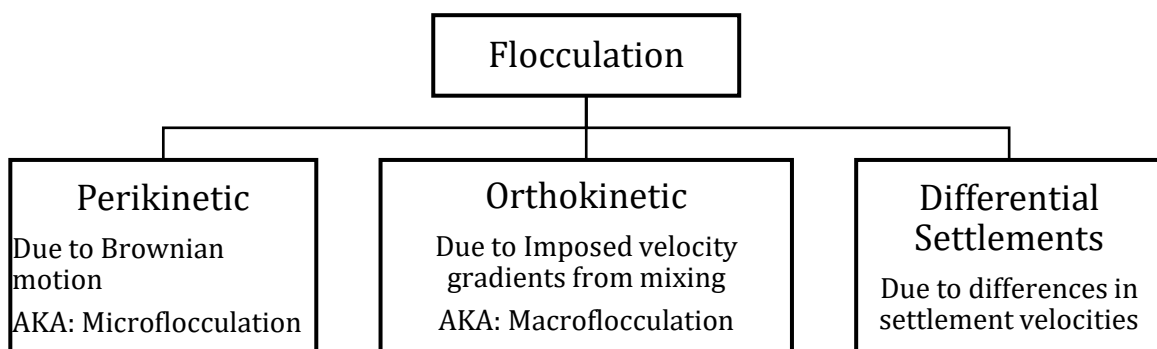


Figure 3-4: Flocculation mechanisms – the modes of transport of colloids leading to the collision

The second step of flocculation, attachment, has occurred. The classical analytical expression of flocculation, originally published by Smoluchowski in 1917, led to several advancements later on through new studies. Smoluchowski had made six assumptions (listed below), to develop the model expressed in equation (39).

1. All particle collisions lead to attachment,
2. Fluid motion is limited to laminar shear,
3. Particles are monodispersed,
4. No breakage of flocs occurs,
5. All particles are spherical and remain so after collision and
6. Collisions take place only between two particles.

In Smoluchowski's original work, the assumption of all collisions leading to attachment, had ignored the effects of electrostatic repulsion, van der Waals or hydrodynamic forces. Modernised theories/models attempted to overcome this limitation and proposed three theories in the late 19th century as illustrated in Figure 3.5 (Thomas, Judd et al. 1999).

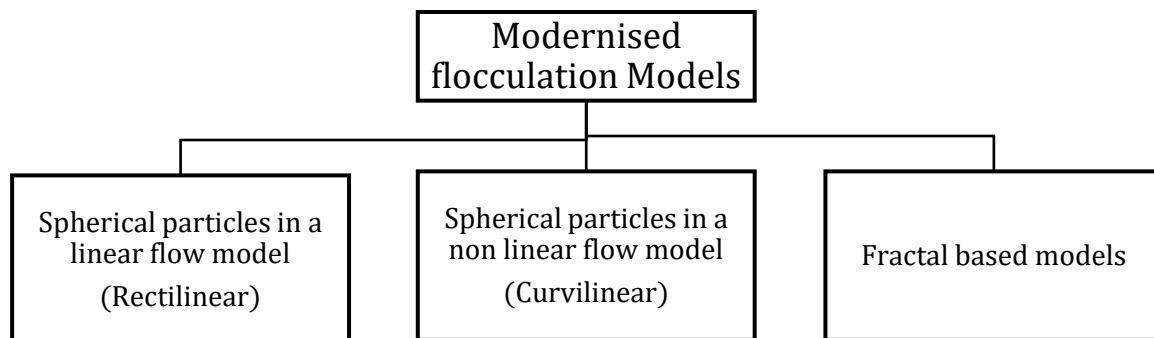


Figure 3-5: Modernised flocculation models

However, later on, the particles were considered as fractal rather than solid objects (Chellam and Wiesner 1993). As a result, the density of the particles decreases with increasing size (Figure 3.6). As per the new assumption, a considerable reduction in the hydrodynamic resistance should be expected when a small particle reaches a

larger porous aggregate (Veerapaneni and Wiesner 1996). Hence, the accuracy of both curvilinear and rectilinear models of flocculation was reconsidered. As per Thomas, Judd et al. (1999), the most suitable model comprises a balance between both of these models.

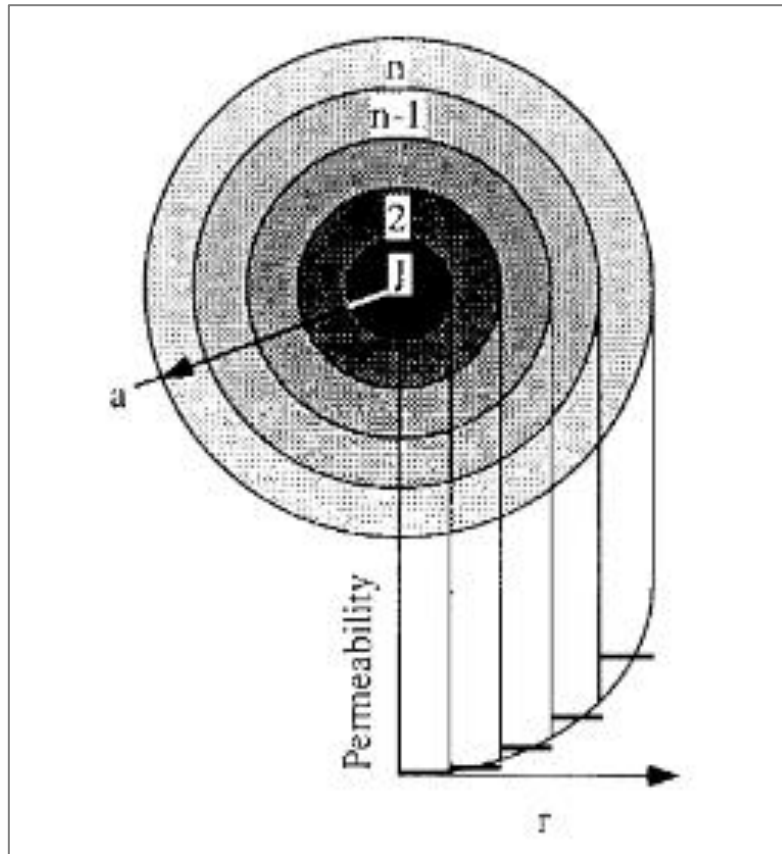


Figure 3-6: Model representation of porous aggregate (Chellam and Wiesner 1993)

Smoluchowski's flocculation model formed the base for all subsequent flocculation modelling studies. The original equation developed by Smoluchowski is expressed below.

The number of collisions occurring between i and j particles in unit time and unit volume, J_{ij} , is given by:

$$J_{ij} = \alpha k_{ij} n_i n_j \quad (39)$$

Where,

α is collision efficiency

k_{ij} is rate order constant for aggregation (l^2s^{-1})

$n_i n_j$ are number of i and j particles per unit volume respectively (Nos l^{-1})

Here k_{ij} depends on several factors, such as particle size and transport mechanism. In considering the rate of aggregation, it must be recognized that not all collisions may be successful in producing aggregates. The fraction of successful collisions is called the collision efficiency and is given the symbol α . If there is strong repulsion between particles, there will not be any collisions that give aggregates and $\alpha = 0$. When there is no significant net repulsion or attraction between particles, then the collision efficiency can approach unity (Elimelech et al., 1995).

Based on the transport mechanisms of particles illustrated in Figure (3.4), the rate of flocculation could be expressed as follows (Eq. 40).

$$J_{ij} = J_{\mu} + J_{DS} + J_M \quad (40)$$

Where,

J_{ij} = rate of attachment between i and j particles (s^{-1})

J_{μ} = rate of attachment due to microscale collisions (s^{-1})

J_M = rate of attachment due to macroscale collisions (s^{-1})

J_{DS} = rate of attachment due to differential setting (s^{-1})

The effectiveness in applications of this equation is limited in real systems due to the idealized systems based on simplifying assumptions used in this equation (Crittenden, Trussell et al. 2012). Nevertheless, this is used in the present research for initial testing, utilizing the same assumptions made in developing Smoluchowski's classical flocculation equation.

Spherical monodispersed particles in a linear flow model were considered for this model, hence the differential settlement theory was not applicable. The Perikineti

and orthokinetic flocculation based model that was used in this study is explained below (Eq. 41 & 42).

$$\frac{dn}{dt} = -K_{M+\mu}n^2 \quad (41)$$

$$K_{M+\mu} = \frac{8kT * 1000}{3\mu} + \frac{2}{3} \bar{G} \alpha d_i^3 * (1/1000) \quad (42)$$

Where:

$K_{M+\mu}$ is rate constant for particle aggregation ($l s^{-1}$),

T is absolute temperature (K),

μ is dynamic viscosity of suspending fluid ($N s m^{-2}$),

k is Boltzmann's constant ($J K^{-1}$),

d_i is particle size (cm),

n is particle number concentration (l^{-1}),

α is collision efficiency (-),

G is velocity gradient (s^{-1}).

3.3.7. Sub-model 5: flotation/settling model

There are diverse physical methods to remove the agglomerated particles generated from the flocculation process. In addition to the settling due to gravity, the floc tends to float, by means of buoyancy forces resulting from the micro-bubbles in EC reactors. This is called electro-flotation, which depends on current density, hydrogen micro-bubble size (20–50 μm), and particle collection efficiency by the micro-bubbles (Holt 2003). There is little evidence in the literature to utilize a flotation/settling model in EC reactors. The study by Holt, Barton et al. (2005) suggested a first-order model based on pollutant removal paths that consider the competitive process between settling and flotation in pollutant removal (Eqs. (43)-(45)).

$$Pollutant (C_{poll}) \xrightarrow{k_1} Surface (C_{Surface}) \quad (43)$$

$$\text{Pollutant } (C_{poll}) \xrightarrow{k_2} \text{Base } (C_{Base}) \quad (44)$$

$$r_{poll} = -\frac{dC_{poll}}{dt} = k_1 C_{poll} + k_2 C_{poll} = (k_1 + k_2) C_{poll} \quad (45)$$

Where:

C_{poll} is pollutant concentration in the bulk solution (mg l^{-1}),

$C_{Surface}$ is pollutant concentration at the surface (mg l^{-1}),

C_{Base} is pollutant concentration at the base (mg l^{-1}),

r_{poll} is rate of electro-flotation and sedimentation ($\text{mg l}^{-1} \text{s}^{-1}$),

k_1 is rate constant of the electro-flotation process (s^{-1}),

k_2 is rate constant of the sedimentation process (s^{-1}).

Concerning the conceptual model developed in this study, dissolved fluoride removal using aluminium electrodes is considered. The settling and flotation model proposed by Holt (2003) requires alternate experimental arrangements to identify the rate constants of the two processes. As per the literature and initial experimental investigations, flotation is the main floc removal mechanism noted during the fluoride removal process. Hence, a conceptual model based on the fundamentals of electro-flotation was considered suitable in this study (Eqs. (46)-(49)).

The microbubble flotation which affects floc flotation and the gas microbubble's rising velocity (V_b) through the water in laminar operating conditions can be calculated using Stoke's law (Coker 2007).

$$V_b = \frac{g}{18\mu} (\rho_L - \rho_g) d^2 \quad (46)$$

Where:

μ is dynamic viscosity of suspending fluid (N s m^{-2}),

g is gravitational acceleration (m s^{-2}),

ρ_L is density of the liquid (kg m^{-3}),

ρ_g is density of the gas (kg m^{-3}),

d is bubble diameter (m).

The flotation kinetic equation describes the kinetic rate of particle or floc removal by collision and attachment to bubbles as expressed by equations (47) & (48) (Haarhoff and Edzwald 2004).

$$\frac{dN_{fd}}{dt} = -\frac{1}{12} \frac{\alpha_{db} \eta_T d_b \varphi_b g}{v/V_b} N_{fd} \quad (47)$$

$$\frac{dN_{fd}}{dt} = -K_f N_{fd} \quad (48)$$

Where:

N_{fd} is floc density (flocs m^{-3}),

α_{db} is collision coefficient between an air bubble and floc,

η_T is collision frequency between the air bubble and floc,

φ_b is air dosage (m^3 air m^{-3} water),

v is kinematic viscosity of suspending fluid ($\text{m}^2 \text{s}^{-1}$),

g is gravitational acceleration (m s^{-2}),

d_b is bubble diameter (m),

V_b is rising velocity of bubbles (m s^{-1}),

K_f is flotation constant (s^{-1}).

The theoretical amount of hydrogen gas H_2 generated during the EC process can be calculated using Faraday's law (Deghles and Kurt 2017).

$$\dot{m}_{\text{H}_2} = \frac{IM}{F} \cdot H \quad (49)$$

Where:

\dot{m}_{H_2} is rate of H_2 gas generation (mg s^{-1}),

M is atomic weight of H_2 (mg mol^{-1}),

F is faraday's constant (96487 C mol^{-1}),

I is electric current (A),

H is the number of hydrogen molecules generated per electron involved in the redox reactions ($=0.5$).

3.4. Conclusion of chapter 3

To achieve objective 1, the design of a process-based conceptual model (PBCM) for a batch electrocoagulation reactor for defluoridation was carried out followed by parameterization of the process kinetics as explained in section 3.3. The PBCM for electrocoagulation defluoridation comprised five sub-models namely, electrolysis, hydrolysis, coagulation, flocculation, and flotation. Proceeding steps focus on the numerical transformation of the model equations into a system of integrated rate equations, and implementation in two computer platforms namely; Microsoft® Excel® ver. 2016 and MATLAB® ver. R2021a. Detail will be discussed in chapter 4.

Chapter 4. Materials and methods – PBCM application to batch electrocoagulation reactors

4.1. Chapter overview

This chapter comprises the discrete-continuous model conversion scheme of PBCM for batch reactor & experimental design of batch electrocoagulation operation. Figure 4.1 illustrates the chapter layout of the thesis and the interconnection of this chapter to the rest.

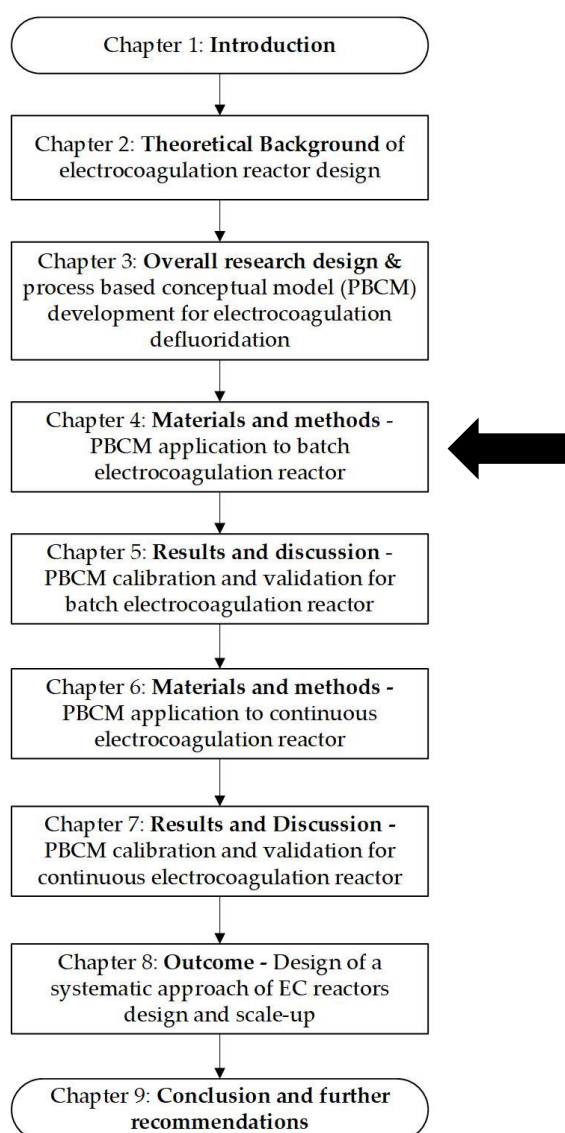


Figure 4-1: The chapter layout of the thesis

4.2. *Discrete-continuous model conversion scheme of the PBCM*

Discretisation refers to the process of transforming given continuous functions or variables into discrete functions or variables, respectively. In this study, the reverse operation of discretisation, which is the conversion of the discrete models into a continuous-time model was a requisite. Hence, the discrete models identified in section 3.3, were transformed into a scheme of continuous-time models by applying the theory of conservation of mass (Eq. 50). The structure of work that is required to produce the scheme of continuous-time models is explained in this section.

Accumulation = Inflow – Outflow + Generation – Dissipation

$$m_{acc} = m_{in} - m_{out} + m_{gen} - m_{dis} \quad (50)$$

The conceptual sub-models identified in section 3.3, are unified concerning time (t) in this section. The configuration of the process-based model into a numeric computing platform requires an in-depth understanding of the interconnectivity between the sub-models. One of the connecting tools applied to link the sub-models is the mass balance equation.

First, the mass balance equation is used to determine the aluminium cation concentration in the reactor. Aluminium cation concentration accumulation for a given time interval is considered as m_{Al-acc} , where, the inflow and outflow are set to zero, considering the closed system.

Using Equations discussed in sections 3.3.1 and 3.3.2, the generation of aluminium at n^{th} time step (t_n) in (mg l^{-1}) can be computed as (Eq.51):

$$m_{Al-gen\ at\ t_n} = K_a(t_n - t_{n-1}) \quad (51)$$

Where $K(a)$ is the rate of aluminium (III) dissolving process ($\text{mg l}^{-1}\text{s}^{-1}$).

Also, the dissipation at n^{th} time step (t_n) in (mg l^{-1}) as (Eq. 52):

$$m_{Al-dis\ at\ t_n} = K_b(t_n - t_{n-1}) \quad (52)$$

Where $K(b)$ is the rate of hydrolysis process ($\text{mg l}^{-1}\text{s}^{-1}$).

Hence, aluminium accumulation at the n^{th} time step (t_n) in (mg l^{-1}) (Eq. 53):

$$m_{Al-acc\ at\ t_n} = K_a(t_n - t_{n-1}) - K_b(t_n - t_{n-1}) + m_{Al-acc\ at\ t_{n-1}} \quad (53)$$

And aluminium hydroxide generation from hydrolysis process at n^{th} time step in (mg l^{-1}) (Eq. 54):

$$m_{Al(OH)_3-gen\ at\ t_n} = m_{Al-dis\ at\ t_n} \times 78/27 \quad (54)$$

Aluminium hydroxide particle dissipation occurs in two methods; the formation of aluminium-hydroxo-fluoride particles as a result of the adsorption process that occurs in the system, which is explained by equation (52), and due to the adsorption on the electrodes. As per Zhu, Zhao et al. (2007), immediately after the adsorption process, a significant proportion of aluminium-hydroxo-fluoride flocs get attached on the electrodes due to the effects of the electric field. Hence, to account for this dissipation of aluminium hydroxide and aluminium-hydroxo-fluoride, a correction factor (K_E) is introduced as outlined in equation (55).

$$m_{Al(OH)_3-dis\ on\ electrodes\ at\ t_n} = K_E \times m_{Al(OH)_3-acc\ at\ t_{n-1}} \quad (55)$$

Hence, the aluminium hydroxide accumulation at n^{th} time step in (mg l^{-1}) (Eq. 56):

$$m_{Al(OH)_3-acc\ at\ t_n} = m_{Al(OH)_3-gen\ at\ t_n} - m_{Al(OH)_3-dis\ at\ t_n} + m_{Al(OH)_3-acc\ at\ t_{n-1}} \quad (56)$$

Aluminium hydroxide colloids accumulation at n^{th} time step in (mol l^{-1}) (Eq. 57):

$$n_{Al(OH)_3\ colloids\ acc\ at\ t_n} = \frac{m_{Al(OH)_3-acc\ at\ t_n}}{(Mass_{Al(OH)_3\ colloid}) \times (N_A)} \quad (57)$$

Where, $Mass_{Al(OH)_3\ colloid}$ is the mass of an $Al(OH)_3$ colloid calculated based on the ring structure formed by six aluminium hydroxide octahedra (Hem and Roberson 1967) and N_A is Avogadro's number ($6.0221409E+23$).

Hem and Roberson (1967), noted aluminium ions are usually octahedral with respect to water molecules or hydroxide when pH is below 7.5.

This behaviour of aluminium ions is dominant up to a lower limit of pH value of 4. A stable ring structure is formed composed of six octahedral aluminium ions joined together by double OH bridges. The six-member-ring unit is apparently the most stable configuration that can be built up from six AlOH octahedra. A schematic representation of the ring structure formed by six AlOH octahedral is given in Figure 4.2. This stable ring structure is what makes hydrolysed aluminium a good adsorbent.

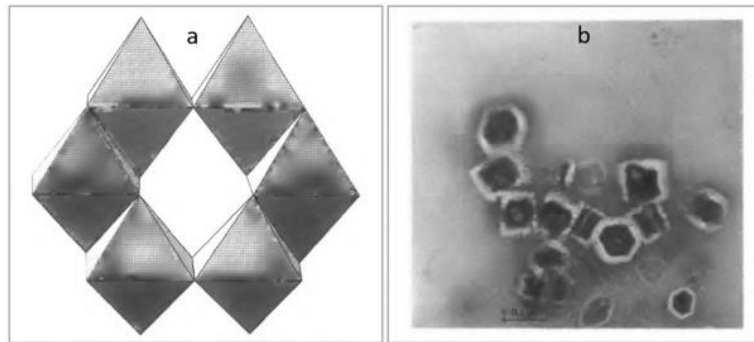


Figure 4-2: (a) Schematic representation of ring structure formed by six aluminium hydroxide octahedral, (b) and Electron photomicrograph of microcrystalline gibbsite (Hem and Roberson 1967).

These colloids behave as the adsorbents in the subsequent adsorption process. In addition to the accumulated $\text{Al}(\text{OH})_3$ colloids, the remaining particles in the reactor from the previous time step (t_{n-1}), also contribute as adsorbents in this process. Hence, the total adsorbent concentration at n^{th} time step $n_{\text{Ad accum at } t_n}$ in (mol l^{-1}) shall be expressed as (Eq. 58),

$$n_{\text{Ad accum at } t_n} = n_{\text{Al}(\text{OH})_3 \text{ colloids acc at } t_n} + N_{(\text{fd})t_n} / N_A \quad (58)$$

Where:

$N_{(\text{fd})t_n}$ is post flotation particle concentration (Nos l^{-1}) (Eq. 64)

N_A is Avogadro's number ($6.0221409\text{E}+23$),

Fluoride adsorption is calculated using the Langmuir adsorption as described in section 3.3.3. The adsorption rate must be calculated for each time step due to the variability of the pollutant concentration (fluoride) in the reactor (Eq.59).

$$q_{e_n} = \frac{q_m K_L C_{f_n}}{1 + K_L C_{f_n}} \quad (59)$$

Where:

q_{e_n} is the amount of pollutant adsorbed per unit mass of adsorbent at equilibrium (mg g^{-1}) at the n^{th} time step.

q_m is the maximum adsorption capacity (mg g^{-1}) Langmuir constant (mg g^{-1}),

K_L is Langmuir constant (l mol^{-1}),

C_{f_n} is the equilibrium concentration of the pollutant (mol l^{-1}) at the n^{th} time step.

The fluoride adsorption at n^{th} time step $m_{F \text{ dis at } t_n}$ in (mg l^{-1}) is then calculated using the total available adsorbents in the reactor as follows (Eq. 60).

$$m_{F \text{ dis at } t_n} = q_{e_n} \times n_{\text{Adsorbents accum at } t_n} \times 19000 \quad (60)$$

Dissolved fluoride was adsorbed onto the Al(OH)_3 particles which could then be considered as the aluminium hydroxide dissipation as represented in equation (Eq. 61).

$$m_{\text{Al(OH)}_3\text{-dis as Al(OH)}_3\text{F at } t_n} = (q_{e_n} \times n_{\text{Ad accum at } t_n} \times M_{\text{Al(OH)}_3\text{-F}}) / N_f \quad (61)$$

Where:

$m_{\text{Al(OH)}_3\text{-dis as Al(OH)}_3\text{F at } t_n}$ is dissipation of Al(OH)_3 due to formation of aluminium-hydroxo-fluoride (mg l^{-1}),

N_f is number of fluoride ions adsorbed on to one AlOH_3 particle (Nos),

$n_{\text{Ad accum at } t_n}$ is total adsorbent concentration at n^{th} time step (mol l^{-1})

$M_{\text{Al(OH)}_3\text{-F}}$ is molar mass of aluminium-hydroxo-fluoride particle, post adsorption process (mg mol^{-1})

q_{e_n} is the amount of pollutant adsorbed per unit mass of adsorbent at equilibrium (mg g^{-1}) at the n^{th} time step.

Hence, the equilibrium fluoride concentration in the reactor at n^{th} time step $m_{F \text{ at } t_n}$ (mg l^{-1}) shall be calculated from the following equation (Eq. 62).

$$m_{F \text{ at } t_n} = m_{F \text{ at } t_{n-1}} - (m_{F \text{ dis at } t_n}) \quad (62)$$

After the adsorption process, the flocculation process is considered. Post flocculation particle concentration $n_{\text{Floc at } t_n}$ (Nos l^{-1}) calculation shall then be calculated using the equation (63) which is derived from the second-order flocculation rate equation detailed in section 3.3.4.

$$n_{\text{Floc at } t_n} = \frac{N_{t_n}}{(1 + K_{M+\mu}(t_n - t_{n-1})N_{t_n})} \quad (63)$$

Where:

$K_{M+\mu}$ is rate constant for particle aggregation (l s^{-1}),

N_{t_n} is pre-flocculation particle concentration (Nos l^{-1}).

Finally, the flotation process is considered. The floc density (mol l^{-1}) after the flotation process at the n^{th} time step which is given as $N_{(\text{fd})t_n}$ is calculated using equation (64) derived based on the principles discussed under section 3.3.5.

$$N_{(\text{fd})t_n} = n_{\text{Floc at } t_n} \times e^{-K_f \times (t_n - t_{n-1})} \quad (64)$$

Where,

$n_{\text{Floc at } t_n}$ is post flotation particle concentration (Nos l^{-1}),

K_f is flotation constant (s^{-1}).

Figure 4.3 illustrates the step-by-step calculation process followed to execute the PBCM using MATLAB® ver. R2021a which is a programming and numeric computing platform (appendix A). The PBCM was then calibrated and validated using literature and laboratory-scale experimental data for fluoride removal using an EC batch reactor with aluminium electrodes. The experimental design has been detailed in section 4.3.

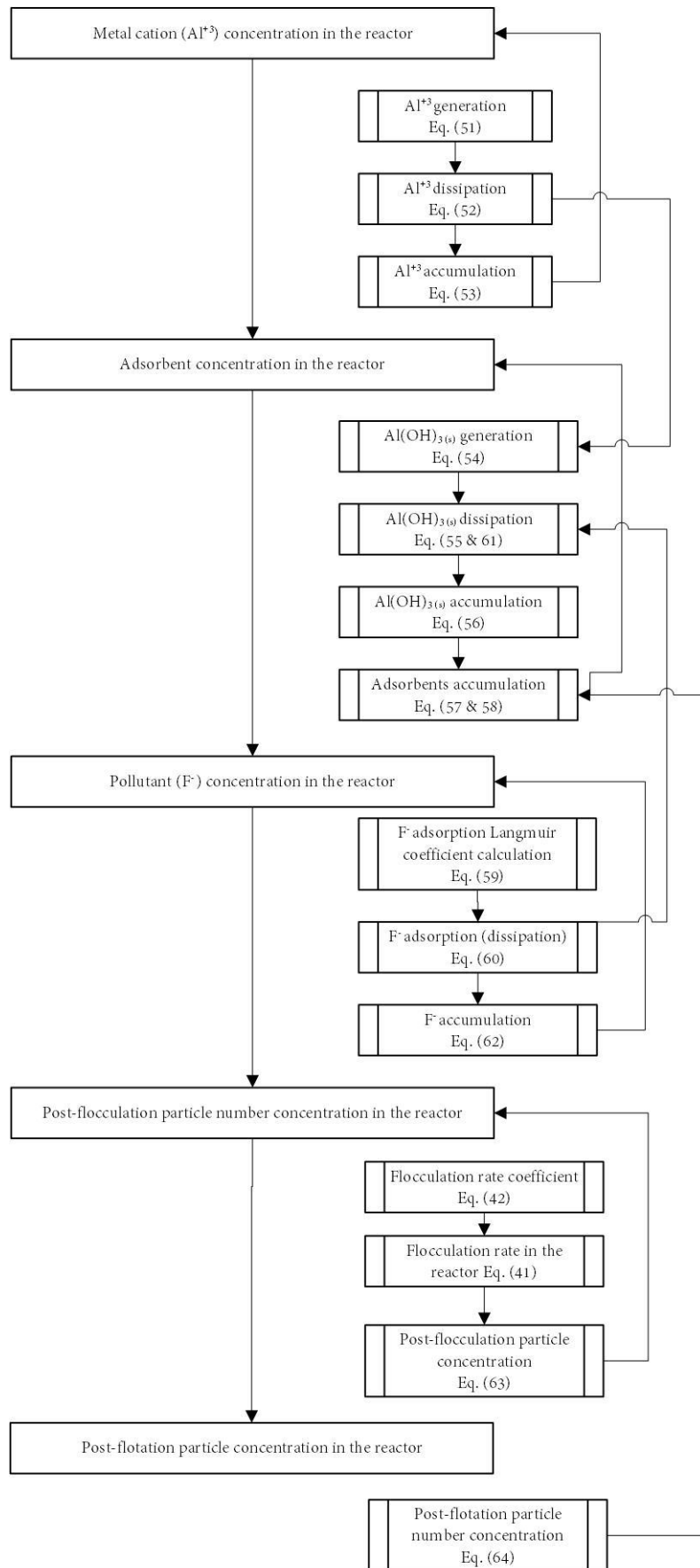


Figure 4-3: Step-by-step calculation process of the model parameters of PBCM

4.3. *Experimental apparatus*

The benchtop scale EC experiments were conducted at the National Institute of Fundamental Studies (NIFS), Sri Lanka. The EC reactor was designed by the author to suit the objectives of the study. The details of the built EC reactor are listed in Table 4.1. The schematic diagram, the plan view of the electrocoagulation box, and the bench-scale EC batch reactor testing set-up are shown in Figure 4.4. Synthetic or spiked samples were used to identify the behaviour of fluoride and the implication of the co-existing ions was tested at the second stage of the investigation. NaF added to distilled water was used and 1 M NaOH and 1:5 hydrochloric acid solutions were added for pH adjustment. Initial pH was maintained at 7 and was monitored and recorded for all experiments. NaHCO₃ was only added in synthetic samples to maintain alkalinity. NaCl (0.1 M) was added to the aqueous solution to promote the conductivity of the required samples. The TISAB buffer was added to the samples to prevent interference from Al³⁺ ions (Emamjomeh, Sivakumar and Varyani, 2011). The experimental method statement is further explained in the following section 4.4.

The experiments were conducted for different initial fluoride levels and supply current conditions (Table 4.2). Samples were extracted in ten minute time intervals for up to one hour. Before each test, the electrodes were cleaned using acetone, and a follow-up HCl solution (10% wt) was used to remove organic impurities on electrode surfaces. At the end of the experimental period, the electrodes were immediately removed. The solution was flocculated for ten minutes via gentle mixing. The samples were extracted using a pipette from the flocculated solution and filtrated by a 0.22µm filter for fluoride analysis. The flocculated solution was mixed rapidly until the floc was completely dissolved and samples were taken for pH adjustment (pH > 13) with 1 M NaOH. The samples were then taken for fluoride analysis. Samples were extracted at the given time intervals and then immediately filtered through a 0.22µm mixed cellulose ester membrane. After each reaction, total aluminium [Al]_T and the dissolved aluminium Al(III) concentration ([Al]_a) were measured from a digested and filtrated

sample, respectively. Also, temperature, electrical conductivity, and pH were checked at regular intervals. Fluoride concentrations were determined using the potentiometric method by a bench top pH/ISE meter (Thermo Orion 4-star™ meter, USA) using combination fluoride ion-selective electrode (ISE, 0.01 lg/L and 2–5 %CV) (Thermo Orion 9609BNWP, USA). Aluminium was analysed using Graphite Furnace Atomic Absorption Spectroscopy (GF-AAS), (AAS GBC 933AA; GF GBC GF 3000; auto sampler GBC PAL 3300, Australia).

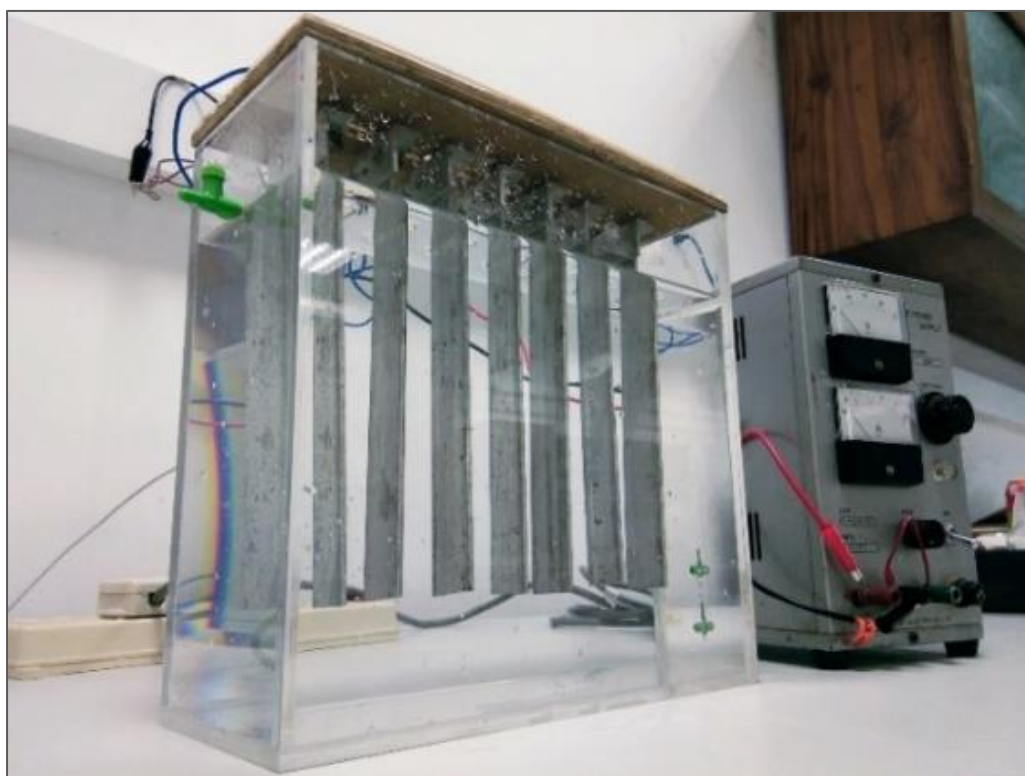


Figure 4-4: Bench-scale EC batch reactor set-up at NIFS Laboratory, Sri Lanka

Table 4-1: Bench-scale EC reactor designed for this study

<i>Parameter</i>	<i>Value</i>
<i>Electrode surface area to reactor volume (A/V)</i>	9 (m ² m ⁻³)
<i>Reactor material</i>	Perspex
<i>Reactor dimensions</i>	250mm L x 100mm W x 250mm H
<i>Maximum fluid height</i>	200mm
<i>Dead volume of the reactor</i>	5 l
<i>Net volume of the reactor</i>	4.84 l
<i>Volume of electrodes</i>	0.16 l
<i>Electrode material</i>	Aluminium (95 - 97 % purity)
<i>No. Of plates</i>	7
<i>Dimensions of electrodes</i>	125 x 60 x 3mm
<i>Submerged depth of electrodes</i>	125mm
<i>Total anode active area</i>	450cm ²
<i>Maximum current density: max current/ active electrode area (I/A)</i>	33.33A m ⁻² (at 1.5A)
<i>Maximum current concentration: max current/ reactor volume (I/V)</i>	309.92A m ⁻³ (at 1.5A)
<i>Gap between electrodes</i>	5 - 30 mm
<i>Electrode thickness</i>	3mm
<i>Electrode configuration</i>	Monopolar

Table 4-2: The operation variables and the calculated design parameters of batch EC reactor experiments

Ref. No.	Initial fluoride concentration (mg l ⁻¹)	Supply Current (A)	I/A (A m ⁻²)	A/V (m ² m ⁻³)	I/V (A m ⁻³)
E1	1.00	0.1	2.22	9.3	20.66
E2	1.00	0.3	6.67	9.3	61.98
E3	1.00	0.5	11.11	9.3	103.31
E4	2.00	0.1	2.22	9.3	20.66
E5	2.00	0.3	6.67	9.3	61.98
E6	2.00	0.5	11.11	9.3	103.31
E7	3.00	0.1	2.22	9.3	20.66
E8	3.00	0.3	6.67	9.3	61.98
E9	3.00	0.5	11.11	9.3	103.31
E10	3.00	0.5	11.11	9.3	103.31
E11	3.00	1.0	22.22	9.3	206.62
E12	3.00	1.5	33.33	9.3	309.92

4.4. Experimental method statement

1. The inlet tank was filled to 80% with deionized water.
2. Inlet water was heated to 20 °C if required.
3. Electrode surfaces were washed with HCl solution (10% wt).
4. Electrodes were soaked in an alkali solution (0.1 mol l⁻¹ NaOH) for twenty seconds.

5. Electrodes were washed with deionized water.
6. Temperature, pH, electrical conductivity of the inlet tank water was measured.
7. A sample was taken and immediately filtered through a 0.22 μm mixed cellulose ester membrane and TISAB buffer was added to the samples to prevent interference from Al^{3+} ions.
8. Dissolved fluoride was measured using a combination fluoride ion-selective electrode (ISE, 0.01 $\mu\text{g/L}$ and 2–5 %CV) (Thermo Orion 9609BNWP, USA).
9. The system of electrodes was installed in the reactor (keeping the system switched off). The polarity of electrodes was altered in each experiment.
10. NaF and NaCl required mass were measured using a scale with a resolution 0.001 g and mixed in a deionized water 500 ml using a magnetic stirrer.
11. NaF and NaCl mixed solution was then introduced into the inlet tank and stirred for 10 min.
12. Samples were taken from the inlet tank for fluoride analysis then immediately filtered through a 0.2 μm mixed cellulose ester membrane and dissolved fluoride was measured after adding the TISAB buffer.
13. The pump was turned on and the system was allowed to run until the preferred water level and then switched off.
14. Power supply was turned on along with the timer, once the required water level was achieved in the EC reactor.
15. Current and voltage between electrodes were taken along with the power supply readings.
16. The measurements were taken in five minutes intervals, for temperature, pH, and electrical conductivity.
17. One filtered sample (20 ml) and two non-filtered samples (20 ml) were extracted from the port installed at the outlet in 5 min intervals.
18. The power supply was switched off after 60 min.
19. The electrodes were taken out immediately, and the solution was flocculated for 10 min by gentle mixing.

20. Two samples were taken from the flocculated solution and one sample was immediately filtered by 0.22 μm filter for fluoride analysis after adding TISAB buffer.
21. The residual flocculated solution was mixed rapidly and a sample was taken for total fluoride measurements.
22. Electrodes were taken out and soaked in NaOH solution for twenty seconds.
23. Samples were analysed for the required parameters or otherwise stored in the refrigerator ($T < 4\text{ }^{\circ}\text{C}$).
24. The reactor was drained and cleaned thoroughly with tap water, and deionized water.

4.5. Conclusion of chapter 4

This chapter explained the discrete-continuous model conversion scheme of PBCM for batch reactor & the experimental design of the batch EC operation that was used to collect primary data for calibration and validation purposes of the model. The next chapter includes a discussion of the results of these primary data and further validation of the model using literature data.

Chapter 5. Results and discussion - PBCM calibration and validation for batch electrocoagulation reactors

5.1. Chapter overview

This chapter comprises the results and discussion of the PBCM calibration and validation using bench-scale experimental data for the batch electrocoagulation operation. Figure 5.1 illustrates the chapter layout of the thesis and the interconnection of this chapter to the overall thesis.

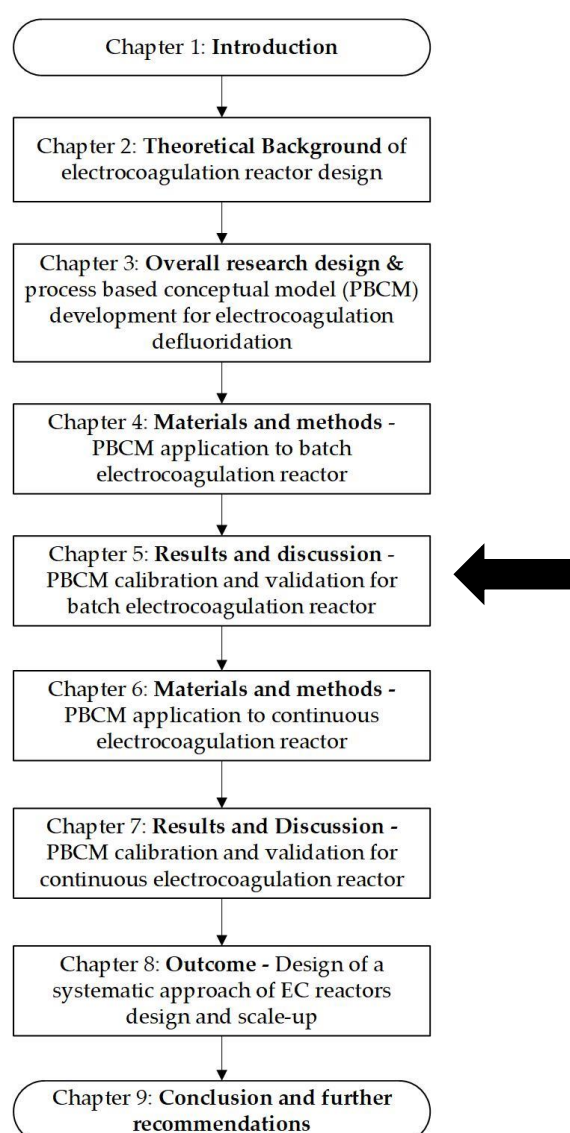


Figure 5-1: The chapter layout of the thesis

5.2. *PBCM calibration and validation using experimental data*

The PBCM model was executed in the selected computer platforms and then calibrated by fine-tuning the parameters identified from the conceptual model (Table 5.1). The process-based conceptual model was first evaluated using Microsoft® Excel® ver. 2016 and MATLAB® ver. R2021a, designed as explicated in section 3.3. The time step and the number of iterations used for model validation operations are 1s and 2s, respectively. The time step sensitivity was measured for 1s – 3600s range and the effect from the number of iterations of the model was studied for the 2 – 1000 steps range. It was noted that the model accuracy was not affected by increased iteration numbers. The accuracy of results increased when the time step decreased. First, the calibration parameter sensitivity was measured using a Microsoft® Excel® ver. 2016 - Solver and then using a trial and error method in MATLAB® ver. R2021a until reaching approximate solutions. Finally, a local sensitivity test was carried out in MATLAB® ver. R2021a using a programme written to analyse each calibration parameter range within the selected domain. As seen in Figures 5.2 and 5.3, the model simulation results agree with the experimentally measured data while the calibration parameter values satisfied the recommended ranges by previous studies as listed in Table 5.1. The model precision was measured using root mean square error (RMSE) and relative standard error (RSE). Initial calibration of the model was conducted using the experimental data resulted from the current 1A (22.22 A m^{-2}). Then the model was validated using the current 0.5A and 1.5A experimental data.

From the comparison of the results between the PBCM and actual data illustrated in Figure 5.2, for the model simulation of current 0.5A (11.11 A m^{-2}), RMSE was found to be 0.1311, and RSE was 0.0821, which indicates good agreement between the model simulation and the experimental data. The rest of the model goodness of fit values are given along with Figure 5.2. However it could be noted that the model simulation of current 1.0A and 1.5A show better agreements with observed data along with lower RMSE values compared to the simulations at current 0.5A. This could be due to the

low performance of the EC reactors at lower current concentration levels (Gourich et al. 2017). The calibrated model simulation could then be used to identify the variation of the intermediate parameters as illustrated in Figure (5.3). All the variations presented in these plots indicate a continuous pattern of increasing with time. Further to this, a comparison of the goodness of fit measures of the model calibration and validation results are summarized in Table (5.1)

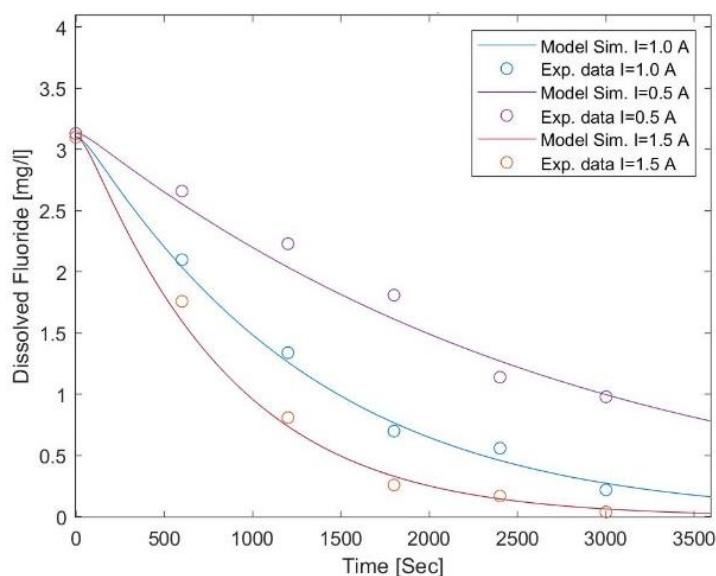


Figure 5-2: The model simulations for laboratory level batch experiment data (Calibration results: 1.0A data, RMSE (1.0A) = 0.0688, RSE (1.0A) = 0.0173, Validation results: 0.5A and 1.5A data, RMSE (0.5A) = 0.1311, RSE (0.5A) = 0.0821, , RMSE (1.5A) = 0.0785, RSE (1.5A) = 0.0375)

Table 5-1: Comparison of the goodness of fit measures of the model calibration and validation results

Experiment			Goodness of fit measures	
Primary data/ Secondary data	Supply Current	Calibration or Validation	RMSE	RSE
Primary data	0.5 A	Validation	0.1311	0.0821
Primary data	1.0 A	Calibration	0.0688	0.0173
Primary data	1.5 A	Validation	0.0785	0.0375
Secondary data	1.0 A	Validation	0.6438	0.4806
Secondary data	1.5 A	Validation	0.6579	0.5753
Secondary data	2.0 A	Validation	0.427	0.0343
Secondary data	2.5 A	Validation	0.4017	0.3362

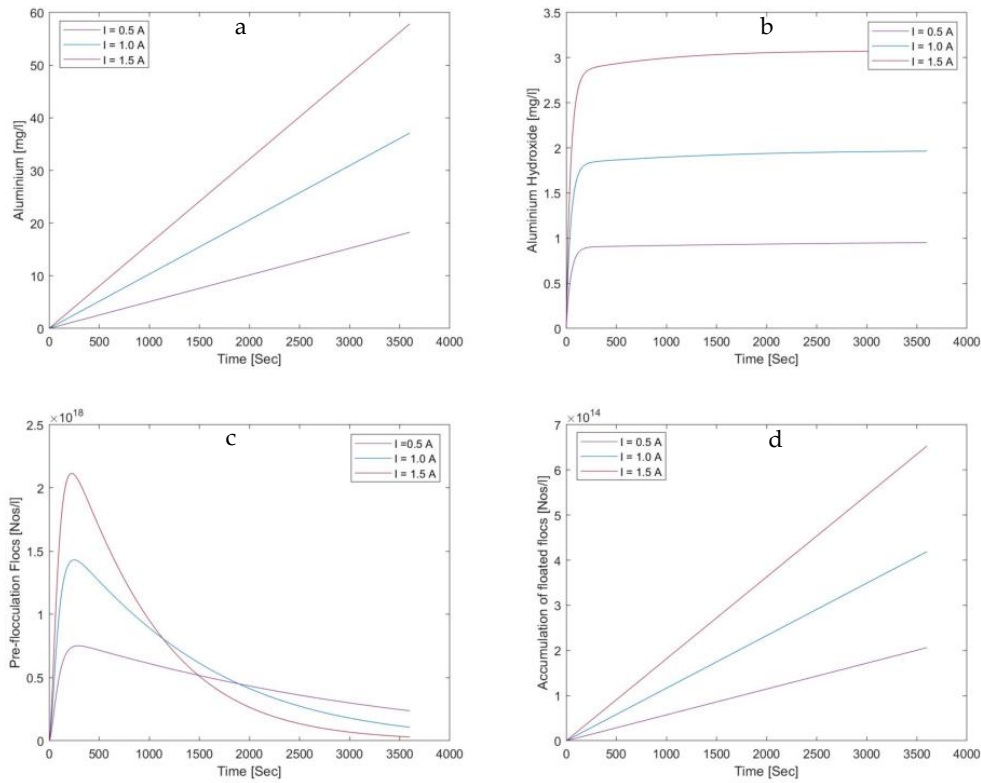


Figure 5-3: Process Based Conceptual Model (PBCM) simulation of intermediate parameters for lab experimental parameter inputs, [a] Al^{3+} vs. time, [b] $\text{Al}(\text{OH})_3(\text{s})$ vs. time, [c] Pre-flocculation flocs concentration vs. time, [d] Accumulation of floated flocs concentration vs. time for the laboratory level batch experiment ($I = 0.5 \text{ A}$, 11.11 A m^{-2})

The visualization of these intermediate parameter variations could help improve the reactor design optimization process. This allows the designers to optimize the electrocoagulation reactors by fine-tuning the experimental values and the reactor geometry values thus minimizing the investments for physical laboratory-level models. As the next step, the PBCM model validation was conducted applying data retrieved from the literature which is detailed in the next section.

5.3. PBCM validation using literature data

Experimental data retrieved from the electrocoagulation batch experiments conducted at the laboratory level by Emamjomeh (2006) were considered for validation of the conceptual model mainly due to the similarity of the batch reactor with the present study. A laboratory batch monopolar electrocoagulation reactor of 3.6 l had been used for these experiments. Five aluminum plate anodes and cathodes of dimensions

250×100×3 mm had been used as electrodes. The gap between the electrode plates were 5mm and the initial fluoride concentrations was 10 mg l⁻¹. From the results of comparison between the PBCM and actual data illustrated in Figure 5.4, the model simulation for current 2.0 A (44.44 A m⁻²) RMSE was found to be 0.4270, and RSE was 0.0343, which indicates good agreement between the model simulation and the experimental data. It is evident that RMSE and RSE results of this section are slightly higher compared to the model simulation results of primary data at section 5.2. This is due to the relatively higher initial concentrations of fluoride used in the experiments conducted by Emamjomeh (2006), which is 10 mg l⁻¹. The rest of the model goodness of fit values are given at the Figure 5.4.

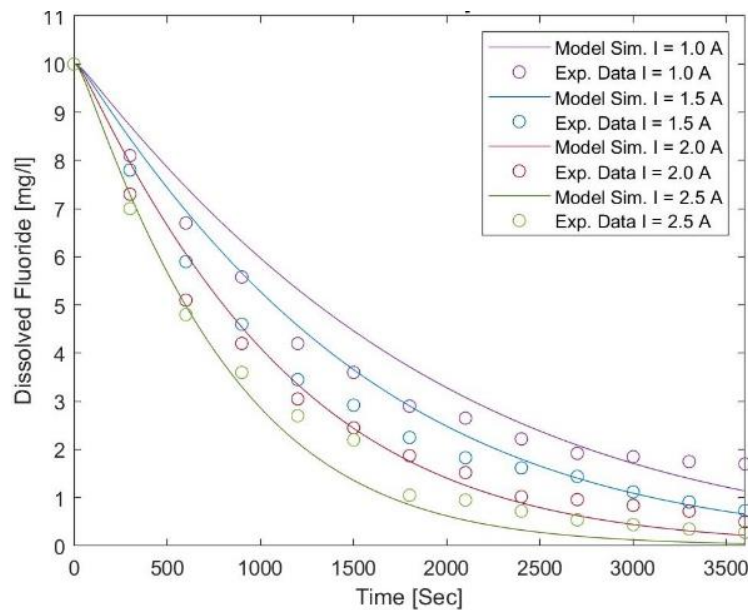


Figure 5-4: The model simulations for laboratory level batch experiment data by Emamjomeh (2006) (RMSE (1.0A) = 0.6438, RSE (1.0A) = 0.4806, RMSE (1.5A) = 0.6579, RSE (1.5A) = 0.5753, RMSE (2.0A) = 0.4270, RSE (2.0A) = 0.0343, RMSE (2.5A) = 0.4017, RSE (2.5A) = 0.3362)

The promising result yielded from the validation process could then be confirmed by comparing the intermediate parameters (Figure 5.5) and data presented by Emamjomeh (2006) in his study. The associated calibration parameters with this trial are listed in Table (5.2).

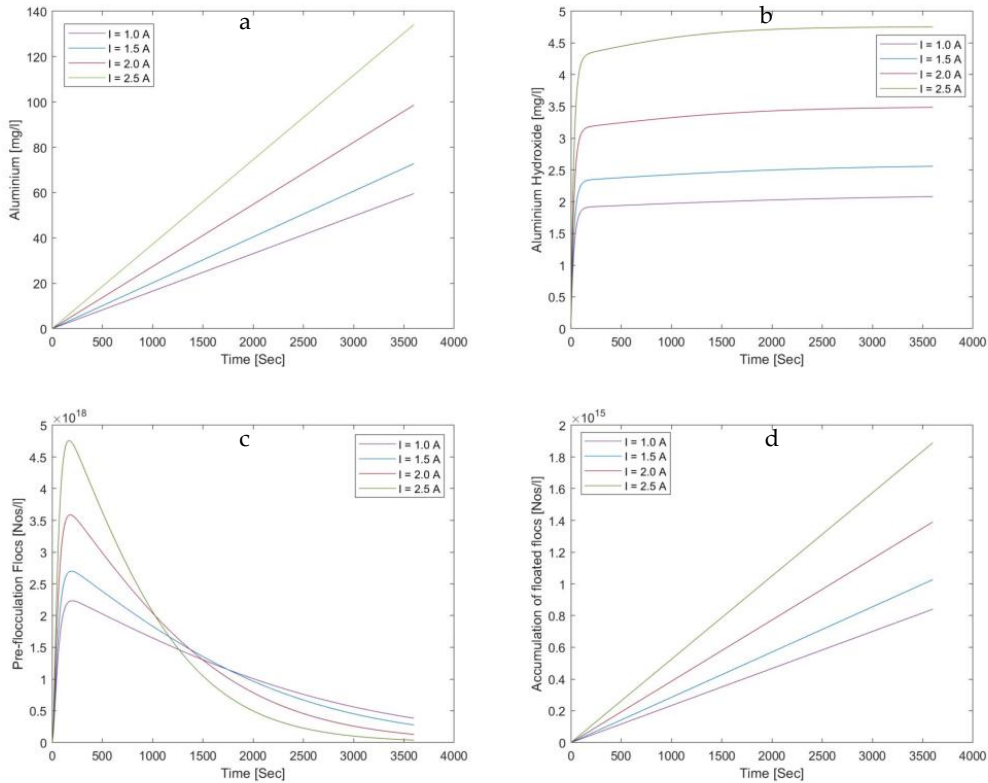


Figure 5-5: Process Based Conceptual Model (PBCM) simulation of intermediate parameters for Emamjomeh (2006) experimental parameter inputs, [a] Al^{3+} vs. time, [b] $\text{Al}(\text{OH})_3(\text{s})$ vs. time, [c] Pre-flocculation flocs concentration vs. time, [d] Accumulation of floated flocs concentration vs. time for the laboratory level batch experiment ($I = 1.5 \text{ A}$, 33.33 A m^{-2})

In comparison to the early attempts by different researchers in developing a model to interpret electrocoagulation, the model presented in this paper, PBCM has yielded many advantages. An empirical mathematical model by Emamjomeh (2006), was developed to understand the fundamental characteristics of EC as an attempt to apply it for fluoride removal. This helped to correlate the experimental rates of removing fluoride with EC operational parameters.

Table 5-2: Calibration parameter values for the process-based model simulation results

No.	Calibration Parameter	References	Boundary conditions		Suggested values for simulations tested	
			Min.	Max.	Figure (5.2)	Figure (5.4)
1	q_m ; the maximum adsorption capacity (mg g^{-1})	Hu, Lo et al. (2007), Bennajah, Gourich et al. (2009), Essadki, Gourich et al. (2010)	0.40	1.40	1.5	1.45
2	K_L ; the Langmuir constant (l mol $^{-1}$)	Hu, Lo et al. (2007), Bennajah, Gourich et al. (2009), Essadki, Gourich et al. (2010)	600	2000	780	615
3	K ; a percentage denoted hydrolysis efficiency	ϵ_{Al} efficiency of hydro-fluoro-aluminium formation (%) (Hu, Lo et al. 2007)	0.763	0.993	0.57	0.57
4	d_j ; colloid size which participates in adsorption and flocculation process (m)	Minimum: From the definition for colloid size; (Metcalf and Eddy 2003). Maximum: From the size of the polymerised particle; (Hem and Roberson 1967)	1.00E-09	5.00E-08	1.70E-09	1.70E-09
5	K_E ; the correction factor denoted adsorption of dissolved fluoride on electrodes	Figures 2,3,5,6 Percentage of fluoride removal graphs in different conditions (Zhu, Zhao et al. 2007)	0.00	0.80	0.02	0.03
6	ϕ ; a correction factor, denoted current efficiency or faradic yield	Faraday's law (Hakizimana, Gourich et al. 2017, Hu, Sun et al. 2017)	1.00	2.00	1.32*	1.23*
7	n ; Al:OH ratio in one ring structure of sweep floc	Colloidal parameters calculated based on the ring structure formed by six aluminium hydroxide octahedra (Hem and Roberson 1967)	2.00	3.00	2.20	2.20
8	α is collision efficiency for macro-flocculation	Orthokinetic flocculation model (MWH Americas, Crittenden Communications et al. 2012)	0.00	1.00	1.00	1.00
9	α_{db} is collision coefficient between an air bubble and floc,	Microbubble flotation model (Haarhoff and Edzwald 2004).	0.00	1.00	0.80	0.80
10	η_T is collision frequency between the air bubble and floc,	Microbubble flotation model (Haarhoff and Edzwald 2004).	0.00	1.00	0.80	0.80

Nevertheless, as Emamjomeh's model was purely empirical, it could be considered a black-box model. The main limitation is that no further directions could be derived from the suggested empirical model for different pollutants except for a few which follow a similar removal pathway as dissolved fluoride.

Another noteworthy study conducted by Holt (2003) attempted to develop a conceptual framework of electrocoagulation by synthesizing from the fundamentals of water treatment. This was the first attempt of that kind which was rooted in three basic processes; coagulant generation, coagulation, and floc removal. The framework proposed relevant mathematical expressions for each process creating the links between the operating parameters and performance. The main limitation of this framework is the inadequacy of knowledge on connections between each process.

The PBCM simulation results show a good agreement with the secondary and primary data retrieved for defluoridation using the EC process. This is the first-ever attempt to produce intermediate parameter variations along with the pollutant concentration levels, from the EC modelling attempts found in the literature. This process-based conceptual model is rooted in the science of pollutant removal mechanisms and conservation of mass and provides more control of design variables over conventional black-box simulations utilized at present.

Further to this, the PBCM could be used to simulate the abatement of pollutants that follow the same removal pathway in EC. Arsenic (V), boron, nonylphenol ethoxylates, COD, and total organic carbon (TOC) in baker's yeast wastewater are a few examples.

5.4. Comparison of total pollutant mass abatement for primary and secondary data

A comparison of total pollutant mass abatement of the simulated and observed experimental data was conducted for each experiment. This was achieved by applying the theory of conservation of mass (Eq. 50) for the total duration of the reactor operation. The comparison was made between the observed pollutant abatement and

the simulated pollutant abatement for each experiment. The equation used for the pollutant abatement calculation is given below (50a, 50b). The results are summarised in the Table (5.3). The observed and simulated pollutant abatement values are in good agreement, thus confirming the validity of the model.

$$\text{Total pollutant abatement (\%)} = \frac{(F_0 \times V - F_f \times V)}{F_0 \times V} \times 100 \% \quad (50a)$$

$$\text{Total pollutant abatement (\%)} = \frac{(F_0 - F_f)}{F_0} \times 100 \% \quad (50b)$$

Here,

F_0 : Initial fluoride concentration (mg l⁻¹)

F_f : Final fluoride concentration (mg l⁻¹)

V : Volume of the batch reactor (l)

Table 5-3: Comparison of total pollutant mass abatement of the simulated and observed experimental data for batch reactor experiments using equation (50b)

Experiment		Observed dissolved fluoride			Model Simulated dissolved fluoride		
Primary data/ Secondary data	Supply Current	At 0 min (mg/l)	At 60 min (mg/l)	Observed removal based on mass balance	At 0 min (mg/l)	At 60 min (mg/l)	Simulated removal based on mass balance
Primary	0.5 A	3.13	0.77	75.4%	3.13	0.78	75.1%
Primary	1.0 A	3.10	0.12	96.1%	3.10	0.16	94.8%
Primary	1.5 A	3.10	0.02	99.4%	3.10	0.03	99.1%
Secondary	1.0 A	10.00	1.70	83.0%	10.00	1.14	88.6%
Secondary	1.5 A	10.00	0.73	92.7%	10.00	0.66	93.4%
Secondary	2.0 A	10.00	0.50	95.0%	10.00	0.22	97.8%
Secondary	2.5 A	10.00	0.28	97.2%	10.00	0.05	99.5%

5.5. Conclusion of chapter 5

Electrocoagulation is an emerging technology that can be promoted as a sustainable technology for a variety of industries if the design and scale-up issues could be suitably addressed. This research devises a proposed model that could be applied to a range of pollutants that follow the same abatement mechanism. Further testing at laboratory and pilot scales will be instrumental in validating the model further, including the revisions for continuous flow reactors. The general conclusions from the study conducted so far are summarised below:

This paper presents a process-based conceptual model that simulates fluoride removal of batch EC reactors, which was then calibrated with experimental data and validated using literature data of lab-scale batch electrocoagulation experimental data. The comparison between the PBCM and experimental data results in a lowest RMSE 0.0688, and RSE 0.0173, which indicates good agreement between the predicted values and the experimental data. The PBCM allowed the identification of a set of calibration parameters that are connected to the physical, chemical, and hydrodynamic features of the EC reactor, thus providing more visibility and controllability for the electrocoagulation reactor sub-processes. The model shall be expanded for the continuous reactor operations, applying the conservation of mass equations.

Chapter 6. Materials and methods for PBCM validation using a continuous electrocoagulation reactor

6.1. Chapter overview

This chapter explains the materials and methods followed to achieve objective 3 of this study, which is the experimental assessment of the integrated conceptual model to address the existing design and modelling issues of EC reactors for varied operating conditions. The chapter layout is illustrated in Figure 6.1.

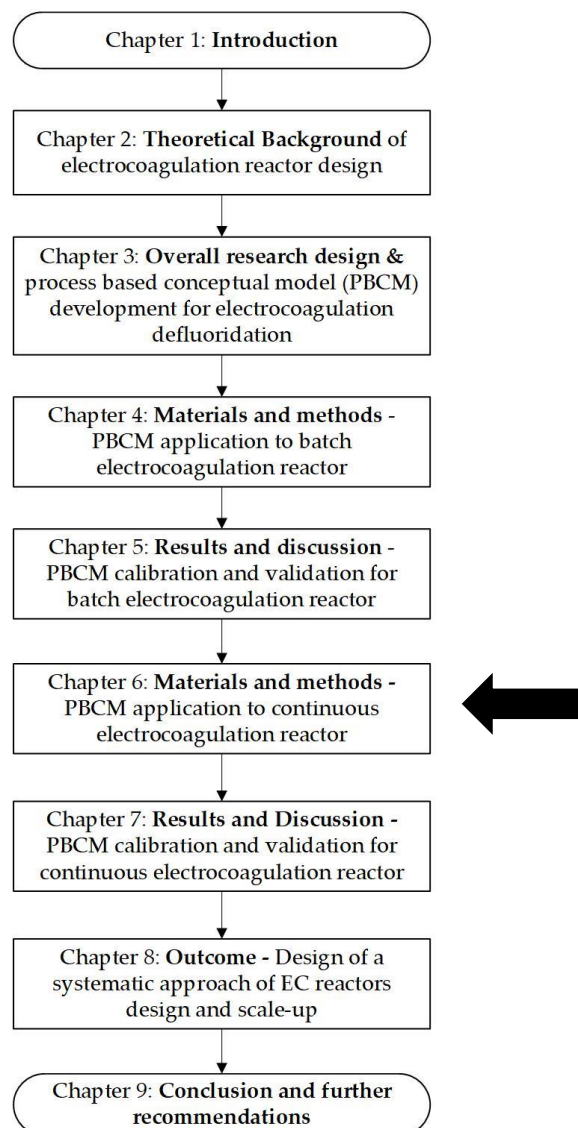


Figure 6-1: The chapter layout of the thesis

In chapters 5 & 6, the model conceptualisation and validation of the batch EC reactors were explained. In section 6.2, the discrete-continuous model conversion scheme of the pre-identified discrete models, to suit the continuous EC reactor operations has been explained in detail. Next, in section 6.3, the experimental procedure which was designed to collect primary data to calibrate and validate this conceptual model has been explained. These experiments were carried out at the Industrial Chemistry Laboratory of Liverpool John Moores University, United Kingdom. Subsequently, the details of the calibration and validation process of the conceptual model are presented in chapter 7.

6.2. Discrete-continuous model conversion scheme of the PBCM in continuous EC reactor

The conversion of the discrete models into a continuous-time model is required to evaluate the real-time variation of the concentrations of the pollutant, coagulant and flocs inside the continuous flow EC reactor. Hence, discrete models identified in section 3.3 as a result of the process-based modelling technique, were transformed into a continuous-time model by applying the theory of conservation of mass (Eq. 65). The scheme of work that is required to produce the explicit scheme of the continuous-time model is explained in this section. Uniform mixing and steady-state operation in the continuous flow process were the main assumptions considered here.

Accumulation = Inflow – Outflow + Generation – Dissipation

$$m_{\text{acc}} = m_{\text{in}} - m_{\text{out}} + m_{\text{gen}} - m_{\text{dis}} \quad (65)$$

The conceptual sub-models that were identified in section 3.3, were unified in this section to suit the operation in a continuous reactor. The interconnectivity between the sub-models is key to structure the process-based model in a numeric computing platform.

First, the mass balance equation is used to determine the aluminium cation concentration in the reactor. Using the equations derived in section 3.3 (Eq. 32 & Eq.

37), aluminium cation generation at n^{th} time step (t_n) ($m_{Al-gen\ at\ t_n}$) in (mg l^{-1}) could be computed as (Eq. 66):

$$m_{Al-gen\ at\ t_n} = K_a(t_n - t_{n-1}) \quad (66)$$

Where, $K(a)$ is rate of aluminium (III) dissolving process ($\text{mg l}^{-1}\text{s}^{-1}$)

Similarly, dissipation at n^{th} time step (t_n) in (mg l^{-1}) is (Eq. 67):

$$m_{Al-dis\ at\ t_n} = K_b(t_n - t_{n-1}) \quad (67)$$

Where $K(b)$ is the rate of hydrolysis process ($\text{mg l}^{-1}\text{s}^{-1}$).

To account for the steady-state continuous flow operation, aluminium cation inflow ($m_{Al-in\ at\ t_n}$) and the outflow ($m_{Al-out\ at\ t_n}$) at n^{th} time step (t_n) in (mg l^{-1}) can be computed as (Eq. 68 & 69):

$$m_{Al-in\ at\ t_n} = C_{Al-in\ at\ t_n} \dot{Q}(t_n - t_{n-1})/V \quad (68)$$

$$m_{Al-out\ at\ t_n} = C_{Al-out\ at\ t_n} \dot{Q}(t_n - t_{n-1})/V \quad (69)$$

Where:

\dot{Q} is flow rate (l s^{-1}),

$C_{Al-in\ at\ t_n}$ is aluminum concentration at the inlet at time t_n (mg l^{-1}),

$C_{Al-out\ at\ t_n}$ is aluminum concentration at the outlet at time t_n (mg l^{-1}),

V is volume of the reactor (l).

Considering the uniform mixing in the reactor, aluminium cation concentration of the outflow ($C_{Al-out\ at\ t_n}$) was assumed to be equal to the aluminium cation concentration inside the reactor ($m_{Al-acc\ at\ t_n}$).

Hence, aluminum cation accumulation at the n^{th} time step (t_n) ($m_{Al-acc \text{ at } t_n}$) in (mg l^{-1}) could be calculated using the equation (70).

$$m_{Al-acc \text{ at } t_n} = m_{Al-gen \text{ at } t_n} - m_{Al-dis \text{ at } t_n} + m_{Al-in \text{ at } t_n} - m_{Al-out \text{ at } t_n} + m_{Al-accum \text{ at } t_{n-1}} \quad (70)$$

Then, aluminium hydroxide generation from hydrolysis process at n^{th} time step is considered in (mg l^{-1}) (Eq. 71):

$$m_{Al(OH)_3-gen \text{ at } t_n} = m_{Al-dis \text{ at } t_n} \times 78/27 \quad (71)$$

Aluminium hydroxide inflow is considered zero and the outflow ($m_{Al(OH)_3-out \text{ at } t_n}$) at n^{th} time step (t_n) in (mg l^{-1}) can be computed as (Eq. 72):

$$m_{Al(OH)_3-out \text{ at } t_n} = C_{Al(OH)_3-out \text{ at } t_n} \dot{Q}(t_n - t_{n-1})/V \quad (72)$$

Where:

\dot{Q} is flow rate (l s^{-1}),

$C_{Al(OH)_3-out \text{ at } t_n}$ is aluminum hydroxide concentration at the outlet at time t_n (mg l^{-1}),

V is volume of the reactor (l).

Aluminium hydroxide dissipation was calculated considering the formation of aluminium-hydroxo-fluoride particles as a result of the adsorption process that occurs in the system, which is explained later in this chapter using equation (78).

Hence, the aluminium hydroxide accumulation at n^{th} time step ($m_{Al(OH)_3-acc \text{ at } t_n}$) in (mg l^{-1}) could be expressed as follows (Eq. 73),

$$m_{Al(OH)_3-acc \text{ at } t_n} = m_{Al(OH)_3-gen \text{ at } t_n} - m_{Al(OH)_3-out \text{ at } t_n} - m_{Al(OH)_3-dis \text{ at } t_n} + m_{Al(OH)_3-acc \text{ at } t_{n-1}} \quad (73)$$

Hem and Roberson (1967), noted aluminium ions are usually octahedral with respect to water molecules or hydroxide when pH is below 7.5.

This behaviour of aluminium ions is dominant up to a lower limit of pH value of 4. A stable ring structure is formed composed of six octahedral aluminium ions joined together by double OH bridges. The six-member-ring unit is apparently the most stable configuration that can be built up from six AlOH octahedra. A schematic representation of the ring structure formed by six AlOH octahedra is given in Figure 6.2. This stable ring structure is what makes hydrolysed aluminium a good adsorbent. Hence, the colloids generated from hydrolysed aluminium could be calculated using equation (Eq. 74).

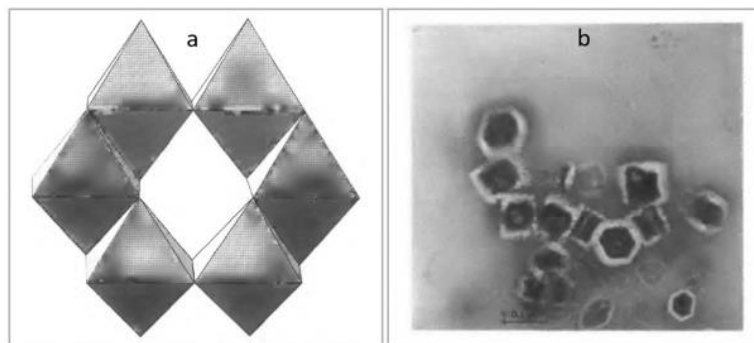


Figure 6-2: (a) Schematic representation of ring structure formed by six aluminium hydroxide octahedra, (b) and Electron photomicrograph of microcrystalline gibbsite (Hem and Roberson 1967).

Aluminium hydroxide colloids at n^{th} time step in (mol l^{-1}):

$$n_{\text{Al(OH)}_3 \text{ colloids acc at } t_n} = \frac{(m_{\text{Al(OH)}_3\text{-acc at } t_n})}{(\text{Mass}_{\text{Al(OH)}_3 \text{ colloid}}) \times (N_A)} \quad (74)$$

Where,

$\text{Mass}_{\text{Al(OH)}_3 \text{ colloid}}$ is the mass of an Al(OH)_3 colloid calculated based on the ring structure formed by six aluminium hydroxide octahedra (Hem and Roberson 1967) and

N_A is Avogadro's number (6.0221409×10^{23}).

In addition to the accumulated Al(OH)_3 colloids, the remaining particles in the reactor from the previous time step (t_{n-1}), also contribute as adsorbents in this process.

Hence, the total adsorbent concentration at n^{th} time step $n_{Ad \text{ accum at } t_n}$ in (mol l^{-1}) shall be expressed as (Eq. 75),

$$n_{Ad \text{ accum at } t_n} = n_{Al(OH)_3 \text{ colloids acc at } t_n} + N_{(fd)t_n}/N_A \quad (75)$$

Where:

$N_{(fd)t_n}$ is post flotation particle concentration (Nos L^{-1}) (Eq. (88))

N_A is Avogadro's number ($6.0221409E+23$).

Then, fluoride adsorption is calculated using the Langmuir adsorption as described in section 3.3. The adsorption rate needs to be calculated for each time step due to the variability of the pollutant concentration (fluoride) in the reactor (Eq. 76).

$$q_{e_n} = \frac{q_m K_L C_{f_n}}{1 + K_L C_{f_n}} \quad (76)$$

Where:

q_{e_n} is the amount of pollutant adsorbed per unit mass of adsorbent at equilibrium (mg g^{-1}) at the n^{th} time step.

q_m is the maximum adsorption capacity (mg g^{-1}) Langmuir constant (mg g^{-1}),

K_L is Langmuir constant (l mol^{-1}),

C_{f_n} is the equilibrium concentration of the pollutant (mol l^{-1}) at the n^{th} time step.

The fluoride adsorption at n^{th} time step $m_{F \text{ dis at } t_n}$ in (mg l^{-1}) is then calculated using the total available adsorbents in the reactor as follows (Eq. 77).

$$m_{F \text{ dis at } t_n} = q_{e_n} \times n_{Adsorbents \text{ accum at } t_n} \times M_F \quad (77)$$

Where, M_F is the molar mass of fluoride which is $19,000$ (mg mol^{-1}).

The dissipated fluoride which was considered in equation (77) is adsorbed onto the $\text{Al}(\text{OH})_3$ particles which could also be considered as the aluminium hydroxide dissipation. This is explained in the equation below (Eq. 78).

$$m_{\text{Al}(\text{OH})_3\text{-dis at } t_n} = (q_{e_n} \times n_{\text{Ad accum at } t_n} \times M_{\text{Al}(\text{OH})_3\text{-F}}) / N_f \quad (78)$$

Where:

$m_{\text{Al}(\text{OH})_3\text{-dis at } t_n}$ is dissipation of $\text{Al}(\text{OH})_3$ (mg l^{-1}),

N_f is number of fluoride ions adsorbed on to one $\text{Al}(\text{OH})_3$ particle (Nos),

$n_{\text{Ad accum at } t_n}$ is total adsorbent concentration at n^{th} time step (mol l^{-1})

$M_{\text{Al}(\text{OH})_3\text{-F}}$ is molar mass of aluminium-hydroxo-fluoride particles, post adsorption process (mg mol^{-1})

q_{e_n} is the amount of pollutant adsorbed per unit mass of adsorbent at equilibrium (mg g^{-1}) at the n^{th} time step.

The dissolved fluoride inflow ($m_{\text{F-in at } t_n}$) and the outflow ($m_{\text{F-out at } t_n}$) at n^{th} time step (t_n) in (mg l^{-1}) can be computed as (Eq. 79 & 80):

$$m_{\text{F-in at } t_n} = C_{\text{F-in at } t_n} \dot{Q}(t_n - t_{n-1}) / V \quad (79)$$

$$m_{\text{F-out at } t_n} = C_{\text{F-out at } t_n} \dot{Q}(t_n - t_{n-1}) / V \quad (80)$$

Where:

\dot{Q} is flow rate (l s^{-1}),

$C_{\text{F-in at } t_n}$ is fluoride concentration at the inlet at time t_n (mg l^{-1}),

$C_{\text{F-out at } t_n}$ is fluoride concentration at the outlet at time t_n (mg l^{-1}),

V is volume of the reactor (l).

Hence, the equilibrium fluoride concentration in the reactor at n^{th} time step $m_{F \text{ at } t_n}$ (mg l^{-1}) shall be calculated from the following equation (Eq. 81).

$$m_{F \text{ at } t_n} = m_{F \text{ at } t_{n-1}} + m_{F\text{-in at } t_n} - m_{F \text{ dis at } t_n} - m_{F\text{-out at } t_n} \quad (81)$$

As per equation (78), the dissipation of aluminium hydroxide is the same process of generation of aluminium-hydroxo-fluoride in the system. Hence, the generation of aluminium-hydroxo-fluoride ($m_{Al(OH)_3F\text{-gen at } t_n}$) in (mol l^{-1}) could be expressed as (Eq. 82),

$$m_{Al(OH)_3F\text{-gen at } t_n} = (q_{e_n} \times n_{Ad \text{ accum at } t_n})/N_f \quad (82)$$

As per Zhu, Zhao et al. (2007), immediately after the adsorption process, a significant proportion of aluminium-hydroxo-fluoride flocs gets attached on the electrodes due to the effects of the electric field. Hence, to account for this dissipation of aluminium-hydroxo-fluoride, a correction factor (K_E) is introduced as explained in the following equation (83).

$$m_{Al(OH)_3F\text{-dis at } t_n} = K_E \times m_{Al(OH)_3F\text{-acc at } t_{n-1}} \quad (83)$$

Where, $m_{Al(OH)_3F\text{-acc at } t_{n-1}}$ represents the aluminium-hydroxo-fluoride accumulation from the time step $n-1$, in (mol l^{-1}).

Then, the inflow of aluminium-hydroxo-fluoride is considered zero and the outflow ($m_{Al(OH)_3F\text{-out at } t_n}$) at n^{th} time step (t_n) in (mol l^{-1}) was computed using the equation (84):

$$m_{Al(OH)_3F\text{-out at } t_n} = C_{Al(OH)_3F\text{-out at } t_n} \dot{Q} (t_n - t_{n-1})/V \quad (84)$$

Where:

\dot{Q} is flow rate (l s^{-1}),

$C_{Al(OH)_3F\text{-out at } t_n}$ is aluminium-hydroxo-fluoride concentration at the outlet at time t_n (mol l^{-1}),

V is volume of the reactor (l).

Thus, the mass balance equation for aluminium-hydroxo-fluoride could be written as follows (Eq. 85),

$$m_{Al(OH)_3F-acc\ at\ t_n} = m_{Al(OH)_3F-gen\ at\ t_n} - m_{Al(OH)_3F-out\ at\ t_n} - m_{Al(OH)_3F-dis\ at\ t_n} + m_{Al(OH)_3F-acc\ at\ t_{n-1}} \quad (85)$$

After the adsorption process, the flocculation process is considered.

The pre-flocculation particle concentration ($n_{Floc_i\ at\ t_n}$) in (Nos l⁻¹) could then be calculated using the equation (86),

$$n_{Floc_i\ at\ t_n} = N_A \times m_{Al(OH)_3F-acc\ at\ t_n} \quad (86)$$

Post flocculation particle concentration $n_{Floc_f\ at\ t_n}$ (Nos l⁻¹) calculation shall then be calculated using the equation (43) which is derived from the second-order flocculation rate equation detailed in section 3.3.6 (Eq. 87).

$$n_{Floc_f\ at\ t_n} = \frac{N_{t_n}}{(1 + K_{M+\mu}(t_n - t_{n-1})N_{t_n})} \quad (87)$$

Where:

$K_{M+\mu}$ is rate constant for particle aggregation (l s⁻¹),

N_{t_n} is pre-flocculation particle concentration (Nos l⁻¹).

Finally, the flotation process was considered. The floc density (Nos l⁻¹) after the flotation process at the nth time step which is given as $N_{(fd)t_n}$ is calculated using equation (43) derived based on the principles discussed under section 3.2.7 (Eq. 88).

$$N_{(fd)t_n} = n_{Floc_f\ at\ t_n} \times e^{-K_f \times (t_n - t_{n-1})} \quad (88)$$

Where,

$n_{Floc_f\ at\ t_n}$ is post flocculation particle concentration (Nos l⁻¹),

K_f is flotation constant (s^{-1}).

Figure 6.3 illustrates the step-by-step calculation process followed to execute the PBCM using MATLAB® ver. R2021a which is a programming and numeric computing platform. This detailed conceptual model was then calibrated and validated using literature and laboratory-scale continuous flow electrocoagulation experimental data for fluoride removal with aluminium electrodes. The information on the calibration results is discussed in the following section.

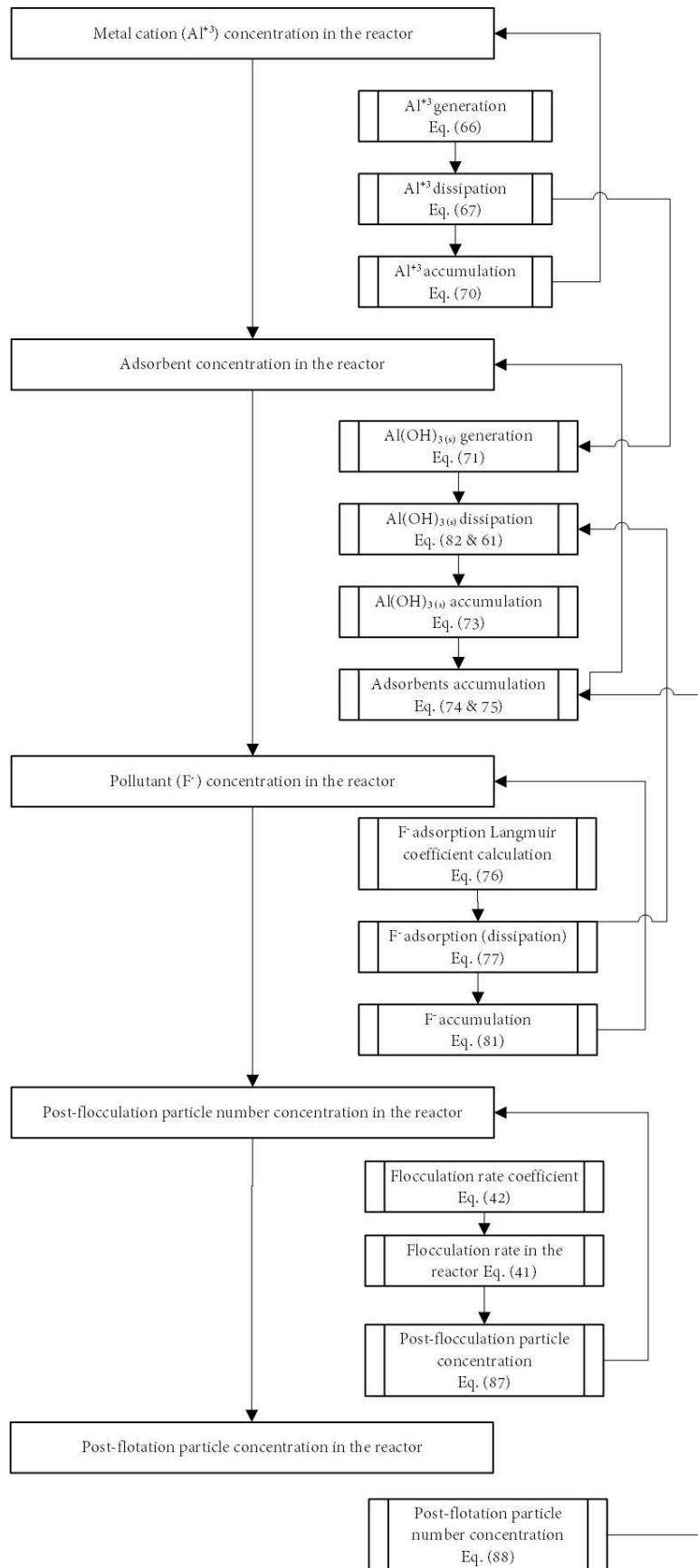


Figure 6-3: Step-by-step calculation process of the model parameters of PBCM

6.3. *Experimental procedure*

6.3.1. **Continuous-flow electrocoagulation laboratory reactor experiments**

A continuous-flow electrocoagulation laboratory reactor was designed by the author and constructed with the support of the laboratory technicians to collect primary data with the aim of calibration and validation of the process based on a conceptual model designed for the steady-state, uniform mix, and continuous flow EC reactor. These laboratory-based experiments were carried out at the Industrial Chemistry Laboratory of Liverpool John Moores University, United Kingdom.

The EC reactor was designed as a continuous flow cell, with no external mixing involved. The flow distribution in the cell was designed to optimize uniform mixing of fluid through upward cross flow, aided by the upward flowing air bubbles generated at the cathodes. A 40 l non-conductive single cell 400 mm length by 200 mm width by 500 mm height was manufactured from glass (Figure 6.4, Tables 6.1 and 6.2). Three different outlet levels were built to achieve three operational volumes of 10 l, 20 l, and 30 l by changing the fluid heights. The cell surface area was 0.08 m² and the maximum cell water height was 375 mm, which resulted in an operational cell volume of 30 l. The electrode area was calculated according to the recommended electrode area to reactor volume (A/V) ratio reported in the literature (Mameri, Yeddou et al. 1998, Hakizimana, Gourich et al. 2017). The A/V ratio at the maximum water level 375 mm, was 7.7 m² m⁻³ and at the general operational height 365 mm, was 11.2 m² m⁻³. The reactor consisted of four aluminium (minimum Al 95.45%, maximum Al 97.35%, 1050AH14 VC1-50, BS EN 485, Aalco Metals Limited, Liverpool) plate anodes and cathodes (360mm x450mm x 3mm). The total dead volume was 28.38 l when the maximum height of fluid in the reactor was 375 mm. The maximum total active anode area was 0.405 m². The gap between the two neighbouring electrode plates was kept constant 50 mm for each run, to allow a smooth flow through the plates and greater

visibility during the operations. The monopolar electrodes were connected in parallel via copper connectors.

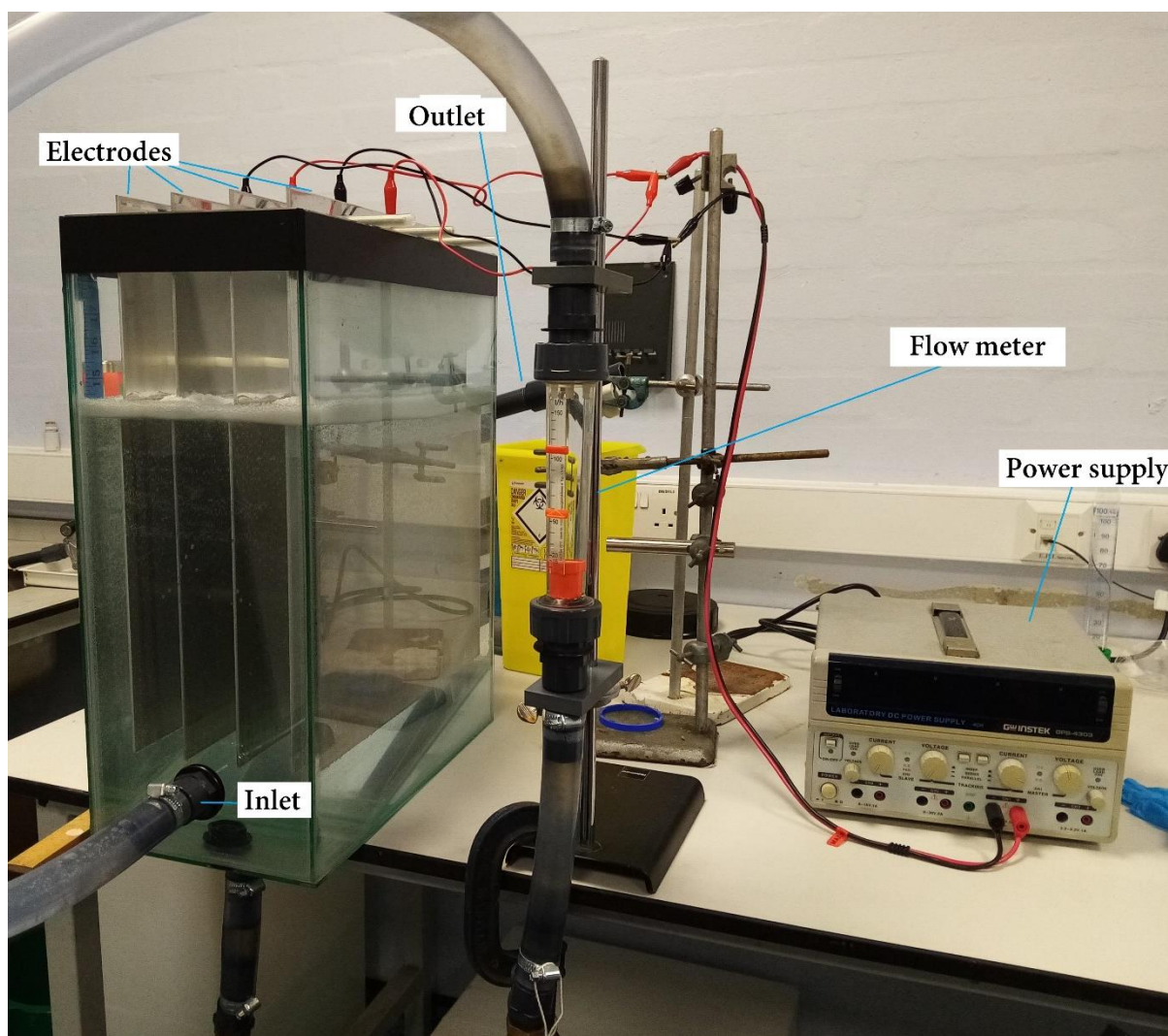


Figure 6-4: Continuous flow electrocoagulation reactor set-up

Table 6-1: Reactor specific parameters of continuous flow electrocoagulation system – part 1

Reactor parameter	Value	Unit
Dead volume of the cell	40	l
Height of the cell	0.50	m
Surface area of cell	0.08	m ²
Length of cell	400	mm
Width of cell	200	mm
Length of electrode	360	mm
Height of electrode	450	mm
Thickness of electrode	3	mm
No. of electrodes	4	
Cell water clearance from top	135	mm
Cell water height	365	mm
Cell active side area	0.07	m ²
Cell water volume (excluding the electrode volume and the bottom wedge)	0.029	m ³
Net cell water volume (including the electrode volume and the bottom wedge)	0.026	m ³
Cell water volume max (not considering the el. Volume)	0.055	m ³

Table 6-2: Reactor specific parameters of continuous flow electrocoagulation system – part 2

Cell inlet and outlet height difference	265	mm
Electrode submerged height	290	mm
Electrodes active anode area maximum (at 375 mm fluid height)	0.405	m ²
Electrodes submerged volume	0.00125	m ³
Electrodes active anode area	0.3132	m ²
Electrode gap	50	mm
Electrode configuration	Monopolar Parallel	
Flow rate	500	ml min ⁻¹
Flow velocity across the cell - horizontal	6.8	mm/min
Hydraulic residence time	52.6	min
Hydraulic residence time min at max height (800 ml min)	37.5	min
Hydraulic diameter (4. A/P) in mm	2	mm
Reynolds number of the flow ($R = \rho VD/\mu$)	227.85	Laminar
Current	3	A
Electrode area/reactor volume (m ² m ⁻³)	11.91	(m ² m ⁻³)
Current/ volume	114.08	A m ⁻³
Current / electrode surface area (A m ⁻²)	9.58	A m ⁻²



Figure 6-5: DC power supply unit (200W, 60 V/ 8 A, 4-Channel Linear DC Power Supply GW Instec GPS 4303)

The influent flow rate was varied from 250 ml min⁻¹ to 800 ml min⁻¹ that corresponds to a hydraulic residence time of 75 min and 37.5 min respectively at the maximum water level of 375 mm. This laboratory test system consisted of a 200W DC power supply unit (60 V/ 8 A, 4-Channel Linear DC Power Supply GW Instec GPS 4303) (Figure 6.5) a submersible pump (1500 l h⁻¹, with head 1.6 m), a variable area flowmeter (DFM Model 185(15), 3/4" (15 - 150 l h⁻¹) accuracy: ±2.5% full scale) (Figure 6.7 (a)), a polypropylene plastic (68 l) raw water reservoir, and a polypropylene plastic (200 l) outlet reservoir.

Synthetic water was prepared using pH-neutral deionized water at T₀= 20°C, by addition of laboratory-grade (Fisher Scientific) NaF and NaCl to acquire the expected initial fluoride concentration and to increase the conductivity respectively. Influent water was stored in a reservoir (68 l) and pumped via a submersible pump at a flow rate range of 250 – 800 ml min⁻¹, maintaining laminar flow in the reactor (Re: 200 to 400). For non-intrusive sampling, a sampling port at the reactor outlet was installed (Figure 6.8 (a)). No external sludge separation mechanism was included. Primarily, initial fluoride concentration and supply current were the parameters that varied to determine the model's robustness to experimental variation. The treated water was

connected to an outlet reservoir. The general duration of the operation was 60 mins, except for a few longer operational experiments of duration 3 to 6 hours. Before each experiment, electrodes were wet-polished and rinsed with 1% hydrochloric acid, and double rinsed with distilled water.

Dissolved fluoride, total aluminium, and dissolved aluminium concentration were analysed using a spectrophotometer (HACH DR2800) (Figure 6.6) and compared with random samples measured using a secondary spectrophotometer of the same category. Fluoride analysis was undertaken following method 8029 and aluminium was analysed following method 8012. The initial pH of the water varied within the range of 7.0 - 7.5 for each experiment. Solution temperature, conductivity, and pH were measured using a multifunctional pH meter (PCE-PHD 1) that was calibrated prior to each analysis (Figure 6.7 (b)).



Figure 6-6: Spectrophotometer (HACH DR2800) and the relevant chemicals used to analyse dissolved fluoride and aluminium.

In addition to the usual dissolved fluoride analysis performed on samples collected in five-minute intervals, a fluoride ion-selective electrode (ISE) (Oakton by Cole-Parmer® Combination Ion-Selective Electrode (ISE), Fluoride (F)) was also used in one experiment. The electrode was immersed in the reactor solution, near the outlet (Figure 6.8- b). Usually TISAB buffer (58 g of NaCl, 57 ml of glacial acetic acid, 4 g 1,2

cyclohexylene diamine tetraacetic (CDTA), 125 mL 6 N NaOH needs to be added to the samples if the fluoride ISE is used. This equalizes the ionic strengths in the sample and acts as a de-complexing agent to release any fluoride ions which may be bound up in complex molecules. Although the TISAB buffer addition is generally expected, during these experiments the ISE was immersed in the reactor directly, with no external buffer addition. The expectation from the fluoride ISE during these experiments was to analyse the dissolved fluoride levels in the solution. Hence, it was expected to have minimal effects on the expected reading due to this change. These results are presented in chapter 6.

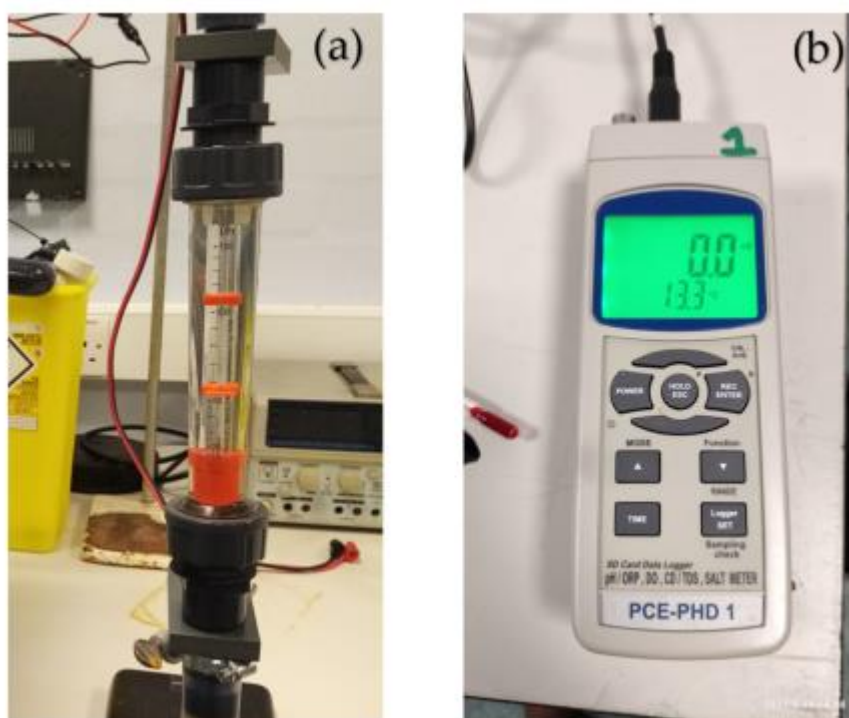


Figure 6-7: (a) Variable area flow meter, (b) Multifunction pH meter

The effects of various operational parameters were measured with the use of the following experimental conditions in continuous flow EC operation. The current was varied from each experiment in the range of 1.0 to 5.0A and held constant during each experiment run. The inter-electrode distance was kept constant for all the experiments (50 mm) thus, the electrical conductivity was elevated up to the range 1300 -1350 (μS

/cm) to lower the overall electrical resistance in the system. Further details of the experimental conditions are summarised in Tables 6.1 and 6.2. Other than meticulously cleaning the electrodes before and after each experiment, the polarisation of the electrodes was changed to avoid the accumulation of a passivating layer. The essential operation variables for the conceptual model and the expected validation parameters from the continuous flow EC reactor experiment are shown in Table 6.3. Before commencing these principal EC experiments, a few preliminary test runs were conducted to evaluate the readiness of the EC treatment unit. These test results are given in annexure (2).

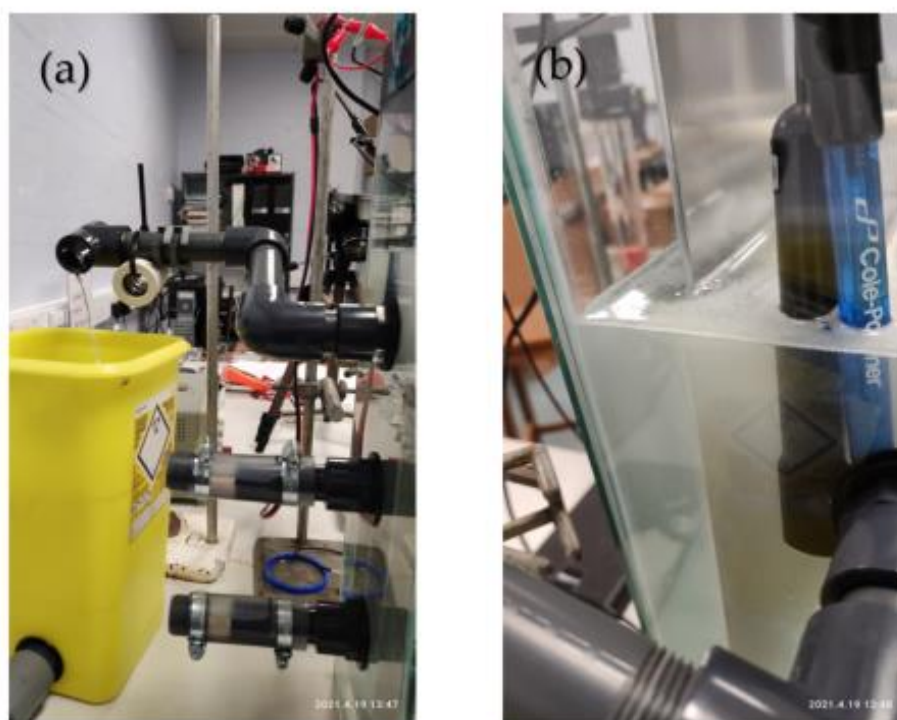


Figure 6-8: (a) Reactor outlets at three levels and the sampling port, (b) Fluoride ion-selective electrode & conductivity probe

Table 6-3: The operation variables and the calculated design parameters for each continuous flow EC reactor experiment

Ref. No.	Initial fluoride concentration (mg l ⁻¹)	Supply Current (A)	I/A (A m ⁻²)	A/V (m ² m ⁻³)	I/V (A m ⁻³)	Voltage (V)	Net Reactor volume (l)
<i>Flow rate: 500 ml min⁻¹, Water level: 365 mm, Duration 60 min</i>							
O1	2	3	9.6	11.2	107.3	7.30	26.3
O2	2	4	12.8	11.2	143.0	9.73	26.3
O3	2	5	16.0	11.2	178.8	12.17	26.3
O4	4	3	9.6	11.2	107.3	7.20	26.3
O5	4	4	12.8	11.2	143.0	9.56	26.3
O6	4	5	16.0	11.2	178.8	11.95	26.3
O7	6	3	9.6	11.2	107.3	7.11	26.3
O8	6	4	12.8	11.2	143.0	9.40	26.3
O9	6	5	16.0	11.2	178.8	11.75	26.3
<i>Flow rate: 800 ml min⁻¹, Water level: 365 mm, Duration 60 min</i>							
O10	2	1	3.19	11.2	38.03	6.40	26.3
<i>Flow rate: 250 ml min⁻¹, Water level: 175 mm, Duration 6 hours</i>							
O11	6	1	9.26	9.06	83.91	4.10	11.9
O12	6	2	18.52	9.06	167.81	8.10	11.9
O13	6	3	27.78	9.06	251.72	12.00	11.9

6.3.2. Experimental method statement

25. The inlet tank was filled to 80% with deionized water.
26. Inlet water was heated to 20 °C if required.
27. Electrode surfaces were washed with HCl solution (10% wt).
28. Electrodes were soaked in an alkali solution (0.1 mol l^{-1} NaOH) for twenty seconds.
29. Electrodes were washed with deionized water.
30. Temperature, pH, electrical conductivity of the inlet tank water was measured.
31. A sample was taken and immediately filtered through a $0.22 \text{ }\mu\text{m}$ mixed cellulose ester membrane and dissolved fluoride was measured using the spectrophotometer (HACH DR2800).
32. The system of electrodes was installed in the reactor (keeping the system switched off). The polarity of electrodes was altered in each experiment, as shown in Figure 6.9.

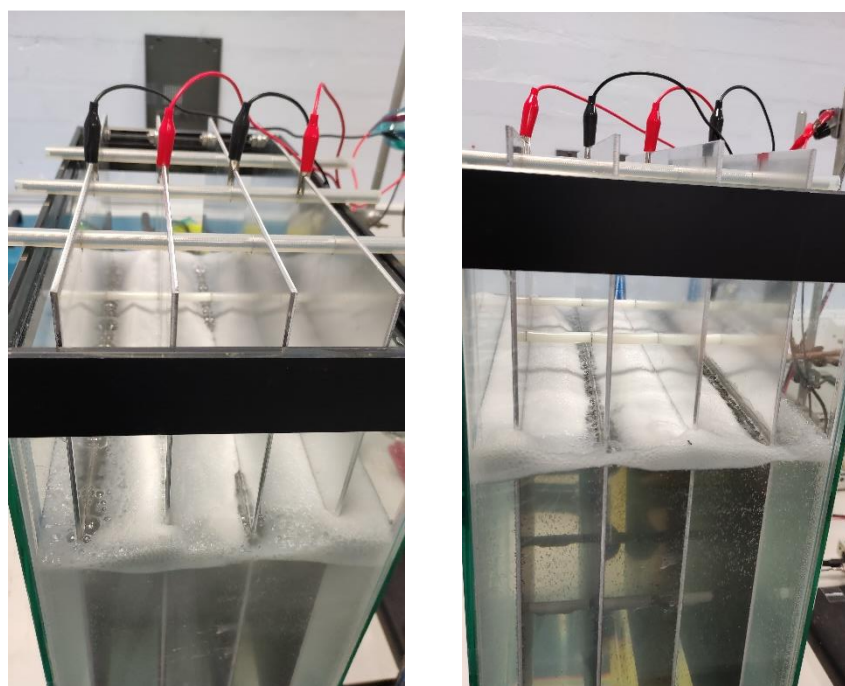


Figure 6-9: Polarity alteration of electrodes by interchanging connections in each experiment

33. NaF and NaCl required mass were measured using a scale with a resolution 0.001 g and mixed in a deionized water 500 ml using a magnetic stirrer.
34. NaF and NaCl mixed solution was then introduced into the inlet tank and stirred for 10 min.
35. Samples were taken from the inlet tank for fluoride analysis then immediately filtered through a 0.2 m mixed cellulose ester membrane and dissolved fluoride was measured (Figure 6.10).



Figure 6-10: Collected samples during an experiment run

36. The pump was turned on and the system was allowed to run until the preferred water level and flow rate were achieved.
37. The power supply was turned on along with the timer, once the required water level was achieved in the EC reactor.
38. Current and voltage between electrodes were taken along with the power supply readings.
39. The measurements were taken in five minutes intervals, for temperature, pH, and electrical conductivity.
40. One filtered sample (20 ml) and two non-filtered samples (20 ml) were extracted from the port installed at the outlet in 5 min intervals.
41. The power supply and the pump were switched off after 60 min for the experiments of duration 60 min, otherwise, the sampling process was continued as mentioned in step 18.

6.4. Calibration and validation process of the conceptual model

6.4.1. Overview of the calibration and validation process

The task of calibration and validation of the conceptual model involved several input variables of mainly four categories, namely reactor and electrode geometry input variables, electrolyte input variables, electrochemical input variables, and experimental input variables. A range of outputs could be determined using the model of two main categories, technical performance and economic performance (Figure 6.12).

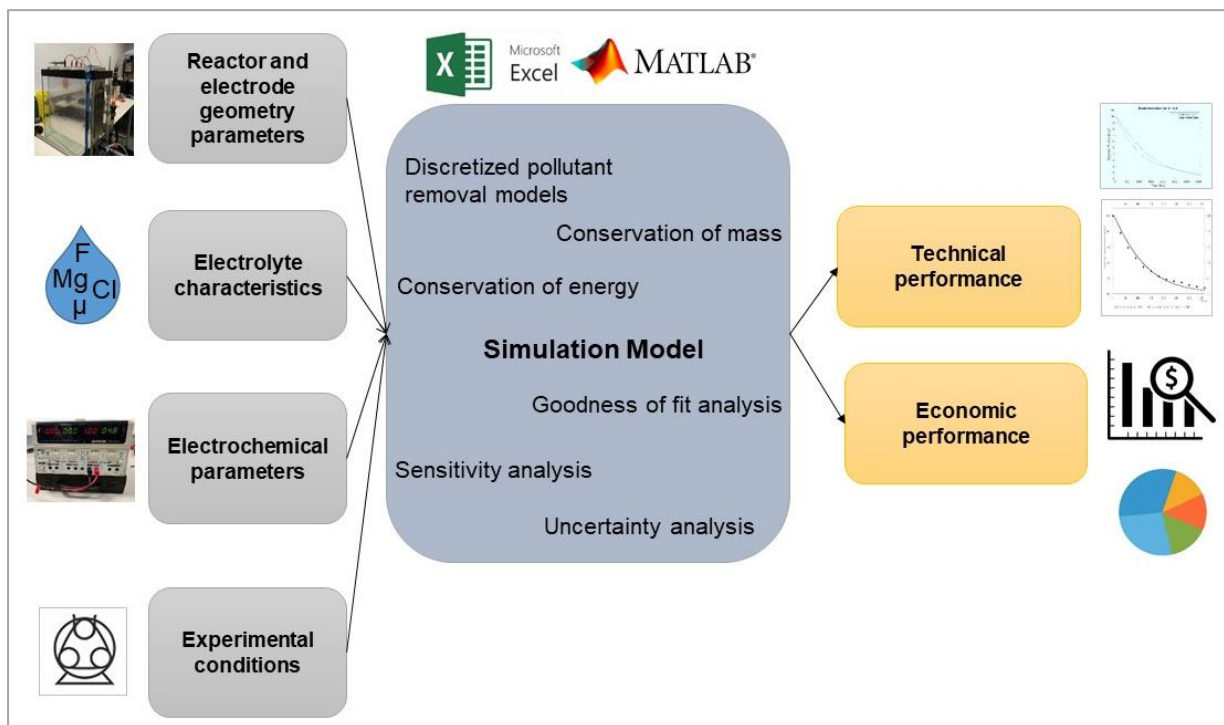


Figure 6-12: Data processing model layout of the PBCM in programming and numeric computing platforms

In addition to the dissolved fluoride and dissolved aluminium levels, the conceptual model was able to calculate the variations of aluminium hydroxide concentration, adsorbent concentration, pre-flocculation particle concentration, post-flocculation flocs concentration, post-flotation flocs concentration, and floated flocs accumulation (Tables 6.4, 6.5, and 6.6). These non-geometric final outputs that are based on the

analysis of electrolytes, were validated using direct continuous measurement (1s) and discontinuous sample analysis (5 min) up to one-hour duration. For the 6 hour long experiments (O11, O12 & O13) the sampling time gap was increased to 30 min, after one hour.

The model validations were carried out using two distinct methods,

1. Direct validation parameters (data read directly from the experiments),
2. Indirect validation parameters (parameters calculated using the experimental data).

Further details on these validation parameters are given below.

Direct validation parameters:

- i. Dissolved fluoride variation (mg l^{-1})
- ii. Dissolved aluminium variation (mg l^{-1})
- iii. Total aluminium variation (mg l^{-1})
- iv. Sludge accumulation variation (mg)
- v. Steady-state time (s)

Indirect validation parameters:

- i. Fluoride attached to flocs variation (mg l^{-1})
- ii. Aluminium in flocs variation (mg l^{-1})
- iii. Particle diameter (m)
- iv. Langmuir constant (mg g^{-1})
- v. Faradic yield correction factor
- vi. Al:OH ratio in the floc

Table 6-4: Input parameters of process-based conceptual model

Parameter category		Parameters
Reactor and electrode geometry input variables		<p>W = reactor width (duct) (m)</p> <p>L = reactor length (duct) (m)</p> <p>H = reactor wetted height (m)</p> <p>E_T= electrode thickness (m)</p> <p>E_H = electrode height (m)</p> <p>E_W = electrode width (m)</p> <p>E_N= number of electrodes (Nos)</p> <p>M = molar mass of the electrode material (mg mol^{-1})</p> <p>D = electrodes gap (m)</p>
Electrolyte input variables	General parameters	<p>C_0 = initial pollutant concentration (mg l^{-1})</p> <p>ρ = density of liquid (kg m^{-3})</p> <p>EC = initial electrical conductivity (S m^{-1})</p> <p>pH = initial pH level</p> <p>T = initial temperature (K)</p> <p>μ = dynamic viscosity of suspended fluid (N s m^{-2})</p>
	Calibration parameters	<p>q_m=Langmuir constant (mg g^{-1})</p> <p>K_L = Langmuir constant (l mol^{-1})</p> <p>K= percentage denoted hydrolysis efficiency</p> <p>D_p = diameter of one AlOH_3 particle in the reactor (m)</p> <p>K_E= electrode adsorption coefficient</p> <p>N_f= number of fluoride adsorbed on to one AlOH_3 particle</p> <p>A = collision efficiency for macro-flocculation</p> <p>α_{db} = collision coefficient between an air bubble and floc</p> <p>η_T = collision frequency between the air bubble and floc</p>
Electrochemical input variables		<p>I= electric current (A)</p> <p>Z= number of electrons transferred in anodic reaction (Z=3 for Aluminium)</p> <p>V = supply voltage (V)</p> <p>R = resistance of wires (ohms)</p>
Experimental variables		<p>T = duration (min)</p> <p>Q = flow rate (l s^{-1})</p> <p>G_e = external mixing velocity gradient (s^{-1})</p>

Table 6-5: Output parameters of process-based conceptual model

Parameter category	Parameters
Technical outputs: Variation over time	F_acc = fluoride accumulation (mg l^{-1})
	F_gen = fluoride generation (mg l^{-1})
	F_dis = fluoride dissipation (mg l^{-1})
	F_in = fluoride inflow (mg l^{-1})
	F_out = fluoride outflow (mg l^{-1})
	F_i = initial fluoride concentration (mg l^{-1})
	Al_gen= generation of aluminium ions (mg l^{-1})
	Al_dis= dissipation of aluminium ions (mg l^{-1})
	Al_out= outflow of aluminium ions (mg l^{-1})
	Al_acc= accumulation of aluminium ions (mg l^{-1})
	AlOH3_gen= generation of Al(OH)_3 (mg l^{-1})
	AlOH3_dis= dissipation of Al(OH)_3 (mg l^{-1})
	AlOH3_out= outflow of Al(OH)_3 (mg l^{-1})
	AlOH3_acc= accumulation of Al(OH)_3 (mg l^{-1})
	AlOH3_p_acc = accumulation of Al(OH)_3 particles (mol l^{-1})
	Total_Ad = total adsorbents (mol l^{-1})
	AlOH3F_gen= generation of $\text{Al(OH)}_3\text{-F}$ (mg l^{-1})
	AlOH3F_dis= dissipation of $\text{Al(OH)}_3\text{-F}$ (mg l^{-1})
	AlOH3F_out= outflow of $\text{Al(OH)}_3\text{-F}$ (mg l^{-1})
	AlOH3F_acc= accumulation of $\text{Al(OH)}_3\text{-F}$ (mg l^{-1})
	N_fl_i = pre-flocculation particle concentration (Nos l^{-1})
	N_fl_f = post-flocculation flocs concentration (Nos l^{-1})
	N_post_float = post flotation flocs concentration (Nos l^{-1})
N_float_acc = floated sludge accumulation (mg)	

Table 6-6: Output parameters of process-based conceptual model

Parameter category	Parameters
Technical outputs: Process constants	f_D = friction factor Re = Reynolds number h_L = head loss across the duct (m) T_{res} = residence time (min) V_f = flow velocity ($m\ s^{-1}$) D_h = hydraulic diameter V_E = electrode volume (m^3) V = working volume of the reactor (l) A = cross sectional area of the reactor (m^2) G = velocity Gradient (s^{-1}) V_{H_2} = generation of H_2 gas volume ($l\ s^{-1}$) V_b = rising velocity of air bubbles ($m\ s^{-1}$) K_f = flotation constant (s^{-1}) ϕ_b = air dosage ($m^3\ air\ m^{-3}\ water$) E_A = active anode area (m^2) I/A = current density ($A\ m^{-2}$) I/V = current concentration $A\ m^{-3}$ $K_{M+\mu}$ = rate constant for particle aggregation ($l\ s^{-1}$)
Technical outputs: Model accuracy indicators	MSE = mean square error $RMSE$ = root-mean-square error RSE = relative standard error $MAPE$ = mean absolute percent error
Economic outputs	TC = total cost ($Rs\ l^{-1}$) TE = energy variation (J)

6.4.2. Calibration parameters

The conceptual model was implemented as a numeric model in two computing platforms namely, Microsoft® Excel® ver. 2016 and MATLAB® ver. R2021a. The model involved ten calibration parameters. The expected ranges and the suitable analytical methods for each parameter were identified using a literature review (Tables 6.7 and 6.8).

Table 6-7: Calibration parameter values for the process-based model simulation results – part 1

Calibration Parameter	References	Boundary conditions		Possible experimental evaluation method/s
		Min	Max	
q_m ; the maximum adsorption capacity (mg g^{-1})	Hu, Lo et al. (2007), Bennajah, Gourich et al. (2009), Essadki, Gourich et al. (2010)	0.40	1.40	Literature data available for different experimental conditions. In order to determine the Langmuir constant, dissolved F ⁻ measurements with time should be collected.
K_L ; the Langmuir constant (l mol^{-1})	Hu, Lo et al. (2007), Bennajah, Gourich et al. (2009), Essadki, Gourich et al. (2010)	600	2000	
K ; a percentage denoted hydrolysis efficiency	ϵ_{Al} efficiency of hydro-fluoro-aluminium formation (%) (Hu, Lo et al. 2007)	0.763	0.993	This parameter is similar to ϵ_{Al} efficiency of hydro-fluoro-aluminum formation (%) measured in Hu et al., 2007. Hydrolysis efficiency is varied with different experimental conditions. There are no studies done to identify the possible variation of hydrolysis efficiency with varied experimental conditions. This could be calculated using dissolved and total aluminium measurements.
K_E ; the correction factor denoted adsorption of dissolved fluoride on electrodes	Figures 2,3,5,6 Percentage of fluoride removal graphs in different conditions (Zhu, Zhao et al. 2007)	0.20	0.80	Dissolved fluoride and the fluoride adsorbed on to flocs should be calculated by conducting a fluoride mass balance for the complete time following the Zhu et al (2007) study. Once the reactor operation is finished, the electrodes need to be removed and the remaining solution should be mixed well and the samples should be tested for dissolved fluoride and total fluoride levels.

Table 6-8: Calibration parameter values for the process-based model simulation results – part 2

ϕ ; a correction factor, denoted current efficiency or faradic yield	Faraday's law (Hakizimana, Gourich et al. 2017, Hu, Sun et al. 2017)	1.00	2.00	The correction factors derived for other experimental conditions are not applicable elsewhere. This could be calculated by taking measurements of dissolved and total aluminium levels and then comparing with the theoretical data.
n ; Al:OH ratio in one ring structure of sweep floc	Colloidal parameters calculated based on the ring structure formed by six aluminium hydroxide octahedra (Hem and Roberson 1967)	2.00	3.00	The Al:OH:F ratio could be determined by analysing the sludge samples with below techniques. Particle characterization (scanning electron microscopy (SEM)) Light microscopy results
α is collision efficiency for macro-flocculation	Orthokinetic flocculation model (MWH Americas, Crittenden Communications et al. 2012)	0.00	1.00	The numerical model calibration results could be used to identify the sensitivity of the model response to these efficient factors for a certain extent. Identification of the particle size variation with respect to time could be useful to identify the flocculation and flotation efficiencies. Hence, particle size measurement using a particle size analyser (PSA) and particle characterization using scanning electron microscopy (SEM) could be recommended.
α_{ab} is collision coefficient between an air bubble and floc	Microbubble flotation model (Haarhoff and Edzwald 2004).	0.00	1.00	
η_T is collision frequency between the air bubble and floc	Microbubble flotation model (Haarhoff and Edzwald 2004).	0.00	1.00	
d_j ; colloid size which participates in adsorption and flocculation process (m)	Minimum: From the definition for colloid size; (Metcalf and Eddy 2003). Maximum: From the size of the polymerised particle; (Hem and Roberson 1967)	1.00E-09	5.00E-08	

The experimental direct data category which was explained in the previous section was used to analyse the electrolysis, hydrolysis and coagulation processes. The evaluation of the subsequent flocculation and floatation processes could be done by studying the sludge accumulation in the reactor over time.

6.4.3. Model accuracy measurement

Any developed predictive models should be assessed on how well the model predictions fit the actual observations (Li 2016). The simplest method of assessing how well a model performs is by calculating the error between the predicted value and the actual value. Quantifying the accuracy of a predictive model could be done using different model accuracy measurement techniques. Namely, correlation coefficient (r), coefficient of determination (r^2), mean squared error (MSE), root mean squared error (RMSE), mean absolute percentage error (MAPE) etc. Generally, rather than utilizing a single technique, a goodness of fit evaluation by a combination of suitable model accuracy measurements would be advantageous.

As per the results from the batch model, the actual experimental data variation for dissolved fluoride with time does not follow a linear relationship. Hence, the most commonly used goodness of fit indicators, r and r^2 were not applicable. Five measures of accuracy were selected based on the applicability in non-linear models, which included one unitless indicator. The model precision measurement techniques used in this study are,

i. Mean square error (MSE)

$$MSE = \sum_{i=1}^N \frac{(Y_{pi} - Y_i)^2}{N} \quad (89)$$

Where:

Y_i is observed value

Y_{pi} is predicted value

N is the number of observations

Interpretation: 0 is perfect fit

ii. Root mean square error (RMSE),

$$RMSE = Sqrt. \sum_{i=1}^N \frac{(Y_{pi} - Y_i)^2}{N} \quad (90)$$

Where:

Y_i is observed value

Y_{pi} is predicted value

N is number of observations

Interpretation: 0 is perfect fit

iii. Relative standard error (RSE),

$$RSE = Sqrt. \sum_{i=1}^N \frac{(Y_{pi} - Y_i)^2}{N-2} \quad (91)$$

Where:

Y_i is observed value

Y_{pi} is predicted value

N is number of observations

Interpretation: 0 is perfect fit

iv. Mean absolute percent error (MAPE).

$$MAPE = \frac{1}{N} \sum_{i=1}^N \frac{|Y_{pi} - Y_i|}{Y_i} \quad (92)$$

Where:

Y_i is observed value

Y_{pi} is predicted value

N is number of observations

Interpretation: 0 is perfect fit

v. Confidence Interval (CI):

As an overall measurement of model validation, calculation of the confidence interval was used, as it provides some quantifiable degree of confidence, for the model predictions. A sample from all possible executions of the model was considered, and then the mean model output value for the specific sample was calculated. Then, this is compared with the mean value of the corresponding experimental data, if the mean model output lies within the confidence interval, preferably 95%.

In addition, data sample assessments were also conducted to ensure the goodness of fit of the model, to avoid any generalisation of errors.

6.5. Conclusion of chapter 6

Chapter 6 consisted of the materials and methods followed to achieve objective 3 of this study, which is the experimental assessment of the integrated conceptual model to address the existing design and modelling issues of EC reactors for varied operating conditions. In section 6.2, the discrete-continuous conversion scheme of this conceptual model for continuous EC reactors was explained in detail. Next, in section 6.3, the experimental procedure which was designed to collect primary data to calibrate and validate this conceptual model was explained. Subsequently, the calibration and validation process of the conceptual model through the experimental data were explained along with the description of the model accuracy assessment method. In the next chapter (Ch.7), the results and discussion based on the data collected through this experimental set-up will be presented.

Chapter 7. Results and discussion – PBCM calibration and validation for continuous electrocoagulation reactor

7.1. Chapter overview

Figure 7.1 illustrates the chapter layout of the thesis and the interconnection of this chapter to the rest. This chapter contains the analysis and discussion of experimental data collected through a carefully designed experimental process of continuous electrocoagulation to calibrate and validate the PBCM. Discussion of these results has been sequenced according to the sub-processes identified in the PBCM, namely electrolysis, hydrolysis, coagulation, flocculation, and flotation.

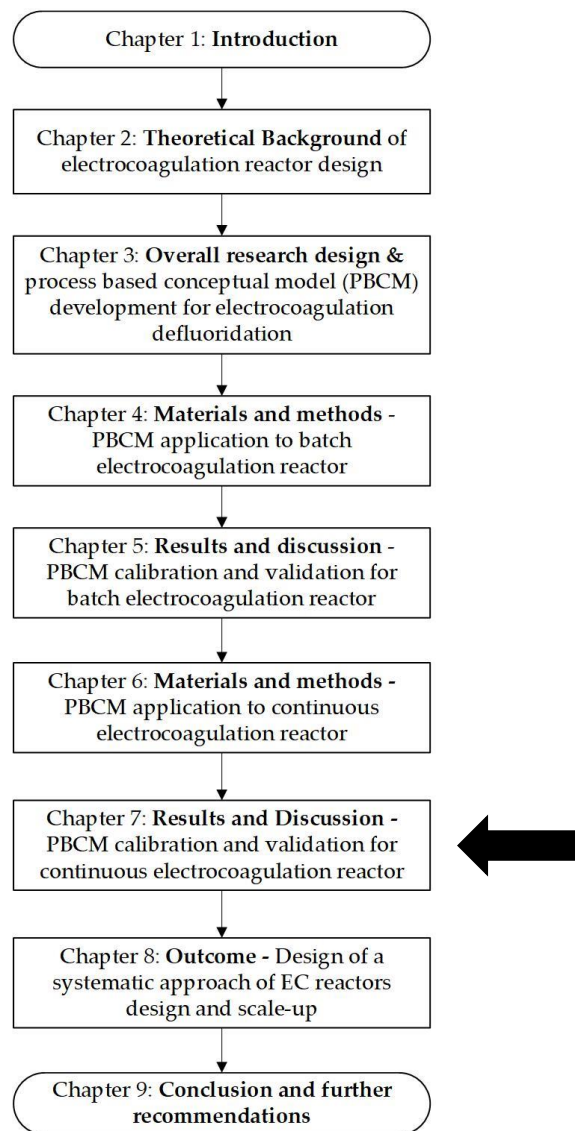


Figure 7-1: The chapter layout of the thesis

Next, the goodness of fit of the model has been discussed using a combination of statistical parameters. Finally, the extended use of the model has been evaluated in terms of application to scale-up/down, longer operation time, different pollutants, etc. Overall, these research findings established the foundation to contextualise the systematic approach of EC reactor design that is explained in chapter 8.

Table 7-1: Calibration parameter values for the process-based model simulation results

No.	Calibration Parameter	References	Boundary conditions	
			Min.	Max.
1	q_m ; the maximum adsorption capacity (mg g^{-1})	Hu, Lo et al. (2007), Bennajah, Gourich et al. (2009), Essadki, Gourich et al. (2010)	0.40	1.40
2	K_L ; the Langmuir constant (l mol^{-1})	Hu, Lo et al. (2007), Bennajah, Gourich et al. (2009), Essadki, Gourich et al. (2010)	600	2000
3	K ; a percentage denoted hydrolysis efficiency	ϵ_{Al} efficiency of hydro-fluoro-aluminium formation (%) (Hu, Lo et al. 2007)	0.763	0.993
4	d_j ; colloid size which participates in adsorption and flocculation process (m)	Minimum: From the definition for colloid size; (Metcalf and Eddy 2003). Maximum: From the size of the polymerised particle; (Hem and Roberson 1967)	1.00E-09	5.00E-08
5	K_E ; the correction factor denoted adsorption of dissolved fluoride on electrodes	Figures 2,3,5,6 Percentage of fluoride removal graphs in different conditions (Zhu, Zhao et al. 2007)	0.00	0.80
6	ϕ ; a correction factor, denoted current efficiency or faradic yield	Faraday's law (Hakizimana, Gourich et al. 2017, Hu, Sun et al. 2017)	1.00	2.00
7	n ; Al:OH ratio in one ring structure of sweep floc	Colloidal parameters calculated based on the ring structure formed by six aluminium hydroxide octahedra (Hem and Roberson 1967)	2.00	3.00
8	α is collision efficiency for macro-flocculation	Orthokinetic flocculation model (MWH Americas, Crittenden Communications et al. 2012)	0.00	1.00
9	α_{db} is collision coefficient between an air bubble and floc,	Microbubble flotation model (Haarhoff and Edzwald 2004).	0.00	1.00
10	η_T is collision frequency between the air bubble and floc,	Microbubble flotation model (Haarhoff and Edzwald 2004).	0.00	1.00

Presented in Tables 7.1 and 7.2 are the calibration parameters used for continuous EC PBCM calibration. Some of the calibration parameter values that were used for the batch model had to be altered suitably during the calibration process of the continuous EC PBCM. The calibrations of the continuous EC model was conducted using the experimental data of O1, O5 and O9. The rest of the experimental data were used to validate the model.

Table 7-2: Calibration parameters used for continuous EC PBCM calibration

Exp.	n	q_m	d_j	K_E	α_{db}	η_T	α	K_L	K	\emptyset
O1	2.2	0.96	1.7E-09	0.02	0.205	0.205	1.0	960	0.775	1.65
O2	2.2	0.96	1.7E-09	0.02	0.250	0.250	1.0	960	0.775	1.68
O3	2.2	0.96	1.7E-09	0.02	0.280	0.280	1.0	960	0.775	1.75
O4	2.2	0.96	1.7E-09	0.02	0.300	0.300	1.0	960	0.775	1.65
O5	2.2	0.96	1.7E-09	0.02	0.320	0.320	1.0	960	0.775	1.68
O6	2.2	0.96	1.7E-09	0.02	0.330	0.330	1.0	960	0.775	1.75
O7	2.2	0.96	1.7E-09	0.02	0.335	0.335	1.0	960	0.775	1.65
O8	2.2	0.96	1.7E-09	0.02	0.341	0.341	1.0	960	0.775	1.68
O9	2.2	0.96	1.7E-09	0.02	0.345	0.345	1.0	960	0.775	1.75
O10	2.2	0.96	1.7E-09	0.02	0.205	0.205	1.0	960	0.775	1.4
O11	2.2	0.96	1.7E-09	0.02	0.600	0.600	1.0	960	0.775	1.05
O12	2.2	0.96	1.7E-09	0.02	0.620	0.620	1.0	960	0.775	1.07
O13	2.2	0.96	1.7E-09	0.02	0.638	0.638	1.0	960	0.775	1.39

7.2. Simulation of the electrolysis process

The electrolysis process is the coagulant generation process of an EC reactor. The metal cation generated from the anodes, would then be hydrolysed into the coagulant leading to the pollutant adsorption, in the defluoridation process using EC. The rate of metal cation (aluminium) generation equation (Eq. 32) was presented in section 3.3.3, and the aluminium accumulation equation (Eq.53) was presented in section 4.2.

The latter was derived using the mass balance application to the electrocoagulation reactor that was considered as a CSTR. The independent variables in this equation are, time, flow rate, and current for the selected electrode material.

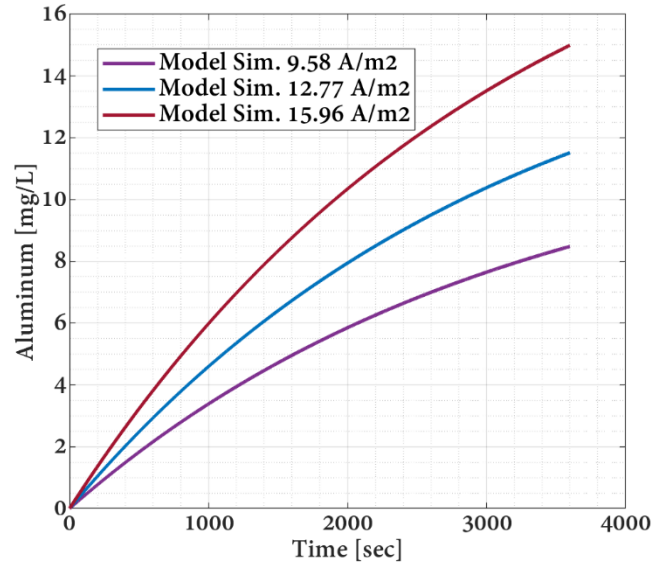


Figure 7-2: Aluminium variation with time for different current densities at initial fluoride concentration 2 mg l^{-1}

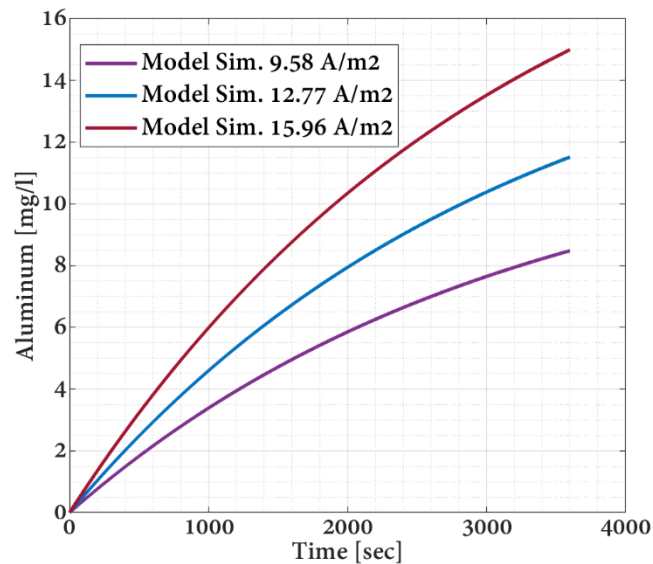


Figure 7-3: Aluminium variation with time for different current densities at initial fluoride concentration 6 mg l^{-1}

The metal cation generation is a zeroth-order rate equation, and the dissipation of aluminium cations also contributes only to the hydrolysis process, hence is considered

independent of the aluminium concentration available at a given time. Hence, the electrolysis process and the aluminium cation accumulation in the reactor are independent of the pollutant concentration in the reactor. This could be identified from the model simulation presented in Figures 7.2 and 7.3.

It could also be noted that the higher the current density, the higher the residual aluminium levels in the solution. As per the fluoride removal efficiencies summarised in Table (7.3), increasing current density has resulted in higher fluoride removal efficiencies. On the other hand, increased current densities would lead to higher residual aluminium levels which need to be controlled. The United States Environmental Protection Agency (US-EPA) in 2017 made the recommendation of Secondary Maximum Contaminant Level (SMCL) as 0.05–0.2 mg l⁻¹ for aluminium in drinking water (Krupińska 2020). The residual Al concentration in drinking water must be lower than 0.2 mg l⁻¹ in agreement with the World Health Organization (WHO) guideline (WHO 2017). Hence, finding an optimum current density that fulfils both criteria is mandatory. The defluoridation efficiency for the experiment O9 has been found as 78%, and the final fluoride level as 1.32 mg l⁻¹ which is below the harmful level of dissolved fluoride (WHO 2017). However, as per Figure (7.3), the experiment O9, which operated in a current density of 15.96 A m⁻² has resulted in a residual aluminium level of 15 mg l⁻¹ after 1 hour of the operation time, which is considerably higher than the recommended residual aluminium level for drinking water. Past studies have demonstrated that employing a settling tank or a sand filter would effectively lower the dissolved aluminium content to acceptable levels. However, higher aluminium generation would not only lead to short life span of electrodes, but also lead to higher sludge discharge, thus increasing the cost for electrode replacement, sludge treatment, and disposal. Hence, identifying the optimum current density is a necessity to acquire sustainable and economical operation in EC. Employing the validated PBCM to find the optimum current density is discussed in chapter 8.

7.3. Simulation of the hydrolysis process

The equation (37) presented in section 3.3.4, was derived following a concept presented by Hu, Lo et al. (2007) where an efficiency factor (ϵ_{Al}) was used to calculate the amount converted from the aluminium cations into aluminium hydroxide. Therefore, in this model, similar to ϵ_{Al} , an efficiency factor (K), is considered (table 7.1) to calculate the amount converted as aluminium hydroxide species out of the dissolved aluminium available in the reactor. This step directly governs the adsorbent generation, hence affecting the pollutant abatement process. The equation (56) presented under section 5.2, explains the aluminium hydroxide accumulation equation resulted from the mass balance application to the EC reactor as a CSTR. Although aluminium hydroxide generation is a zeroth-order rate equation, the model simulation of accumulation of aluminium hydroxide graph (Figure 7.4) revealed a notable variation with time compared to dissolved aluminium Figures (7.2 & 7.3).

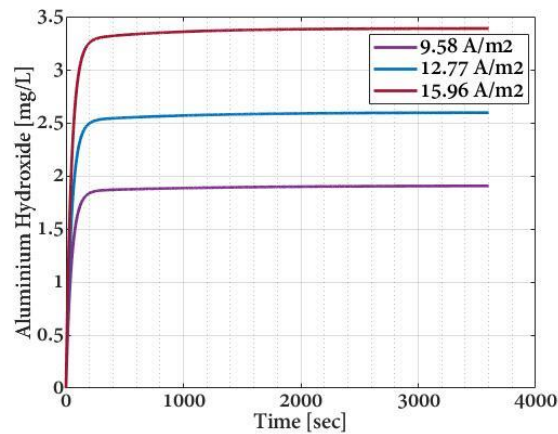


Figure 7-4: Model simulation of aluminium hydroxide variation with time for different current densities at initial fluoride concentration 2 mg l^{-1}

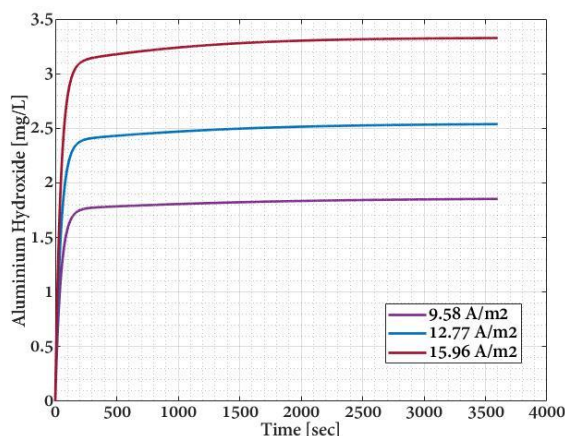


Figure 7-5: Model simulation of aluminium hydroxide variation with time for different current densities at initial fluoride concentration 6 mg l^{-1}

It could be noted that, during the initial 200 s, aluminium hydroxide concentration increases rapidly and then maintains an approximately constant value throughout the reactor operation time. It was also evident that the aluminium hydroxide concentration is independent of initial fluoride concentration variations when compared to the Figures (7.4) and (7.5). A further emphasised illustration of the variation of aluminium hydroxide concentration in the reactor during the first 300 s of the operation is shown in Figure (7.6). It could be noted that the initial increment of the concentration is non-linear and lasts for approximately 200 s. The hydrolysis rate is governed by the efficiency factor (K), hence higher (K) values indicate a higher conversion rate of dissolved aluminium into aluminium hydroxide thus resulting in higher fluoride removal. Hence, taking suitable steps to increase hydrolysis efficiency (K), especially during the initial 200 s of the reactor operation may significantly increase the overall fluoride removal efficiency. The suitable measures to achieve this result, are discussed in more detail in chapter 8.

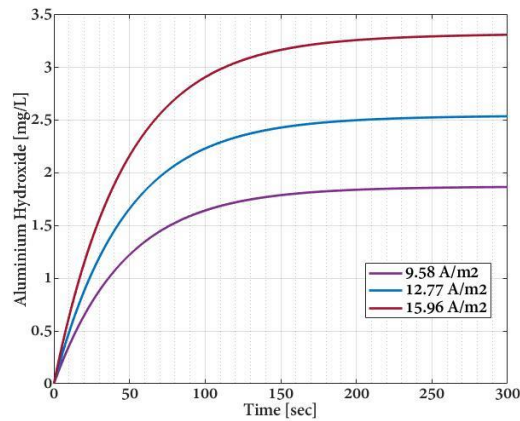


Figure 7-6: Model simulation of aluminium hydroxide variation during the initial 300 s for different current densities at initial fluoride concentration 2 mg l^{-1}

7. 4. Simulation of the coagulation process

As the next discussion theme, the two primary destabilisation techniques, charge neutralisation (coagulation) followed by entrapment in a precipitate (sweep flocculation) were considered. The Langmuir Isotherm was considered as the coagulation model equation as explained in section 3.3.5 (Eq. 38).

$$q_e = \frac{q_m K_L C_e}{1 + K_L C_e} \quad (38)$$

Where:

q_e is the amount of pollutant adsorbed per unit mass of adsorbent at equilibrium (mg g^{-1}),

q_m is the maximum adsorption capacity (mg g^{-1}),

K_L is Langmuir constant (l mol^{-1}),

C_e is the equilibrium concentration of the pollutant (mol l^{-1}).

The adsorbent concentration (mol l^{-1}) represented in Figure (7.7) and q_e which is the amount of pollutant adsorbed per unit mass of adsorbent at equilibrium (mg g^{-1}) illustrated in Figure (7.8), constitute the equation for fluoride adsorption in a given time (Figure 7.9). As expressed from equation (38), the variation of q_e is related to the fluoride concentration in the reactor, hence along with the fluoride concentration reduction, a gradual reduction of q_e could be noticed over time (Figure 7.8, appendix C).

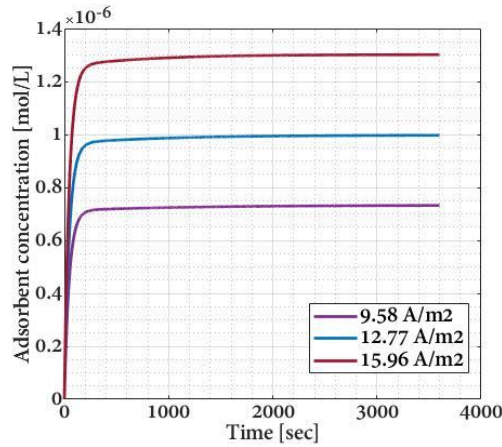


Figure 7-7: Model simulation of adsorbent concentration variation with time for different current densities at initial fluoride concentration 2 mg l^{-1}

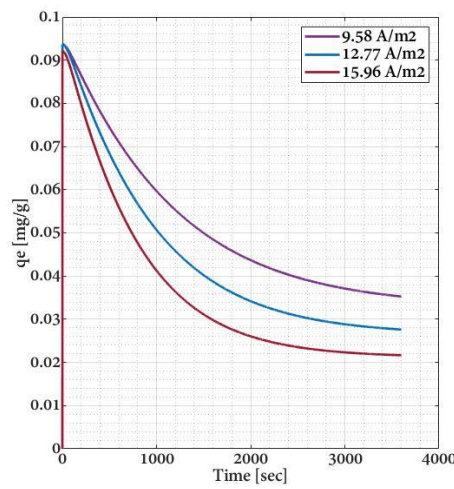


Figure 7-8: Model simulation of q_e variation with time for different current densities at initial fluoride concentration 2 mg l^{-1}

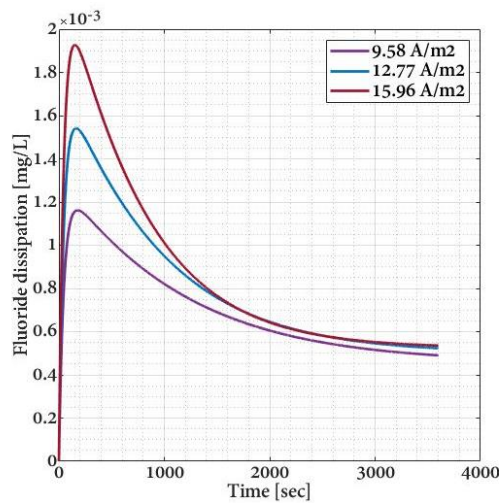


Figure 7-9: Model simulation of dissipation of fluoride variation with time for different current densities at initial fluoride concentration 2 mg l^{-1}

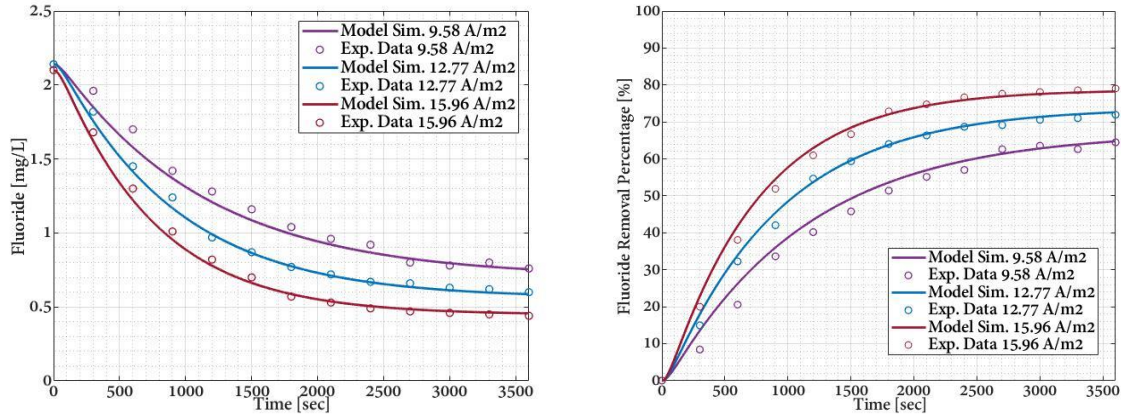


Figure 7-10: Model simulation of fluoride variation with time for different current densities at initial fluoride concentration 2 mg l^{-1} (Calibration curve: Model Sim. at 9.58 A m^{-2} , Validation curves: Model Sim. at 12.77 A m^{-2} and 15.96 A m^{-2})

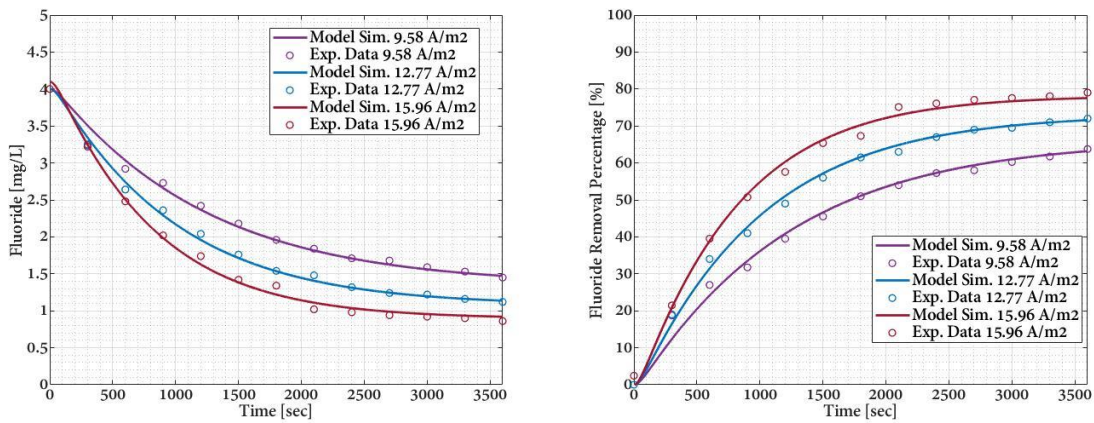


Figure 7-11: Model simulation of fluoride variation with time for different current densities at initial fluoride concentration 4 mg l^{-1} (Calibration curve: Model Sim. at 12.77 A m^{-2} , Validation curves: Model Sim. at 9.58 A m^{-2} and 15.96 A m^{-2})

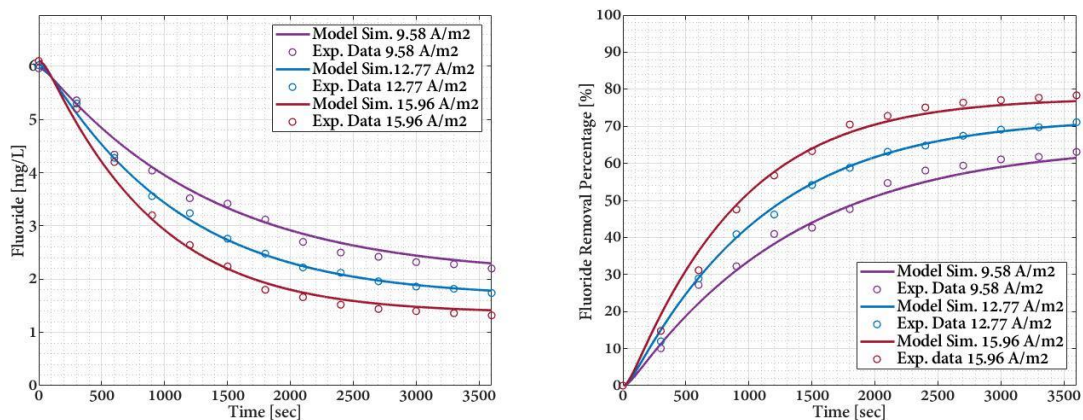


Figure 7-12: Model simulation of fluoride variation with time for different current densities at initial fluoride concentration 6 mg l^{-1} (Calibration curve: Model Sim. at 15.96 A m^{-2} , Validation curves: Model Sim. at 9.58 A m^{-2} and 12.77 A m^{-2})

The model predictions of dissolved fluoride variation and the fluoride removal percentage were then studied (Figure 7.10 to 7.12). The experimental data and the model predictions were in close agreement. The statistical analysis for the evaluation of the goodness of fit of the PBCM is discussed in section 6.9. A good agreement could be noted between the model predictions and the experimental data graphs. Predicted fluoride concentrations seem to reach a constant value from approximately 3000 s, agreeing with the experimental findings. This reflects the hydraulic detention time (HDT) of the reactor.

The results of the model validation from dissolved fluoride concentrations, confirm the suitability of the PBCM for a given experimental condition. The adaptability of the model for varied experimental conditions using the same reactor was then evaluated. This was evaluated by comparing the predicted and experimental defluoridation efficiencies of EC experiments conducted for a duration of 3600 s. The dissolved fluoride concentrations of 10 min intervals, obtained from the experiments O1 to O13 are summarized in Table (7.3). The overall efficiencies of these experiments are then presented in Figure (7.13). Here the efficiency has been calculated considering the difference of initial and final concentrations of dissolved fluoride inside the reactor. It could be noted that from O1 to O3, from O4 to O6, and from O7 to O9, the defluoridation efficiency gradually rises. This is due to the increment in the current densities, hence agrees with what has been found in previous studies (Mameri, Yeddou et al. 1998, Hu, Lo et al. 2007). A similar pattern of results was obtained from the model simulations, for varied supply current densities. The only calibration parameter that was amended in these simulations was the correction factor, denoted current efficiency or faradic yield (\varnothing). Further to this, demonstrating the consistency with the former studies, the experiments with the same supply current densities such as O1, O4, and O7 resulted in approximately the same defluoridation efficiencies. Interestingly, the model demonstration was broadly in line with this behaviour of the EC operations.

Most importantly, the changes made to the experimental conditions were well simulated by amending only the experimental parameters entered into the model. Amending the calibration parameters was required only if a direct link between the experimental condition and the calibration parameter existed. For example, change of supply current would demand amending the correction factor, denoted current efficiency or faradic yield (\emptyset). These changes are further explained in chapter 8. It should be noted that throughout experiments O1 to O9, the water height and flow rate was kept at the same value. The suitability of the model to predict different scales of similar EC reactors will be discussed later in section 7.9.

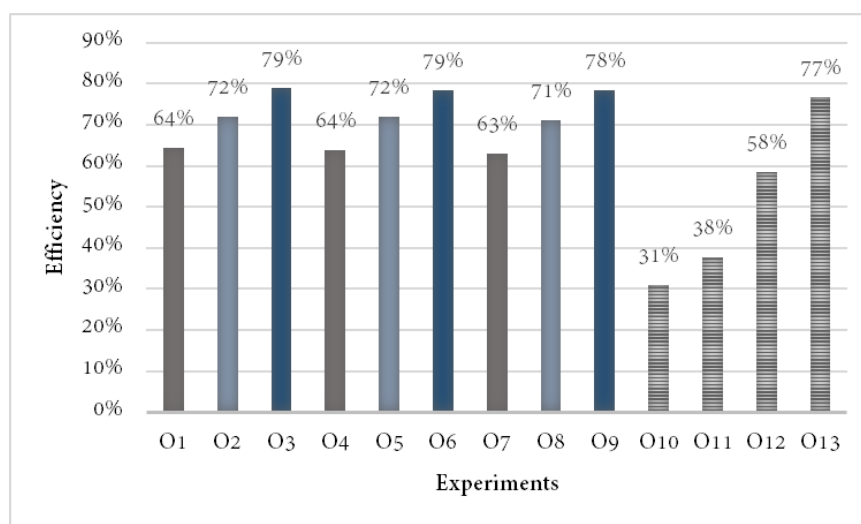


Figure 7-13: Experimental fluoride removal efficiency for continuous EC defluoridation experiments

Table 7-3: The results of dissolved fluoride concentrations for continuous EC defluoridation experiments (Calibration parameters are given in Table (7-2))

Exp.	At 0 min (mg l ⁻¹)	At 10 min (mg l ⁻¹)	At 20 min (mg l ⁻¹)	At 30 min (mg l ⁻¹)	At 40 min (mg l ⁻¹)	At 50 min (mg l ⁻¹)	At 60 min (mg l ⁻¹)
O1	2.14	1.70	1.28	1.04	0.92	0.78	0.76
O2	2.14	1.45	0.97	0.77	0.67	0.63	0.60
O3	2.10	1.30	0.82	0.57	0.49	0.46	0.44
O4	4.00	2.92	2.42	1.96	1.71	1.59	1.45
O5	4.00	2.82	2.04	1.54	1.36	1.22	1.12
O6	4.00	2.48	1.74	1.34	0.98	0.92	0.86
O7	5.96	4.34	3.52	3.12	2.50	2.32	2.20
O8	6.02	4.28	3.24	2.48	2.12	1.86	1.74
O9	6.10	4.20	2.64	1.80	1.52	1.40	1.32
O10	2.1	1.92	1.82	1.72	1.62	1.52	1.45
O11	6.10	5.16	4.64	4.32	4.02	3.96	3.80
O12	6.10	4.76	4.04	3.34	2.88	2.70	2.54
O13	6.00	3.60	2.42	2.00	1.68	1.50	1.40

Comparison of total pollutant mass balance calculations of the simulated and observed experimental data was conducted for each continuous EC reactor experiment. This was achieved by applying the theory of conservation of mass (Eq. 65) for the total duration of the reactor operation. The comparison was made between the observed pollutant abatement and the simulated pollutant abatement for each experiment. The equation used for the pollutant abatement calculation is given below. The results are summarised in the Table (7-4). The observed and simulated pollutant abatement values are in good agreement, thus confirming the validity of the model.

$$\text{Total pollutant abatement \%} = \frac{(\sum(F_{in\ at\ t} - F_{out\ at\ t})Q \cdot \Delta t) + (F_0 - F_f)V}{(\sum(F_{in\ at\ t})Q \cdot \Delta t) + F_0 \cdot V} \cdot 100 \% \quad (65a)$$

Here,

$F_{in\ at\ t}$: Inlet fluoride concentration at t (mg l⁻¹)

$F_{out\ at\ t}$: Outlet fluoride concentration at t (mg l^{-1})

Δt : Time gap considered (s)

F_0 : Initial fluoride concentration (mg l^{-1})

F_f : Final fluoride concentration (mg l^{-1})

Q : Inlet (same as outlet) flowrate (l s^{-1})

V : Volume of the reactor (l)

Table 7-4: Comparison of total pollutant mass abatement of the simulated and observed experimental data for continuous reactor experiments using equation (65a)

Experiment Number	Observed dissolved fluoride			Model Simulated dissolved fluoride		
	At 0 min (mg/l)	At 60 min (mg/l)	Observed pollutant removal based on mass balance	At 0 min (mg/l)	At 60 min (mg/l)	Simulated pollutant removal based on mass balance
01	2.14	0.76	56.5%	2.14	0.75	59.7%
02	2.14	0.60	65.8%	2.14	0.59	66.3%
03	2.10	0.44	73.0%	2.10	0.46	72.8%
04	4.00	1.45	56.3%	4.00	1.47	55.9%
05	4.00	1.12	64.5%	4.00	1.14	64.8%
06	4.00	0.86	71.5%	4.00	0.92	70.9%
07	5.96	2.20	55.9%	5.96	2.30	54.0%
08	6.02	1.74	63.3%	6.02	1.78	63.1%
09	6.10	1.32	71.1%	6.10	1.42	70.3%
010	2.10	1.45	24.0%	2.10	1.49	23.6%

7.5. Simulation of the flocculation process

The conventional pollutant abatement models that usually simulate the pollutant removal efficiencies fail to simulate the intermediate steps or operations that occurred simultaneously with an EC reactor. But as clearly shown in former sections, this PBCM has been able to provide a better understanding of the intermediate process variations over time. After the coagulation process, the flocculation and flotation occur in the EC reactor. Generally in water treatment, the process could be broadly categorised into chemical and physical processing units. In chemical units, a chemically induced

response is mainly responsible for pollutant abatement, and the physical processing units create a physical change to the treated water and improve the usability of the water for example by removing the suspended particles. The flocculation and flotation in operations as defluoridation could be categorised as physical processing operations. From the results shown in Figures (7.14) and (7.15), an interesting variation of the pre-flocculation flocs could be noted. Similar to the aluminium hydroxide variation presented in Figure (7.6), a gradual increase of pre-flocculation flocs during the initial 200 s could be noted. Then the flocs concentration gradually decreases over the complete time-span tested.

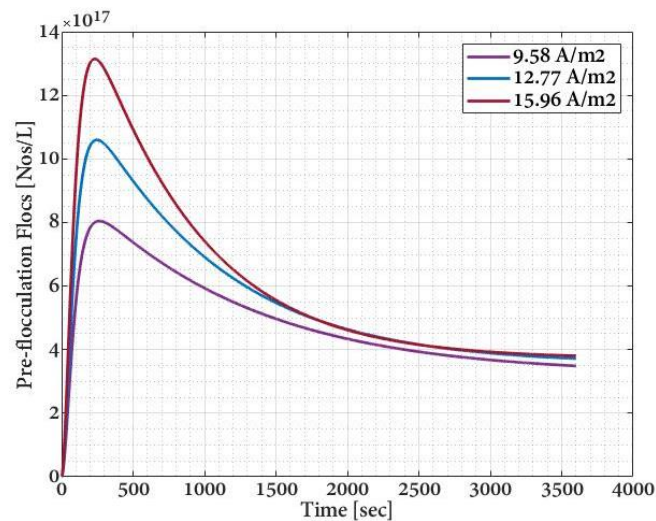
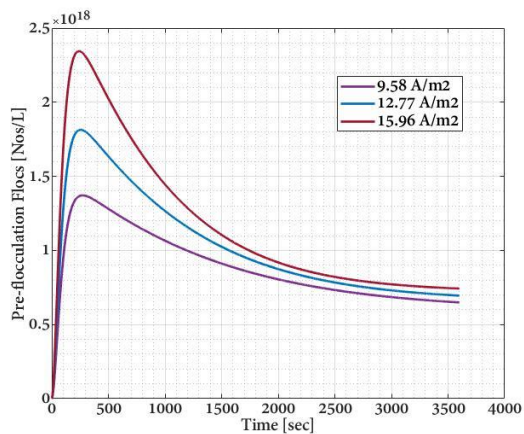
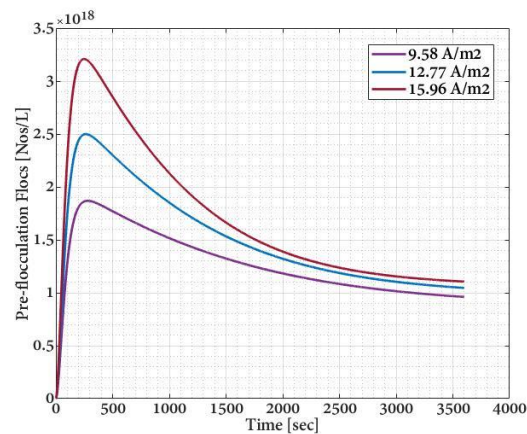


Figure 7-14: Model simulation of pre-flocculation flocs variation with time for different current densities at initial fluoride concentration 2 mg l^{-1}



(a)



(b)

Figure 7-15: Model simulation of pre-flocculation flocs variation with time for different current densities at initial fluoride concentration (a) 4 mg l^{-1} , (b) 6 mg l^{-1}

The flocs evolution in the reactor identified during experiment O1 is shown in Figure 7.16. Water clarity was reduced during the initial 300 s (5 min) of the experiment and gradually improved towards the end of the experiment by 3600 s (1 hour). Hence, it could be highlighted that the model simulations are following the visible flocs evolution noted during the EC operations.

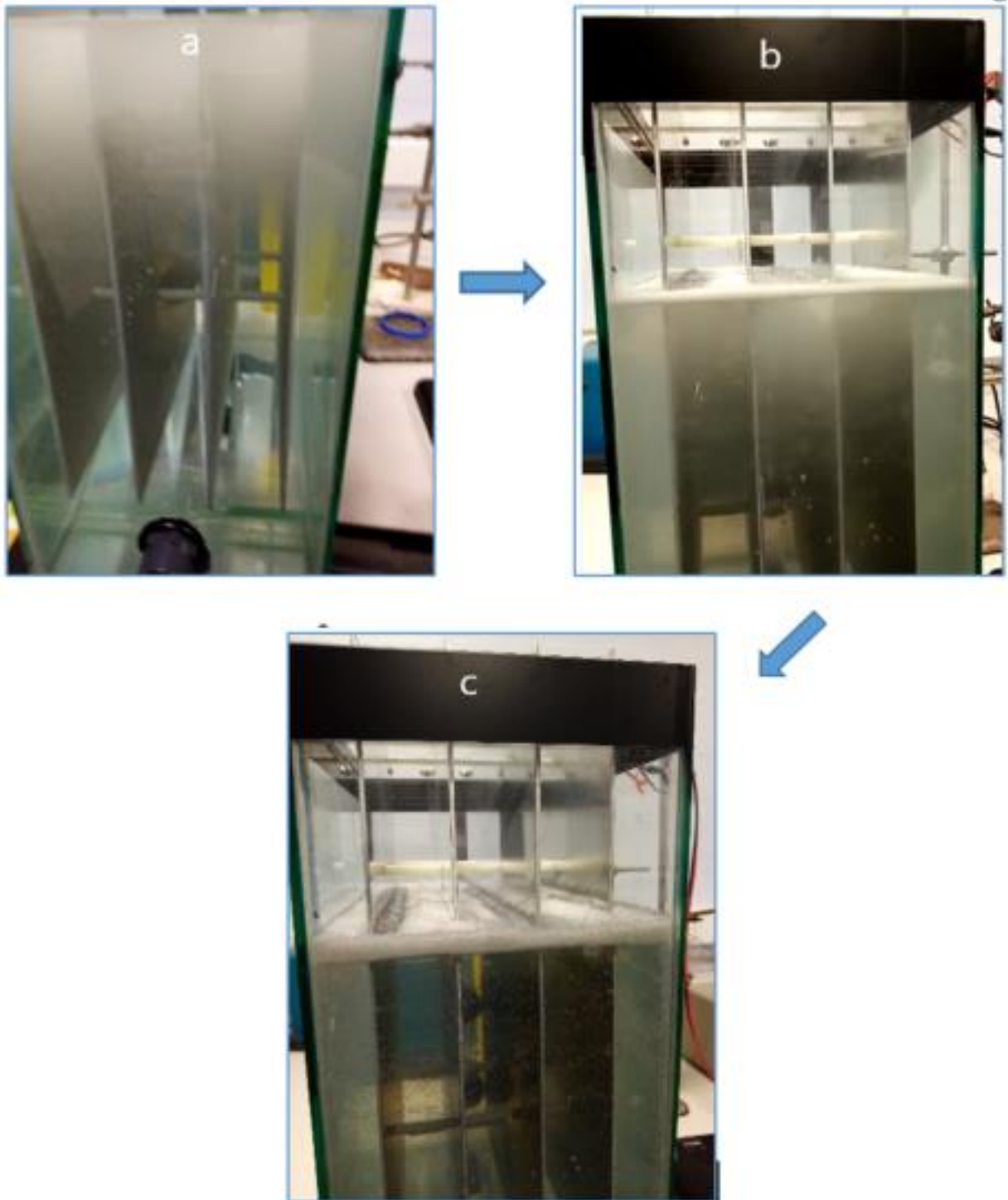


Figure 7-16: Floc evolution during experiment O1 (9.58 A/m^2 , 2 mg/L) (a) 300 s (b) 1200 s (c) 3600 s

7.6. *Simulation of the flotation process*

In the drinking water treatment process, settling tanks and flotation processes are employed to assist solid-water separation usually following the flocculation process. These clarification units are important to ensure the improved physical quality of drinking water. In the EC defluoridation, flotation is more effective than the solid-water separation process due to the simultaneous H₂ bubble production that occurs at the cathode. The flotation model (Eq. 47) used in this study which was discussed in section 3.3.7, is a first-order rate equation, hence depends on the floc concentration in the reactor. The accumulation of floated flocs simulation from the model is illustrated in Figures (7.17), (7.18a), and (7.18b). The accumulation of floated flocs variation shows a linear relationship with time and indicates a clear impact for current density variations. The two calibration parameters related to the flotation model are the collision coefficient between an air bubble and floc (α_{db}) and the collision frequency between the air bubble and floc (η_T). The calibration of the flotation model was carried out by evaluating the total floated floc mass in response to the variations of α_{db} and η_T . The comparison of the calibrated model simulation and experimental data for accumulation of floated flocs in 1 hour operation time of continuous EC reactor is illustrated in Figure (7.19). The (α_{db}) and (η_T) values were tuned until the experimental floated floc amount and the model simulations were approximately equal. This helped identify the value range applicable for the experimental set-up employed. However, when considering this model to be used to predict sludge production, further comparison of the resulting ranges of both (α_{db}) and (η_T) in batch, continuous and scale-up experiments would be required. A possible approach is calibrating the model, using few experimental set-ups and interpolating or extrapolating the (α_{db}) and (η_T) values. The batch EC PBCM calibration process resulted in values for both (α_{db}) and (η_T) in the range from 0.600 to 0.750. The continuous EC PBCM calibration resulted in values ranging from 0.205 to 0.345 for the 26.3 l reactor and from 0.600 to 0.638 for the 11.9 l reactor. This result indicates the effect of reactor size on the efficiency of the flotation process. Generally, the flotation efficiency seems relatively

higher in smaller reactors. Hence, the scale-up reactor designs would require additional precautions to improve the flotation efficiency. The floated flocs accumulated in the reactor during the continuous EC experiments are illustrated by Figures (7.20), (7.21), and (7.22), included in Table 7.4.

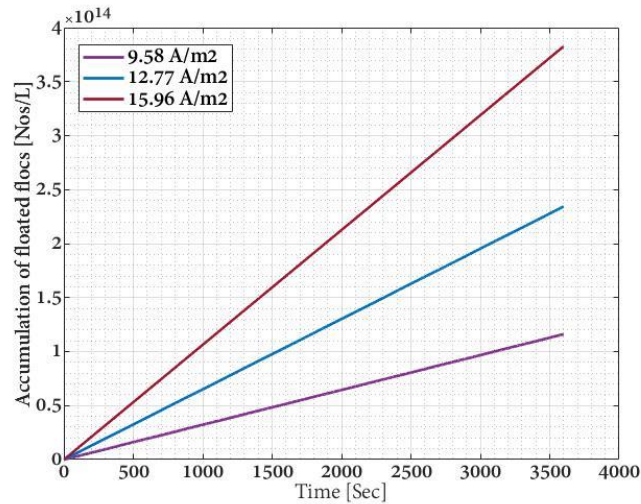


Figure 7-17: Model simulation of accumulation of floated flocs variation with time for different current densities at initial fluoride concentration 2 mg l^{-1}

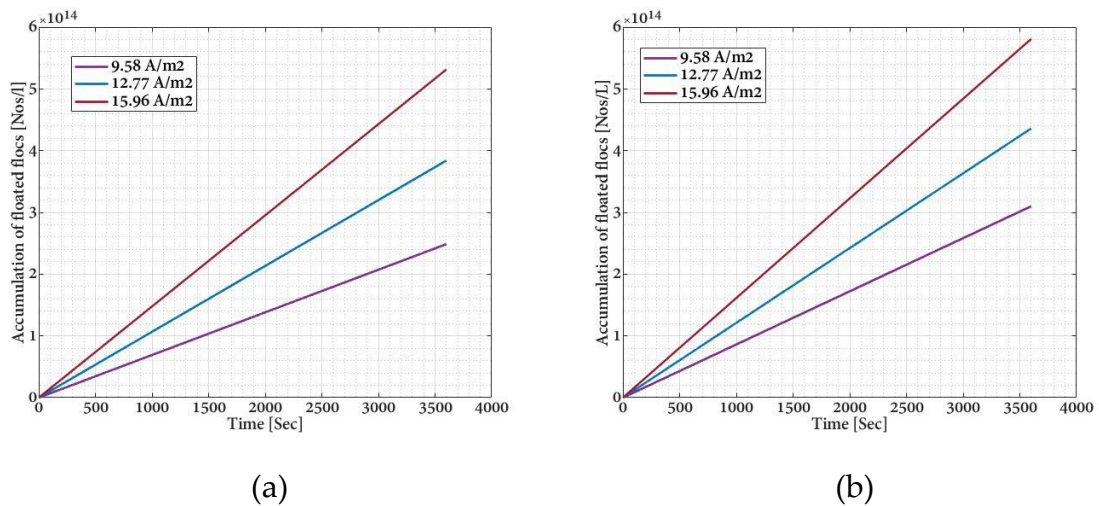


Figure 7-18: Model simulation of accumulation of floated flocs variation with time for different current densities at initial fluoride concentration (a) 4 mg l^{-1} , (b) 6 mg l^{-1}

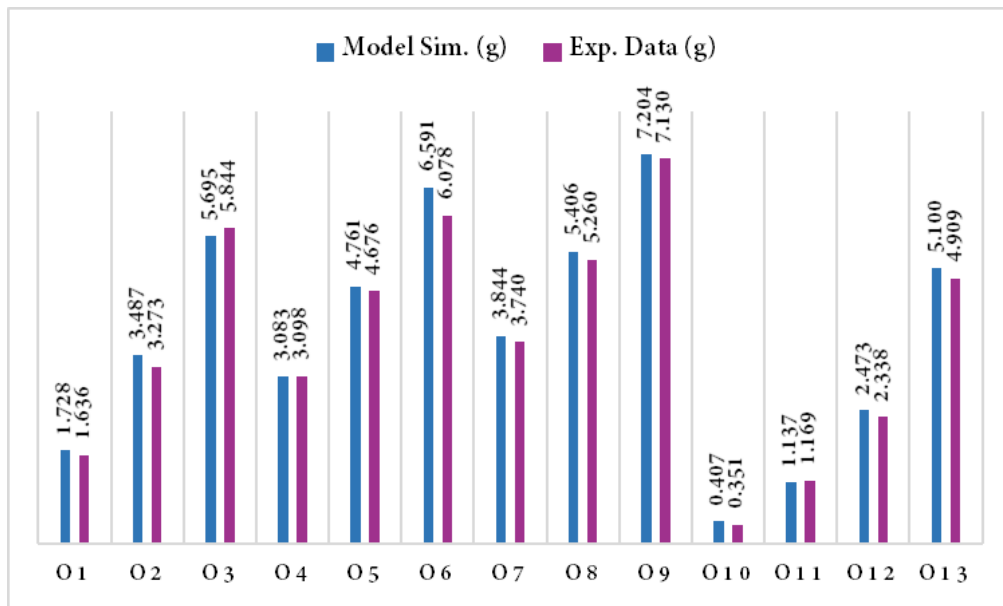
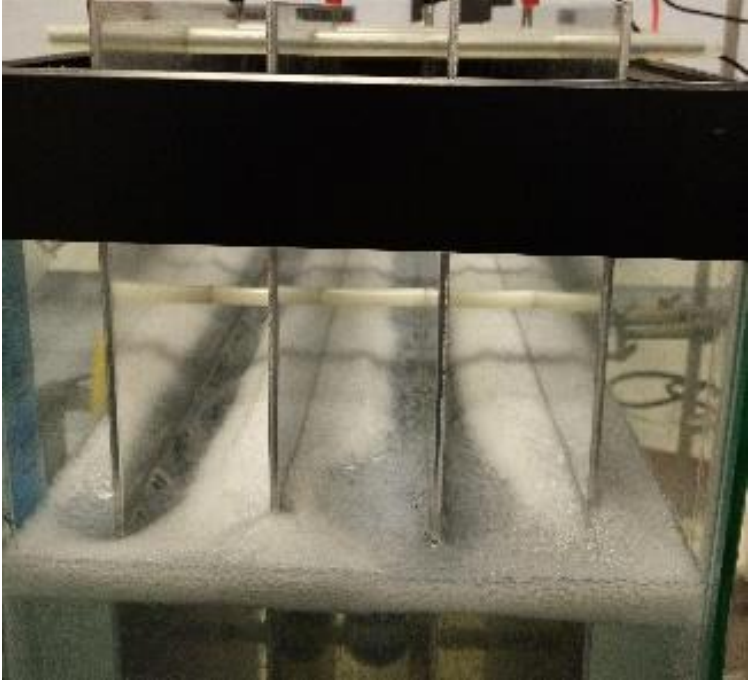
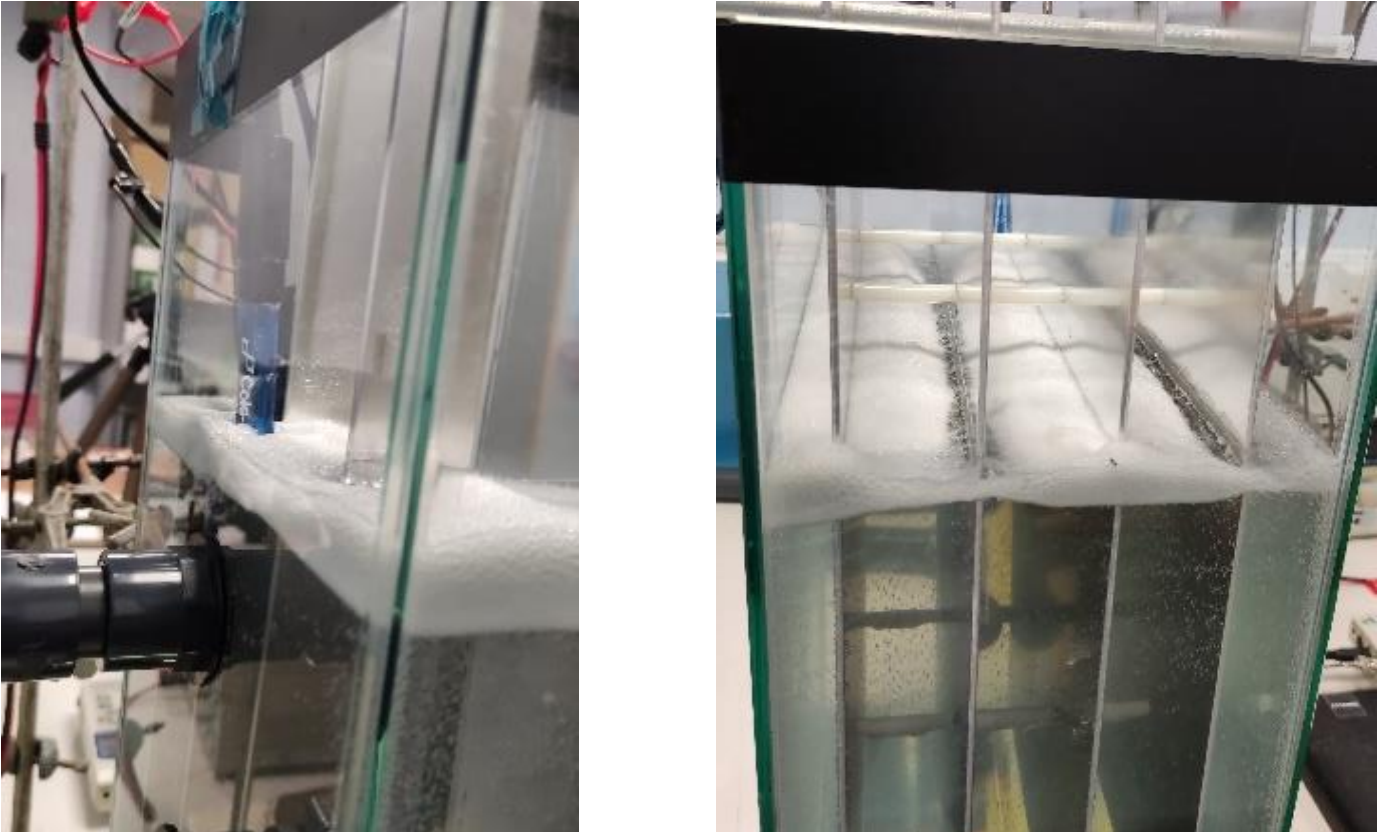
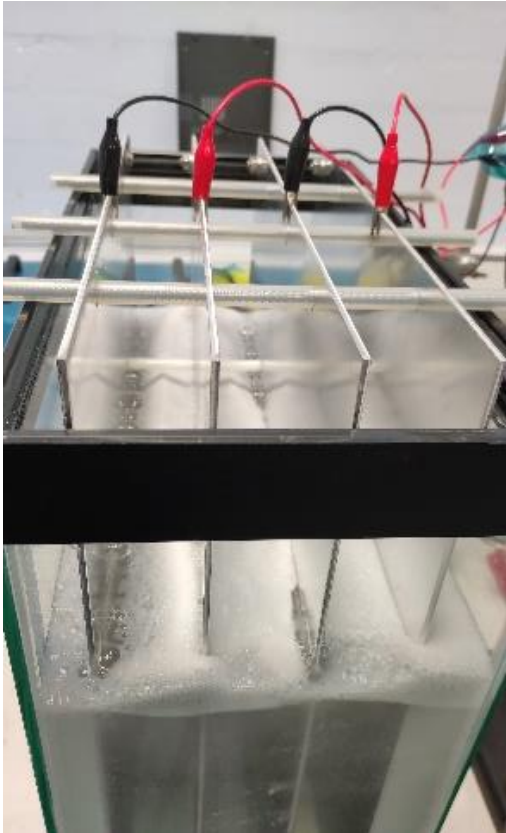
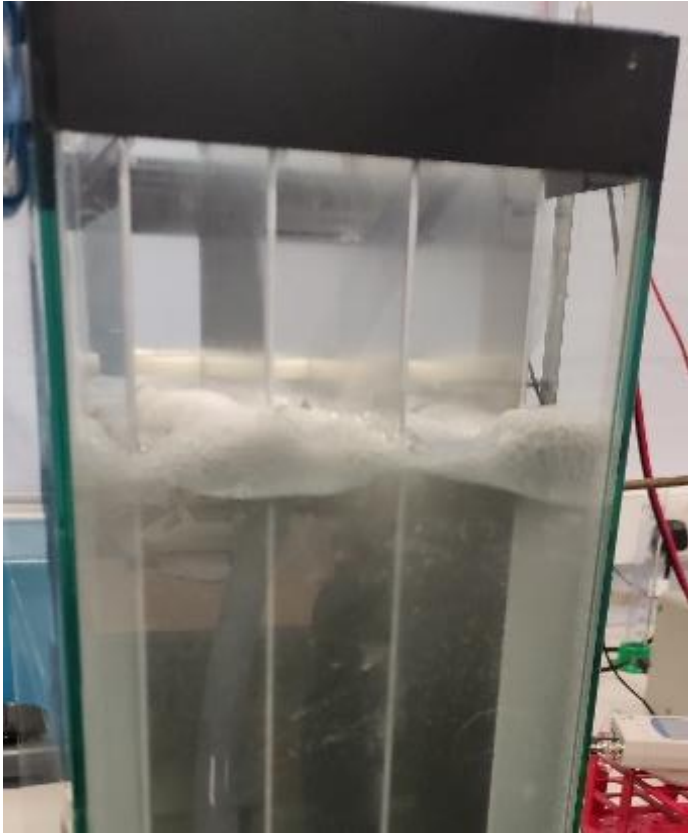


Figure 7-19: Comparison of model simulation and experimental data for accumulation of floated flocs (g) in 1 hour operation time of continuous EC reactor (Calibration parameters are given in Table 7-2)

Table 7-5: Floated flocs accumulation after 3600 s of continuous EC experiments O1, O4 and O9

<p>Experimental details</p>	<p>Figures of floated flocs</p>	
<p>Figure 7-20: Floated flocs accumulation after 3600 s of EC experiment O1</p> <p>Current density: 9.58 A/m²</p> <p>Initial fluoride concentration: 2 mg/L</p>		

Experimental details	Figures of floated flocs
<p>Figure 7-21: Floated flocs accumulation after 3600 s of EC experiment O4. Current density: 9.58 A/m²</p> <p>Initial fluoride concentration: 4 mg/L</p>	

Experimental details	Figures of floated flocs	
<p>Figure 7-22: Floated flocs accumulation after 3600 s of EC experiment O9 Current density: 15.96 A/m² Initial fluoride concentration: 6 mg/L</p>		

7.7. Simulation of floc adsorption on electrodes

The phenomenon of floc adsorption on electrodes in EC was first discussed by Zhu, Zhao et al. (2007). In the PBCM design, the flocs adsorption to electrodes was attributed to two processes, namely dissipation of aluminium hydroxide and dissipation of aluminium-hydroxo-fluoride as explained in section 6.2 (Eq. 83). Following the calibration process, the variations of total floc adsorption on electrodes could be identified as given in Figure (7.23).

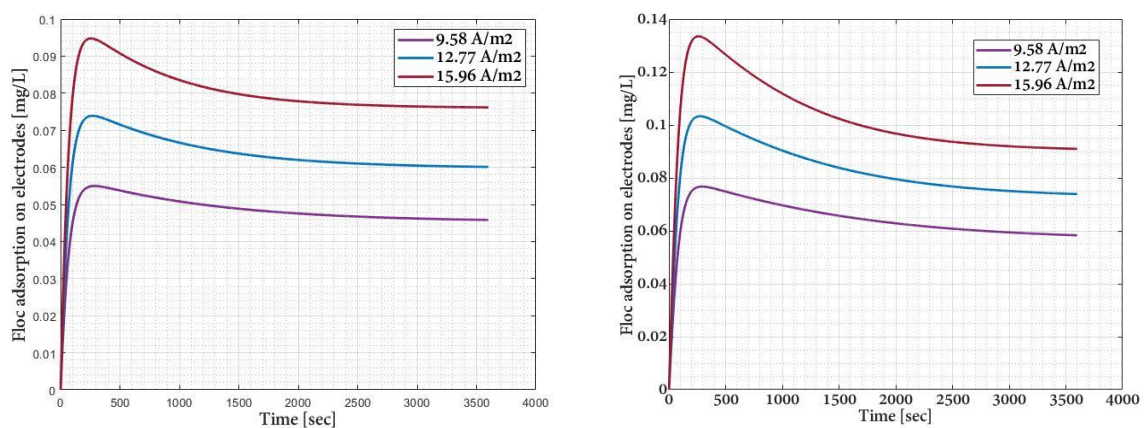


Figure 7-23: Model simulation of adsorption of flocs on electrodes variation with time for different current densities at initial fluoride concentration (a) 2 mg l^{-1} , (b) 6 mg l^{-1}

These results are in agreement with the findings of the former study mentioned above. It could be observed that with the increment of current density, the number of flocs adsorbed onto the electrodes has been increased owing to the higher floc concentrations available in the reactor. When studying the adsorption variation over time, a gradual increase in adsorption during the initial 250 s could be noted in all cases. Higher initial concentrations of fluoride also led to a slight increment in the electrode adsorption as compared in Figures (7.23a) and (7.23b).

7.8. Energy calculation and economic optimisation

A comparison of energy consumption for each experiment was performed and the results are given in Table (7.5). Here, the energy has been calculated using the

measured voltage and current, for one hour of EC reactor operation per litre of water treated. The variation of the energy per treated volume of water has been compared in Figure 7.24.

Table 7-6: Energy consumption related parameters and calculation of continuous EC experiments (Calibration parameters are given in Table 7-2)

Experiment	Current Density ($A\ m^{-2}$)	Current (A)	Voltage (V)	Energy ($kJ\ h^{-1}$)	Energy per treated volume ($kJ\ h^{-1}l^{-1}$)
01	9.58	3.00	7.30	78.84	2.63
02	12.77	4.00	9.73	140.16	4.67
03	15.96	5.00	12.17	219.00	7.30
04	9.58	3.00	7.20	77.76	2.59
05	12.77	4.00	9.56	137.66	4.59
06	15.96	5.00	11.95	215.10	7.17
07	9.58	3.00	7.11	76.79	2.56
08	12.77	4.00	9.40	135.36	4.51
09	15.96	5.00	11.75	211.50	7.05
010	3.19	1.00	6.40	23.04	0.48
011	9.26	1.00	4.10	14.76	0.98
012	18.52	2.00	8.10	58.32	3.89
013	27.78	3.00	12.00	129.60	8.64

The hourly energy consumption per treated water volume has increased with the increment of supply current density, agreeing with past studies. The hourly energy consumption which is used for the above comparison and also in many past studies is less effective as a comparison measure for EC operations with different initial concentrations. For higher initial concentrations, the EC operation time should be increased to reach the acceptable pollutant concentrations. Hence, for such comparisons, total energy consumption to reach an agreed pollutant concentration level should be studied. Understandably, increasing operation time increases the energy consumption to treat water. Hence, designing and optimising the reactor to operate at the maximum pollutant removal efficiency is paramount to reduce the energy consumption for treating water using EC. Emamjomeh, Sivakumar et al. (2011) considered four cost items to calculate the total cost of the EC operation, namely,

energy consumption (16.7%), aluminium plate consumption (52.8%), pH adjustment (8.3%), and sludge treatment (22.2%).

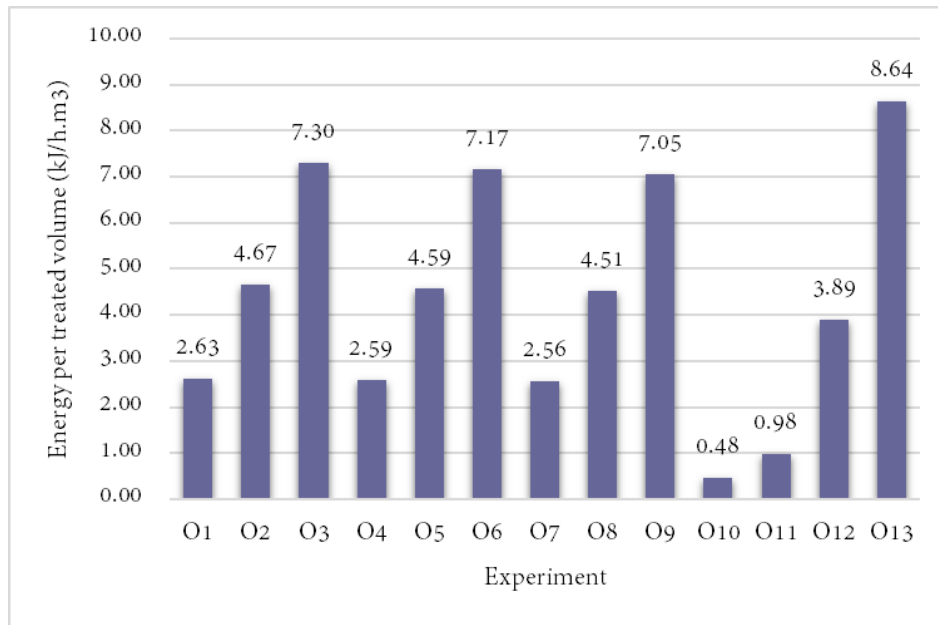


Figure 7-24: Energy consumption related parameters and calculation of continuous EC experiments (Calibration parameters are given in Table 7-2)

It is important to highlight, the requirement of supplying the minimum cell potential for the half-cell reactions to occur. The overall potential equation for a reactor could be expressed from equation (11).

$$E_{cell} = E_{ca} - E_{an} - E_{so} - E_{lo} \quad (11)$$

Where,

E_{cell} is the overall potential of the reactor (V)

E_{ca} is cathodic potential (V)

E_{an} is anodic potential (V)

E_{so} is solution potential (V)

E_{lo} is loss potential (V)

When comparing the energy requirements at different scales, here the E_{an} would mostly remain constant for a selected electrode material and E_{ca} varies for different influent conditions, as there could be additional reactions occurring at the cathode apart from reduction of H_2O . However, if the same inlet water is tested at both lab and pilot scales E_{an} and E_{ca} would be approximately equal, irrespective of the size of the reactors. E_{so} depends on the distance between the electrodes, current density and the electrical conductivity of the solution. Hence keeping the three parameters constant at the lab and pilot level would result in equal values of E_{so} . E_{lo} accounts for the energy losses occurring within the reactor such as the energy required to exceed the passivating layer. E_{lo} increases with time and the quantities should be proportional to the passivating layer size.

7.9. *The goodness of fit and the precision of the Model*

Evaluation of model prediction accuracy was conducted using Mean Squared Error (MSE), Root Mean Square Error (RMSE), Relative Squared Error (RSE), and Mean Absolute Percentage Error (MAPE). A quantitative comparison of the accuracy of the model could be done by evaluating these parameters (Table 7.6). From the selected predictors, MAPE is scale-independent, thus could be used to compare prediction accuracy on different scales. MSE, RMSE, and RSE values were found less than 1 for all experiments conducted. MAPE was found less than 5% for all experiments except O9. Here, O9 resulted in MAPE of 5.35% that could be attributed to the lower operating efficiency that resulted from employing improper current density $3.19A\ m^{-2}$. This current density is lower than the recommended value for effective EC operations. Overall, this goodness of fit measure is in line with the requirements, thus confirming the accuracy of the model.

Evaluation of the error percentages of fluoride concentrations diagram (Figure 7.25) provides an improved understanding of the model accuracy. The comparison of the statistical parameters calculated for these two data sets that are presented in Table 7.7, is important to correctly interpret the results.

Table 7-7: Model prediction accuracy measures of continuous EC PBCM (Calibration parameters are given in Table 7-2)

Experiment	Calibration/ Validation	Volume of reactor (l)	MSE	RMSE	RSE	MAPE
O1	Calibration	26.3	0.0040	0.0629	0.0552	4.3156
O2	Validation	26.3	0.0010	0.0322	0.0237	2.4256
O3	Validation	26.3	0.0014	0.0372	0.0171	3.7337
O4	Validation	26.3	0.0079	0.0891	0.0098	2.3504
O5	Calibration	26.3	0.0034	0.0586	0.0067	2.1926
O6	Validation	26.3	0.0042	0.0649	0.0082	4.6713
O7	Validation	26.3	0.0197	0.1403	0.1085	4.1566
O8	Validation	26.3	0.0048	0.0689	0.0209	1.5652
O9	Calibration	26.3	0.0203	0.1426	0.0065	5.3496
O10	Validation	26.3	0.0010	0.0321	0.0064	1.7398
O11	Validation	11.9	0.0425	0.2061	0.2328	4.3514
O12	Validation	11.9	0.0039	0.0627	0.0068	1.4119
O13	Validation	11.9	0.0096	0.0978	0.0405	3.0016

Here, the calibrations of the continuous EC model were conducted using the experimental data of O1, O5 and O9. The rest of the experimental data were used to validate the model.

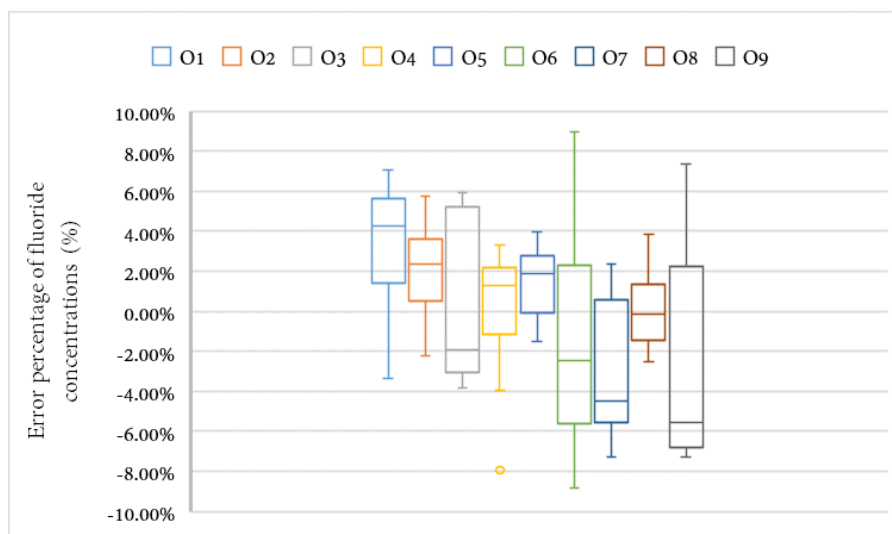


Figure 7-25: Percentages of error of fluoride concentration measurements in experiments O1 to O9 (Calibration parameters are given in Table 7-2)

The individual readings error percentage values that are illustrated in Figure (7.25), range between $\pm 8.3\%$. However, the mean value of the two data sets is approximately equal with an error of 0.18%.

Table 7-8: Statistical parameters of two data sets of fluoride concentrations

<i>Model Predictions</i>		<i>Experimental Data</i>	
Mean	1.82632	Mean	1.82963
Standard Error	0.106084	Standard Error	0.106676
Median	1.57	Median	1.565
Mode	0.956	Mode	1.96
Standard Deviation	1.102454	Standard Deviation	1.10861
Sample Variance	1.215404	Sample Variance	1.229017
Kurtosis	0.997595	Kurtosis	1.276486
Skewness	1.134764	Skewness	1.190592
Range	4.8343	Range	4.92
Minimum	0.457	Minimum	0.44
Maximum	5.2913	Maximum	5.36
Sum	197.2426	Sum	197.6
Count	108	Count	108
Confidence Level (95.0%)	0.210298	Confidence Level (95.0%)	0.211473

In addition to the accuracy of the model, it is also important to evaluate the precision of the model. In this study, the model precision was measured by evaluating the confidence interval and relationship between experimental & theoretical data. It could be noted from Figure 7.26, that there is a good agreement between the experimental fluoride concentrations and model simulations of fluoride concentrations where R^2 is 0.994, thus evidencing the higher precision of the model predictions.

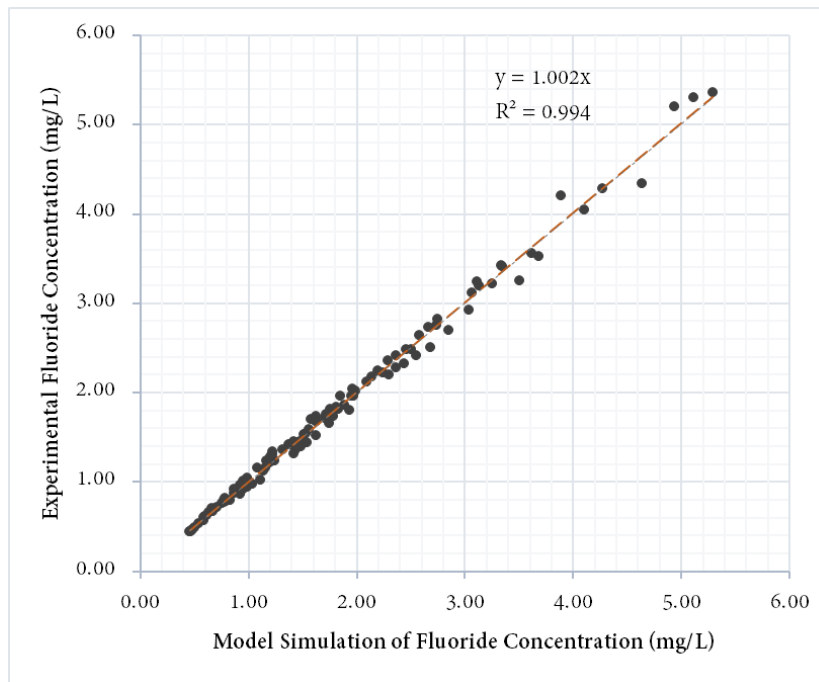


Figure 7-26: Relationship between experimental fluoride concentrations and model simulations of fluoride concentrations of continuous EC defluoridation process conducted (Experiments O1 to O9)

7.10. Scale-up/down operation

Mathematical and conceptual model simulations or processes not only increase the controllability of the systems but also help reduce the cost and effort in conducting laboratory and pilot-scale testing during the design stage, hence enabling the designers to develop large scale processes economically. Hence, it is important to evaluate the applicability and adaptability of the developed conceptual and mathematical process-based model in varied scales. In this study, the experiments O11, O12, O13 were conducted using a scaled-down EC reactor to evaluate the suitability of the PBCM for scale-up/down variations. The MATLAB® ver. R2021a model simulation results for theoretical fluoride concentrations and experimental data comparison are illustrated in Figure (7.27). The estimated calibration parameters for these experiments are listed in Table (7.2). The fluoride removal patterns were similar in all cases while experiments O7 and O12 showed much similar removal efficiencies. Also, it is worth noting the similarity of sub-process parameter variations of the scaled-down version illustrated by Figures (7.28a) and (7.28b).

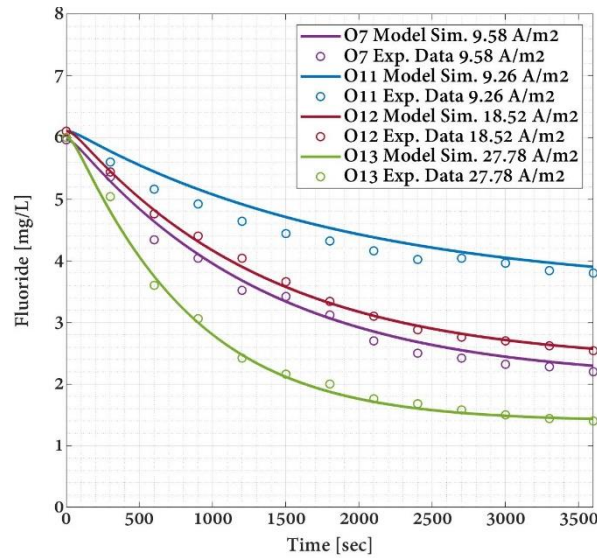


Figure 7-27: Comparison of fluoride concentrations of experiments O7, O11, O12, and O13

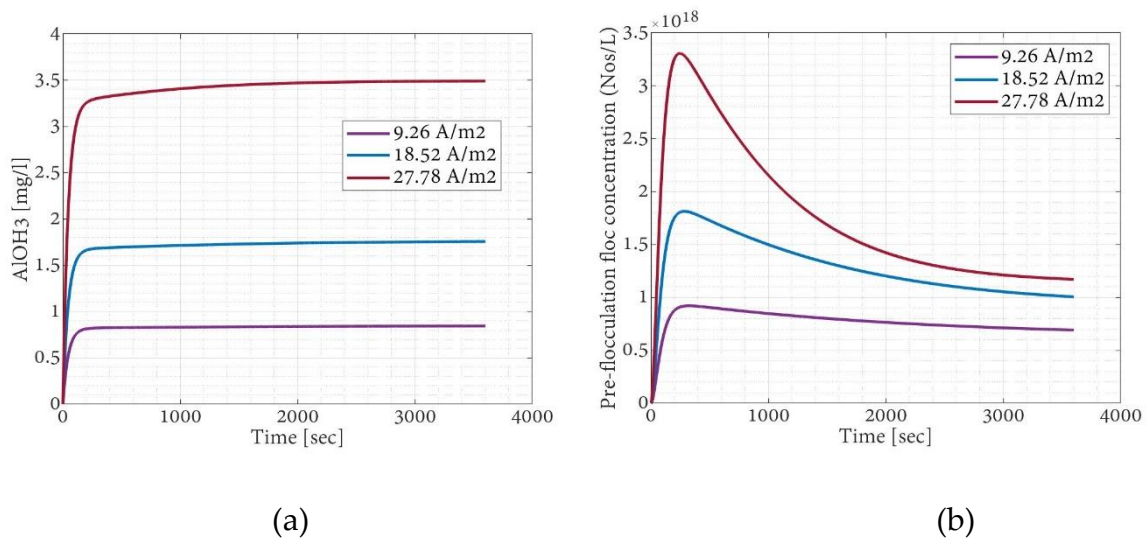


Figure 7-28: Model simulation of (a) aluminium hydroxide concentration (mg l^{-1}), and (b) pre-flocculation floc concentration (Nos l^{-1}) variation with time for different current densities

Hydrodynamic parameters of these two experiments are listed in Table (7.8), and a comparison of EC energy consumption and fluoride removal efficiency data are listed in Table (7.9). The use of dimensional analysis for EC process scale-up is limited and quite conflicted in the literature. Zolotukhin (1989) scaled up an EC-flotation system from laboratory to industrial scale by studying five dimensionless scale-up parameters to ensure correct sizing and proportioning of the reactors.

Table 7-9: Hydrodynamic parameters comparison of O7 and O12 experiments

Notation	Parameter	Prototype	Model		
		07,08,09	011,012,013		
ρ	Density (kg m ⁻³)	1000	1000		
Q	Flow (ml min ⁻¹)	500	250		
V	Velocity (m s ⁻¹)	0.000114	0.000119		
D	Hydraulic Diameter (m)	0.313978	0.254545		
μ	Viscosity (N s m ⁻²) at 20 C	0.001002	0.001002		
h	Height (m)	0.365	0.175		
L	Length (m)	0.400	0.400		
w	Width (m)	0.200	0.200		
A	Duct cross section area (m ²)	0.073	0.035		
P	Wetted perimeter (m)	0.930	0.550		
Vol	Volume (m ³)	0.029	0.014		
σ	Surface tension (J m ⁻²) at 20 °C	0.0728	0.0728		
Kw	Water permeability (h m ⁻¹)	1.25663E-06	1.25663E-06		
Non dimensional similarity of Prototype (O7) and Model (O11)					07/O11
Re	Reynolds Number (Eq.26)	35.8	30.2		1.2
Fr	Froude Number (Eq.27)	6.50E-05	7.53E-05		0.9
We	Weber Number (Eq.28)	7.17E-05	7.79E-05		0.9
Hr	Geometric Similarity (Hp/Hm)	0.365	0.175		2.1
Wr	Geometric Similarity (Wp/Wm)	0.200	0.200		1.0
Lr	Geometric Similarity (Lp/Lm)	0.400	0.400		1.0
Vr	Geometric Similarity (Vp/Vm)	0.029	0.014		2.1
SGr	Gas Saturation Similarity (Eq.30)	-1.687	-1.687		1.0

The dimensionless parameters were Reynolds number, Froude number, Weber criteria, gas saturation similarity, and geometric similarity. Conversely, Holt et al. (2005) dispute the use of dimensional analysis, the applicability of which may be inherently limited for EC, due to the complexity of the internal processes. However, in this study, the dimensionless parameters used by Zolotukhin (1989) were evaluated between the scaled-down reactor runs (O11, O12, and O13) and the prototype (O1 to O10).

Table 7-10: EC energy consumption and fluoride removal efficiency data comparison

Parameters	07	08	09	011	012	013
Flow rate (ml min ⁻¹)	500	500	500	250	250	250
Current (A)	3.00	4.00	5.00	1.00	2.00	3.00
Electrode Area (m ²)	0.313	0.313	0.313	0.108	0.108	0.108
Reactor Volume (l)	26.3	26.3	26.3	11.9	11.9	11.9
Fluoride removal efficiency in 1 hour (%)	61.5	70.4	76.8	36.0	57.8	76.1
Voltage (V)	7.1	7.1	7.1	4.1	8.1	12.0
Power (W)	21.3	28.4	35.6	4.1	16.2	36.0
Current density (A m ⁻²)	9.6	12.8	16.0	9.3	18.5	27.8
Current concentration (A m ⁻³)	114.1	152.1	190.1	83.9	167.8	251.7
Electrode area/Reactor volume (m ² m ⁻³)	11.9	11.9	11.9	9.1	9.1	9.1
Electrical energy per volume (kWh m ⁻³)	2559.6	3412.8	4266.0	984.0	3888.0	8640.0

It could be noted from the results summarized in Table (7.9), the experiment pairs O7, O12 and O9, O13 have approximately equal fluoride removal efficiencies. However, when the electrode area to reactor volume ratios (A/V) are compared it could be noted that similar pollutant removal efficiencies could be gained by altering the flow rate and supply current to the system even though the A/V of the two reactors are not

equal. In addition, the dimensionless parameter analysis that is summarised in Table (7.8) provides useful insight into the hydrodynamic aspects of the reactor operations.

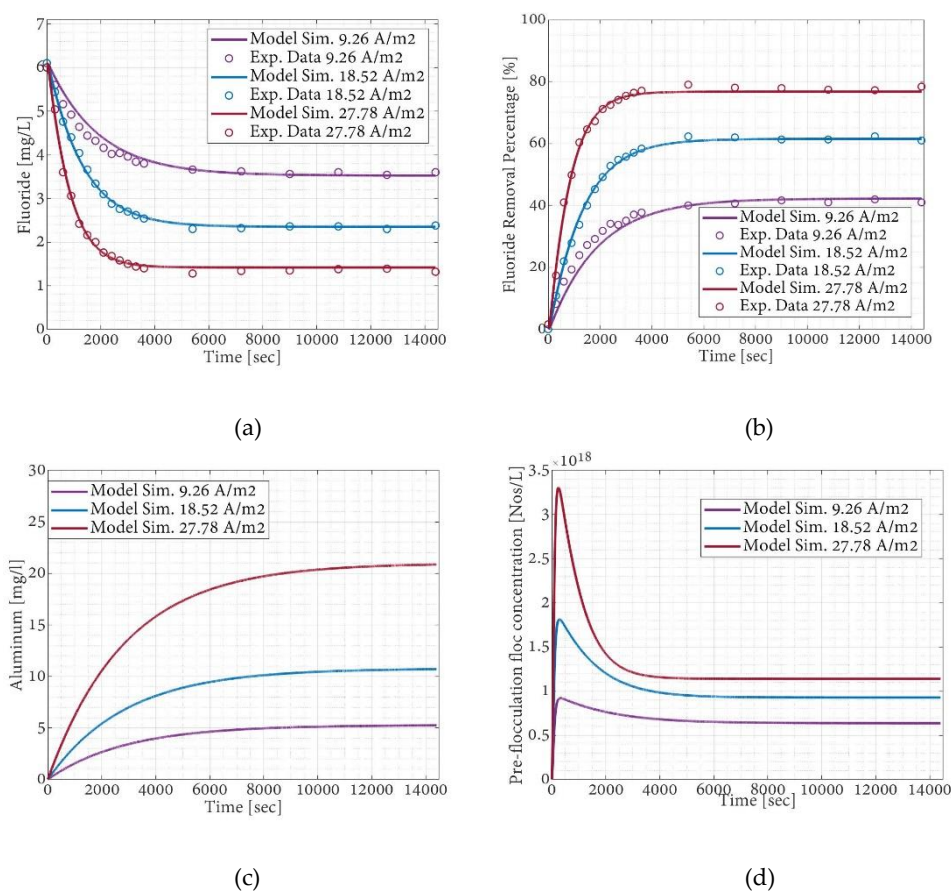


Figure 7-29: Continuous EC defluoridation reactor longer operational results (a) dissolved fluoride concentration (mg l^{-1}), (b) fluoride removal efficiency (%), (c) dissolved aluminium concentration (mg l^{-1}), and (d) pre-flocculation floc concentration (Nos l^{-1})

The scaled-down version of the reactor has been considered as the model in this comparison. It could be noted that Re , Fr , and We are approximately equal in prototype and the model making the dimensionless similarity ratio closer to 1. It is important to highlight the disparity of the current density noted between pairs O7, O12 and O9, O13. The energy consumption per unit volume was also compared, and the comparison of O9 and O13 shows a higher energy requirement for O13, which is the scaled-down version. When compared O9 and O13 data listed in Table (7.9), the power supply for both operations have been approximately equal, while the 1 hour operations have been able to lower the dissolved fluoride amounts by similar

amounts. However, the calculation has been done for the energy consumption per treated volume instead energy consumption per unit time. Hence, the scaled-down version O13 which has a lower a lower reactor volume and flow rate compared to O9, shows a higher energy requirement of 8640 kWh m^{-3} .

Next, the continuous EC defluoridation reactor experimental data were compared with the PBCM simulations for longer operational durations up to 6 hours. The resulting variations are illustrated in Figure (7.29). The model simulations are in good agreement with the experimental data of dissolved fluoride concentrations which become approximately constant after the hydraulic detention time.

7.11. Sensitivity analysis for optimization of the model

The optimization process was carried out using local sensitivity testing for 10 calibration parameters that resulted from the process-based conceptual model. Local sensitivity analysis allowed the variation of a single input parameter while the other parameters were kept constant at the identified optimum value during the calibration process. The variation of the RMSE value of the fluoride concentration data between model simulation and the experimental runs were compared for varied input values of each calibration parameter within the recommended range. The variation of RMSE against the log value of the calibration parameter was plotted to get a visible variation of the results of local sensitivity (Figure 7.30).

Local sensitivity analysis was performed using MATLAB® ver. R2021a and the results were then used to calculate p-value for the one-sample t-test. One-sample t-test examines whether the mean of a population is statistically different from a known or hypothesized value. In addition, the local sensitivity test results were then analysed using Microsoft® Excel® ver. 2016 regression analysis package. Here, the input calibration parameter log values were analysed against the resulting RMSE value in the MATLAB® based PBCM. These results are summarised in Table (7.10), along with

the ranking of the calibration parameters reached based on the local sensitivity test results. The detailed results of these analyses are given in appendix (D).

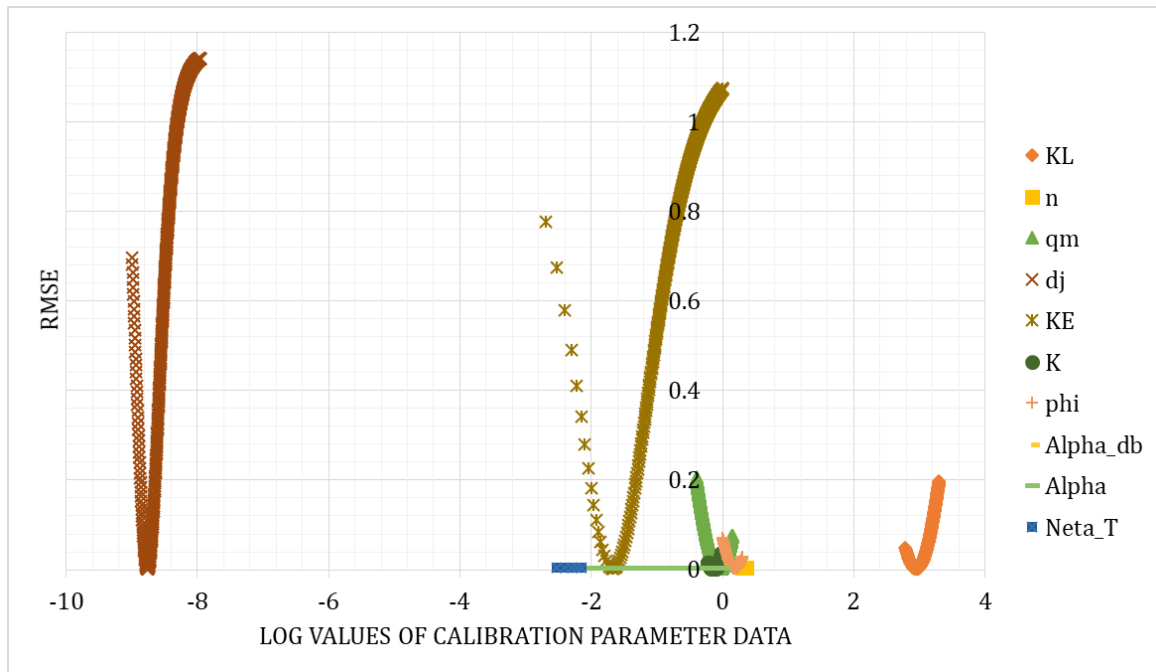


Figure 7-30: Local sensitivity results comparison of the calibration parameters and resulted RMSE value of the MATLAB® based PBCM

Microsoft® Excel® ver. 2016 based regression analysis of the input calibration parameter log values and RMSE values produced residual vs. log value of calibration parameter value graphs, which further explains the sensitivity of the model to each calibration parameter variation. These plots are summarised in Figures (7.31 and 7.32).

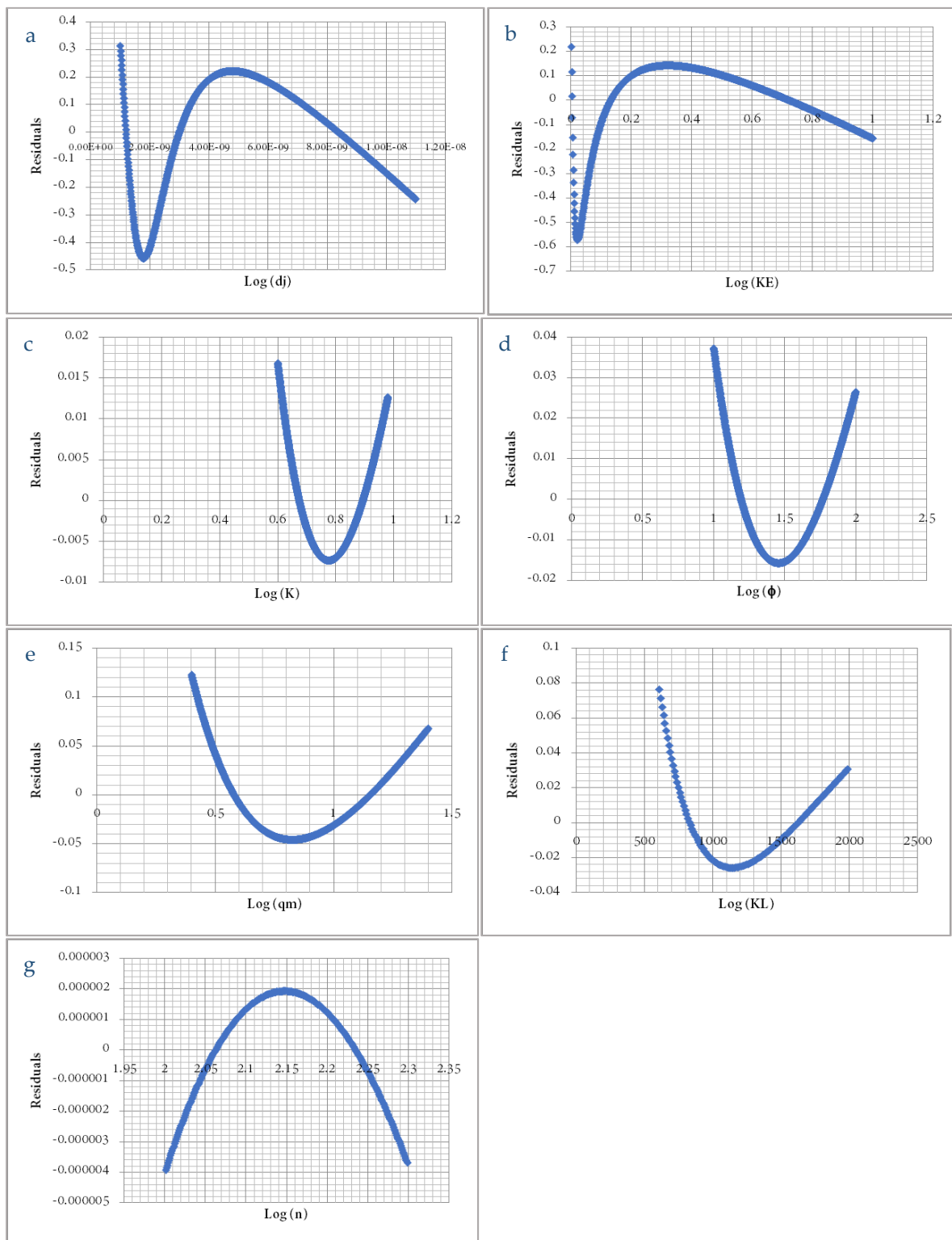


Figure 7-31: Residual plots of calibration parameters (a) d_j , (b) K_E , (c) K , (d) ϕ , (e) q_m , (f) K_L , (g) n

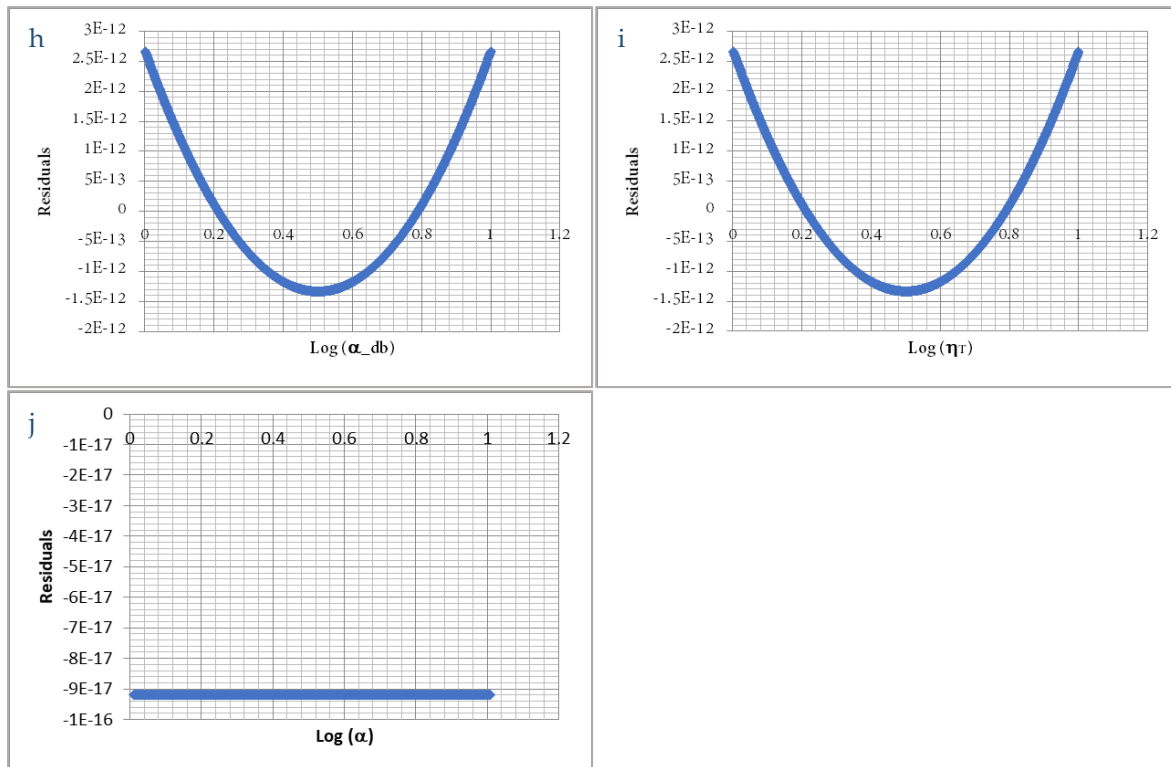


Figure 7-32: Residual plots of calibration parameters (h) α_{db} , (i) η_T , (j) α

Overall comparison of results between the calibration parameters and the resulting RMSE value from the MATLAB® model achieved from the local sensitivity test are illustrated in Figure 7.30. For the local sensitivity analysis, the d_j ; colloid size which participates in the adsorption and flocculation process was found to be among the most sensitive parameters for the PBCM, which is also noticeable from Figure (7.30). The three parameters, α_{db} , η_T and α were found to be the least sensitive, hence ranked 8th, 9th and 10th respectively. Here, α_{db} and η_T are related to the flotation process sub-model and despite the least sensitivity resulted for the fluoride concentration variation, these parameters expressed sensitivity for the floated flocs accumulation variation with a p-value of 2.09E-303. However, the calibration parameter α , which is the collision efficiency for macro-flocculation resulted in zero sensitivity for both fluoride variation and floated flocs accumulation variation with a p-value of zero.

Table 7-11: Summary of sensitivity analysis on the calibration parameters

No	Calibration Parameter	Local Sensitivity			Ranking based on sensitivity (1 = Highest sensitivity)
		Multiple R	Standard Error	P Value of one sample t-test	
1	d_j ; colloid size which participates in adsorption and flocculation process (m)	8.37E-01	1.89E-01	0.00E+00	1
2	KE; the correction factor denoted adsorption of dissolved fluoride on electrodes	7.97E-01	1.47E-01	0.00E+00	2
3	K; a percentage denoted hydrolysis efficiency	7.48E-01	6.58E-03	3.22E-204	3
4	ϕ ; a correction factor, denoted current efficiency or faradic yield	5.49E-01	1.42E-02	3.20E-167	4
5	q_m ; the maximum adsorption capacity (mg g^{-1})	4.66E-01	4.16E-02	7.30E-145	5
6	K_L ; the Langmuir constant (L mol^{-1})	9.24E-01	2.36E-02	9.50E-27	6
7	n ; Al:OH ratio in one ring structure of sweep floc	1.00E+00	1.73E-06	0.00E+00	7
8	α_{db} is collision coefficient between an air bubble and floc	1.00E+00	1.20E-12	0.00E+00	8
9	η_T is collision frequency between the air bubble and floc	1.00E+00	1.20E-12	0.00E+00	9
10	α is collision efficiency for macro-flocculation	1.00E+00	0.00E+00	0.00E+00	10

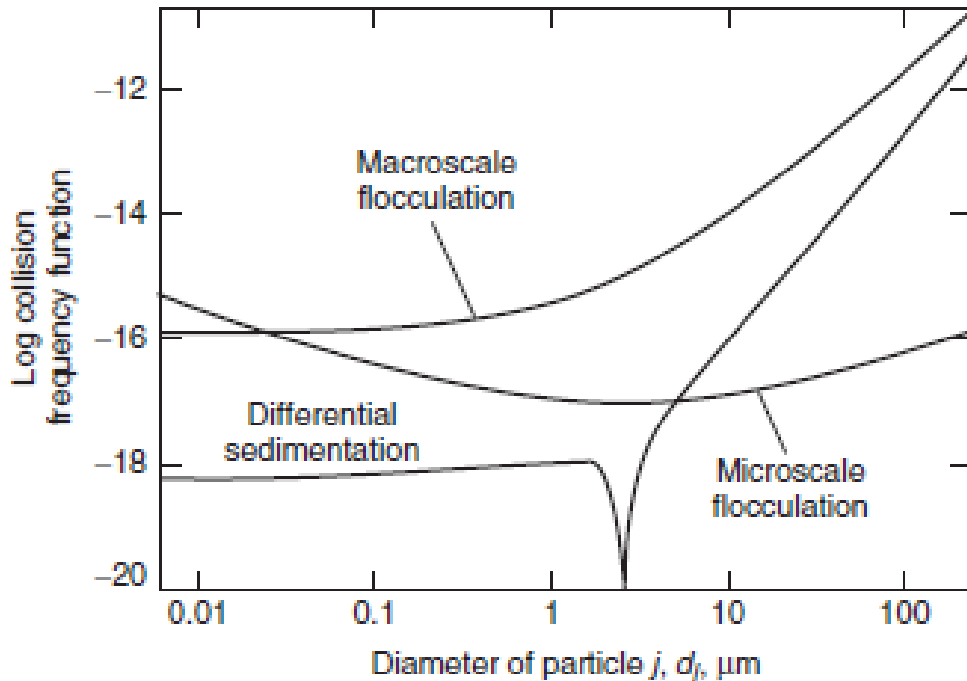


Figure 7-33: Collision frequency functions for macroscale (orthokinetic) flocculation, microscale (perikinetic) flocculation, and differential settling (MWH Americas, Crittenden Communications et al. 2012)

The collision frequency function diagram (Figure 7.33) illustrates the dominance of each flocculation mechanism for a range of particle diameters. This diagram explains the behaviour of a system containing particles d_i of size $2.0\mu\text{m}$, with particles with sizes from 0.01 to $50\mu\text{m}$. In addition, here the G value has been considered as 100s^{-1} , the water temperature of 15°C , and the density of particles as of 1.1 g cm^{-3} . According to this diagram, the main flocculation mechanism for particles with a size less than $0.1\mu\text{m}$ is microscale mixing. Macroscale mixing becomes dominant for the size range of 0.1 to $30\mu\text{m}$. In contrast to this, Wang (1991) suggested that the kinetic model for monodispersed suspension operating in the laminar region considers the hydrodynamic or van der Waals forces as insignificant, which means microscale (perikinetic) flocculation is not considered in continuous flow reactors. However, the PBCM designed for defluoridation using EC reactors in the current study was designed using both macroscale (orthokinetic) flocculation and microscale

(perikinetic) flocculation models. The particle diameter resulting from the calibration process was $0.0017\mu\text{m}$, and α , the collision efficiency for macroscale (perikinetic) flocculation resulted as the least sensitive calibration parameter for this defluoridation operation with a p-value equal to zero at the local sensitivity analysis. This result agrees with the collision frequency function (Figure 7.33) which suggests that the main flocculation mechanism for particles with a size less than $0.1\mu\text{m}$ is microscale mixing. It is important to highlight that α , the collision efficiency for macroscale (perikinetic) flocculation could be of significance for floated flocs accumulation in other suitable operational conditions where particle size ranges between 0.1 to $30\mu\text{m}$. Hence it is essential, α to be considered as a calibration parameter for future operations, irrespective of the insignificance resulting from this study.

7.12. *Process-based conceptual model validation – secondary data*

In this section, the PBCM for continuous EC defluoridation was evaluated using the literature data of Emamjomeh, Sivakumar et al. (2011). The relevant calibration parameters employed in this evaluation process are listed in Table (7-11). The model simulation and experimental defluoridation efficiency percentages are in good agreement with an R^2 value of 0.9453, as illustrated in Figure (7.34).

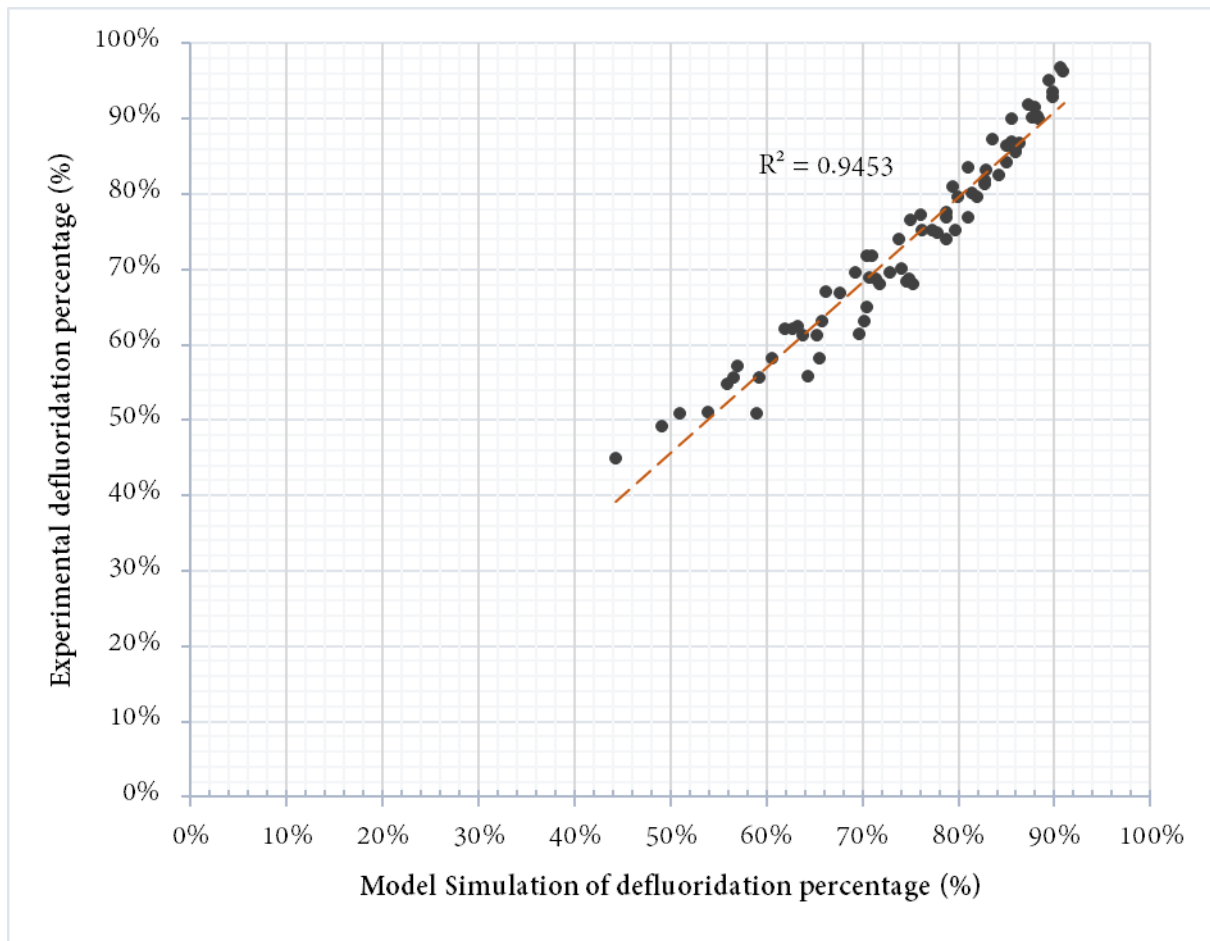


Figure 7-34: PBCM for continuous EC defluoridation efficiency simulation and experimental defluoridation efficiency comparison for Emamjomeh, Sivakumar et al. (2011) data

Table 7-12: Calibration parameters employed for PBCM for continuous EC defluoridation efficiency simulation and experimental defluoridation efficiency comparison for Emamjomeh, Sivakumar et al. (2011) data

I/A (A m ⁻²)	n	q_m	d_j	K_E	α_{db}	η_T	α	K_L	K	Ø
12.50	2.2	1.30	1.7E-09	0.02	0.205	0.205	1	1035	0.775	1.65
18.75	2.2	1.30	1.7E-09	0.02	0.205	0.205	1	1035	0.775	1.31
25.00	2.2	1.30	1.7E-09	0.02	0.205	0.205	1	1035	0.775	1.14
31.25	2.2	1.30	1.7E-09	0.02	0.205	0.205	1	1035	0.775	1.03

The model simulations were carried out for a total of 72 experimental runs, conducted using four different current densities (12.50 A m^{-2} , 18.75 A m^{-2} , 25.00 A m^{-2} , & 31.25 A m^{-2}), six different feed flow rates (0.15 L/min , 0.20 L/min , 0.25 L/min , 0.30 L/min , 0.35 L/min , & 0.40 L/min), and three different initial fluoride levels (10 mg l^{-1} , 15 mg l^{-1} , & 25 mg l^{-1}). The adaptability of the model to analyse EC reactors with dynamic operating parameters, with the least effort and cost involvement, is well demonstrated by this evaluation. It could be noted that N_f , D_p and K values are not changed from the model simulations conducted with primary data. The Langmuir constants (q_m , K_L) and current efficiency (\emptyset) were the parameters adjusted in the calibration process of the model for the secondary data. Also, it's important to note that the sludge quantity data from the EC reactor were not available, hence the flotation model related calibration parameters, (α_{db}) and (η_T) values have not been adjusted. It is also interesting to note that, once the (q_m) and (K_L) were adjusted for one set of experimental conditions of the given EC reactor, they remained unchanged for the rest of the model calibrations. Although alterations made to the current density demanded adjustments to the current efficiency factor (\emptyset), the other two variations made in the operational conditions (feed flow rate & initial fluoride concentration) did not involve alterations to any of the calibration parameters.

Another important observation is the linear relationship between the current efficiency factor (\emptyset) and current density. This was evident at both batch and continuous operations at lab and pilot scales. The comparison of the current efficiency factor (\emptyset) against current density for both primary and secondary data considered in this study is given in Figure (7.35). This is a useful finding, which could help minimize the experimental runs during the PBCM model calibration and optimization process.

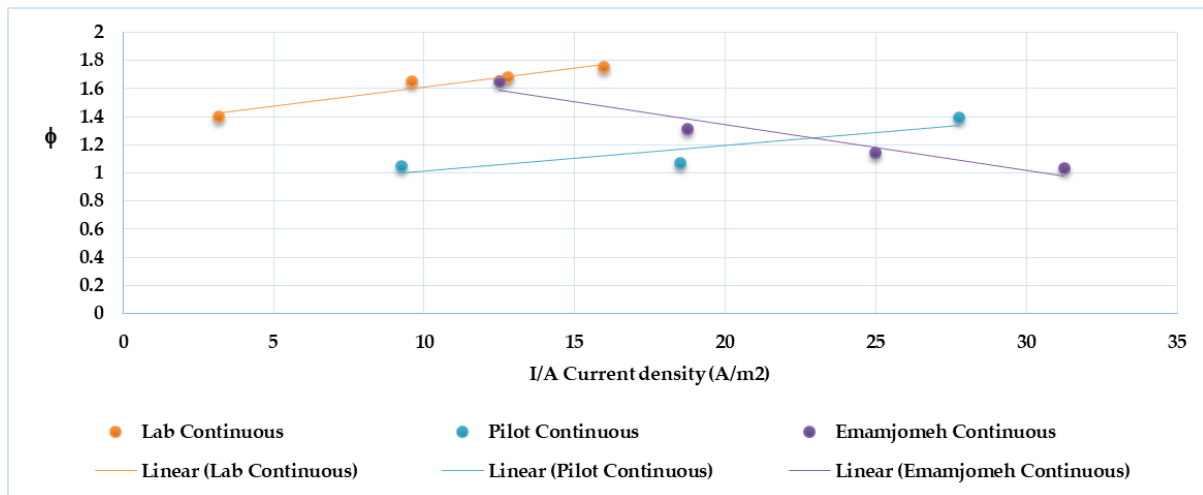


Figure 7-35: Comparison of current efficiency factor (ϕ) against current density for both primary and secondary data considered in this study

7.13. Chapter 7 conclusion

In this chapter, the experimental data collected from the continuous EC reactor operated at the Industrial Chemistry Lab of Liverpool John Moores University, UK, were analysed and discussed aiming to calibrate and validate the PBCM for continuous EC defluoridation reactors. Then, for further validation of the model, secondary data extracted from the literature were used, which resulted in promising results on the adaptability of the PBCM in different experimental conditions. The discussions were sequenced according to the sub-processes identified in the PBCM, namely electrolysis, hydrolysis, coagulation, flocculation, and flotation. The goodness of fit analysis of the model yielded good results. From this chapter, the extended use of the model could be well evaluated in terms of application to scale-up/down, longer operation time, different pollutants, etc., which was the base for the content in chapter 8. Chapter 8, includes the contextualisation of the established knowledge base on the systematic EC reactor design framework resulting from this valuable research study.

Chapter 8. Conclusions and further recommendations

8.1. *Overview of the study*

Electrocoagulation (EC) is an emerging water and wastewater treatment technology that possesses the potential to be promoted as a sustainable technology for a variety of industries given that the operational optimization issues could be suitably addressed. The conventional EC design approach follows a black-box design approach, while white-box modelling is widely applied in other water treatment systems, with learning, design and process optimisation as the main applications. Hence, to address this gap in EC design and modelling aspects, this study aimed to develop a novel process-based conceptual model (PBCM) consisting of theoretical and empirical approaches to address the design and modelling issues such as scale-up, the effect of physical, chemical, and hydrodynamic parameters on the efficiency of electrocoagulation reactors in water and industrial wastewater treatment.

The objectives are listed below.

Objective 1: Critically evaluate the internal processes, industrial applications and existing knowledge on numerical and conceptual-based models to address design and performance optimization issues of EC units.

Objective 2: Design and validate an integrated PBCM for EC reactors using the process-based kinetics associated with EC operation.

Objective 3: Assess experimentally, the PBCM to address the existing design and modelling issues of EC reactors for varied operating conditions such as different inlet pollutant concentrations, varied sludge removal conditions, supply current variations and different inter-electrode distances.

Objective 4: Assess the PBCM at pilot scale to derive a systematic approach of EC reactors' design and scale-up.

Objective 5: Establish a methodology/model which can simultaneously address the prediction of pollution removal, settling/flotation, scale-up and techno-economic optimization.

Objective one was achieved through a critical evaluation of the literature by understanding the scientific and mechanistic approaches developed over the years for electrocoagulation modelling. The second objective was achieved by designing a process-based conceptual model (PBCM) for batch and continuous electrocoagulation reactors for defluoridation. Here, the EC process was conceptualized as a conventional water treatment process. This engineering approach helped identify the pollutant abatement and floc aggregation mechanisms, which resulted in the discretisation of the defluoridation process in the EC reactor. The next step was the numerical transformation of the model equations into a system of integrated rate equations. These process models were interconnected based on the principle of conservation of mass. The batch and continuous conceptual models were then implemented in two computer platforms namely, Microsoft® Excel® ver. 2016 and MATLAB® ver. R2021a. Retrieving primary data using a laboratory-scale batch EC reactor, experiments were carried out at the National Institute of Fundamental Studies, Sri Lanka, for initial model calibrations and validations.

To achieve the third and fourth objectives, a laboratory-scale continuous electrocoagulation reactor was designed & built at the Industrial Chemistry Laboratory of Liverpool John Moores University, United Kingdom. The experiments were conducted at two geometric scales. The extrapolation of the PBCM for varied operating conditions and scales was evaluated. Additionally, the optimization of retention time and the relationship of hydrodynamic parameters were analysed using the novel model.

Finally, the fifth objective was achieved by designing a PBCM for defluoridation using EC technology, incorporating the effect of physical, chemical, and hydrodynamic parameters. The proposed PBCM complements the process knowledge in EC pollutant abatement, hence allows the designers to have more control on operational parameters such as pollutant load, flow rate, supply current density, etc. By modifying a few model parameters, a calibrated PBCM could be obtained which then could easily be optimised for the required influent load. In addition to estimation of effluent pollutant concentration, the optimised white-box PBCM could be employed for the assessment of intermediate process variations and sludge load analysis. Microsoft® Excel® ver. 2016 and MATLAB® ver. R2021a were used as numerical computing platforms for the PBCM design tool with an in-built calibration mechanism that follows the local sensitivity analysis. This model could also be implemented on existing EC water treatment reactors to fine-tune the process variables to reach economical operating conditions.

8.2. Outcome – Proposed systematic approach for EC reactors design and scale-up

The conceptual process-based model (PBCM) proposed for defluoridation using EC in this study is summarised in Figure 3.3 in the chapter 3. The step-by-step guide for the discrete-continuous conversion scheme of the PBCM for both batch and continuous reactors which have been explained in chapters 4 and 6 are illustrated in Figures 4.3 and 6.3 respectively. The continuous scheme was then analysed using Microsoft® Excel® ver. 2016 and MATLAB® ver. R2021a (appendix B).

The PBCM for defluoridation using EC, resulted in ten calibration parameters, out of which, seven remained unchanged for a selected pollutant type, in both laboratory and pilot scales. However, three of the calibration parameters (ϕ , α_{ab} , and η_T) were varying along with the supply current density, exhibiting a linear relationship at both laboratory and operational scales (Figure 7.35). Accordingly, the PBCM for

defluoridation using EC proposed in this study has shown promising results allowing more controllability of process variables, while increasing the predictability of EC reactor operations. In addition to this, the overall operational advantages and limitations of the proposed PBCM for defluoridation using EC are listed in Tables 9.1 and 9.2 presented in chapter 9. The conventional EC reactor design process consisted generally of the below three steps.

1. Laboratory level reactor operation and optimization using statistical or empirical methods.
2. Scale-up for the required operational requirements using the electrode area to reactor volume ratio (A/V).
3. Optimization of the operational scale reactor through experimental runs to match the performance achieved at the laboratory scale.

The proposed EC design methodology of this study is explained below.

1. Laboratory level reactor experiments (minimum 3 tests with pollutant removal efficiency $> 50\%$) PBCM optimization operations USING MS Excel or MATLAB, and determining the values for the 10 calibration parameters listed in Table 8.1.

The MATLAB® programmes of the process-based conceptual models for electrocoagulation batch and continuous reactors are given in the appendix A and B respectively.

2. Scale-up for the required operational requirements using Re to calculate the cross-sectional dimensions (should be a laminar flow) and the electrode area to reactor volume ratio (A/V) to calculate the electrode size and reactor volume.
3. Operational level reactor experiments (minimum 3 tests with pollutant removal efficiency $> 50\%$) for different supply current density values to determine ϕ , α_{db} , and η_T suitable to be used in the PBCM optimization operations at operational scale.

4. Evaluate the optimum reactor operating conditions at the operational level using the PBCM operations USING Microsoft® Excel® or MATLAB® or a similar numerical computer platform.

Table 8-1: Calibration parameter sensitivity to experimental parameters (I/A: Current density, Co: Initial pollutant concentration, Q: Flow rate)

Calibration Parameter	Lab-scale			Operational or Pilot-scale		
	Parameter determining method	Response to I/A	Response to Co, Q	Parameter determining method	Response to I/A	Response to Co, Q
q_m ; the maximum adsorption capacity (mg g^{-1})	Calibrated value at the lab-scale	Constant	Constant	Same as lab scale	Constant	Constant
K_L ; the Langmuir constant (L/mol)	Calibrated value at the lab-scale	Constant	Constant	Same as lab scale	Constant	Constant
K ; a percentage denoted hydrolysis efficiency	Calibrated value at the lab-scale	Constant	Constant	Same as lab scale	Constant	Constant
d_j ; colloid size which participates in adsorption and flocculation process (m)	Calibrated value at the lab-scale	Constant	Constant	Same as lab scale	Constant	Constant
K_E ; the correction factor denoted adsorption of dissolved fluoride on electrodes	Calibrated value at the lab-scale	Constant	Constant	Same as lab scale	Constant	Constant
ϕ ; a correction factor denoted current efficiency or faradic yield	Calibrated value at the lab-scale	Varies	Constant	Re-calculate	Varies	Constant
n ; Al:OH ratio in one ring structure of sweep floc	Calibrated value at the lab-scale	Constant	Constant	Same as lab scale	Constant	Constant
α is collision efficiency for macro-flocculation	Calibrated value at the lab-scale	Constant	Constant	Same as lab scale	Constant	Constant
α_{ab} is collision coefficient between an air bubble and floc	Calibrated value at the lab-scale	Varies	Constant	Re-calculate	Varies	Constant
η_T is collision frequency between the air bubble and floc,	Calibrated value at the lab-scale	Varies	Constant	Re-calculate	Varies	Constant

8.3. *Significance of the outcome*

Although the conventional EC reactor design method is effective at the laboratory scale, the transfer of optimum operational parameters to the larger scales has been problematic to date. Experiment-based process optimization is expensive and time-consuming. On the other hand, in the conventional EC design method, the results are substantially dependent on the employed design of experiments, hence it does not guarantee the optimum operational conditions. The proposed PBCM for electrocoagulation reactor design in this study eliminates the cost and time factor of scale-up experiments to a greater extent and guarantees better optimization possibilities at the operational scale. Most importantly the proposed model transforms the data obtained from experiments and model simulations into quantitative and qualitative knowledge, which helps in decision-making processes. This significantly bridges the gap between laboratory and operational-scale applications of EC.

In addition, at the operational scales, process optimisation is often needed when new operational demands are enforced on existing EC plants. Furthermore, substantial changes in the pollutant loadings could occur, or pollutant removal deficiencies could be identified during the operational period of the EC plant. In this context, the proposed PBCM in EC could be useful to achieve process optimisation operations in a short period. Additionally, the design issues, such as electrode size, type and arrangement, economic analysis (energy cost and reactor volume trade-offs), or evaluation of a pre or post-treatment step shall be easily evaluated using the PBCM. The operational advantages and limitations of the proposed model are listed in Tables 9.1 and 9.2.

Table 8-2: Operational advantages of the proposed model

Advantages of the proposed model
1. Provides more controllability of process variables in EC operations.
2. Provides a thorough understanding of the internal process variations in EC operations.
3. Eliminates the cost and time factor of scale-up experiments to a greater extent, and guarantees better optimization possibility at the operational scale.
4. With zero experimental runs (Offline process optimisation) the simulations shall produce a specific range of values for optimum operational conditions by using the boundary conditions of the calibration parameters.
5. Effective transfer of optimum operational parameters conditions across varied reactor scales.
6. Transforms the data obtained from experiments and model simulations into quantitative and qualitative knowledge, which helps in decision-making processes.
7. Process predictability with dynamic operation conditions.
8. Predictability of the sludge loadings and variations with time.
9. Provides a platform for techno-economic analysis of EC reactors.
10. Usage of the model across different flow rates, assuring the laminar flow inside the reactor.

Table 8-3: Operational limitations of the proposed model

Limitations of the proposed model
1. Requires a numeric computer platform to operate.
2. Requires a good understanding of the pollutant abatement process of the selected pollutant using EC.
3. Requires some experimental runs to be conducted (Online process optimisation) along with the simulations to reach an exact solution for optimum operating conditions.
4. Uncertainty of applicability of the model for turbulent flow conditions inside the reactor.

8.4. *Contribution to knowledge*

The important findings resulted from this study are,

1. The process-based conceptual **modelling technique** that could be successfully implemented across different EC reactor types and varied pollutant conditions.
2. The **novel numeric computing platform model** established on pollutant abatement mechanisms to assist economic optimization and scale-up in EC. This model was tested for defluoridation using EC reactors with parallel plates in non-dynamic conditions, by evaluating the process optimisation, sludge predictions, scale-up operations, and internal process behaviour variations. The model could also be tested for dynamic conditions. The proposed PBCM usage could be extended for different other pollutants that are removed through the same adsorption mechanism, and for different EC reactor or electrode arrangements by incorporating a few changes to the numerical model.
3. Real-time **flocs behaviour** evaluation that results from the integrated sub-process models shall be useful in decision making of process modifications such as external mixing, external chemical additions that could be incorporated into the existing EC reactor for improved operational conditions.
4. Identification of **ten calibration parameters** that are physical and chemical parameters paramount in EC reactor design, along with possible relationships that could be derived between the aforementioned physical, chemical parameters and operational conditions.

8.5. *Research limitations of this study*

Limitations of this study were,

1. Laminar flow conditions in the reactor should be guaranteed to apply the proposed PBCM.

2. The derivation of the possible links between the calibration parameters and hydrodynamic parameters such as Re , We , Sh , Sc were not fully established which require more experimental data.
3. Accurate measurement of dissolved aluminium in the system could be used as an additional calibration parameter during the calibration process.
4. Global sensitivity of the calibration parameters was not evaluated due to the complex nature of the combined effect of the calibration parameters.
5. The application of this model to real water was not tested during this study.
6. The model applicability is valid for a limited pH range.
7. The spatial variation of the pollutant concentration cannot be predicted from the proposed PBCM.
8. The applicability of the PBCM to different other pollutants was not tested.
9. Applicable for batch and continuous reactors with complete mixed flow regimes.

8.6. *Impact from the research*

The significance of the contribution from this research is a novel numeric computing platform model established on pollutant abatement mechanisms to assist economic optimization and scale-up in EC. Rather than using a generic statistical modelling approach this model has been able to aid the understanding of the significance of the internal sub-process hence allowing the designers to have more control over the operational variables. This could significantly impact the industrial wastewater treatment process by widening the designers' ability to optimize and scale up the treatment process economically. This would be an added advantage to promote EC systems since it has the option of automation which permits systems to be remotely handled.

In addition, the study was conducted as a sub-project of the National Research Council of Sri Lanka (NRCSL) funded project (Ref. No: TO-NRC-16-015) conducted in parallel in Sri Lanka titled "Development of a model treatment facility for remediation of total

dissolved solids and fluoride in groundwater – a sustainable solution for dry zone drinking water problems”. Integrating an electrocoagulation reactor for the proposed treatment system was considered for this project. This demanded further research to address the key operational challenge of high residual aluminium amounts in treated water that limited the EC application in Sri Lanka. The novel model developed by this study shall be used to optimise residual aluminium removal with carefully designed experimental runs that incorporate changes of flocculation and flotation methods (use of external mixing, bubble generation, etc.). Addressing this issue would significantly widen the application of EC for drinking water treatment especially in developing countries where low-cost sustainable treatment methods are in high demand.

8.7. Recommendations for further studies

Recommendations for further studies are discussed under two aspects, the potential for PBCM advancement relating to the depth of knowledge and scope of application. A firmer scientific EC reactor design framework has been proposed through this study. The potential of PBCM advancement relating to the depth of knowledge is,

1. Accurate measurement of dissolved aluminium in the system could be used as an additional calibration parameter during the calibration process.
2. Global sensitivity of the calibration parameters was not evaluated due to the complex nature of the combined effect of the calibration parameters.
3. The derivation of the possible links between the calibration parameters and hydrodynamic parameters such as Re , We Sh , Sc using an adequate amount of experimental data to improve the dimensional consistency between small and large-scale processes.
4. Experimenting with the PBCM simulations for real water sources with high fluoride levels with dynamic/ non-dynamic operating conditions.
5. Investigation at defined pH values to refine the operable pH ranges in EC for defluoridation.

6. Residual aluminium removal optimization shall be evaluated using the proposed PBCM and carefully designed experimental runs that incorporate changes of flocculation and flotation methods. Addressing this issue would significantly widen the application of EC for drinking water treatment.

The potential of PBCM advancement relating to the scope of application are,

1. Experimenting with the applicability of the proposed PBCM to different other pollutants with/without amendments to the model using a similar experimental methodology to that followed in this study.
Abatement of pollutants that follows the same removal pathway (adsorption) in EC would require no/minimal amendments to the proposed PBCM. Arsenic (V), boron, nonylphenol ethoxylates, COD, total organic carbon (TOC) in Baker's yeast wastewater and COD in Laundry wastewater are a few examples. The body of knowledge developed in this study shall lead to the study of possible modelling approaches for the removal of pollutants that follow other removal pathways listed below apart from the pathway used in the proposed PBCM which is adsorption on precipitates and electrodes.
 - i. Precipitation
 - ii. Co-precipitation
 - iii. Electro-oxidation or electro reduction
 - iv. Physical enmeshment
 - v. Bulk chemical reaction
2. Evaluation of the spatial variation of the pollutant concentration within the EC reactor using the proposed PBCM.
3. Evaluation of the PBCM with amendments for plug-flow conditions.
4. Investigation at defined pH values to refine the operable pH range relationship in EC for different pollutant types.

REFERENCES

- Akinmolayan, F. (2017). Mathematical Modelling of Clean Water Treatment Works, UCL (University College London).
- Aleboye, A., N. Daneshvar and M. B. Kasiri (2008). "Optimization of C.I. Acid Red 14 azo dye removal by electrocoagulation batch process with response surface methodology." Chemical Engineering and Processing: Process Intensification **47**(5): 827-832.
- Almazán-Ruiz, F. J., F. V. Caballero, M. R. Cruz-Díaz, E. P. Rivero and I. González (2012). "Scale-up of rotating cylinder electrode electrochemical reactor for Cu(II) recovery: Experimental and simulation study in turbulence regimen." Electrochimica Acta **77**: 262-271.
- An, C., G. Huang, Y. Yao and S. Zhao (2017). "Emerging usage of electrocoagulation technology for oil removal from wastewater: A review." Science of The Total Environment **579**: 537-556.
- Andreas, O. (2014). "The Dim-DoE framework for Scale-Up in Chemical Engineering."
- Ayres, R. U. W., B. (2003). Two Paradigms of Production and Growth. Fontainebleau, Center for the Management of Environmental Resources (CMER), INSEAD.
- Bennajah, M., B. Gourich, A. H. Essadki, C. Vial and H. Delmas (2009). "Defluoridation of Morocco drinking water by electrocoagulation/electroflotation in an electrochemical external-loop airlift reactor." Chemical Engineering Journal **148**(1): 122-131.
- Bonilla, C. F. (1947). "Possibilities of the electronic coagulator for water treatment." Water Sewage **85**: 21, 22, 44, 45.
- Bratby, J. (2006). Coagulation and Flocculation in Water and Wastewater Treatment. London, UNITED KINGDOM, IWA Publishing.
- Chavalparit, O. and M. Ongwandee (2009). "Optimizing electrocoagulation process for the treatment of biodiesel wastewater using response surface methodology." Journal of Environmental Sciences **21**(11): 1491-1496.

- Chellam, S. and M. R. Wiesner (1993). "Fluid mechanics and fractal aggregates." Water Research **27**(9): 1493-1496.
- Chen, G. (2004). "Electrochemical technologies in wastewater treatment." Separation and Purification Technology **38**(1): 11-41.
- Choudhary, A. and S. Mathur (2017). "Performance evaluation of 3D rotating anode in electro coagulation reactor: Part I: Effect of impeller." Journal of Water Process Engineering **19**: 322-330.
- Coker, A. K. (2007). 6 - MECHANICAL SEPARATIONS. Ludwig's Applied Process Design for Chemical and Petrochemical Plants (Fourth Edition). A. K. Coker. Burlington, Gulf Professional Publishing: 371-443.
- Crittenden, J. C., R. R. Trussell, D. W. Hand, K. J. Howe, G. Tchobanoglous and G. Tchobanoglous (2012). MWH's Water Treatment : Principles and Design. Somerset, Somerset: Wiley.
- Deghles, A. and U. Kurt (2017). "Hydrogen Gas Production from Tannery Wastewater by Electrocoagulation of a Continuous Mode with Simultaneous Pollutants Removal." IOSR Journal of Applied Chemistry (IOSR-IAC) **10**(3): 40-50.
- Duan, Y. and F. Shi (2014). Chapter 2 - Bioreactor design for algal growth as a sustainable energy source. Reactor and Process Design in Sustainable Energy Technology. F. Shi. Amsterdam, Elsevier: 27-60.
- Emamjomeh, M. M. and M. Sivakumar (2009). "Review of pollutants removed by electrocoagulation and electrocoagulation/flotation processes." Journal of Environmental Management **90**(5): 1663-1679.
- Emamjomeh, M. M., M. Sivakumar and A. S. Varyani (2011). "Analysis and the understanding of fluoride removal mechanisms by an electrocoagulation/flotation (ECF) process." Desalination **275**(1-3): 102-106.
- Essadki, A. H., B. Gourich, M. Azzi, C. Vial and H. Delmas (2010). "Kinetic study of defluoridation of drinking water by electrocoagulation/electroflotation in a stirred tank reactor and in an external-loop airlift reactor." Chemical Engineering Journal **164**(1): 106-114.

Essadki, A. H., B. Gourich, C. Vial, H. Delmas and M. Bennajah (2009). "Defluoridation of drinking water by electrocoagulation/electroflotation in a stirred tank reactor with a comparative performance to an external-loop airlift reactor." Journal of Hazardous Materials **168**(2–3): 1325-1333.

Garcia-Lara, A. M., C. Montero-Ocampo, F. Equihua-Guillen, J. E. Camporredondo-Saucedo, R. Servin-Castaneda and C. R. Muniz-Valdes (2014). "Arsenic Removal from Natural Groundwater by Electrocoagulation Using Response Surface Methodology." JOURNAL OF CHEMISTRY.

Genawi, N. M., M. H. Ibrahim, M. H. El-Naas and A. E. Alshaik (2020). "Chromium Removal from Tannery Wastewater by Electrocoagulation: Optimization and Sludge Characterization." Water **12**(5): 1374.

Ghosh, D., C. R. Medhi and M. K. Purkait (2008). "Treatment of fluoride containing drinking water by electrocoagulation using monopolar and bipolar electrode connections." Chemosphere **73**(9): 1393-1400.

Goodridge, F. (1985). "Electrochemical cell design : Edited by R. E. White Plenum Press, New York, 1984, 398 pp., \$65.00." Electrochimica Acta **30**(11): 1577-1578.

Graça, N. S., A. M. Ribeiro and A. E. Rodrigues (2019). "Removal of Fluoride from Water by a Continuous Electrocoagulation Process." Industrial & Engineering Chemistry Research **58**(13): 5314-5321.

Güçlü, D. (2015). "Optimization of electrocoagulation of pistachio processing wastewaters using the response surface methodology." Desalination and Water Treatment **54**(12): 3338-3347.

Guzmán, A., J. L. Nava, O. Coreño, I. Rodríguez and S. Gutiérrez (2016). "Arsenic and fluoride removal from groundwater by electrocoagulation using a continuous filter-press reactor." Chemosphere **144**: 2113-2120.

Haarhoff, J. and J. K. Edzwald (2004). "Dissolved air flotation modelling: insights and shortcomings." Journal of Water Supply: Research and Technology-Aqua **53**(3): 127-150.

- Hakizimana, J. N., B. Gourich, M. Chafi, Y. Stiriba, C. Vial, P. Drogui and J. Naja (2017). "Electrocoagulation process in water treatment: A review of electrocoagulation modeling approaches." Desalination **404**: 1-21.
- Hansen, H. K., P. Nuñez, D. Raboy, I. Schippacasse and R. Grandon (2007). "Electrocoagulation in wastewater containing arsenic: Comparing different process designs." Electrochimica Acta **52**(10): 3464-3470.
- Hashim, K. S., A. Shaw, R. Al Khaddar, M. O. Pedrola and D. Phipps (2017). "Energy efficient electrocoagulation using a new flow column reactor to remove nitrate from drinking water – Experimental, statistical, and economic approach." Journal of Environmental Management **196**: 224-233.
- Hem, J. D. and C. E. Roberson (1967). "Form and stability of aluminum hydroxide complexes in dilute solution." U.S. Geol. Survey Water-Supply Paper I827-A: 55
- Holt, P. K. (2003). "Electrocoagulation: unravelling and synthesising the mechanisms behind a water treatment process." PhD thesis, Faculty of Engineering, The University of Sydney.
- Holt, P. K., G. W. Barton and C. A. Mitchell (2005). "The future for electrocoagulation as a localised water treatment technology." Chemosphere **59**(3): 355-367.
- Hu, C.-Y., S.-L. Lo and W.-H. Kuan (2007). "Simulation the kinetics of fluoride removal by electrocoagulation (EC) process using aluminum electrodes." Journal of Hazardous Materials **145**(1–2): 180-185.
- Hu, C., J. Sun, S. Wang, R. Liu, H. Liu and J. Qu (2017). "Enhanced efficiency in HA removal by electrocoagulation through optimizing flocs properties: Role of current density and pH." Separation and Purification Technology **175**: 248-254.
- Isa, M. H., E. H. Ezechi, Z. Ahmed, S. F. Magram and S. R. M. Kutty (2014). "Boron removal by electrocoagulation and recovery." Water Research **51**: 113-123.
- Kabdaşlı, I., I. Arslan-Alaton, T. Ölmez-Hancı and O. Tünay (2012). "Electrocoagulation applications for industrial wastewaters: a critical review." Environmental Technology Reviews **1**(1): 2-45.

- Khayet, M., A. Y. Zahrim and N. Hilal (2011). "Modelling and optimization of coagulation of highly concentrated industrial grade leather dye by response surface methodology." Chemical Engineering Journal **167**(1): 77-83.
- Krupińska, I. (2020). "Aluminium Drinking Water Treatment Residuals and Their Toxic Impact on Human Health." Molecules (Basel, Switzerland) **25**(3): 641.
- Li, J. (2016). "Assessing spatial predictive models in the environmental sciences: Accuracy measures, data variation and variance explained." Environmental Modelling & Software **80**: 1-8.
- Lu, J., Z. Wang, X. Ma, Q. Tang and Y. Li (2017). "Modeling of the electrocoagulation process: A study on the mass transfer of electrolysis and hydrolysis products." Chemical Engineering Science **165**: 165-176.
- Makwana, A. R. and M. M. Ahammed (2016). "Continuous electrocoagulation process for the post-treatment of anaerobically treated municipal wastewater." Process Safety and Environmental Protection **102**: 724-733.
- Mameri, N., A. R. Yeddou, H. Lounici, D. Belhocine, H. Grib and B. Bariou (1998). "Defluoridation of septentrional Sahara water of north Africa by electrocoagulation process using bipolar aluminium electrodes." Water Research **32**(5): 1604-1612.
- Mauter, M. S., I. Zucker, F. Perreault, J. R. Werber, J.-H. Kim and M. Elimelech (2018). "The role of nanotechnology in tackling global water challenges." Nature Sustainability **1**(4): 166-175.
- Mbacké, M. K., C. Kane, N. O. Diallo, C. M. Diop, F. Chauvet, M. Comtat and T. Tzedakis (2016). "Electrocoagulation process applied on pollutants treatment-experimental optimization and fundamental investigation of the crystal violet dye removal." Journal of Environmental Chemical Engineering **4**(4, Part A): 4001-4011.
- Metcalf, L. and H. Eddy (2003). Wastewater engineering. McGraw-Hill Inc., New York, Metcalf & Eddy Inc.
- Muhammad Niza, N., N. Abdul Razak, M. S. Yusoff, M. A. A. Mohd Zainuri, M. I. Emmanuel, A. Mohamed Hussen Shadi, M. H. Mohd Hanif and M. A. Kamaruddin (2021). "Hydrodynamic study of bubble characteristics and bubble rise velocities in

batch electrocoagulation with vibration-induced electrode plates using the PIV technique." Separation and Purification Technology **258**: 118089.

Mulyadi, H., R. Amin and A. F. Kennaird (2001). Practical Approach to Determine Residual Gas Saturation and Gas-Water Relative Permeability.

MWH Americas, S., S. Crittenden Communications, R. R. Trussell, D. W. Hand, G. Tchobanoglous, K. J. Howe and J. C. Crittenden (2012). Principles of Water Treatment. Somerset, Somerset: John Wiley & Sons, Incorporated.

Ntambwe Kambuyi, T., B. Bejjany, B. Lekhlif, H. Mellouk, K. Digua and A. Dani (2021). "Design of a continuous-flow single-channel reactor using optimal experimental data from batch reactor for turbidity removal by electrocoagulation." Journal of Environmental Chemical Engineering **9**(1): 104651.

Powell-water. (2016). "Powell Water." Retrieved October, 2021, from <https://powellwater.com/electrocoagulation-vs-chemical-coagulation/>.

Proxa-water. (2021). "Proxa", from <https://www.proxawater.com/2017/03/08/chemical-industry-south-africa/>.

Rodrigo, C. J. C. S. P. C. M. A. (2016). "Optimization of a combined electrocoagulation-electroflotation reactor." Environ Sci Pollut Res **23**: 9700-9711.

Song, P., Z. Yang, H. Xu, J. Huang, X. Yang, F. Yue and L. Wang (2016). "Arsenic removal from contaminated drinking water by electrocoagulation using hybrid Fe–Al electrodes: response surface methodology and mechanism study." Desalination & Water Treatment **57**(10): 4548.

Strokach, P. P. (1975). "Electrochem." Ind. Process. Bio: 55, 375.

Sulaymon, A. H. a. A., A. H. (2012). "Scale-Up of Electrochemical Reactors."

Tezcan Un, U., A. S. Koparal and U. Bakir Ogutveren (2013). "Fluoride removal from water and wastewater with a batch cylindrical electrode using electrocoagulation." Chemical Engineering Journal **223**: 110-115.

Thakur, L. S. and P. Mondal (2016). "Techno-economic evaluation of simultaneous arsenic and fluoride removal from synthetic groundwater by electrocoagulation

process: optimization through response surface methodology." Desalination and Water Treatment **57**(59): 28847-28863.

Thomas, D. N., S. J. Judd and N. Fawcett (1999). "Flocculation modelling: a review." Water Research **33**(7): 1579-1592.

Tir, M. and N. Moulai-Mostefa (2008). "Optimization of oil removal from oily wastewater by electrocoagulation using response surface method." Journal of Hazardous Materials **158**(1): 107-115.

UN-Water (2021). Summary Progress Update 2021-SDG 6 - water and sanitation for all. Version. Geneva, Switzerland.

UN-Water (2021). UN-Water, 2020: Summary Progress Update 2021 - SDG 6 - water and sanitation for all. **Version 1**.

UnitedNations. (2019). "Sustainable Development Goals." Retrieved Jan 2020, 2020, from <https://www.un.org/sustainabledevelopment/water-and-sanitation/>.

Veerapaneni, S. and M. R. Wiesner (1996). "Hydrodynamics of Fractal Aggregates with Radially Varying Permeability." Journal of Colloid and Interface Science **177**(1): 45-57.

Wang, N. (1991). Modelling of flocculation kinetics in water treatment, Retrospective Thesis and Dissertations.

WHO, W. H. O. (2017). Guidelines for drinking-water quality fourth edition incorporating the first addendum.

. Geneva, Licence: CC BY-NC-SA 3.0 IGO.

Yehya, T., M. Chafi, W. Balla, C. Vial, A. Essadki and B. Gourich (2014). "Experimental analysis and modeling of denitrification using electrocoagulation process." Separation and Purification Technology **132**: 644-654.

Yoosefian, M., S. Ahmadzadeh, M. Aghasi and M. Dolatabadi (2017). "Optimization of electrocoagulation process for efficient removal of ciprofloxacin antibiotic using iron electrode; kinetic and isotherm studies of adsorption." Journal of Molecular Liquids **225**: 544-553.

Zhang, F., C. Yang, H. Zhu, Y. Li and W. Gui (2020). "An integrated prediction model of heavy metal ion concentration for iron electrocoagulation process." Chemical Engineering Journal **391**: 123628.

Zhao, S., G. Huang, G. Cheng, Y. Wang and H. Fu (2014). "Hardness, COD and turbidity removals from produced water by electrocoagulation pretreatment prior to Reverse Osmosis membranes." Desalination **344**: 454-462.

Zhu, J., H. Zhao and J. Ni (2007). "Fluoride distribution in electrocoagulation defluoridation process." Separation and Purification Technology **56**(2): 184-191.

Zlokarnik, M. (2001). "DIMENSIONAL ANALYSIS AND SCALE-UP IN THEORY AND INDUSTRIAL APPLICATION*." Journal of Liposome Research **11**(4): 269.

APPENDICES

(A) *MATLAB® electrocoagulation batch reactor process-based conceptual model*

```

%Aluminum dissolution
% V= Working volume of the reactor (L)
% k= Correction factor, denoted current efficiency or faradic yield
% I= Electric current (A)
% M= Atomic weight of the electrode material (mg/mol)
% Z= Number of electrons transferred (z=3 for Aluminium)
% F= Faraday's constant (C/mol)
% Al_gen= Generation of aluminium ions (mg/l)
% Al_dis= Dissipation of aluminium ions (mg/l)
% Al_in= Inflow of aluminium ions (mg/l)
% Al_out= Outflow of aluminium ions (mg/l)
% Al_acc= Accumulation of aluminium ions (mg/l)
% K= Percentage denoted hydrolysis efficiency
% dt= time step gap (s)
% Q = flow rate (L/s)
% Den_w = Density of liquid (kg/m3)
% g = Gravitational acceleration (m/s2)
% Vf= flow velocity (m/s)
% Dh = Hydraulic diameter
% G = Velocity Gradient (s-1)
% H = Wetted height (m)
% W = Reactor width (duct) (m)
% A = Cross sectional area of the reactor in the direction of the flow (m2)
% L = Length of the duct (length of the reactor, towards the flow direction (m)
% fD = Fritcion factor
% Re = Reynolds number
% hL = Head loss across the duct (m)
% t_Res = Resident time (s)
% VE = Electrode volume (m3)
% VB = Reactor bottom wedge volume (m3)
%E_t = Electrode thickness (m)
%E_h = Electrode height (m)
%E_w = Electrode width (m)
%E_n = Number of electrodes (Nos)

%KL1 = Langmuir constant of Al(OH)3
%KL2 = Langmuir constant of post flotation step flocs

```

Experimental Data

```

%Experimental Data
t_end=3601;
I = 1.5;
Q=0/60; % 0.5 L/min converted to L/s
H = 0.200;

```

```
F_acc =3.10;
F_acc (1:t_end,1)=3.10;
F_0=3.10;%new addition
T = 293.15;
```

Calibration factors

```
Nf=2.2;
qm =1.5;
Dp =1.7*10^-9 ;
Dp2 = 1.7*10^-9;
K_E=0.02;
Alpha_b=0.71;
Col_f=0.71;
Alpha = 1;
KL1=780;
KL2=780;
K=0.57;
k=1.32;
EXP_ALL=[];
EXP_ALL(1,:)=[0 601 1201 1801 2401 3001 3601]; %time
EXP_ALL(2,:)=[3.10 1.76 0.81 0.26 0.17 0.04 0.02];% Fluoride
exp_n=1
```

Process 1: Aluminum dissolution in water

```
dt=1;
M=27000;
Z=3;
F=96487;
Den_w = 1000;
g = 9.81;
Mu = 1.002*10^-3;
W = 0.102;
L = 0.250;
A = W*H;
Vf = Q/(A*1000);
E_h = 0.125;
E_w = 0.060;
E_n = 7;
E_t = 0.003;
VE = E_h*E_w*E_t*E_n;
V = ((H*W*L)-VE)*1000;
Al_gen =(k*I*M)/(Z*F*V)*dt;
Al_dis=Al_gen*K*dt;
Al_in=0;
Al_out=0;
Al_out(1:t_end,1)=0;
time=(0:1:t_end-1)';
Al_acc=0 ;
Al_acc(1:t_end,1)=0;
for t=2:t_end
    Al_acc(t)= (Al_gen - Al_dis + Al_in +Al_acc(t-1)- Al_out (t-1));
```

```
Al_out(t)=Q*Al_acc(t)*1/V;
```

```
end
```

Process 2: Hydrolysis

```
% AlOH3_gen= Generation of AlOH3 (mg/l)
% AlOH3_dis= Dissipation of AlOH3 (mg/l)
% AlOH3_in= Inflow of AlOH3 (mg/l)
% AlOH3_out= Outflow of AlOH3 (mg/l)
% AlOH3_acc= Accumulation of AlOH3 (mg/l)
% AlOH3_p_acc = Accumulation of AlOH3 particles (mol/l)
% Calculation of Mass of one AlOH3 particle
% Mass_AlOH3_particle= Mass of one AlOH3 particle (mg)
% Dr = Diameter of the Al-OH ring structure (m)
% Dp = Diameter of one AlOH3 particle in the reactor (m)
% Vr = Volume of the Al-OH ring structure (m3)
% Vp = Volume of one AlOH3 particle in the reactor (m3)
% Nr = Number of AlOH rings in one AlOH3 particle (Nos)
% N_Al_p = Number of Al in one particle (Nos)
% N_OH_p = Number of OH on one particle (Nos)
% N_OH_r = Number of OH attached to one Al ion in a ring (Nos)
% N_F_p = Number of F in one particle post adsorption (Nos)
% amu = Atomic mass unit in (g)
% M_AlOH3 = Molar mass of AlOH3 (mg)
% M_AlOH3_F = Molar mass of AlOH3_F (mg)
% Na = Avogadro Number
% Mass_Avg_AlOH3_F = Average mass of AlOH3-F floc or particle (g)
% N_floc = Number of particles in one floating floc (Nos)
% M_AlOH3 = 51047.802;% mg
% N_F_p= (13*N_Al_p);%as per the literature data for sludge composition (Al to
F ration which is between 13 - 17.5 w/w)Emamjomeh, Bennajah, Mameri, Hu
% M_AlOH3_F = 51047.802+19000*N_F_p;

Na=6.02214086*10^23;
Dr=9*10^-10;
Vr=4/3*pi*(Dr/2)^3;
Vp=4/3*pi*(Dp/2)^3;
Nr=Vp/Vr;
N_Al_p=Nr*6;
N_OH_r=2.2 ;
N_OH_p=N_Al_p*N_OH_r;
amu= 1.6605390402*10^-24;
Mass_AlOH3_particle=amu*((N_Al_p*26.982)+(15.999+1.00794)*N_OH_p)*1000;
M_AlOH3 = 51047.802;% mg
N_F_p= (3*N_Al_p)-(N_OH_p);
M_AlOH3_F = 51047.802+19000*N_F_p;
Mass_Avg_AlOH3_F = ((Mass_AlOH3_particle + N_F_p*(1/Na)* 19000))/1000;%in g
Dfloc=15*10^-6;
Vfloc=4/3*pi*(Dfloc/2)^3;
Nfloc= 12*(Dfloc/Dp);
```

```
Mass_AlOH3_floc=Mass_Avg_AlOH3_F*Nfloc; %in g
```

Process 3, 4 & 5: Adsorption, Flocculation and Flotation

```
% F_acc = Fluoride accumulation (mg/l)
% F_gen = Fluoride generation (mg/l)
% F_dis = Fluoride dissipation (mg/l)
% F_in = Fluoride inflow (mg/l)
% F_out = Fluoride outflow (mg/l)
% F_i = Initial fluoride concentration (mg/l)
% AlOH3_particle_conc = Al(OH)3_particle concentration(mol/l)
% Total_Ad = Total adsorbent concentration (mol/l)
% N_float_acc = Floated particle accumulation (Nos/l)
% qm=Langmuir constant (mg/g)
% KL=Langmuir constant (L/mol)
% qe=Amount of pollutant adsorbed per unit mass of adsorbent at equilibrium
(mg/g)
% Nf=Number of fluoride adsorbed on to one AlOH3 particle
% F_0= Inlet fluoride concentration (mg/l)
AlOH3_acc =0;
AlOH3_in=0;
AlOH3_acc (1:t_end,1)=0;
Total_Ad = 0;
Total_Ad (1:t_end,1)=0;
N_float_acc =0;
N_float_acc (1:t_end,1)=0;
%AlOH3-F_gen = AlOH3-F generation (Nos/l)
AlOH3_F_acc = 0;
AlOH3_F_acc(1:t_end,1)=0; %Nos/L
AlOH3_out=0;
AlOH3_out(1:t_end,1)=0;
F_in=Q*F_0/V;
AlOH3_F_out = 0;
AlOH3_F_out(1:t_end,1)=0;
% k_b=Boltzmann_s Constant (J/K)
% T = absolute temperature (K)
% Mu = Viscosity of suspended fluid (Ns/m2)
% Dp = particle size (m)
% K_floc= Rate constant for particle aggregation (L/s)
% Alpha = Collision efficiency
Dh= (4*H*W)/(2*H+W);
Re = Den_w*Vf*Dh/Mu;
fD = 64/Re;
hL = 0; % (fD*L*Vf^2)/(Dh*2*g);
t_Res = V/Q;
G = ((Den_w*g*hL)/(Mu*t_Res))^0.5;
k_b =1.38064852*10^(-23);
%Perikinetic flocculation or micro flocculation = (8*k_b*T*1000)/(3* Mu); is
Not considered in continuous flow, as
%the flocculation constant required for water - in laminar flow is only Macro
flocculation or Orthokinetic flocculation
N_floc_f =0;
N_floc_f (1:t_end,1)=0;
N_floc_i =0;
N_floc_i (1:t_end,1)=0;
```

```

AlOH3_F_gen = 0;
AlOH3_F_gen(1:t_end,1)=0;
% Hydrogen bubbles generation
%VH2_gen = Generation of H2 gas volume (l/s)
%M_H2 = Atomic weight of H2 (mg/mol)
%H = Number of hydrogen molecules generated per electron involved in the redox
reaction
%Den_H2 = Density of H2 gas (mg/l)
% Hc = Cell height (m)
% Wc = Cell width (m)
% Lc = Cell length (m)
%V = Working volume of cell (L)
M_H2 = 2000;
Den_H2 = 82.7;
VH2_gen = k*(I*M_H2*H/F)/Den_H2;
%Rising velocity of H2 bubbles
% Db = Bubble diameter (m)
%Vb = Rising velocity of air bubbles (m/s)
Db = 0.00007 ;
Vb = (g/(18*Mu))*( Den_w - Den_H2*10^-6)*Db^2;
%Flotation constant calculation
%Kf = Flotation constant (1/s)
% Alpha_b= Collision coefficient between air bubble and floc
% Col_f = Collision frequency between air bubble and floc
%pi_b = Air dosage (m3 air/m3 water)
% N_after_float = Number of flocs after flotation (Nos/L)
% K_E= Electrode adsorbtion coefficient
% N_floc_i = Number concentration of flocs - ready for flocculation
% N_floc_f = Number concentration of flocs - final - post flocculation
pi_b = (VH2_gen)*1000/V;%check in the batch model
Kf=(Alpha_b*Col_f*Db*pi_b*g*Vb* Den_w)/(12*Mu);

% N_float_acc = Floated particle accumulation (Nos/l)
% N_after_float= Particle concentration after flotation (Nos/l)

N_after_float=0;
N_after_float (1:t_end,1)=0;
F_Removal_Percentage=0;
F_Removal_Percentage (1:t_end,1)=0;
qe=0;
qe(1:t_end,1)=0;
F_acc_mol =0;
F_acc_mol (1:t_end,1)=0;
F_dis = 0;
F_dis (1:t_end,1)=0;
F_out = 0;
F_out (1:t_end,1)=0;
N_floc_f_out = 0;
N_floc_f_out (1:t_end,1)=0;
KL = KL1;
KL (1:t_end,1)=KL1;
K_floc =0;
K_floc(1:t_end,1)=0;

```

```

%D_p is the average particle diameter considering the mix of floccs
D_p=Dp;
D_p (1:t_end,1)=Dp;

F_Elec=0;
F_Elec (1:t_end,1)=0;
for t=(2:t_end)

AlOH3_gen =K*Al_gen*78/27;
AlOH3_acc (t)=(AlOH3_acc (t-1)+AlOH3_gen + AlOH3_in - AlOH3_out (t-1)-AlOH3_acc
(t-1)*K_E-(AlOH3_F_gen (t-1)*M_AlOH3));
AlOH3_out (t)= AlOH3_acc (t)*Q*1/V;
Total_Ad (t) = (((AlOH3_acc (t))/Mass_AlOH3_particle)/Na)+N_after_float(t-
1)/Na;
F_acc_mol (t)=F_acc (t-1)/19000;
KL(t)=((((AlOH3_acc (t))/Mass_AlOH3_particle)/Na)*KL1+(N_after_float(t-
1)/Na)*KL2)/Total_Ad (t);
qe (t) =((qm*KL (t)*F_acc_mol (t))/(1+(KL(t)* F_acc_mol(t))));
F_dis (t) = Total_Ad (t)*qe (t) *19000;
F_acc (t) = (F_acc (t-1) - F_dis (t-1) + F_in - F_out (t-1));% mg/L F_out(t) =
F_acc (t)*Q/V;% mg/L
AlOH3_F_gen (t)= ((qe (t) *Total_Ad (t))/Nf); % mol/l
AlOH3_F_acc(t) = (AlOH3_F_gen (t) + AlOH3_F_acc (t-1))- AlOH3_F_out (t-1)-
AlOH3_F_acc (t-1)*K_E;% mol/l AlOH3_F_out (t) = AlOH3_F_acc(t)*Q/V;% mol/l
N_floc_i (t) = (AlOH3_F_acc(t)*Na);%
D_p(t)= (((AlOH3_acc (t))/Mass_AlOH3_particle)/Na)*Dp+(N_after_float(t-
1)/Na)*Dp2)/Total_Ad (t);
% if D_p (t) < 0.1 *10^-6 %Reference is the collision frequency graph
K_floc (t)= ((8*k_b*T*1000)/(3* Mu));
N_floc_f(t) = (N_floc_i (t) /(1+K_floc (t)*dt*N_floc_i (t)) - N_floc_f_out (t-
1));
N_floc_f_out (t) = N_floc_f (t)*Q/V;
N_after_float(t) = (N_floc_f (t) *exp(-Kf*dt));
N_float_acc(t) = (N_floc_f (t) - N_after_float (t) + N_float_acc(t-1));
F_Removal_Percentage (t) = ((F_0-F_acc(t))/F_0)*100;
F_Elec (t) =AlOH3_F_acc (t-1)*K_E*M_AlOH3_F+AlOH3_acc (t-1)*K_E;
end
for i=1:6
    diff_t=600;
X(i)=F_acc((i)*diff_t+1);
end
X
F_acc(601)
F_acc(1201)
F_acc(1801)
F_acc(2401)
F_acc(3001)
F_acc(3601)
for j=1:6
    diff_t=600;
Al(j)=Al_acc((j)*diff_t+1);
end

```

```

Al
x_end=F_acc(t_end) % in mg/L
Rem_eff=(F_0-x_end)/F_0*100

Total_al_gen=((k*I*M)/(Z*F))*t_end% mg
x_end=F_acc(t_end) % in mg/L
Total_f= N_float_acc (t_end)*V*Mass_AlOH3_floc % in (g)
Final_dAl = Al_acc(t_end) % in mg/L
Al_ratio=(146.89-18.18)/Final_dAl

```

PLOTS OF THE OUTPUTS

```

y=EXP_ALL(2,2:7); %we are using exp 01
yhat=X(1,1:6);
Time=EXP_ALL(1,2:7);
RMSE = sum((y - yhat).^2)/6
RMSD=sqrt(RMSE)
RSE = sqrt(sum(y-yhat).^2)/4
MAPE=(abs((y(1)-X(1))/y(1))+abs((y(2)-X(2))/y(2))+abs((y(3)-
X(3))/y(3))+abs((y(4)-X(4))/y(4))+abs((y(5)-X(5))/y(5))+abs((y(6)-
X(6))/y(6)))/6*100
Error_10=abs((y(1)-X(1))/y(1))*100
Error_20=abs((y(2)-X(2))/y(2))*100
Error_30=abs((y(3)-X(3))/y(3))*100
Error_40=abs((y(4)-X(4))/y(4))*100
Error_50=abs((y(5)-X(5))/y(5))*100
Error_60=abs((y(6)-X(6))/y(6))*100
plot(time, F_acc);
hold on
plot (EXP_ALL(1,:), EXP_ALL(2,:), 'o');
xlabel('Time [Sec]');
ylabel('Dissolved Fluoride [mg/l]')
xlim([0 t_end])
ylim([0 F_0+1])
title('Model Simulation for Experimental Data')
hold off
legend('show')
legend({'Model Sim. I=1.5 A','Exp. data I=1.5 A'})
F_rem_exp=((F_0-y).^1)/F_0*100);
plot(time, F_Removal_Percentage)
hold on
plot(Time,F_rem_exp,'o');
xlabel('Time [sec]');
ylabel('F Removal Percentage [%]')
xlim([0 t_end])
ylim([0 100])
hold off
plot(time, D_p);
xlabel('time [sec]');
ylabel('D_p [m]')
plot(time, KL);

```

```
xlabel('time [sec]');
ylabel('KL')
plot(time, Al_acc);
xlabel('Time [Sec]');
ylabel('Aluminium [mg/l]')
legend('I = 1.5 A')
plot(time, AlOH3_acc);
xlabel('Time [Sec]');
ylabel('Aluminium Hydroxide [mg/l]')
legend('I = 1.5 A')
plot(time, N_floc_i);
xlabel('Time [Sec]');
ylabel('Pre-flocculation Flocc [Nos/l]')
legend('I = 1.5 A')
plot(time, N_floc_f);
xlabel('time [sec]');
ylabel('N floc_f [Nos/l]')
plot(time, N_after_float);
xlabel('time [sec]');
ylabel('N after_float [Nos/l]')
plot(time, N_float_acc);
xlabel('Time [Sec]');
ylabel('Accumulation of floated flocc [Nos/l]')
legend('I = 1.5 A')
```

(B)MATLAB® electrocoagulation continuous reactor process-based conceptual model

```
% Aluminum dissolution
% V= Working volume of the reactor (L)
% k= Correction factor, denoted current efficiency or faradic yield
% I= Electric current (A)
% M= Atomic weight of the electrode material (mg/mol)
% Z= Number of electrons transferred (z=3 for Aluminium)
% F= Faraday's constant (C/mol)
% Al_gen= Generation of aluminium ions (mg/l)
% Al_dis= Dissipation of aluminium ions (mg/l)
% Al_in= Inflow of aluminium ions (mg/l)
% Al_out= Outflow of aluminium ions (mg/l)
% Al_acc= Accumulation of aluminium ions (mg/l)
% dt= time step gap (s)
%Continuous model
% Q = flow rate (L/s)
% Den_w = Density of liquid (kg/m3)
% g = Gravitational acceleration (m/s2)
% Vf= flow velocity (m/s)
% Dh = Hydraulic diameter
% G = Velocity Gradient (s-1)
% H = Wetted height (m)
% W = Reactor width (duct) (m)
% A = Cross sectional area of the reactor in the direction of the flow (m2)
% L = Length of the duct (length of the reactor, towards the flow direction (m)
% fD = Friction factor
% Re = Reynolds number
% hL = Head loss across the duct (m)
% t_Res = Resident time (s)
% VE = Electrode volume (m3)
% VB = Reactor bottom wedge volume (m3)
%E_t = Electrode thickness (m)
%E_h = Electrode height (m)
%E_w = Electrode width (m)
%E_n = Number of electrodes (Nos)
% qm=Langmuir constant (mg/g)
%KL1 = Langmuir constant of Al(OH)3 (0.4 to 1.4, 0.55)
%KL2 = Langmuir constant of post flotation step floccs (600 to 2000, 1300)
% K= Percentage denoted hydrolysis efficiency (0.763 to 0.993, 0.910)
% Dp = Diameter of one AlOH3 particle in the reactor in m (1 x 10 ^-9 to 5
% x 10^ -8)
% K_E= Electrode adsorption coefficient(0.2 to 0.8, 0.5)
% Nf=Number of fluoride adsorbed on to one AlOH3 particle (2.2)
```

Experimental Data

```
%Experimental Data
t_end=3601;
I = 3;
Q=0.5/60; % 0.5 L/min converted to L/s
```

```
H = 0.365;
F_acc = 2.14;
F_acc (1:t_end,1)=2.14;
F_0=2.14;%new addition
T = 293.15;
```

Calibration factors

```
% Most sensitive five calibration factors
Nf=2.2; % DONT CHANGE Number of fluoride adsorbed on to one AlOH3 particle
qm =0.96; %DONT CHANGE

Dp =1.7 *10^-9;
Dp2 = 1.7*10^-9;
K_E=0.02;
Alpha_b=0.205;
Col_f=0.205;
Alpha = 1;
KL1=960;
KL2=960;
K=0.775;
k=1.65;

%data
EXP_ALL=[];
EXP_ALL(1,:)=[0 301 601 901 1201 1501 1801 2101 2401 2701 3001 3301 3601]; %time
EXP_ALL(2,:)=[2.14 1.96 1.70 1.42 1.28 1.16 1.04 0.96 0.92 0.80 0.78 0.80
.76];%01 Fluoride
EXP_ALL(3,:)=[0.00 0.51 1.02 1.23 1.44 1.64 1.84 2.06 2.32 2.78 3.25 3.38
3.56];%01 Aluiminium
exp_n=1
```

Process 1: Aluminum dissolution in water

```
dt=1;
M=27000;
Z=3;
F=96487;
Den_w = 1000;
g = 9.81;
Mu = 1.002*10^-3;
W = 0.200;
L = 0.400;
A = W*H;
Vf = Q/(A*1000); % m/s
E_h = H - 0.075;
E_w = 0.360;
E_n = 4;
E_t = 0.003;
VE = E_h*E_w*E_t*E_n;
VB = (0.5*0.055*0.3*0.2);
V = ((H*W*L)-VE-VB)*1000;
```

```

Al_gen =(k*I*M)/(Z*F*V)*dt;
Al_dis=Al_gen*K*dt;
Al_in=0;
Al_out=0;
Al_out(1:t_end,1)=0;

time=(0:1:t_end-1)';
Al_acc=0 ;
Al_acc(1:t_end,1)=0;
for t=2:t_end

    Al_acc(t)= (Al_gen - Al_dis + Al_in +Al_acc(t-1)- Al_out (t-1)
Al_out(t)=Q*Al_acc(t)*1/V;

end

```

Process 2: Hydrolysis

```

% AlOH3_gen= Generation of AlOH3 (mg/l)
% AlOH3_dis= Dissipation of AlOH3 (mg/l)
% AlOH3_in= Inflow of AlOH3 (mg/l)
% AlOH3_out= Outflow of AlOH3 (mg/l)
% AlOH3_acc= Accumulation of AlOH3 (mg/l)
% AlOH3_p_acc = Accumulation of AlOH3 particles (mol/l)
% Calculation of Mass of one AlOH3 particle
% Mass_AlOH3_particle= Mass of one AlOH3 particle (mg)
% Dr = Diameter of the Al-OH ring structure (m)
% Dp = Diameter of one AlOH3 particle in the reactor (m)
% Vr = Volume of the Al-OH ring structure (m3)
% Vp = Volume of one AlOH3 particle in the reactor (m3)
% Nr = Number of AlOH rings in one AlOH3 particle (Nos)
% N_Al_p = Number of Al in one particle (Nos)
% N_OH_p = Number of OH on one particle (Nos)
%N_OH_r = Number of OH attached to one Al ion in a ring (Nos)
% N_F_p = Number of F in one particle post adsorption (Nos)
% amu = Atomic mass unit in (g)
% M_AlOH3 = Molar mass of AlOH3 (mg)
% M_AlOH3_F = Molar mass of AlOH3_F (mg)
% Na = Avogadro Number
% Mass_Avg_AlOH3_F = Average mass of AlOH3-F floc or particle (g)
% N_floc = Number of particles in one floating floc (Nos)

Na=6.02214086*10^23;
Dr=9*10^-10;
Vr=4/3*pi*(Dr/2)^3;
Vp=4/3*pi*(Dp/2)^3;
Nr=Vp/Vr;
N_Al_p=Nr*6;
N_OH_r=2.2 ;
N_OH_p=N_Al_p*N_OH_r;

```

```

amu= 1.6605390402*10^-24;
Mass_AlOH3_particle=amu*((N_Al_p*26.982)+(15.999+1.00794)*N_OH_p)*1000;
M_AlOH3 = 51047.802;% mg
N_F_p= (3*N_Al_p)-(N_OH_p);
M_AlOH3_F = 51047.802+19000*N_F_p;
Mass_Avg_AlOH3_F = ((Mass_AlOH3_particle + N_F_p*(1/Na)* 19000))/1000;%in g
Dfloc=15*10^-6; %the floc diameter in m (as per emamjomeh)
Vfloc=4/3*pi*(Dfloc/2)^3;
Nfloc= 12*Dfloc/Dp;
Mass_AlOH3_floc=Mass_Avg_AlOH3_F*Nfloc; %in g

```

Process 3, 4 & 5: Adsorption, Flocculation and Flotation

```

% F_acc = Fluoride accumulation (mg/l)
% F_gen = Fluoride generation (mg/l)
% F_dis = Fluoride dissipation (mg/l)
% F_in = Fluoride inflow (mg/l)
% F_out = Fluoride outflow (mg/l)
% F_i = Initial fluoride concentration (mg/l)
% AlOH3_particle_conc = Al(OH)3_particle concentration(mol/l)
% Total_Ad = Total adsorbent concentration (mol/l)
% N_float_acc = Floated particle accumulation (Nos/l)
% qm=Langmuir constant (mg/g)
% KL=Langmuir constant (L/mol)
% qe=Amount of pollutant adsorbed per unit mass of adsorbent at equilibrium
(mg/g)
% Nf=Number of fluoride adsorbed on to one AlOH3 particle
% F_0= Inlet fluoride concentration (mg/l)

AlOH3_acc =0;
AlOH3_in=0;
AlOH3_acc (1:t_end,1)=0;
Total_Ad = 0;
Total_Ad (1:t_end,1)=0;
N_float_acc =0;
N_float_acc (1:t_end,1)=0;
%AlOH3-F_gen = AlOH3-F generation (Nos/l)
AlOH3_F_acc = 0;
AlOH3_F_acc(1:t_end,1)=0; %Nos/L
AlOH3_out=0;
AlOH3_out(1:t_end,1)=0;
F_in=Q*F_0/V;
AlOH3_F_out = 0;
AlOH3_F_out(1:t_end,1)=0; %Nos/L
% k_b=Boltzmann_s Constant (J/K)
% T = absolute temperature (K)
% Mu = Viscosity of suspended fluid (Ns/m2)
% Dp = particle size (m)
% K_floc= Rate constant for particle aggregation (L/s)
% Alpha = ?: Collision efficiency
Dh= (4*H*W)/(2*H+W);
Re = Den_w*Vf*Dh/Mu;
fD = 64/Re;
hL = (fD*L*Vf^2)/(Dh*2*g);

```

```

t_Res = V/Q;

G = ((Den_w*g*hL)/(Mu*t_Res))^0.5;
k_b =1.38064852*10^(-23);
N_floc_f =0;
N_floc_f (1:t_end,1)=0;
N_floc_i =0;
N_floc_i (1:t_end,1)=0;
AlOH3_F_gen = 0;
AlOH3_F_gen(1:t_end,1)=0;
% Hydrogen bubbles generation
%VH2_gen = Generation of H2 gas volume (l/s)
%M_H2 = Atomic weight of H2 (mg/mol)
%H = Number of hydrogen molecules generated per electron involved in the redox
reaction
%Den_H2 = Density of H2 gas (mg/l)
% Hc = Cell height (m)
% Wc = Cell width (m)
% Lc = Cell length (m)
%V = Working volume of cell (L)
M_H2 = 2000;
Den_H2 = 82.7;
VH2_gen = k*(I*M_H2*H/F)/Den_H2;
%Rising velocity of H2 bubbles
% Db = Bubble diameter (m)
%Vb = Rising velocity of air bubbles (m/s)
Db = 0.00007 ;
Vb = (g/(18*Mu))*( Den_w - Den_H2*10^-6)*Db^2;
%Flotation constant calculation
%Kf = Flotation constant (1/s)
% Alpha_b= Collision coefficient between air bubble and floc
% Col_f = Collision frequency between air bubble and floc
%pi_b = Air dosage (m3 air/m3 water)
% N_after_float = Number of flocs after flotation (Nos/L)
% K_E= Electrode adsorbtion coefficient
% N_floc_i = Number concentration of flocs - ready for flocculation
% N_floc_f = Number concentration of flocs - final - post flocculation
pi_b = (VH2_gen)/Q;%check in the batch model
Kf=(Alpha_b*Col_f*Db*pi_b*g*Vb* Den_w)/(12*Mu);

% N_float_acc = Floated particle accumulation (Nos/l)
% N_after_float= Particle concentration after flotation (Nos/l)

N_after_float=0;
N_after_float (1:t_end,1)=0;
F_Removal_Percentage=0;
F_Removal_Percentage (1:t_end,1)=0;
qe=0;
qe(1:t_end,1)=0;
F_acc_mol =0;
F_acc_mol (1:t_end,1)=0;
F_dis = 0;

```

```

F_dis (1:t_end,1)=0;
F_out = 0;
F_out (1:t_end,1)=0;
N_floc_f_out = 0;
N_floc_f_out (1:t_end,1)=0;
KL = KL1;
KL (1:t_end,1)=KL1;
K_floc =0;
K_floc(1:t_end,1)=0;
%D_p is the average particle diameter considering the mix of flocs
D_p=Dp;
D_p (1:t_end,1)=Dp;
F_Elec=0;
F_Elec (1:t_end,1)=0;
for t=(2:t_end)

AlOH3_gen =K*Al_gen*78/27;
AlOH3_acc (t) =(AlOH3_acc (t-1)+AlOH3_gen + AlOH3_in - AlOH3_out (t-1)-AlOH3_acc
(t-1)*K_E-(AlOH3_F_gen (t-1)*M_AlOH3));% mg/L
AlOH3_out (t)= AlOH3_acc (t)*Q*1/V; % mg/L
Total_Ad (t) = (((AlOH3_acc (t))/Mass_AlOH3_particle)/Na)+N_after_float(t-
1)/Na; % mol/L
F_acc_mol (t)=F_acc (t-1)/19000;%
KL(t)=((((AlOH3_acc (t))/Mass_AlOH3_particle)/Na)*KL1+(N_after_float(t-
1)/Na)*KL2)/Total_Ad (t);
qe (t) =((qm*KL (t)*F_acc_mol (t))/(1+(KL(t)* F_acc_mol(t))));
F_dis (t) = Total_Ad (t)*qe (t) *19000; % mg/L
F_acc (t) = (F_acc (t-1) - F_dis (t-1) + F_in - F_out (t-1));% mg/L
F_out(t) = F_acc (t)*Q/V;% mg/L
AlOH3_F_gen (t)= ((qe (t) *Total_Ad (t))/Nf); % mol/l
AlOH3_F_acc(t) = (AlOH3_F_gen (t) + AlOH3_F_acc (t-1))- AlOH3_F_out (t-1)-
AlOH3_F_acc (t-1)*K_E;% mol/l
AlOH3_F_out (t) = AlOH3_F_acc(t)*Q/V;% mol/l
N_floc_i (t) = (AlOH3_F_acc(t)*Na;
D_p(t)= (((AlOH3_acc (t))/Mass_AlOH3_particle)/Na)*Dp+(N_after_float(t-
1)/Na)*Dp2)/Total_Ad (t);
if D_p (t) < 0.1 *10^-6 %Reference is the collision frequency graph

K_floc (t)= ((8*k_b*T*1000)/(3* Mu))+
(2/3)*G*Alpha*(D_p(t)^3)*(100^3)*(1/1000);
else
K_floc (t)= (2/3)*G*Alpha*(D_p(t)^3)*(100^3)*(1/1000);
end
N_floc_f(t) = (N_floc_i (t) /(1+K_floc (t)*dt*N_floc_i (t)) - N_floc_f_out (t-
1));% Nos/L (N_Floc out component is included here)
N_floc_f_out (t) = N_floc_f (t)*Q/V;
N_after_float(t) = (N_floc_f (t) *exp(-Kf*dt) );
N_float_acc(t) = (N_floc_f (t) - N_after_float (t) + N_float_acc(t-1));
F_Removal_Percentage (t) = ((F_0-F_acc(t))/F_0)*100;
F_Elec (t) =AlOH3_F_acc (t-1)*K_E*M_AlOH3_F+AlOH3_acc (t-1)*K_E;
end
for i=1:12
diff_t=300;

```

```

X(i)=F_acc((i)*diff_t+1);
end

for j=1:12
    diff_t=300;
Al(j)=Al_acc((j)*diff_t+1);
end
Al
x_end=F_acc(t_end) % in mg/L
Rem_eff=(F_0-x_end)/F_0*100
Total_f= N_float_acc (t_end)*V*Mass_AlOH3_floc % in (g)
Final_dAl = Al_acc(t_end) % in mg/L
Total_al_gen=((k*I*M)/(Z*F))*t_end% mg
%ENERGY CALCULATIONS
% A_Elec = Electrode active anode area (m2)
% Th_Voltage = Theoretical voltage based on equation I/A=Cond x V/d
% E_d = Distance between electrodes (m)
%Cond = mesured conductivity in reactor (s/m)
%R=Resistance of wires (ohm)
% Voltage = Measured Voltage (V)
E_d = 0.05;
A_Elec = E_h*E_w*(E_n-1);
Cond= 1335 * 10^-4; %(s/m)
R = 0.04168; %ohm
Th_Voltage=I/A_Elec*E_d/Cond*(E_n-2)+I*R
Voltage = 6.4; %(V)
Power = I*Voltage %(W)
Energy_J = Power*3600 % J
Energy_kWh=Power/1000*1 %kwh
Current_density=I/A_Elec
Current_concentration = I/V
Surface_volume_ratio=A_Elec/V

```

PLOTS OF THE OUTPUTS

```

y=EXP_ALL(2,2:13);
yhat=X
Time=EXP_ALL(1,:);
RMSE = sum((y - yhat).^2)/12
RMSD=sqrt(RMSE)
RSE = sqrt(sum(y-yhat).^2)/10
MAPE=(abs((y(1)-X(1))/y(1))+abs((y(2)-X(2))/y(2))+abs((y(3)-
X(3))/y(3))+abs((y(4)-X(4))/y(4))+abs((y(5)-X(5))/y(5))+abs((y(6)-
X(6))/y(6))+abs((y(7)-X(7))/y(7))+abs((y(8)-X(8))/y(8))+abs((y(9)-
X(9))/y(9))+abs((y(10)-X(10))/y(10))+abs((y(11)-X(11))/y(11))+abs((y(12)-
X(12))/y(12)))/12*100
Error_5=abs((y(1)-X(1))/y(1))*100
Error_10=abs((y(2)-X(2))/y(2))*100
Error_15=abs((y(3)-X(3))/y(3))*100
Error_20=abs((y(4)-X(4))/y(4))*100
Error_25=abs((y(5)-X(5))/y(5))*100
Error_30=abs((y(6)-X(6))/y(6))*100

```

```

Error_35=abs((y(7)-X(7))/y(7))*100
Error_40=abs((y(8)-X(8))/y(8))*100
Error_45=abs((y(9)-X(9))/y(9))*100
Error_50=abs((y(10)-X(10))/y(10))*100
Error_55=abs((y(11)-X(11))/y(11))*100
Error_60=abs((y(12)-X(12))/y(12))*100
Exp_fl_data=EXP_ALL(2,:);
plot(time, F_acc);
hold on
plot (Time, Exp_fl_data, 'o');
xlabel('Time [sec]');
ylabel('Fluoride [mg/l]')
xlim([0 t_end])
ylim([0 F_0+1])
% title('Model Simulation for 01')
hold off
legend('show')
legend({'Model Sim. I=3 A', 'Exp. data I=3 A'})
y_all=EXP_ALL(2,1:13);
F_rem_exp=((F_0-y_all).^1)/F_0*100);
plot(time, F_Removal_Percentage)
hold on
plot(Time,F_rem_exp, 'o');
xlabel('Time [sec]');
ylabel('F Removal Percentage [%]')
xlim([0 t_end])
ylim([0 100])
hold off
legend({'Model Sim. I=3 A', 'Exp. data I=3 A'})
Exp_al_data = EXP_ALL(3,:);
plot(time, Al_acc);
hold on
plot(Time,Exp_al_data, 'o');
xlabel('Time [sec]');
ylabel('Aluminum [mg/l]')
hold off
legend('I=3 A')
plot(time, Total_Ad);
xlabel('Time [sec]');
ylabel('Adsorbent concentration [mol/L]')
legend('I=3 A')
plot(time, qe);
xlabel('Time [sec]');
ylabel('qe [mg/g]')
legend('I=3 A')
plot(time, F_dis);
xlabel('Time [sec]');
ylabel('Fluoride dissipation [mg/L]')
legend('I=3 A')
plot(time, AlOH3_acc);
xlabel('Time [sec]');
ylabel('Aluminium Hydroxide [mg/l]')
legend('I=3 A')

```

```
plot(time, N_floc_i);
xlabel('Time [sec]');
ylabel('Pre-flocculation Flocs [Nos/l]')
legend('I=3 A')
plot(time, N_floc_f);
xlabel('Time [sec]');
ylabel('N_floc_f [Nos/l]')
plot(time, N_after_float);
xlabel('Time [sec]');
ylabel('N_after_float [Nos/l]')
plot(time, F_Elec);
xlabel('Time [sec]');
ylabel('Floc adsorption on electrodes [mg/l]')
legend('I=3 A')
plot (time, ecdf(F_Elec));
xlabel('Time [sec]');
ylabel('Cum. Floc adsorption on electrodes [mg/l]')
legend('I=3 A')
xlim([0 4000])
ylim([0.000 1.200])
plot(time, N_float_acc);
xlabel('Time [Sec]');
ylabel('Accumulation of floated flocs [Nos/l]')
legend('I = 3.0 A')
grid on
```

(C) Dissolved fluoride concentration (mg l⁻¹) results of laboratory-scale continuous EC operations

Table C-1: Dissolved fluoride concentration (mg l⁻¹) results of laboratory-scale continuous EC operations

Experiment	0 min	5 min	10 min	15 min	20 min	25 min	30 min	35 min	40 min	45 min	50 min	55 min	60 min	Removal efficiency
O1	2.14	1.96	1.70	1.42	1.28	1.16	1.04	0.96	0.92	0.80	0.78	0.80	0.76	64%
O2	2.14	1.82	1.45	1.24	0.97	0.87	0.77	0.72	0.67	0.66	0.63	0.62	0.60	72%
O3	2.10	1.68	1.30	1.01	0.82	0.70	0.57	0.53	0.49	0.47	0.46	0.45	0.44	79%
O4	4.00	3.25	2.92	2.73	2.42	2.18	1.96	1.84	1.71	1.68	1.59	1.53	1.45	64%
O5	4.00	3.41	2.82	2.36	2.04	1.76	1.54	1.41	1.36	1.24	1.22	1.16	1.12	72%
O6	4.00	3.22	2.48	2.02	1.74	1.42	1.34	1.02	0.98	0.94	0.92	0.90	0.86	79%
O7	5.96	5.36	4.34	4.04	3.52	3.42	3.12	2.70	2.50	2.42	2.32	2.28	2.20	63%
O8	6.02	5.3	4.28	3.56	3.24	2.76	2.48	2.22	2.12	1.96	1.86	1.82	1.74	71%
O9	6.10	5.20	4.20	3.20	2.64	2.24	1.80	1.66	1.52	1.44	1.40	1.36	1.32	78%
O10	2.1	1.96	1.92	1.88	1.82	1.76	1.72	1.66	1.62	1.58	1.52	1.48	1.45	31%
O11	6.10	5.60	5.16	4.92	4.64	4.44	4.32	4.16	4.02	4.04	3.96	3.84	3.80	38%
O12	6.10	5.44	4.76	4.40	4.04	3.66	3.34	3.10	2.88	2.76	2.70	2.62	2.54	58%
O13	6.00	5.04	3.60	3.06	2.42	2.16	2.00	1.76	1.68	1.58	1.50	1.44	1.40	77%

(D) Residual plots and regression analysis results summaries of calibration parameters

i. Residual plots of calibration parameters

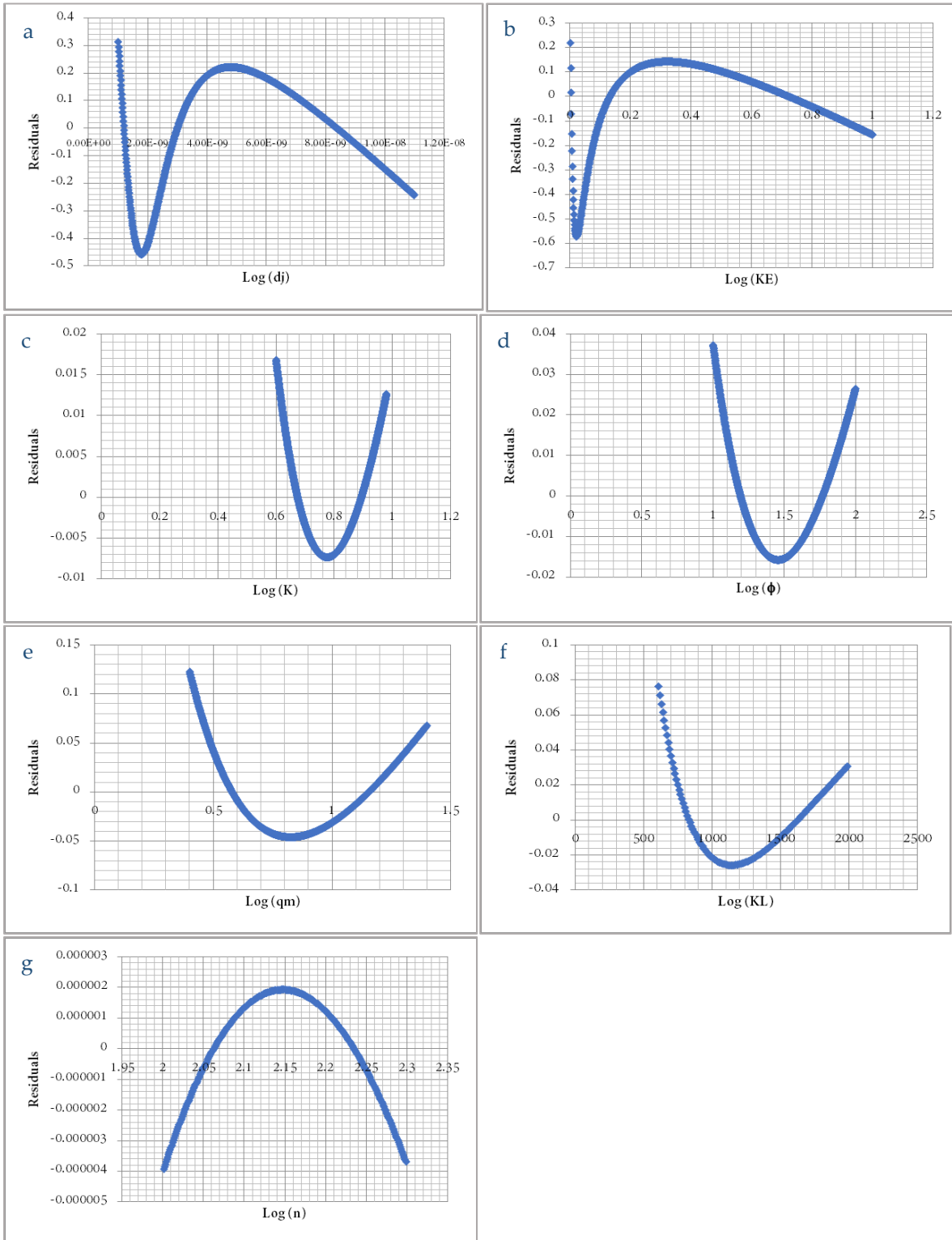


Figure D-1: Residual plots of calibration parameters (a) d_j , (b) K_E , (c) K , (d) ϕ , (e) q_m , (f) K_L , (g) n

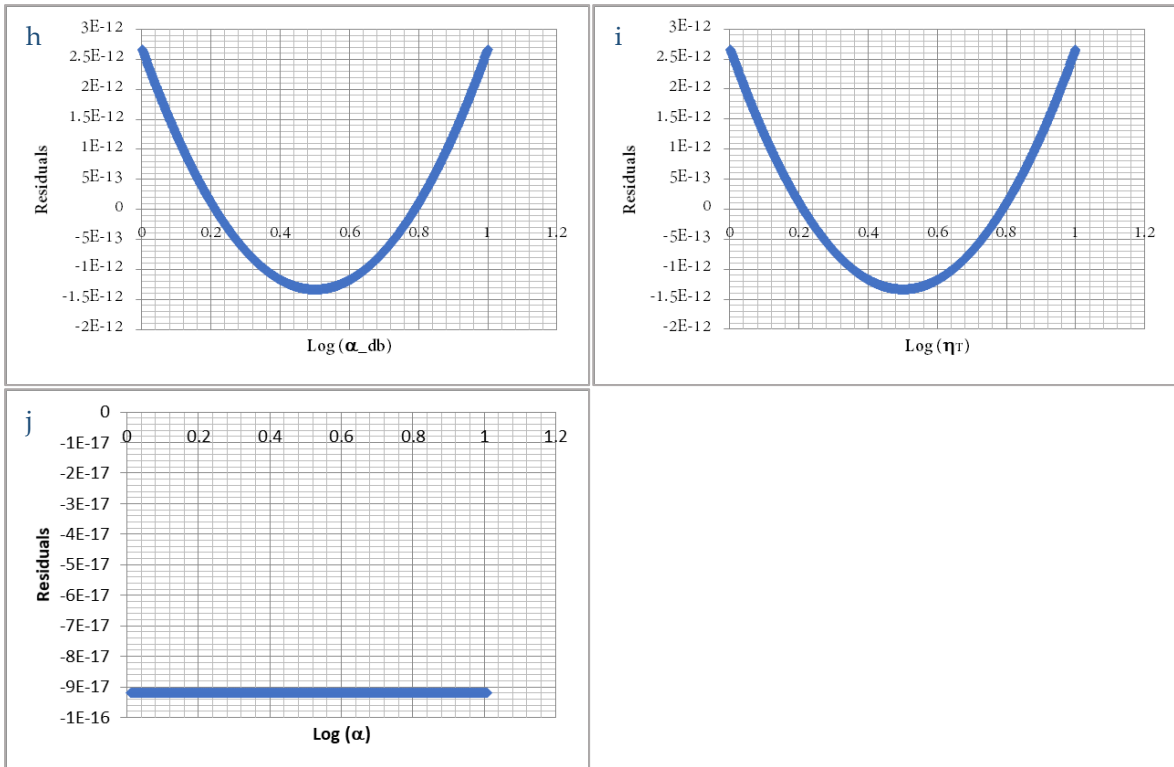


Figure D-2: Residual plots of calibration parameters (h) α_{db} , (i) $\eta\tau$, (j) α

ii. Regression analysis of K_L local sensitivity test

SUMMARY OUTPUT

<i>Regression Statistics</i>					
Multiple R		0.924227904			
R Square		0.854197218			
Adjusted R Square		0.853132964			
Standard Error		0.023555869			
Observations		139			

<i>ANOVA</i>					
	<i>df</i>	<i>SS</i>	<i>MS</i>	<i>F</i>	<i>Significance F</i>
Regression	1	0.445359973	0.4454	802.6254204	3.84091E-59
Residual	137	0.07601842	0.0006		
Total	138	0.521378393			

	<i>Coefficients</i>	<i>Standard Error</i>	<i>t Stat</i>	<i>P-value</i>	<i>Lower 95%</i>
Intercept	0.113326085	0.006774574	16.728	6.54491E-35	-0.12672234
X Variable 1	0.00014107	4.97942E-06	28.331	3.84091E-59	0.000131224

	<i>Upper 95%</i>	<i>Lower 95.0%</i>	<i>Upper 95.0%</i>
Intercept	0.099929831	-0.12672234	0.0999
X Variable 1	0.000150917	0.000131224	0.0002

iii. Regression Analysis of n Local Sensitivity Test

SUMMARY OUTPUT

<i>Regression Statistics</i>	
	0.99957478
Multiple R	4
	0.99914974
R Square	9
Adjusted R Square	0.99914688
	7
Standard Error	1.72908E-06
Observations	299

ANOVA

	<i>df</i>	<i>SS</i>	<i>MS</i>	<i>F</i>	<i>Significance F</i>
				349011.74	
Regression	1	1.04345E-06	1.04345E-06	5	0
Residual	297	8.87948E-10	2.98972E-12		
Total	298	1.04434E-06			

	<i>Coefficients</i>	<i>Standard Error</i>	<i>t Stat</i>	<i>P-value</i>	<i>Lower 95%</i>
Intercept	0.00244478		980.731639		0.00243987
	1	2.49281E-06	8	0	6
X Variable 1	0.00068441		590.772159		0.00068213
	8	1.15852E-06	7	0	9

	<i>Upper 95%</i>	<i>Lower 95.0%</i>	<i>Upper 95.0%</i>
Intercept	0.00244968		0.00244968
	7	0.002439876	7
X Variable 1	0.00068669		0.00068669
	8	0.000682139	8

iv. Regression Analysis of q_m Local Sensitivity Test

SUMMARY OUTPUT

<i>Regression Statistics</i>	
Multiple R	0.465987
R Square	0.217143
Adjusted R Square	0.216358
Standard Error	0.041626
Observations	999

ANOVA

	<i>df</i>	<i>SS</i>	<i>MS</i>	<i>F</i>	<i>Significance F</i>
Regression	1	0.47916	0.47916	276.5412	5.41E-55
Residual	997	1.727491	0.001733		
Total	998	2.206651			

	<i>Coefficients</i>	<i>Standard Error</i>	<i>t Stat</i>	<i>P-value</i>	<i>Lower 95%</i>
Intercept	0.113729	0.004316	26.35121	1.5E-116	0.105259
X Variable 1	-0.07594	0.004567	-16.6295	5.41E-55	-0.0849
	<i>Upper 95%</i>	<i>Lower 95.0%</i>	<i>Upper 95.0%</i>		
Intercept	0.122198	0.105259	0.122198		
X Variable 1	-0.06698	-0.0849	-0.06698		

v. Regression Analysis of d_j Local Sensitivity Test

SUMMARY OUTPUT

<i>Regression Statistics</i>	
Multiple R	0.836656
R Square	0.699993
Adjusted R Square	0.699692
Standard Error	0.189223
Observations	999

ANOVA

	<i>df</i>	<i>SS</i>	<i>MS</i>	<i>F</i>	<i>Significance F</i>
Regression	1	83.29179	83.29179	2326.251	6.8E-263
Residual	997	35.69774	0.035805		
Total	998	118.9895			

	<i>Coefficients</i>	<i>Standard Error</i>	<i>t Stat</i>	<i>P-value</i>	<i>Lower 95%</i>
Intercept	0.283351	0.01382	20.50339	3.15E-78	0.256232
X Variable 1	1E+08	2075943	48.23123	6.8E-263	96051553
	<i>Upper 95%</i>	<i>Lower 95.0%</i>	<i>Upper 95.0%</i>		
Intercept	0.31047	0.256232	0.31047		
X Variable 1	1.04E+08	96051553	1.04E+08		

vi. Regression Analysis of K_E Local Sensitivity Test

SUMMARY OUTPUT

<i>Regression Statistics</i>	
Multiple R	0.797442
R Square	0.635914
Adjusted R Square	0.635548
Standard Error	0.146808
Observations	999

ANOVA

	<i>df</i>	<i>SS</i>	<i>MS</i>	<i>F</i>	<i>Significance F</i>
Regression	1	37.53102	37.53102	1741.361	5.8E-221
Residual	997	21.48804	0.021553		
Total	998	59.01906			

	<i>Coefficients</i>	<i>Standard Error</i>	<i>t Stat</i>	<i>P-value</i>	<i>Lower 95%</i>
Intercept	0.558635	0.009311	60.00016	0	0.540364
X Variable 1	0.672106	0.016106	41.72961	5.8E-221	0.6405
	<i>Upper 95%</i>	<i>Lower 95.0%</i>	<i>Upper 95.0%</i>		
Intercept	0.576905	0.540364	0.576905		
X Variable 1	0.703712	0.6405	0.703712		

vii. Regression Analysis of K Local Sensitivity Test

SUMMARY OUTPUT

<i>Regression Statistics</i>	
Multiple R	0.748151
R Square	0.559729
Adjusted R Square	0.559288
Standard Error	0.006583
Observations	999

ANOVA

	<i>df</i>	<i>SS</i>	<i>MS</i>	<i>F</i>	<i>Significance F</i>
Regression	1	0.054922	0.054922	1267.515	8.4E-180
Residual	997	0.0432	4.33E-05		
Total	998	0.098122			

	<i>Coefficients</i>	<i>Standard Error</i>	<i>t Stat</i>	<i>P-value</i>	<i>Lower 95%</i>
Intercept	-0.04115	0.001516	-27.1466	6E-122	-0.04412
X Variable 1	0.06766	0.0019	35.60218	8.4E-180	0.063931
	<i>Upper 95%</i>	<i>Lower 95.0%</i>	<i>Upper 95.0%</i>		
Intercept	-0.03817	-0.04412	-0.03817		
X Variable 1	0.071389	0.063931	0.071389		

viii. Regression Analysis of ϕ Local Sensitivity Test

SUMMARY OUTPUT

<i>Regression Statistics</i>	
Multiple R	0.548956
R Square	0.301352
Adjusted R Square	0.300651
Standard Error	0.014189
Observations	999

ANOVA

	<i>df</i>	<i>SS</i>	<i>MS</i>	<i>F</i>	<i>Significance F</i>
Regression	1	0.086581	0.086581	430.0424	1.06E-79
Residual	997	0.200727	0.000201		
Total	998	0.287307			

	<i>Coefficients</i>	<i>Standard Error</i>	<i>t Stat</i>	<i>P-value</i>	<i>Lower 95%</i>
Intercept	0.066548	0.002378	27.98745	1.1E-127	0.061882
X Variable 1	-0.03228	0.001557	-20.7375	1.06E-79	-0.03534
	<i>Upper 95%</i>	<i>Lower 95.0%</i>	<i>Upper 95.0%</i>		
Intercept	0.071214	0.061882	0.071214		
X Variable 1	-0.02923	-0.03534	-0.02923		

ix. Regression Analysis of α_{ab} & η_T Local Sensitivity Test

SUMMARY OUTPUT

<i>Regression Statistics</i>	
Multiple R	1
R Square	1
Adjusted R Square	1
Standard Error	1.2E-12
Observations	999

ANOVA

	<i>df</i>	<i>SS</i>	<i>MS</i>	<i>F</i>	<i>Significance F</i>
Regression	1	2.96E-14	2.96E-14	2.07E+10	0
Residual	997	1.43E-21	1.43E-24		
Total	998	2.96E-14			

	<i>Coefficients</i>	<i>Standard Error</i>	<i>t Stat</i>	<i>P-value</i>	<i>Lower 95%</i>
Intercept	0.003952	7.59E-14	5.21E+10	0	0.003952
X Variable 1	-1.9E-08	1.31E-13	-143953	0	-1.9E-08
	<i>Upper 95%</i>	<i>Lower 95.0%</i>	<i>Upper 95.0%</i>		
Intercept	0.003952	0.003952	0.003952		
X Variable 1	-1.9E-08	-1.9E-08	-1.9E-08		

x. Regression Analysis of α Local Sensitivity Test

SUMMARY OUTPUT

<i>Regression Statistics</i>	
Multiple R	1
R Square	1
Adjusted R Square	1
Standard Error	0
Observations	999

ANOVA

	<i>df</i>	<i>SS</i>	<i>MS</i>	<i>F</i>	<i>Significance F</i>
Regression	1	8.44E-30	8.44E-30	#NUM!	#NUM!
Residual	997	0	0		
Total	998	8.44E-30			

	<i>Coefficients</i>	<i>Standard Error</i>	<i>t Stat</i>	<i>P-value</i>	<i>Lower 95%</i>
Intercept	0.003952	0	65535	#NUM!	0.003952
X Variable 1	0	0	65535	#NUM!	0
	<i>Upper 95%</i>	<i>Lower 95.0%</i>	<i>Upper 95.0%</i>		
Intercept	0.003952	0.003952	0.003952		
X Variable 1	0	0	0		

-----END-----
